

# **Establishing a Viable and Reliable Proton-Induced Single Event Effect Test Methodology and Environment at iThemba LABS in South Africa**

by

Arno Barnard



*Dissertation presented for the degree of Doctor of Philosophy in the  
Faculty of Engineering at Stellenbosch University*

December 2020

---

# Plagiarism Declaration

---

1. Plagiarism is the use of ideas, material and other intellectual property of another's work and to present it as my own.
2. I agree that plagiarism is a punishable offence because it constitutes theft.
3. I also understand that direct translations are plagiarism.
4. Accordingly all quotations and contributions from any source whatsoever (including the internet) have been cited fully. I understand that the reproduction of text without quotation marks (even when the source is cited) is plagiarism.
5. I declare that the work contained in this dissertation, except where otherwise stated, is my original work and that I have not previously (in its entirety or in part) submitted it for obtaining any qualification.

A. Barnard <b>Initials and surname</b>	27 June 2020 <b>Date</b>

---

# Abstract

---

## **Establishing a Viable and Reliable Proton-Induced Single Event Effect Test Methodology and Environment at iThemba LABS in South Africa**

A. Barnard

*Promotor: Prof. W. H. Steyn*

*Faculty of Engineering*

*Department of Electrical & Electronic Engineering*

Dissertation: PhD (Electronic Engineering)

December 2020

This dissertation details the establishment of a new Single-Event Effect (SEE) testing environment at iThemba LABS (iTLL). The research intends to improve access to SEE testing for space-related research organisations and industries in developing countries and specifically South Africa. The development and verification of the proton-induced SEE testing of electronic systems facility at iTLL, using a novel Beam Loss Monitor (BLM) based dosimetry system, is presented. The facility design and dosimetry system response are simulated and verified through in-beam measurements using 66 MeV and 200 MeV protons. The design is adaptable and successfully applied to two different beam delivery points. The proton beam profiles achieved, using this design, had favourable uniformity with variances of less than 10% over the beam spot and a shadow area of with a maximum intensity of less than 0.34% of the spot intensity. The dual-BLM based dosimetry system provides a fast and accurate way to validate the beam profile before tests, in addition to monitoring the proton flux during tests. The system produced real-time measurements that closely matched simulated particle distributions. Additionally, the presented user guide aims to assist future SEE research at this facility. Through this research, the first high-energy proton-beam based SEE testing facility in Africa and the Southern hemisphere is realised, supporting research into SEEs in electronics and the associated mitigation techniques.

---

# Uittreksel

---

## Vestiging van 'n Lewensvatbare en Betroubare Proton Geïnduseerde Enkelgebeurteniseffek Toetsmetodologie en Omgewing by iThemba LABS in Suid-Afrika

A. Barnard

*Promotor: Prof. W. H. Steyn*

*Fakulteit Ingenieurswese*

*Departement Elektries & Elektroniese Ingenieurswese*

Proefskrif: PhD (Elektroniese Ingenieurswese)

Desember 2020

Hierdie proefskrif detailleer die vestiging van 'n nuwe Enkelgebeurteniseffek (EGE) toetsomgewing by iThemba LABS (iTTL). Die navorsing het ten doel gehad om toegang tot EGE-toetse vir ruimte-verwante navorsingsorganisasies en nywerhede in ontwikkelende lande en spesifiek Suid-Afrika te verbeter. Die ontwikkeling en verifikasie van die proton-geïnduseerde EGE-toetsing van elektroniese stelsels fasiliteit by iTTL, met behulp van 'n nuwe *Beam Loss Monitor (BLM)* gebaseerde dosimetriestelsel, word aangebied. Die fasiliteit se ontwerp en respons van die dosimetriestelsel word gesimuleer en geverifieer deur bundelmetings op beide 66 MeV en 200 MeV protone. Die ontwerp is aanpasbaar en is suksesvol op twee verskillende bundelafleweringpunte toegepas. Die proton bundelprofiel, behaal deur gebruik te maak van hierdie ontwerp, het 'n goeie eenvormigheid met afwykings van minder as 10% oor die bundelkol en 'n skaduarea met 'n maksimum intensiteit van minder as 0,34% van die kolintensiteit. Die dubbele-BLM gebaseerde dosimetriestelsel bied 'n vinnige en akkurate manier om die bundelprofiel te bevestig voor toetse, bykomend tot die monitering van die protonvloed tydens toetse. Die stelsel het intydse metings gelewer wat ooreenstem met gesimuleerde deeltjieverspredings. 'n Gebruikersgids word aangebied om toekomstige EGE navorsing by hierdie fasiliteit te ondersteun. Deur middel van hierdie navorsing word die eerste hoë-energie-protonbundel-gebaseerde EGE-toetsfasiliteit in Afrika en die Suidelike Halfrond gerealiseer, wat navorsing oor EGEs in elektronika, en die gepaardgaande versagtingstegnieke ondersteun.

---

# Acknowledgements

---

I would like to thank the National Research Foundation (NRF) iThemba LABS (iTLL) for supporting this research by providing access to their cyclotron facility. I would also like to thank iTLL management and staff, specifically R.Smit, R. Neveling, R. Nchodu, E.A. de Kock and J. Symonds, for supporting this research and assistance during Single-Event Effect (SEE) tests. I would also like to thank F. Smith for the continued collaboration and his use of the facility for SEE mitigation research.

I would like to thank my supervisor for his patience and belief in my ability to complete this work.

I want to thank my family for their continued interest, support, encouragement and understanding while working on this project.

Finally, I want to thank my wife, Cindy, for managing our family and lives while I spent hours working at home and the office. Without her continued support and belief in my abilities, this work would not have been possible.

---

# Contents

---

<b>Abstract</b>	<b>iii</b>
<b>Uittreksel</b>	<b>iv</b>
<b>Acknowledgements</b>	<b>v</b>
<b>Contents</b>	<b>vi</b>
<b>List of Figures</b>	<b>ix</b>
<b>List of Tables</b>	<b>xiii</b>
<b>Acronyms</b>	<b>xiv</b>
<b>1 Introduction</b>	<b>1</b>
1.1 Small satellites, their technology and development . . . . .	1
1.1.1 The low-cost driven small satellite context . . . . .	2
1.1.2 The use of Commercial-Off-The-Shelf components in the space context . .	4
1.2 African satellite and space industry context . . . . .	5
1.2.1 Need for radiation testing in South African satellite programmes . . . . .	6
1.2.2 The sensible radiation effects to test for . . . . .	7
1.2.3 Facility options for SEE testing . . . . .	8
1.3 Problem statements, research questions and contributions . . . . .	9
1.4 Dissertation Layout . . . . .	11
<b>2 Literature Study</b>	<b>12</b>
2.1 Overview of high-energy-particle induced radiation effects . . . . .	12
2.1.1 Brief overview of Single-Event Effects . . . . .	13
2.2 Radiation sources used for Single-Event Effect testing . . . . .	14
2.3 Radiation testing in the South African context . . . . .	16
2.3.1 Radiation testing in South Africa - historic . . . . .	16
2.3.2 iThemba LABS overview and available beams . . . . .	19
2.4 Viable beam and location selection at iTL . . . . .	21
2.4.1 The case for using proton beams at iTL . . . . .	21
2.5 Viability of various SEE test locations at iTL . . . . .	23
2.5.1 The Proton Therapy Vault . . . . .	23
2.5.2 The Neutron Therapy Vault . . . . .	24
2.5.3 The A-line with scattering chamber . . . . .	24

2.5.4	The D-line vault . . . . .	26
2.5.5	The F/G-line vault and S-line vault . . . . .	26
2.5.6	The N-line vault . . . . .	26
2.5.7	Comparison of location suitability . . . . .	27
2.6	Selected international test standards and guidelines . . . . .	29
2.6.1	JEDEC Standard JESD57 - 1996/2003 . . . . .	30
2.6.2	JEDEC Standard JESD234 - 2013 . . . . .	32
2.6.3	Test Method Standard MIL-STD-750 - 2013 . . . . .	35
2.6.4	Test Method Standard MIL-STD-883 - 2015 . . . . .	36
2.6.5	ESCC Basic Specification No. 25100, issue 2 of 2014 . . . . .	37
2.6.6	ASTM-F1192-11 - 2011 . . . . .	39
2.6.7	JEDEC Standard JESD89A - 2006 . . . . .	40
2.6.8	Discussion on standards and guides . . . . .	40
2.7	SEE proton test facilities overview . . . . .	41
2.7.1	JYFL/RADEF . . . . .	42
2.7.2	PSI - PIF . . . . .	42
2.7.3	North American Proton Facilities for Radiation Testing . . . . .	42
2.8	Overview of SEE rate prediction . . . . .	44
2.9	A proton-induced SEE test facility for iTL . . . . .	45
2.9.1	The standards for SEE testing for COTS-based systems in the South African context . . . . .	46
2.9.2	The viable approach for SEE testing at iTL . . . . .	46
2.9.3	Affordable development through utilising the available resources at iTL . . . . .	47
2.9.4	Practical suggestion to improve on initial SEE test attempts at iTL . . . . .	49
<b>3</b>	<b>Exploring a viable, sustainable and flexible SEE test setup for iTL</b>	<b>52</b>
3.1	SEE Proton Testing Facility Design Drivers and Evolution . . . . .	52
3.2	Simulations of the proton beam for candidate iTL locations . . . . .	53
3.2.1	The Proton Therapy Vault . . . . .	54
3.2.2	Simulating the A-line beam . . . . .	59
3.3	Dosimeter selection . . . . .	60
3.3.1	BLM device as a dosimeter for SEE testing . . . . .	61
3.3.2	Effectiveness of BLM device as a dosimeter in a pulsed proton beam . . . . .	61
3.4	Converting the A-line for SEE testing . . . . .	65
3.4.1	Beam delivery and configuration for in-air testing . . . . .	67
3.4.2	Vacuum window design . . . . .	69
3.4.3	Dosimeter positioning . . . . .	70
3.4.4	A-line in-air configuration summary . . . . .	71
3.5	Converting the NTV for SEE testing . . . . .	71
3.5.1	Proton beam delivery to NTV . . . . .	72
3.5.2	Beam, spot, and shadow forming . . . . .	73
3.5.3	DUT beam energy degrading . . . . .	75
3.5.4	Beam dosimetry, monitoring, and exposure control . . . . .	76
3.5.5	DUT positioning and interfacing . . . . .	77
<b>4</b>	<b>Implementations of a SEE test environment at iTL</b>	<b>79</b>
4.1	Experimental Verification at A-line . . . . .	79
4.1.1	Magnetic spreading of the proton beam . . . . .	79
4.1.2	Passive spreading of the proton beam . . . . .	86
4.2	Experimental Verification at NTV . . . . .	98
4.2.1	66 MeV proton beam in air, December 2017 . . . . .	98
4.2.2	200 MeV proton beam in air, October 2018 . . . . .	114

4.2.3	66 MeV proton beam in air, January 2019 . . . . .	128
4.3	Results summary . . . . .	139
<b>5</b>	<b>Conclusions</b>	<b>141</b>
5.1	Conclusion from conducted research . . . . .	141
5.1.1	SRIM simulation to design configuration . . . . .	142
5.1.2	Dual-BLM dosimetry system . . . . .	143
5.1.3	Quality and repeatability of the beamforming configuration . . . . .	144
5.1.4	Multiple device option using the DUT position platform . . . . .	146
5.1.5	Efficient use of beam time and application for beam time . . . . .	146
5.2	Limitations . . . . .	147
5.3	Future work . . . . .	148
	<b>Appendices</b>	<b>150</b>
<b>A</b>	<b>iTL SEE Test Guide</b>	<b>151</b>
A.1	iThemba LABS application for beam time . . . . .	151
A.2	iThemba LABS liaisons as of January 2020 . . . . .	151
A.3	Physical / Mechanical Set-up . . . . .	152
A.3.1	Test setup and common elements . . . . .	152
A.3.2	Preparing the A-line vault . . . . .	156
A.3.3	Preparing the N-line vault . . . . .	156
A.3.4	Preparing the Proton therapy vault . . . . .	156
A.3.5	Preparing the Neutron therapy vault . . . . .	157
A.3.6	Preparing the D-line vault . . . . .	157
A.3.7	Preparing the S-line vault . . . . .	158
A.4	Electrical/Communication set-up . . . . .	158
A.4.1	Power supply . . . . .	158
A.4.2	Communication / Data interfaces . . . . .	159
A.4.3	Beam Line Monitors . . . . .	159
A.4.4	DUT positioning platform and Camera . . . . .	159
A.4.5	USB devices via Raspberry Pi . . . . .	160
<b>B</b>	<b>Example SRIM Configuration File - TRIM.IN</b>	<b>161</b>
	<b>References</b>	<b>163</b>



---

## List of Figures

---

1.1	The 8 Edison Demonstration of Smallsat Networks (EDSN) flight units, flight spares and engineering units. . . . .	3
1.2	Map of on-orbit reset events for Sumbandilasat OBC. . . . .	5
2.1	General layout of iThemba LABS Cape Town Cyclotron facility up to 2019. . . . .	19
3.1	SRIM simulated beam distribution using at the A-line vault. . . . .	54
3.2	SRIM simulated energy spectra for various thickness plexiglass degraders after scattering a 66 MeV incoming beam using a 1mm Pb sheet. . . . .	55
3.3	Simulated elements and geometry of proton treatment nozzle in PTV. . . . .	55
3.4	SRIM simulated energy spectrum of transmitted protons after each of the first six PTV beam nozzle elements at iTL. . . . .	56
3.5	Beam shape after a) Vacuum Window and b) Reference Ion Chamber. . . . .	57
	(a) Vacuum Window . . . . .	57
	(b) Reference Ion Chamber . . . . .	57
3.6	Beam shape after a) MWIC and b) Lead scattering plate. . . . .	57
	(a) Multi-Wire Ionisation Chamber . . . . .	57
	(b) Lead scattering plate . . . . .	57
3.7	Beam shape after a) Quad Ion Chamber and b) Dual Transmission Chamber. . . . .	58
	(a) Quad Ion Chamber . . . . .	58
	(b) Dual Transmission Chamber . . . . .	58
3.8	Illustration of three different scenarios associated with three frequency ranges of SSC beam pulses with BLM sensor recovery. . . . .	62
3.9	Probability of proton strikes on the BLM detector area using SRIM data for NTV setup in 2019. . . . .	63
3.10	Expected BLM counts using SRIM data for NTV setup in 2019. . . . .	64
3.11	Probability of proton strikes on the BLM detector area for small beam currents. . . . .	65
3.12	Expected BLM counts for small beam currents. . . . .	65
3.13	Rendered 3D model of the vacuum connector for the A-line. . . . .	66
3.14	Conceptual design of SEE proton testing beam delivery system for the A-line. . . . .	68
3.15	Remotely controlled DUT positioning platform in the A-line scattering chamber. . . . .	68
3.16	Beam line elements at (a) upstream and (b) downstream positions in A-line. . . . .	70
	(a) Pb sheet for passive spreading (left) and manufactured upstream vacuum window (right). . . . .	70
	(b) Manufactured downstream vacuum window (left), second scintillating target, and in-beam BLM. . . . .	70
3.17	Conceptual beam delivery design for SEE testing in Neutron Vault. . . . .	72
3.18	Diagram for the generic geometry of the collimator configuration. . . . .	74

3.19	User interface software for the linear movement DUT position platform for SEE testing in the NTV. . . . .	77
4.1	Configuration setup for a) Botma's 2013, and b) Smith's 2015 SEE tests with the central scintillation target in its ladder, and the mounted Device Under Test (DUT) boards. . . . .	81
	(a) CubeComputer alignment setup . . . . .	81
	(b) Field Programmable Gate Array (FPGA) development board alignment setup	81
4.2	The resulting beam spot as indicated by the scintillation target using (a) the magnetic spreading technique, and (b) passive spreading. . . . .	83
	(a) Magnetically spread beam spot . . . . .	83
	(b) Passively spread beam . . . . .	83
4.3	Configuration setup for beam profile characterisation measurements at the A-line vault. . . . .	88
4.4	Geometry of the setup for beam characterisation measurements at the A-line vault. .	88
4.5	SRIM simulated beam spot intensity for 66 MeV protons in A-line configuration. . .	90
4.6	SRIM simulated beam profiles with fitted Gaussian functions for 66 MeV protons in A-line configuration. . . . .	90
4.7	SRIM simulated beam profiles at target plane and arc extremity plane for 66 MeV protons in A-line. . . . .	91
4.8	SRIM simulated beam profiles at target plane and arc extremity plane for 66 MeV protons in A-line. . . . .	92
4.9	Raw measurements to determine optimal beam intensity for A-line profile beam profile measurement. . . . .	93
4.10	First profile measurements with interpolated (and mirrored) data points, and the Gaussian function fit to the dataset. . . . .	94
4.11	In-beam BLM data over all runs. . . . .	95
4.12	Fixed BLM data over all runs. . . . .	96
4.13	Gaussian fit of measured data from calibration run 2. . . . .	97
4.14	Central beam spot measurements with fitted Gaussian from full width data. . . . .	97
4.15	Geometry of the collimator and BLM configuration for 66 MeV SEE tests at the Neutron Therapy Vault (NTV). . . . .	99
4.16	Configuration details of beam delivery system for 66 MeV SEE test at NTV. . . . .	100
	(a) Havar exit window with protective carbon cap in the background, the 1 mm Pb sheet mounted across the opening, and collimator 1 and 2 in the foreground. 100	
	(b) From right to left the 1 mm Pb sheet, collimator 1 and collimator 2. The current reference BLM is visible in the foreground. . . . .	100
4.17	Configuration setup for beam profile characterisation measurements and SEE tests at the NTV. . . . .	100
4.18	The linear movement positioning platform mounted on the support rails with the mounted in-beam BLM, fourth collimator, and degrader sheet holder visible. . . . .	102
4.19	SRIM simulated beam spot intensity for 66 MeV protons, from (a) Point beam source and (b) 3 mm Gaussian beam, in NTV configuration. . . . .	104
	(a) Point beam, no degrader . . . . .	104
	(b) 3 mm Gaussian beam, no degrader . . . . .	104
4.20	SRIM simulated beam spot intensity for 66 MeV protons, from (a) Point beam source and (b) 3 mm Gaussian beam, in NTV configuration using 8 mm energy degrader. .	105
	(a) Point beam, 8 mm degrader . . . . .	105
	(b) 3 mm Gaussian beam, 8 mm degrader . . . . .	105
4.21	SRIM simulated beam spot intensity for 66 MeV protons, from (a) Point beam source and (b) 3 mm Gaussian beam, in NTV configuration using 16 mm energy degrader. .	105
	(a) Point beam, 16 mm degrader . . . . .	105
	(b) 3 mm Gaussian beam, 16 mm degrader . . . . .	105

4.22	SRIM simulated beam spot intensity for 66 MeV protons, from (a) Point beam source and (b) 3 mm Gaussian beam, in NTV configuration using 24 mm energy degrader. . . . .	106
(a)	Point beam, 24 mm degrader . . . . .	106
(b)	3 mm Gaussian beam, 24 mm degrader . . . . .	106
4.23	NTV beam calibration measurement. . . . .	107
4.24	First horizontal wide-beam profile measurement before aligning the data with the position information. . . . .	108
4.25	Second horizontal wide-beam profile measurement. . . . .	109
4.26	Position aligned data of the second horizontal wide-beam profile measurement. . . . .	109
4.27	Central beam profile measurement in both horizontal and vertical planes. . . . .	110
4.28	Central beam horizontal profile, averaged and normalised. . . . .	111
4.29	Central beam vertical profile, averaged and normalised. . . . .	112
4.30	Normalised horizontal and vertical central beam spot profile showing good uniformity of the beam over the beam spot. . . . .	112
4.31	Details of mechanical configuration elements for the 200 MeV proton test October 2018 in NTV. . . . .	116
(a)	The current author levelling the Proton Radiotherapy Verification and Dosimetry Applications (PRAVDA) bench during preparation. The linear DUT positioning platform can be seen mounted on the right end of the bench. . . . .	116
(b)	3.46 mm Pb sheet mounted in holder to the left, with collimators 1 and 2 to the right. . . . .	116
4.32	Python script inputs and calculated results for collimator placement for the 2018 200 MeV SEE test at NTV. . . . .	117
4.33	Geometry of the collimator and BLM configuration for 200 MeV SEE tests at the NTV. . . . .	117
4.34	SRIM simulated beam spot intensity for 200 MeV protons, with a) 2.8 m air b) 4 m air, in NTV configuration using 1 mm Pb spreader. . . . .	119
(a)	1 mm Pb spreader, 2.8 m air . . . . .	119
(b)	1 mm Pb spreader, 4 m air . . . . .	119
4.35	SRIM simulated beam spot intensity for 200 MeV protons, with a) 2.8 m air b) 4 m air, in NTV configuration using 2 mm Pb spreader. . . . .	119
(a)	2 mm Pb spreader, 2.8 m air . . . . .	119
(b)	2 mm Pb spreader, 4 m air . . . . .	119
4.36	SRIM simulated beam spot intensity for 200 MeV protons, with 4 m air, in NTV configuration using 3 mm Pb spreader. . . . .	120
4.37	5 mm×5 mm averaged centre slice of SRIM simulated beam spot intensity for 200 MeV protons. . . . .	121
4.38	Horizontal beam spot profile measurement of 200 MeV proton beam at 10 nA. . . . .	122
4.39	Raw per second sampled data from in-beam and reference BLMs. . . . .	123
4.40	Horizontal profile measurement showing the in-beam BLM, normalised in-beam BLM (to reference) and reference BLM values. . . . .	123
4.41	Vertical profile measurement showing the in-beam, normalised (to reference) and reference BLM values. Beam current at 0.5 nA. . . . .	124
4.42	Combined horizontal and vertical beam spot profile measurements, both normalised to the reference BLM values. Beam current at 0.5 nA. . . . .	125
4.43	Detail of configuration elements for 66 MeV experiment in iTL NTV, January 2019. . . . .	129
(a)	Configuration elements: (1) Reference BLM, (2) Pb sheet, (3) Collimators 1 and 2, (4) Collimator 3, (5) Collimator 4, (6) DUT positioning platform, (7) PRAVDA bench. . . . .	129
(b)	In-beam BLM and its calibration box mounted to the DUT positioning platform. . . . .	129
(c)	Reference BLM position for 66 MeV SEE tests at the NTV, January 2019. Good photos of the configuration help to verify measurements. . . . .	129

4.44	Python script inputs and calculated results for collimator placement for the 2019 66 MeV SEE test at NTV. . . . .	130
4.45	Geometry of the collimator and BLM configuration for 66 MeV SEE tests at the NTV, January 2019. . . . .	130
4.46	The new prototype BLM pulse logger using prototype signal conditioning circuitry and an Arty development board. . . . .	131
4.47	BLM calibration pulse counts showing (a) a settling period at start-up, and (b) a stable calibration count rate, for 66 MeV experiment in iTL NTV, January 2019. . . . .	132
	(a) In-beam and reference BLM pulse rates showing decreasing transient behaviour immediately after start-up. . . . .	132
	(b) In-beam and reference BLM pulse rates showing steady state values after roughly 800 seconds. . . . .	132
4.48	Reference BLM to beam current over a range of currents. . . . .	133
	(a) In-beam BLM average values as a function of the beam current supplied. Significant saturation of the measurement starts occurring above 15 nA. . . . .	133
	(b) Reference BLM average values as a function of the beam current supplied. The relationship is very close to perfectly linear, as expected. Linear function fit to the measured data is shown. . . . .	133
4.49	Beam intensity measurements showing beam stability for (a) the in-beam BLM only, and (b) the reference BLM only, at 2 nA for 66 MeV experiment in iTL NTV, January 2019. . . . .	134
	(a) In-beam BLM stability measurement showing some drift over a period of roughly 10 minutes. . . . .	134
	(b) Reference BLM stability measurement showing significant variation and a similar drift pattern to the in-beam values over a period of roughly 10 minutes. . . . .	134
4.50	Combined central profile - Raw in-beam BLM values (this is true dose over spot) - 2 nA. . . . .	135
4.51	Wide horizontal profile - Raw in-beam BLM and reference BLM values - 2 nA. . . . .	136
4.52	Monitored beam beam intensity using both BLMs during device exposure. . . . .	137
	(a) Two 5 nA runs show there are some beam drift and variation present. The exposure duty cycle, of roughly 30%, for this microprocessor experiment, is also evident. . . . .	137
	(b) Two 15 nA runs show there is some beam drift and variation present. The exposure duty cycle, of roughly 15%, is much shorter compared to the 5 nA runs. . . . .	137
4.53	Latent radiation level immediately after beam is switch off at the end of a device exposure. . . . .	137
	(a) Monitored latent radiation during 25 nA run. . . . .	137
	(b) Monitored latent radiation during 30 nA run. . . . .	137
A.1	Conceptual test set-up diagram. Set-up seen from above. . . . .	153

---

## List of Tables

---

2.1	Summary of evaluation of different SEE testing locations at iTL, valid up to 2017. . . . .	27
2.2	Summary of evaluation of different SEE testing locations at iTL, valid from 2017. . . . .	28
2.3	Key space radiation test standards. . . . .	29
2.4	Key space radiation test guidelines. . . . .	30
2.5	North American Proton Facility options (2016) . . . . .	43
3.1	Summary of proton energy statistics of 200 MeV proton point-beam after each PTV nozzle element. . . . .	56
3.2	Summary of proton distribution statistics of 200 MeV proton point-beam after each PTV nozzle element. . . . .	58
3.3	Summary of proton energy and distribution statistics of 66 MeV proton point-beam passing through Al and Pb scattering sheets of varying thickness and 500 mm air. . . . .	60
3.4	Analysis for Al and Pb scattering sheets of varying thickness and 500 mm air. . . . .	60
3.5	Stopping Range of Ions in Matter (SRIM) results: Vacuum window material + 1.4 m Air(ICRU-104) effects on 66 MeV protons. . . . .	70
4.1	Beam activation times, exposure duration, and effects observed at iTL A-line vault experiment on 2013/10/13. . . . .	83
4.2	Normalised In-beam BLM pulse counts for each lateral position during iTL A-line vault experiment on 2016/06/09. . . . .	92
4.3	Inputs and calculated results for collimator placement for NTV experiment on 2017/12/19. DUT distance, spot diameter, and collimator dimensions are all inputs. . . . .	101
4.4	Beam energy mean ( $\mu_{Energy}$ ) and energy standard deviation ( $\sigma_{Energy}$ ) from SRIM simulation results for varying thickness degraders for NTV experiment on 2017/12/19. . . . .	103
4.5	SRIM layer material stack and thickness configuration for beam spot simulation of NTV experiment on 2017/12/19. . . . .	104
4.6	BLM measurements for beam intensity calibration at iTL neutron therapy vault experiment on 2017/12/19. . . . .	107
4.7	Summary of activities and approximate time spent thereon during SEE test window in iTL NTV, December 2017. . . . .	113
4.8	Mean, standard deviation and mean loss % of beam energy distributions for different thickness Pb sheets and different distances to DUT. . . . .	120
4.9	Measurements of the beam shadow during device exposure using 200 MeV protons, at iTL NTV, October 2018. . . . .	125
4.10	Summary of activities and approximate time spent thereon during SEE test window in iTL NTV, October 2018. . . . .	126
4.11	Beam intensity averages and ratios for beam currents ranging from 5 nA to 30 nA for January 2019 experiment. . . . .	132

---

# Acronyms

---

- <sup>60</sup>Co** Cobalt-60. 17
- 8P8C** 8 position 8 contact. 102
- ASTM** American Society for Testing and Materials. 29, 40
- BJT** Bipolar Junction Transistor. 7, 13
- BLM** Beam Loss Monitor. iii, iv, x–xiii, 11, 49, 50, 52, 61, 62, 64, 65, 68, 70, 71, 76–78, 86–96, 98–103, 106–108, 110–118, 121–125, 127–141, 143–149, 152, 154–159
- BNC** Bayonet Neill–Concelman. 102
- CAN** Controller Area Network. 66, 82, 84
- CC** Current-to-Count. 107
- CCTV** Closed Circuit Television. 78, 80, 85, 86, 89, 101, 118
- CMOS** Complementary Metal Oxide Semiconductor. 7, 14, 38
- COTS** Commercial-Off-The-Shelf. 2–5, 10, 14, 15, 17, 20, 21, 30, 45, 46, 82, 127, 134, 149
- DAQ** Data Acquisition. 88, 89, 96, 102, 113, 114, 117, 118, 122, 127–129, 133, 136, 138, 139, 143, 144, 148
- DD** Displacement Damage. 7, 14, 15, 32–34, 127
- DoD** Department of Defence. 29, 35, 40
- DSP** Digital Signal Processor. 17, 18
- DUT** Device Under Test. x, xi, xiii, 17, 18, 20, 23, 25, 26, 30–35, 37–39, 41, 42, 44, 45, 47, 49, 50, 53, 54, 56, 58, 59, 61, 66–68, 71–78, 80–87, 89, 94, 96, 99–102, 106, 108–111, 113–121, 125–127, 129, 130, 134–137, 139–141, 143, 145–148, 152–159
- EDAC** Error Detection and Correction. 84
- ESA** European Space Agency. 6, 29, 41, 42, 45
- ESCC** European Space Components Coordination. 29, 37
- FET** Field Effect Transistor. 31

- FPGA** Field Programmable Gate Array. x, 18, 20, 66, 81, 82, 84, 113, 114, 129, 139, 142, 147, 148
- GCR** Galactic Cosmic Ray. 46
- IC** Integrated Circuit. 14, 15, 73
- ISS** International Space Station. 2, 4
- iTL** iThemba LABS. iii–v, xi–xiii, 6, 9–11, 16–28, 30, 41, 45–47, 49–53, 61, 65, 67, 69–71, 75, 79, 81, 83, 84, 86, 88, 89, 92, 96, 98, 102, 107, 113–115, 117, 120, 125–129, 132, 134, 139–144, 146–149, 151, 152, 155, 156, 159
- IUCF** Indiana University Cyclotron Facility. 4, 42
- JEDEC** Joint Electron Device Engineering Council. 29, 33, 40
- JESD** JEDEC Standard. 30, 31, 33, 34, 40
- LAN** Local Area Network. 77, 118
- LEO** Low Earth Orbit. 7, 12, 13, 16, 17, 21, 37, 46, 84
- LEP** Low-Energy Proton. 4
- LET** Linear Energy Transfer. 16, 31, 38, 39, 148
- LSP** Lead Scattering Plate. 57–59
- MBU** Multi-Bit Upset. 13, 14, 32, 40, 47
- MIP** Minimum Ionising Particle. 61, 131
- MOSFET** Metal–Oxide–Semiconductor Field-Effect Transistor. 13, 14, 36
- MWIC** Multi-Wire Ionisation Chamber. 58, 156
- NASA** National Aeronautics and Space Administration. 2, 3, 6, 8, 21, 29, 30, 41, 42, 44
- NIEL** Non-Ionising Energy Loss. 7
- NMU** Nelson Mandela University. 146, 159
- NRF** National Research Foundation. v, 9
- NTV** Neutron Therapy Vault. x–xiii, 20, 21, 24, 26–29, 47, 52, 64, 71–73, 76, 77, 79, 90, 98–100, 103, 104, 107, 113, 115–118, 120, 122, 124–132, 134, 135, 139, 141, 144–147, 157, 158
- OBC** On-Board Computer. 4, 6, 10, 142
- OS** Operating System. 82
- PAC** Programme Advisory Committee. 47, 114, 115, 147, 148, 151
- PBS** Pencil Beam Scanning. 43
- PC** Personal Computer. 77, 85
- PCB** Printed Circuit Board. 26, 73, 139
- PRaVDA** Proton Radiotherapy Verification and Dosimetry Applications. xi, 116, 118, 128, 129, 145, 147, 157, 158

- PTV** Proton Therapy Vault. 17, 18, 20, 23, 27, 28, 47, 52–54, 56, 69, 71–73, 98, 103, 115, 156–158
- RHA** Radiation Hardness Assurance. 4, 6, 12, 13, 149
- RIC** Reference Ionisation Chamber. 57, 58
- SEB** Single-Event Burnout. 7, 16, 32, 34, 36, 38, 40
- SEE** Single-Event Effect. iii, v, ix–xiii, 4–34, 36–41, 44–54, 61, 62, 64–68, 70–73, 75–77, 79–87, 96–100, 103, 106, 112–118, 120, 126–131, 134, 137–149, 151–155, 157, 158
- SEFI** Single-Event Functional Interrupt. 8, 14, 32, 33, 37, 40, 47, 127, 138–140
- SEGR** Single-Event Gate Rupture. 7, 16, 31, 32, 34, 36, 38, 40
- SEL** Single-Event Latchup. 6–8, 14, 16, 21, 31–34, 38–40, 46, 47, 53, 84, 115, 127, 140
- SER** Soft Error Rate. 40
- SET** Single-Event Transient. 7, 8, 13, 14, 32, 37, 38, 40, 47, 82, 84, 140, 142
- SEU** Single-Event Upset. 6–8, 13, 14, 16–18, 32, 38–40, 46, 65, 83, 84, 113, 115, 127, 128, 140
- SNL** Sandia National Laboratories. 29, 30
- SPC** Solid-Pole Cyclotron. 19
- SPENVIS** SPace ENVironment Information System. 45
- SRAM** Static Random-Access Memory. 4, 6, 20, 113, 126
- SRIM** Stopping Range of Ions in Matter. xiii, 50–56, 59, 60, 62, 63, 69, 70, 73, 76, 86, 89–91, 93, 95, 98, 99, 101, 103, 104, 106, 114, 115, 118, 120, 121, 124, 127, 139, 141–145, 148, 153, 154
- SSC** Separate Sector Cyclotron. 18–22, 25, 61, 62, 75, 81, 89, 93, 102, 115, 118, 122, 133, 136, 138, 140, 146, 147, 149
- TID** Total Ionisation Dose. 4, 6, 7, 13, 15–17, 30, 32–34, 36–38, 84, 135, 143
- UART** Universal Asynchronous Receiver-Transmitter. 66
- USA** United States of America. 9, 29, 35, 40
- USB** Universal Serial Bus. 66, 158, 160



---

# CHAPTER 1

## Introduction

---

Space missions epitomise extreme engineering in many ways. From fuelling the cold-war to putting the first men on the moon, and recently landing on an asteroid, space missions have often served as powerful inspirational platforms. Since the 1957 launch of Sputnik 1, artificial satellites have been an integral part of driving innovation, research, education, technology spin-offs, and commerce in both developed and, in recent years, developing countries. The impact of technology spin-offs due to space-based missions is significant, as detailed in [1].

Every nation, or commercial entity, that wants to embark on space system development must confront the reality that space is a challenging operational environment for engineered objects. The difficulty and risk of space missions are well known and system failures all too common. Due to the inaccessibility to most space systems after launch, the impact of any system failure is typically much more severe than for terrestrial systems that can be repaired or replaced.

*This chapter introduces the changing landscape of satellites becoming smaller and much more accessible to developing nations, while the technology these satellites rely on pose a significant risk to their mission and challenges to their designers. The South African context and need for radiation response data are discussed, and the solution of establishing an appropriate local accessible Single-Event Effect (SEE) test environment at iThemba LABS (iTTL) is presented.*

### 1.1 Small satellites, their technology and development

Smaller, more affordable satellites provide access to space for developing nations and organisations with limited budgets, like universities. The technology, driving miniaturisation and cost reduction, is unfortunately not designed for the harsh radiation environment these systems are exposed to during operation, causing operational errors and failures.

### 1.1.1 The low-cost driven small satellite context

*The proliferation of small satellites, in particular CubeSats, have resulted in space becoming very accessible to a variety of users over the last 15 years, including many developing countries. This section gives a brief overview of the developments leading to small satellites and the rise of their popularity.*

Soon after the cold war space race began, the dominant philosophy to satellite design was 'bigger is better', since this approach allowed for more redundancy and capability per satellite. For many years this philosophy was maintained due to the immense expense of launching a satellite and the coupled limited availability of launch opportunities. Two consumer technology developments forced the space industry to change this philosophy: cell phones, automobiles.

Since the first cell phones came to market in 1983 [2], the cellular industry has been part of numerous electronic technology revolutions in recent times. Together with automotive electronics, these consumer products drove the development of smaller, lower power, reliable computing electronics and sensors.

The use of these new generation Commercial-Off-The-Shelf (COTS) components allowed satellites to be much smaller while maintaining the same capabilities, that resulted in them having much less mass and therefore incurring much lower launching costs. The advent of private rocket companies, of which currently SpaceX is arguably the most influential, have caused satellite launch costs to reduce by up to 50% [3]. Since 2013 private companies have started brokering launch opportunities for CubeSats from the International Space Station (ISS) [4]. These developments have reduced the cost of access to space significantly, providing new opportunities for traditional space organisations like the National Aeronautics and Space Administration (NASA), researchers with limited budgets, and for entrepreneurs to commercialise space [5].

Probably the most tangible impact of electronic miniaturisation in space systems is the proliferation of nanosatellites, so-called due to their low mass. Satellites can be categorised by mass, although there is currently no consensus on the mass categories. One NASA web page [6] classifies small satellites to have a mass less than 180kg and nanosatellites ranging from 1-10kg. CubeSats, so-called by the original designers Heidt et al.[7], are nanosatellites.

The proliferation of CubeSats is evident from the data provided by Swartwout's Cubesat Database [8]. Swartwout also analyses the enormous impact this new technology has in the space industry in [9]. In the last fifteen years, 712 CubeSats were deployed in space from June 2003 to April 2018 [10]. CubeSats became popular due to their loosely defined electrical standard, with some developers claiming there is no such thing as a CubeSat standard while providing some level of standardisation of the mechanical design format [11]. The latter allows launch service providers, like Innovative Solutions In Space [12], to provide standardised launch interfaces for CubeSat developers, who do not have to design a custom launch vehicle adapter system. Figure 1.1 shows an example of multiple identical CubeSats developed by NASA to demonstrate small satellite networks in space [13].

One of the other attractions for researchers to CubeSats is, as mentioned, the loosely defined electrical standard that allows researchers, and university teams, in particular, to explore the use of new generation consumer electronic components (referred to as COTS components by the aerospace community) in satellite systems. Using CubeSats as test vehicles for science and

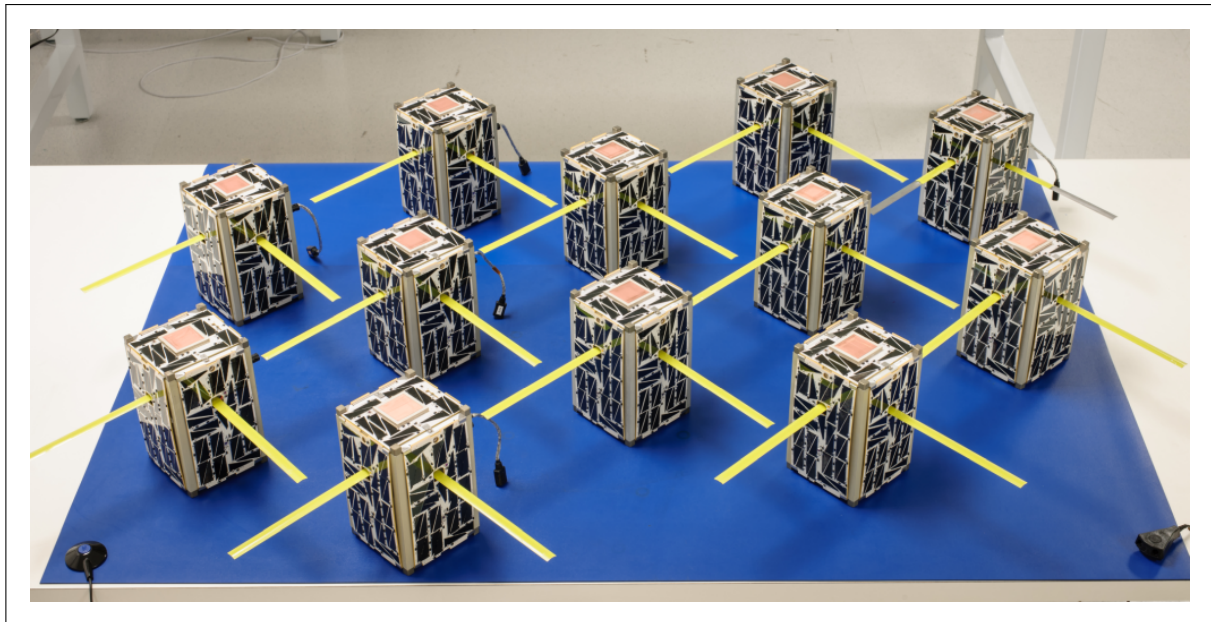


**Figure 1.1:** The 8 Edison Demonstration of Smallsat Networks (EDSN) flight units, flight spares and engineering units. The satellites are all 2U CubeSats measuring roughly 100 mm  $\times$  100 mm  $\times$  200 mm. Image Credit: NASA Ames Research Center [13].

exploration allows research into component reliability, system complexity, and constellation flying to be conducted at a fraction of the cost compared to using traditional larger satellite platforms.

Through analysing [8], CubeSat projects started with small teams like universities and start-up companies with missions aimed at technology demonstration, gaining experience, education, and high-risk missions. The timelines involved in development are often very short and budgets limited. The mission and orbit options often result in a shorter design life for CubeSats. However, with more commercial and scientific missions in recent years, the need for a longer design life increased. As such CubeSats continue to push the boundaries of new technology and system performance. The demand for radiation tolerance information on components increases with increased design life and increased mission requirements.

**Conclusion:** With short development cycles, the timelines for radiation testing of candidate CubeSat electronic components are also short. Radiation testing of CubeSat (almost exclusively COTS-based) electronics should ideally be very accessible and have fast turnaround times.

### 1.1.2 The use of Commercial-Off-The-Shelf components in the space context

*Their radiation tolerance determines the scope in which COTS components can be used for space applications. In this section, the risk of using COTS components and their application scope in CubeSat missions are discussed.*

COTS components are the commercial components anyone can buy from suppliers. In contrast, radiation-hardened components are specifically designed for use in environments with high levels of radiation and often have restricted distribution. Compared to COTS parts, radiation-hardened versions can cost up to  $1000\times$  more, making them extremely inaccessible to budget-constrained space projects.

Even though COTS components can be sensitive to radiation-induced errors, when coupled with an often relatively benign radiation environment, e.g. the ISS orbit into which many nanosatellites are deployed, the low cost and availability of COTS components make them very attractive options for nanosatellite missions. The impact of radiation effects on missions is further reduced by some COTS components exhibiting reasonable tolerance to specific radiation effects [14]. However, even with the lowered radiation effects risk, radiation effects mitigation cannot be ignored for these type of missions. A few compendiums on radiation tolerance of COTS components have been published (of which [14] is one example) that shows the requirement for continued testing of COTS components.

Radiation effects mitigation for COTS-based space systems is still a critical requirement. The number of SEEs experienced by the On-Board Computer (OBC) of a micro-satellite designed exclusively with COTS components [15], is shown in Figure 1.2. Clearly, with this number of events, if no effort were put into the mitigation of SEEs, the mission would have had little chance of success. With sensible mitigation techniques applied to the design of the OBC, the satellite mission was a success, and the system was fully operational, producing 1909 high-resolution images of the earth [16]. Although sufficient SEE mitigation can be done by applying general mitigation techniques, full Radiation Hardness Assurance (RHA) is the only effective way to ensure spacecraft are adequately protected against radiation damage effects.

Many investigations have been, and are being, conducted into effective RHA procedures, models, and acceptable margins to allow for feasible COTS component operation in spacecraft. More recently CubeSats have become a direct component in the RHA chain. In [17], a CubeSat was used as a platform for validating RHA models and assumptions of radiation-induced errors. The RHA approach applied to a CubeSat, called RadFxSat, using COTS components is from [17]. The RadFxSat mission evaluated the contribution of Low-Energy Proton (LEP) induced errors to the overall in-orbit error rates.

RadFxSat's bus components were tested for Total Ionisation Dose (TID) tolerance up to 10 krad(Si) using a  $^{137}\text{Cs}$  source. Proton-induced SEE tests were conducted at a system level at Indiana University Cyclotron Facility (IUCF)'s RB1 line. Low energy proton tests were conducted on the payload's sensitive Static Random-Access Memory (SRAM) at the Vanderbilt Pelletron.

COTS components present multiple challenges for the RHA community, including limited information about device structure, variability in manufacturing, and a relatively short product life cycle. One way devices are evaluated for radiation tolerance is to do complete three dimensional (3D) analysis of radiation-induced charge using radiation transport codes in combina-

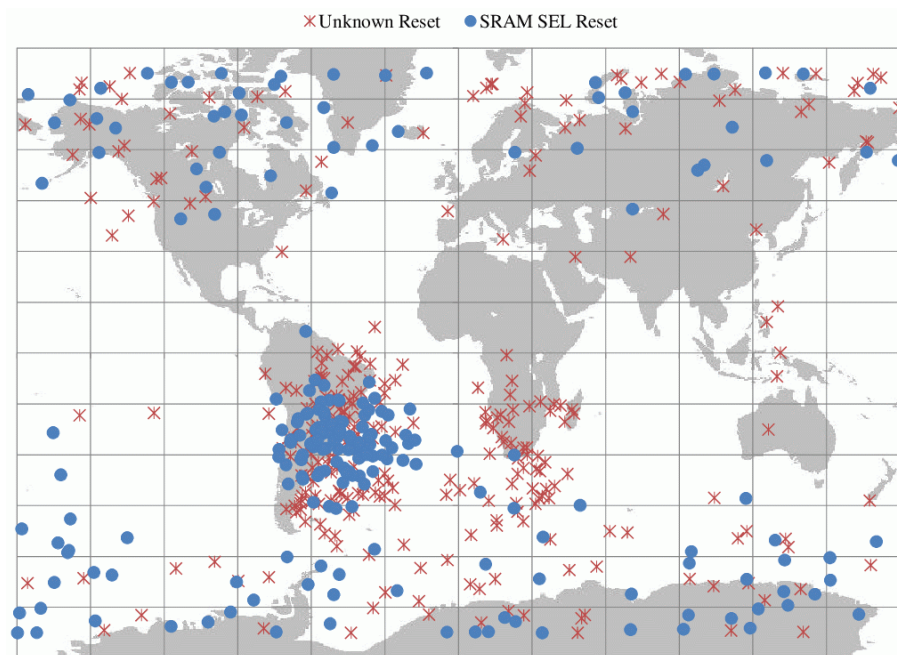


**Figure 1.2:** Map of on-orbit reset events for Sumbandilasat OBC during two years of operations in space [15]. Events are grouped in SRAM SEL events and unknown reset events. A large number of reset events are evident and the events are concentrated in the South Atlantic Anomaly and polar regions.

tion with Technology Computer-Aided Design (TCAD) tools. However, since the COTS market is highly competitive, *structure design details at the silicon level of components are rarely available* to researchers and designers. The manufacturing environment of COTS components *will allow for manufacturing variability* within the device's electrical specifications. However, small variability in design that might not influence the device's electrical characteristics can significantly affect the radiation response of a device. Finally, many COTS devices *have much shorter product life cycles* than their high-reliability counterparts, which is mainly due to the high rate at which the consumer electronics market is changing.

**Conclusion:** The nature and economics of COTS components make it challenging to estimate radiation response resulting in the need for SEE testing to provide data on device sensitivity to radiation effects.

## 1.2 African satellite and space industry context

*African countries have in the last two decades embarked on several projects, research and commercial, involving the development of space-based electronic systems and satellites. This effort has mostly been in collaboration with established space-faring nations [18] since there are limited local testing and integration facilities, and no launch facilities on the continent.* African countries have developed some capability in developing space systems. Most notably South Africa, where various institutions, including the South African government, have developed five micro- (and nano-) satellites, since 1992, that operated successfully in space [19; 15; 20]. Although some Total-Ionization-Dose testing was done on components used in these satellite projects [21], no SEE testing was

done until very recently. With six South African companies and three research groups at leading universities, focused on the development of satellite systems, the need for reliable SEE testing has grown significantly.

### 1.2.1 Need for radiation testing in South African satellite programmes

According to Peterson [22], the first Single-Event Upset (SEU) was observed on a satellite in 1975 and from 1979, IBM and others started programmes to test microelectronics, using alpha emitters and terrestrial cosmic rays, for sensitivity to ionising radiation. Peterson also lists some 58 satellites where SEEs have had an impact. To this list, at least three satellites built in South Africa since 1992 can be added.

SUNSAT, operational 1999-2001, had SRAM SEUs that necessitated a rewrite of on-board computer software to keep the satellite working. SRAM micro Single-Event Latchups (SELs) affected Sumbandila-Sat, operational 2007-2009, which again required software and operational improvements to manage the problem. Similar SRAM sensitivity was observed on SaudiSat 3, built by a former South African satellite company SunSpace for KACST (King Abdulaziz City for Science & Technology) Space Research Institute. There is also a high likelihood that SumbandilaSat became nonoperational due to an SEU in the power management unit. These radiation-induced problems were not unexpected since none of the electronic parts used for either of the mentioned satellites was explicitly tested for SEEs. The major contributing factor for not doing any SEE testing on previous South African satellites was budgetary. There was not enough time and money budgeted in these programmes to support lengthy, and costly SEE testing at international facilities.

Similarly, none of the SUNSAT electronic devices was tested for TID sensitivity, with device selection based on published results of TID tests done on commercial components by researchers and space agencies like the NASA and the European Space Agency (ESA). Progress was made during the SumbandilaSat programme with regards to TID testing, where many candidate electronic devices were successfully tested [21].

TID testing was established in the South African satellite and research communities during the SumbandilaSat project. A TID testing environment was developed using a high activity  $^{60}\text{Co}$  source available at a local Agricultural Research Council facility. Since the SumbandilaSat project, researchers and industry have followed a low-cost TID test methodology described in [21] for TID RHA. The test methods and results agreed well with international practices and understanding. Currently, there is no reason to believe that any of the satellite systems built have had any TID related issues.

Regarding SEE testing, no official tests were done as part of the design cycle of a South African satellite project, except for CubeComputer, which was done as an afterthought, when through this research effort, SEE tests at iTL became possible. However, on SUNSAT, SumbandilaSat and SaudiSat 3 various issues with SEEs have been observed, that caused reworking and rewriting of OBC software to keep the satellites operational. A more risky approach is acceptable the first time, but given the problems experienced, the failure risk of future missions should be lowered. Lowering the mission risk is especially important as the stakes are raised, with future commercial ventures and larger satellites.

The void left regarding SEE testing for satellite candidate electronic devices, prompted most of the research presented in this dissertation. South Africa, as a developing country, aiming to keep contributing to satellite technology, must start understanding and applying radiation hardness assurance as part of our satellite projects.

**Conclusion:** It is essential that SEE testing be investigated and the capability to conduct these test in an acceptable way be developed in South Africa.

### 1.2.2 The sensible radiation effects to test for

The high energy particles in Low Earth Orbit (LEO) interacts with spacecraft and affect the materials and electronic components through two primary mechanisms. The first mechanism is through lattice displacement, where the atoms of the material are displaced from its original position and in the process changing the material properties. The second mechanism is through ionising effects from the charged high energy particles depositing charge as they move through materials and leave behind ion tracks [23].

The resulting effects from the two mechanisms can be grouped as Displacement Damage (DD) and Non-Ionising Energy Loss (NIEL), TID, and SEEs. TID effects in semiconductor devices being the accumulation of trapped charges, is a slow degrading effect on semiconductors. DD is mainly a concern for silicon based imaging devices, solar panels, and some Bipolar Junction Transistor (BJT)s [24], while SEEs affect Complementary Metal Oxide Semiconductor (CMOS) based digital and power electronics.

TID tests can still be done in South Africa at little cost and with high repeatability and reliability in results. Of course, improvements can be made, since on some aspects TID tests are not fully following the best-suggested practices, especially regarding underestimation of received dose. Underestimating the dose received is not so serious in this context as it results in more conservative testing. The most significant risk of underestimating the received dose is that a suspect device, one that fails close to the required total dose, might be needlessly disqualified for space use.

For the remaining effects, to keep the scope of this research effort manageable while aiming to maximise the application scope, it was decided to first focus on SEE testing in this work and expand to DD and NIEL research in future. Expanding to DD and NIEL should not change the basic methodology much, since testing for both typically require a high energy particle accelerator beam, leaving SEE testing aspects to be further explored.

How SEE tests should be done for SEL, SEU, Single-Event Gate Rupture (SEGR), Single-Event Burnout (SEB), Single-Event Transient (SET) differ greatly, according to international standards and guidelines, that is further discussed in chapter 2. Certain of these SEEs can only be observed reliably under very specific test conditions. A good example is SEL: It can be reliably observed in sensitive devices when using heavy-ion beams, less so when using proton beams with energies less than 180 MeV [25]. SEE's dependency on particle type and energy places very specific requirements on the beam used for testing.

In following the international standards, the second result of these specific conditions for specific SEEs is that a device is only deemed characterised for radiation response once all of the following types of beams have been used to test the device's SEE response: Heavy-ion beam,

50 MeV to 200 MeV proton beam, and applicable neutron beam. The last fact, combined with the fact that these type of tests can only be done at high energy accelerator facilities, are the two most significant cost drivers. It should be noted that not all accelerator facilities are the same. Depending on the accelerator type and size, the research focus areas of the staff, and the physical infrastructure, only certain types of beams, within certain energy ranges, will be available at a specific facility.

From a user point of view, the satellite industry and researchers in South Africa are interested in learning as much as possible from any SEE test. If SEE tests can investigate multiple effects during the same test, it would be ideal. However, it will rarely be possible to define an experiment that can test for “any possible” SEE. The South African industry is interested in SEU, SET, Single-Event Functional Interrupt (SEFI), and SEL device cross-section characterisation, while South African researchers are mostly active in developing SEE mitigation schemes and circuit designs [26; 27].

**Conclusion:** There is a need to test for several SEEs on electronics. The facility where testing will be done plays a big part in deciding which SEE can be tested for effectively at that facility. However, the argument is not only about what is the best beam a facility can deliver, but also in which SEEs are industry and academia interested.

### 1.2.3 Facility options for SEE testing

*The existing options available for SEE testing are inaccessible due to the associated high cost of testing. The closest existing facilities are in Europe, and regular testing there will incur excessive travel costs and logistics to transport irradiated components. The complexity of accelerator and component preparation for heavy-ion testing further restricts possible test options. Proton test option is feasible for the South African context.*

When considering the test options for the various SEE effects, there are two dominant test methodologies, heavy-ion testing and proton testing. Heavy-ion testing is done using particle accelerators delivering high energy heavy-ion beams. Proton testing is done at similar (rarely the same) accelerator facilities delivering low, medium and high energy particle beams.

In comparison with heavy-ion testing, proton testing is much less complicated. For heavy-ion testing, components are usually delidded. For device characterisation, different ions at different energies are required (details are covered in chapter 2). Each ion/energy combination requires a significant time to set up, which makes heavy-ion testing infeasible except at facilities dedicated to heavy-ion testing. Proton testing is much more feasible since proton beams are much more common at cyclotron facilities, specifically those that support medical radiation therapy.

There exists a compendium of irradiation test facilities (from RADECS 2011), summarised in [28]. With the recent closure of several proton-beam based testing facilities, including Indiana University Proton therapy centre and The Svedberg laboratory at Uppsala University in 2015, there is more pressure on the limited available beam time of existing test facilities. Label [29] discusses details of current facilities investigated by NASA for use as proton test facilities.



Unfortunately, these facilities are not easily accessible to the South African market due to cost, distance, import/export restrictions and facility availability. Facilities are typically booked well in advance and test time is at a premium.

International facilities, most of which are in Europe, the United States of America (USA) or Russia, can be approached to test for SEEs. Travel expenses are a factor, apart from logistical challenges to schedule a test, as well as acquiring and transportation of irradiated devices after testing. Although international test options should not be dismissed out of hand, options closer to home should be investigated.

iTL is a national laboratory of the National Research Foundation (NRF). With a K=200 cyclotron, iTL provides a unique opportunity to develop and establish a SEE test capability that could provide a much-needed research environment for SEE related research, including, but not limited to, space component characterisation, material science, and mitigation techniques. iTL is the only cyclotron facility in Africa that can provide proton beams with energies up to 200 MeV.

In addition to the cyclotron capabilities, iTL has:

- a research focus and mandate;
- expertise in particle beams and particle physics;
- expertise in radiation environments and experimental vaults;
- particle beams that can be used for a wide range of SEE tests;
- some history of ad-hoc SEE test being conducted (see section 2.3.2.1).

Since no sustainable SEE test capability existed at iTL, the establishment of such a facility is required. A viable solution will have to be aligned with iTL mandates, schedules, infrastructure, and processes.

**Conclusion:** The clear choice of facility for this work is iTL. At iTL proton testing will first be explored since it can be used to investigate several different SEEs in electronics and is achievable with the current iTL infrastructure and schedule.

### 1.3 Problem statements, research questions and contributions

African countries, and South Africa in particular, have been investing in space technology and projects. South African satellites, although being successful in their missions, have experienced SEE induced failures and damage. This situation is due to:

1. the lack of access to a SEE test facility for the South African satellite community, both researchers and industry;
2. the lack of a practical and viable SEE test methodology applied to iTL in South Africa;
3. the lack of historical data on the reliability and practices of SEE testing done at iTL in South Africa.

It is paramount that SEE testing capability be established and local SEE testing facilities be developed. The only high energy accelerator in Africa is the 200 MeV Cyclotron at iTL, Cape Town, South Africa. Therefore the following *research questions* need to be addressed:

1. Which type of SEE testing is the most desirable to conduct at iTL, based on requirements to adhere to international standards, as well as the needs expressed by South African satellite community?
2. Can a viable SEE test environment be established at iTL?
3. Is the SEE test environment at iTL accessible, adaptable, reliable, and sustainable?

The rest of the document will describe the research conducted to answer these research questions. The solution required a flexible and lean design approach to allow for easy adaptation to different beam delivery locations at iTL. The use of simulations to design the beamforming and distribution is a crucial component, as beam delivery calibration time before testing is severely limited. A novel dosimetry system is developed to allow for both beam distribution profiling and intensity monitoring during testing. The design allows for multiple test boards that can be remotely placed in the beam spot to improve effective beam time utilisation.

In completion of this research the following *contributions* have been made:

1. Proton testing was identified as the appropriate testing methodology for the South African small satellite community using mostly COTS devices.
2. A viable test design for in-air medium- to high-energy proton-beam based SEE testing at iTL was developed.
3. The establishment of a proton-induced SEE testing environment that allows for good quality beamforming, reliable dosimetry, and repeatability while being flexible enough to be applied at the different iTL locations.
4. A record of the development, implementation, and operational results of the SEE test environment at iTL.
5. A paper outlining the use and limitations of a COTS based OBC, resulting in the need for SEE device characterisation published and presented at the 2011 IEEE Radiation Effects Data Workshop [15].
6. A paper describing the SEE test facility and its test record up to 2018 was published and presented at the 2018 18th European Conference on Radiation and Its Effects on Components and Systems (RADECS) [30].

Many of the building blocks for the developed solution is not new, but they have been combined in a novel way to provide a solution to the unique problem of establishing an SEE test environment at iTL. The following novel elements form part of the established SEE test environment:

1. It is the first proton-induced SEE test environment capable of using medium and high energy proton beams in Africa.
2. It is the only beam delivery configuration for SEE testing designed to be adaptable to many different beam delivery points. Other proton beam test facilities are either dedicated facilities or use dedicated test locations for proton based testing.

3. A novel approach to dosimetry using a dual-Beam Loss Monitor is developed, that serves to measure the beam spot and beam shadow profiles, while also monitoring beam intensity during device exposure.

## 1.4 Dissertation Layout

The layout of the document is summarised as follows:

- Chapter 1:** This chapter presents a brief introduction, summarised motivation for the research, and the research questions themselves.
- Chapter 2:** An overview and discussions of relevant literature are presented in this chapter. The types of radiation effect and radiation sources are covered to set the foundation for the development of a viable test methodology. The history of ad-hoc SEE tests at iTL is presented, followed by a discussion of the results and limitation of these historical tests. iTL is introduced, and an overview of the facility is presented, followed by discussions on viable beam and location options at iTL. A selection of international test standards and guidelines are reviewed, followed by a review of relevant proton testing facilities. A short overview of SEE rate prediction is presented, to contextualise the type of data required from proton testing. The chapter concludes with a discussion on the elements required for a viable approach to proton based SEE testing at iTL.
- Chapter 3:** The chapter explores the design for a viable SEE test environment at iTL. Simulations of the most promising beam delivery locations are presented to determine if the requirements from the SEE standards can be met using feasible beam delivery options. A conceptual design of a new beam delivery and dosimetry system for SEE testing at iThemba Labs is proposed with specific application to two iTL beam locations.
- Chapter 4:** Implementation of the proposed beam delivery system is presented. The novel use of the dual-BLM dosimetry system to enable both beam distribution profiling and in-situ beam intensity monitoring. The beam profiling procedure, measurements and results are presented for four separate experiments at two locations. The measured beam geometric profile is compared to simulated results and summaries of the SEE test performed during the experiments are presented. The chapter concludes with a summary of the results.
- Chapter 5:** The dissertation will conclude with the contributions made by this research, the conclusions drawn, as well as recommendations for future work to be done resulting from this research.

---

## CHAPTER 2

# Literature Study

---

*As described in the previous chapter, there is a need to do more advanced radiation testing for research and satellite projects in South Africa. The RHA landscape must be contextualised so that the optimal choices for viable radiation testing can be made. Brief overviews of radiation effects in general and SEEs in particular are presented followed by the selection of applicable SEEs a viable SEE test methodology should test for.*

The South African context, both in terms of the history of previous radiation tests and the facilities available will be presented. An overview of some similar international facilities is required to serve as examples of the state of the art technology applied in the field. Finally, some standards and guidelines for radiation testing will be reviewed and where applicable will serve as a baseline for the design goals of the test methodology developed in this work.

### 2.1 Overview of high-energy-particle induced radiation effects

*In this section the radiation environment considered is limited to the LEO environment. The radiation effects that are present in the LEO environment are briefly discussed and SEEs as choice for the focus of radiation testing development is motivated. Finally an overview of SEEs is presented and the most viable applicable effects to test for in the South African context are identified.*

Satellites are designed to operate in space. Apart from thermal, vacuum, weight, vibration, and general reliability design challenges, satellite engineers are faced with designing a satellite system to be tolerant of induced errors due to ionising radiation. To aid in the design of radiation-tolerant systems, engineers and scientists use various RHA methods and principles from well-established standards (for more details, see Section 2.6). However, different space systems will be exposed to different radiation environments and consequently must be designed to meet different radiation tolerance levels. The variability in the environment stems from the non-uniform radiation environment that exists from LEO to deep interplanetary space.

Given the context of South African satellite activities that are aimed predominantly at LEO applications, combined with the growing demand for CubeSat sized systems, it makes sense to limit the scope of the considered radiation environment to LEO conditions.

Wertz and Larson [31, ch. 8], Petersen [22, ch. 2], and Schwank et al. [32] give excellent overviews of single event environments in space. For LEO orbits protons tend to dominate in terms of flux density. Even though there are some heavy-ion galactic cosmic rays and solar protons present, the associated induced error contribution is relatively small on average. However, space systems cannot be designed for the average expected SEE rates only. A single destructive particle strike can cause complete system failure, and the heavy-ion induced effects should therefore not be ignored. Some form of mitigation of heavy-ion induced effects should always be implemented in LEO systems.

The different types of SEEs satellites can experience in LEO will be considered next.

### 2.1.1 Brief overview of Single-Event Effects

To choose an appropriate SEE test regime, the different types of SEEs and how they are induced, must be considered. As will be seen in Section 2.6, full SEE RHA can only be achieved if components and devices are terrestrially tested for both TID and SEEs. Additionally, a component (or device) can only be considered fully SEE characterised if it is tested using heavy-ions, high energy protons, and high energy neutrons. The rationale behind this requirement is based on the limitations of each type of terrestrial beam or radiation field have. No current human-made radiation field can fully represent the space environment. As such, different beams and beam energies are used to highlight specific device responses in the hope that dominant SEE types are identified, and since the data is not contaminated by multiple SEE types, risk factors and mitigation techniques can be tailored to the specific SEE.

SEEs can be grouped into temporary and permanent effects, where *temporary effects* refers to either a transient short duration signal or an effect that does not cause immediate damage and can be corrected in-circuit. *Permanent effects* refer to an effect that keeps the circuitry in an undesired state until the supply power is removed or an effect that causes permanent non-correctable damage.

The basic SEEs to consider are described and defined by [23], [22, ch. 1], [33, p. 39-60], and [34]. A summary of each effect follows:

- **Single-Event Upset** is a temporary effect typically affecting an electronic storage element by changing its state. Storage elements include memory cells, registers and latches. SEUs can either be a directly induced effect through a particle depositing charge in one of the critical transistors of a storage element circuit or by inducing an SET that is captured by a storage element. An SEU can usually be corrected by overwriting (or resetting) the storage element value to its correct value.
- **Multi-Bit Upset** is the same mechanism as an SEU but with multiple memory elements corrupted due to a single particle strike. This effect has become more prevalent, the more technology feature sizes are reduced, to the point where Multi-Bit Upset (MBU) effects can dominate over SEUs [35].
- **Single-Event Transient** is a transient signal induced by deposition of charge close to a charge sensitive area of a transistor, like its base (BJT) or gate (Metal–Oxide–Semiconductor

Field-Effect Transistor (MOSFET)). The deposited charge is amplified due to the nature of the transistor's operation, and a transient signal is produced at the transistor's output. This transient then propagates through the circuit elements and can either affect a storage circuit or analogue sensing circuit or be masked and absorbed through filtering effects in the circuits.

- **Single-Event Latchup** can typically be a permanent destructive effect since it latches a component (like a transistor) into a high current state through the forming of a parasitic thyristor structure during charge deposition. If the component remains in this high current state for too long, localised heating can permanently damage the component. The associated increase in current can be used to trigger external monitoring circuitry to power cycle the affected device. More recently *micro*-latchups have been regularly observed in both terrestrial testing and as on-orbit effects [17; 15]. Micro-latchups typically cause a much lower increase in device current making its detection much harder. On the positive side, due to the much lower current intensity, the associated thermal effects are much less.
- **Single-Event Snapback** is similar to SEL and occurs near the drain junction of a N-channel power MOSFET causing the transistor to switch on. The resulting high current condition can cause localised heating and permanent damage.
- **Single-Event Burnout** is caused by the substrate close to the source of a power MOSFET becoming forward biased resulting in a drain-source voltage exceeding the breakdown voltage and eventually a high current destructive heat-generating permanent condition [36].
- **Single-Event Gate Rupture** typically happens in high power MOSFET devices and some linear Integrated Circuits (ICs). The deposited charge in the vicinity of the high-intensity electric fields causes a high current path destroying the gate or a dielectric layer of the device.
- **Single-Event Functional Interrupt** is not a basic effect, but rather the manifested negative effect on the functionality of a system due to a temporary SEE. The presence of an SEU, SET, SEL, or MBU can all cause a system to function incorrectly.

High energy radiation typically affect semiconductor devices the most. Passive electronic components are mostly very tolerant to radiation damage. DD can affect dielectric layers in some linear devices [37] and charge collection gains in CMOS imaging devices [38]. Considering the architecture of a typical modern CubeSat, apart from passive components, semiconductor components account for the majority of circuit elements. Semiconductor ICs form the basis of the complex functionality space systems are designed to have. As such, SEEs testing of ICs should be the focus of the radiation test methodology for COTS based nanosatellite projects. With ICs as the focus, the tests should focus on the detection of SEU, MBU, SET, SEL, and SEFI events.

## 2.2 Radiation sources used for Single-Event Effect testing

*An overview of some types of sources used for radiation testing is presented and the viability of each is explored.*

Radioactive material, high energy pulsed lasers, and particle accelerators are all sources that can be used to induce charge, and therefore SEEs in semiconductor devices.

Radioactive sources like  $^{60}\text{Co}$  and  $^{137}\text{Cs}$  are used for TID since they produce specific monoenergetic gamma rays that can induce trapped charge in the devices but do not have enough energy to cause SEEs. Many radioactive materials decay by producing alpha particles; however, the dose rate from these materials are usually relatively low too since the materials must be stored and handled safely. Unless they have incredibly high energy, alpha particles have a short penetration range (up to a few hundred  $\mu\text{m}$ ) in materials like silicon. When testing devices using alpha particles, the device packaging must typically be removed to allow the alphas to penetrate the active silicon. Pulsed laser sources can induce a charge in accurately control areas and in accurately controlled doses to cause SEEs. However, the active silicon of the device must be exposed to the laser light for this approach to work. By removing the device packaging or by working on unpackaged evaluation ICs devices can successfully be exposed to the laser light.

Both radioactive sources and pulsed laser testing have their uses in SEE research, but given the context of working with COTS devices and the typical investment (both in labour and money) required for device preparation, these sources are not considered to be viable options for SEE testing in the South African context. According to [23], pulsed laser testing as well as the use of  $^{252}\text{Cf}$  sources are considered supplementary test options and cannot be used to replace heavy-ion beam or proton beam SEE testing.

Particle accelerator beams are used in a variety of ways to induce errors and damage in electronics. Heavy-ion beams, proton beams, and neutron beams are used as ionising and non-ionising radiation sources in SEE and DD testing. The following paragraphs provide a summary of each beam's typical characteristics and use.

- **Heavy-ion beams** are a good option to identify SEEs accurately. By using different ions at different energies, the penetration range of the ion into the device can be accurately controlled. Heavy-ions directly ionises the semiconductor materials to deposit charge. Due to the relatively short ranges of accelerator produced heavy-ions devices must be de-lidded and tests must be done in a vacuum to allow the ions to reach the active silicon. Access to heavy-ion beams is limited, as the production of the source ions and consequent cyclotron tuning can take significant time [39].
- **Neutron beams** are available in two variations, namely, spallation neutron sources and monoenergetic neutron beams. Spallation neutron sources are created by proton bombardment of specific targets including tungsten, lead, and liquid mercury [40; 41; 42; 43], that emits spalled neutrons. The emitted neutrons are not monoenergetic and cover a large energy spectrum. Spallation sources are good to characterise aeronautical electronics, as the neutron energy spectrum resembles the natural neutron spectrum at high altitudes. Secondly, monoenergetic neutron beams can be created by proton bombardment of different targets including scandium, lithium fluoride, deuterium and tritium loaded titanium [44]. Since neutrons are not charged particles, they cannot be guided or contained using magnetic fields, that complicates the design of neutron beam delivery systems.
- **Proton beams** are the primary beams of many high energy cyclotrons [45]. Depending on the accelerator, proton beams ranging from a few MeV to the 6.5 TeV of the Large

Hadron Collider are possible. The proliferation of proton beam accelerators as medical treatment facilities is evident from [45; 29]. Proton beams are therefore fairly accessible to the radiation testing community.

Since heavy-ion beams directly induce SEEs, they can accurately identify and localise sensitive device areas. For acceptance testing regarding SEL, SEGR, and SEB a single test at maximum Linear Energy Transfer (LET) can be sufficient. However, to achieve complete device characterisation, the cross-section of SEUs must be obtained. A cross-section measurement can only be done by using a variety of heavy-ion beam energies and heavy-ion species [46]. Depending on the accelerator facility used, it might not be possible to change ion species readily, or ions might be changed as fast as devices can be changed [39].

The difficulty with neutron beams for LEO testing is twofold. Firstly, if a spallation source is used, an event cross-section for the specific SEE cannot be obtained as it is not possible to differentiate which neutron energy caused which event. Without a cross-section description, the prediction of on-orbit rates is limited. Secondly, when working with quasi-mono-energetic neutron beams obtaining a cross-section response is also challenging. Degraders cannot be used to lower the neutron beam energy reliably. Thus the input beam energy on the target must be changed to generate neutrons at lower energy, which can be a time-consuming process.

Protons beams have the advantage of being very accessible due to their extensive use in medical therapy applications. Proton beam energy can be reliably degraded using degrader sheets if care is taken to consider the energy spread created [39]. One disadvantage of high energy,  $\geq 20$  MeV, proton beams is that the SEEs are induced indirectly by through interactions generating secondary particles with unknown energies and locations. As such the exact SEE cross-section cannot be determined in terms of particle LET. In proton dominated environments the latter limitation is of less concern. Unless proton beams  $\geq 180$  MeV can be used, SEL effects will not be reliably induced.

Thus, the selection of a viable particle beam is heavily dependent on the capabilities of the facility at which testing will be done. Consequently, an exploration of the capabilities of iTL is required.

## 2.3 Radiation testing in the South African context

*This work is aimed at establishing more advanced radiation testing capabilities in South Africa. The historic context of radiation testing in South Africa will be discussed in the following sections to set the stage and motivate some choices of an improved and innovative approach to SEE testing at iTL.*

### 2.3.1 Radiation testing in South Africa - historic

Section 1.2.2 gave a short description to motivate why SEE testing in particular is being explored. However, the test environment is only half of the bigger picture. An understanding of the current research and industry approach to the limited radiation testing is required to allow for the development of a test methodology that is acceptable and accessible to the South African satellite community. First historic TID testing will be discussed, followed by historic SEE testing.



### 2.3.1.1 Historic Total Ionisation Dose testing

During the process of developing low-cost test procedures for TID testing, as part of the SumbandilaSat project, valuable test experience was gained by the current author. Being both destructive and unpredictable, TID testing of COTS components demands specific attention to test design and preparation. As detailed by Barnard [21], thorough in-situ testing allowed for accurate identification of DUT degradation response. Proper pre-testing of the DUT electrical test setup ensured minimal delays during radiation test sessions, greatly improved the probability of successfully executing test procedures, and enabled accurate capture of test measurement data.

Some modifications to recommended TID test practices were required to optimally use the TID facility. Even though the TID test procedures did not follow all the recommended test practices, as set out in the relevant TID test standards, the deviation from recommended practice did not cause the procedures to fall outside any procedural limits specified by the relevant standards. Using the adapted practices resulted in the production of good TID test data, as reported in [21], and a successful TID test campaign to select new generation COTS components for SumbandilaSat.

Many improvements to the test process aimed to reduce test costs while maintaining test integrity. These improvements reduced the required human involvement during irradiation sessions which significantly reduced staff costs. Establishing test procedure guidelines reduced test planning time while improving the efficiency of cooperation between researchers and facility operators. Given the big difference in operational complexity and cost of a Cobalt-60 ( $^{60}\text{Co}$ ) facility versus a high energy accelerator facility, proper SEE test procedures and guidelines will be critical to enable a sustainable SEE test environment.

### 2.3.1.2 Historic Single-Event Effect testing

Before the research, for this work began, SEE testing has been done at iThemba Laboratories by only two MSc degree students, the first was Berner [47] in 2002 and the second Van der Horst [48] in 2007. It should be noted that both these projects were once-off ad-hoc masters degree projects that were not part of any radiation test programme development.

Berner's project consisted of evaluating a candidate Digital Signal Processor (DSP) for use as an on-board processor in a LEO microsatellite. Although some rough cross-section data was gathered, the SEU tests done focused on the efficacy of the mitigation techniques applied to protect the processor's memory. Berner tested using both the A-line scattering chamber and the Proton Therapy Vault (PTV) (for more details on these locations see Section 2.3.2). Berner decided to do only proton testing, and in both tests, he was dependent on beam analysis, planning and dosimetry were done by iTL staff.

The A-line experiment was not successful and is not adequately documented in terms of the specific test configuration used. The experiment was done in a vacuum, but the specific proton beam energy is not mentioned. Some form of dosimetry was present, as the total fluence for the test is reported. However, no details regarding the dosimetry method used, nor the expected accuracy thereof is reported. According to Berner, the SEE testing on the DSP in the A-line chamber "did not provide any proper results" [47].

Further limitations of using the A-line listed by Berner include the long DUT setup time as the chamber took about two hours to reach the required low pressure for the beamline to operate. He also mentions that the dosimetry system was not integrated and required measurements to be written down by hand.

Berner's experiment using the PTV was more successful than the A-line experiment. Three proton beam energies were used during the tests, 200 MeV, 65 MeV, and 45 MeV. However, it is not reported how these beam energies were created. Two options exist, either through the Separate Sector Cyclotron (SSC) being set to the required energy, which would take significant time, or the beam was degraded for the 65 MeV and 45 MeV runs.

The PTV configuration is adequately documented, although the specifics of the beam delivery and dosimetry is not known. Berner describes the calibration procedure used and the way dosimetry control was handled. His descriptions correlate well with the standard configuration of the proton line as described by [49], although it cannot be guaranteed that all the same beam delivery elements were present in the PTV in 2001 test. A relatively accurate calibration procedure can be assumed in 2001 at the PTV since the line was regularly used for medical therapy.

The results from the SEE tests on the DSP were partially successful. A limited SEU cross-section curve for the on-chip memory could be derived. The most limiting factor was the lowest energy data being generated at 45 MeV. The issue with the PTV was that the beamline that fed it was not designed for low energy protons, it was designed for 200 MeV, and as such the upstream beam monitoring equipment tend to become less accurate as the energy is lowered. The Wellhofer method for calibrating the beam energy is also a limiting factor as the ion chamber used in the tank cannot be moved closer to the front wall, limiting the minimum depth of water at which the measurements can be done.

Van der Horst tested the efficacy of mitigation techniques applied to a soft-core processor, PicoBlaze, in a Xilinx FPGA. Similarly to Berner, Van der Horst also tested using the proton therapy vault. In contrast to Berner, Van der Horst used only a 100 MeV beam for irradiation of his devices, due to monitoring equipment becoming inaccurate at energies below 80 MeV. Although Van der Horst states that the radiation tests were done to different dose levels, the dose rates are not reported. The tests done by Van der Horst was spread over two months and conducted in three sessions. The SEE experimentation sessions are reported to have taken roughly 4 hours each.

The positives to take from Van der Horst's work is that it indicates that the test setup was to an extent repeatable. There was, however, some discrepancy causing the data from the second of the three sessions to be disregarded. Since only one beam energy was used, Van Der Horst assumed the upset threshold energy to be 1 MeV and used the cross-section data from the experiments as the saturation value.

The experiments were done up to a fluence of only  $3.85 \times 10^9$  protons/cm<sup>2</sup>. Unfortunately, Van Der Horst does not motivate the reason for this fluence level directly. It is assumed from other comments in his report that it might have been due to the current limit for operation of a beamline designed and regularly used for proton therapy.

Similar to Berner's experiments, Van Der Horst was dependent on iTL staff for support regarding the dosimetry and beam delivery, and therefore no details regarding the exact confi-

guration used are presented. It must be assumed that a configuration similar to the ones used for therapy was used as this would result in the least amount of uncertainty in measurements and allow for established procedures to be followed.

Finally, Van der Horst recommended that a more integrated SEE test option be investigated to allow for more automated testing. The 282 test runs he conducted over his three sessions shows the importance of working towards a more sustainable solution.

### 2.3.2 iThemba LABS overview and available beams

iThemba Laboratories for Accelerator Based Sciences (iThemba LABS) is the only organisation on the African continent operating cyclotron facilities [50]. The Cape Town facility, which is the most appropriate to explore for SEE testing of electronics have four cyclotrons, a K=200 SSC, two Solid-Pole Cyclotrons (SPCs) one with K=8 and one with K=11, and a 3 MeV Tandemtron [50]. The general layout of the iTL cyclotron facility up to 2019 is shown in Figure 2.1.

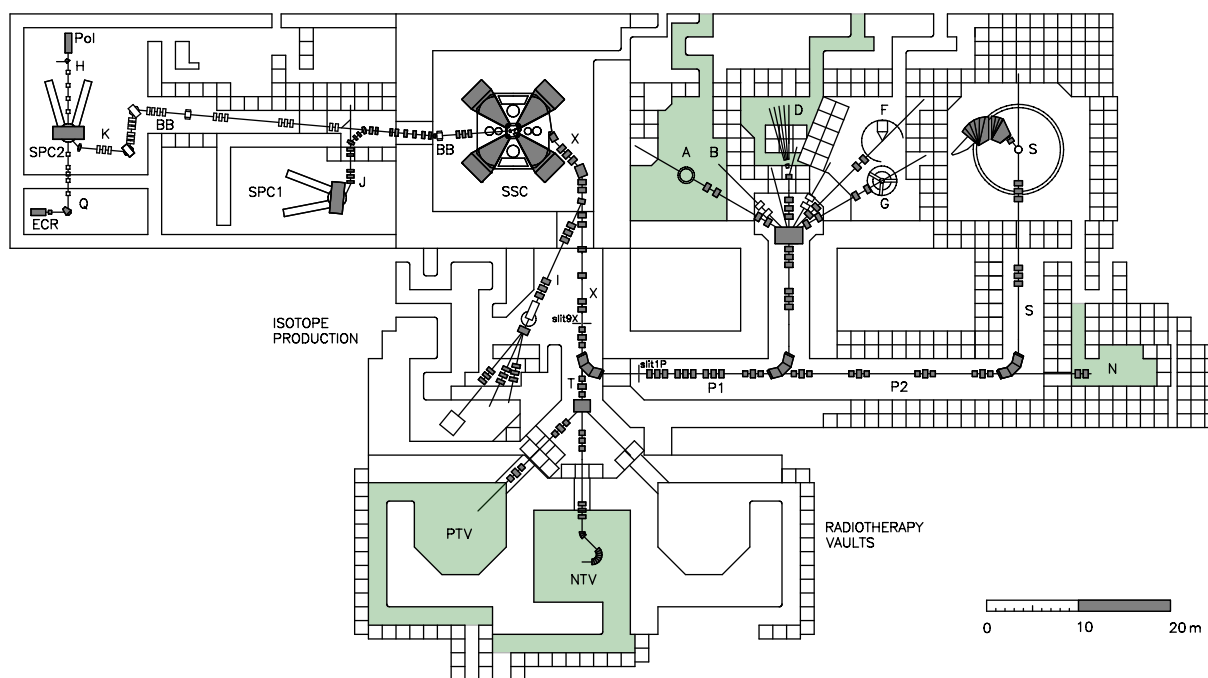


**Figure 2.1:** General layout of iThemba LABS Cape Town Cyclotron facility up to 2019. The vaults highlighted are those considered for SEE testing. Image adapted from original layout drawings courtesy of iThemba LABS.

The K=200 SSC at iTL is mainly used for sub-atomic physics research, radiobiology research, and isotope production. The SSC is fed with one of two SPCs, a K=8 (SPC1) for protons and a K=11 (SPC2) for light ions, heavy ions and polarised protons [51; 52]. The full cyclotron parameters can be found at [53].

The facility is able to supply via the SSC proton beams ranging from 66 MeV up to 200 MeV, as well as light and heavier ions including  $^2\text{H}$ ,  $^3,4\text{He}$ ,  $^{14}\text{N}$ ,  $^{16,18}\text{O}$ ,  $^{20}\text{Ne}$ ,  $^{36,40}\text{Ar}$ ,  $^{86}\text{Kr}$ , and  $^{129}\text{Xe}$  [52; 54].

The high energy particle beams can be delivered to various vaults, each originally designed with specific research in mind. As of the start of 2019 examples are the A-line scattering cham-

ber vault, the K=600 magnetic spectrometer vault (S-line), the Neutron beam vault (D-line), the Proton Therapy Vault, the Neutron Therapy Vault, and the AFRODITE gamma-ray spectrometer vault (F-line, G-line). However, during 2019 a new development was funded and initiated at iTL. The construction process of adding a new commercial 70 MeV cyclotron for isotope production has begun, that changes the layout of the laboratory significantly. The PTV and NTV is being decommissioned and disassembled. Radiobiology research will continue at the new radiobiology beamline (B-line) that is expected to be commissioned in 2020.

Considering the lead up to this work already began in 2007, the discussions and design choices will be in the context of the facilities available up to 2019. Since the historic SEE experiments, up to 2007, some initial SEE experiments were conducted at iTL, although with some limitations, which is discussed in the following section.

### 2.3.2.1 Limitations of initial SEE testing at iTL

Initial SEE tests done at iTL were ad-hoc student projects, but the projects highlighted test methodology issues prompting the research covered in this work. The projects of Berner [47] and Van der Horst [48] were discussed in Section 2.3.1.2 as part of the historic tests, while Thesnaar's project [55] is discussed in Section 4.1 as it formed part of the effort to improve the test methodology at iTL. The students tested mitigation techniques applied to SRAM and SPCs and did rough device characterisation using mainly two locations: (1) the A-line scattering vacuum chamber, and (2) the proton therapy beamline. Although these tests could provide definitive results for determining the effectiveness of a chosen mitigation scheme, they had many limitations, specifically regarding repeatability in design, efficient use of beam time, range of energy used, and record of dosimetry methods used.

The setups could not easily be reproduced between projects, due to the ad-hoc nature of the designs and limited documentation on beamline configuration details. With severe time and budget constraints, the test setup approaches followed used the available facilities with minimal modification.

The A-line scattering chamber was used "as-is". The vacuum chamber in the A-line is quite large at 1.5 m diameter and can take up to 4 hours to pump down to the required beamline pressure levels. The impact on SEE testing is long preparation times, and long delays when the DUT must be replaced. Working in vacuum at the A-line also presented DUT design challenges. To operate in vacuum, most COTS development boards must be specially modified, and some components replaced. With limited vacuum connectivity options, custom vacuum rated signal and power connectors were required in some cases. The latter fact is highlighted explicitly by Thesnaar's and Bothma's projects (see Section 4.1 for more details).

Dosimetry at the A-line was problematic since no specific instrumentation was available to determine in-situ exposure levels accurately, the researchers relied on pre- and post-exposure current measurements from the main beamline monitoring system. However, due to the geometry of the delivered beam, the SSC had to operate at sufficiently low current levels to limit the proton flux levels at the DUT. At these low current levels, the SSC current is unstable, varying up to 20-30% during a 60 second DUT exposure.

The proton therapy line was designed to provide very high accuracy in beam shaping, monitoring, and dosimetry. Beam quality is assured using a range of permanently installed and

carefully calibrated monitoring and beam shaping devices. This design is unfortunately not readily adaptable to lower beam energies, <80 MeV or currents due to the layout and operating limits of the in-beam equipment.

However, the main obstacle to using the proton therapy line was availability. Since the proton therapy line was designed for a 200 MeV proton beam, it could usually only be used when the SSC was set to deliver a 200 MeV beam. Due to the expense and time required to set up the SSC at 200 MeV, it is only done when it is specifically required for an experiment, which happens infrequently. Therefore, SEE testing could only be done immediately before or after other 200 MeV experiments or therapy sessions, which severely limited the SEE test opportunities.

The specific challenges with the two beamlines used, the scheduling limitations, and the amount of effort needed to prepare the locations for SEE tests makes the approach unsustainable. A re-think of the approach to SEE testing is required and should start by re-evaluating the different beamline options.

## 2.4 Viable beam and location selection at iTL

*Availability and sustainability are the major drivers for the viability of SEE test facility design at iTL. Consequently, proton beam irradiation was selected as the radiation source, with the A-line vault and NTV as the most viable locations. The motivation for these choices is discussed in the following sections.*

### 2.4.1 The case for using proton beams at iTL

First, the general case for using proton testing as a sufficient method to screen COTS components for use in LEO radiation environments must be established.

The proton test guideline presented by [37], states that proton testing is a lower-cost alternative to full components characterisation requiring heavy-ion testing. Proton beams are easy to degrade using basic materials and methods. The authors of [37] suggest that proton energies from 20 MeV to 180 MeV is a minimum requirement. They also encourage the use of 400 MeV protons if possible, although methods for using 200 MeV test data to estimate device response can be sufficient for SEL acceptance testing.

Various sources have shown that proton beam data can be used to estimate the heavy-ion response of devices when using proper scaling factors and techniques. An initial study to show that proton data can be used to estimate the upper bound of heavy-ion response was done by [56]. Examples of acceptance testing of COTS devices using proton beams for LEO environments were presented in [57]. Later work [58] presented methods for estimating heavy-ion device response using 200 MeV proton test data. Proposed estimation techniques to improve on the method from [56] is presented in [59]. More recently [60] presented a generalised linear model to more accurately bound estimates of heavy-ion SEE susceptibility using proton SEE data.

The approach to use proton testing as an adequate screening technique is well established. A simplified test methodology is presented in [61] to successfully screen COTS components. NASA also applies a reduced test approach for applicable LEO missions using 200 MeV protons [14].

Cyclotron facilities are expensive to operate, as stated during a meeting with iTL staff: *“If you want to use the beam commercially, you are looking at about R90k per hour to cover costs.”* Beam time must be allocated to the best possible application the facility is mandated to do. It is not uncommon that these accelerators aim to operate continuously to try and fit in as much beam time as possible. Cyclotron energy changes, as well as shutdown and startup procedures, take up a significant portion of the operational time, typically 5%-6% of the scheduled beamtime for iTL [54]. From an operational standpoint, the beam delivery location, ion species, or beam energy should not be changed once the SSC is operational and stable. The focus and steering magnets along beamlines take time to settle and can cause significant variations in beam current, position and shape over the settling time. By using the same energies and ions as the experiments and operations most frequently available, the facility availability and beam time usage can be further increased.

The SSC beam time slots has long lead times and much competition. Even though the SSC can produce all the possible beams required for testing, only one of those beams can be set up for a typical test session (8-hour shift). If the beams required for a heavy-ion cross-section test must be set up, for say four different ion species, the setup time, with ion source preparation performed prior to testing, could (optimistically) be 4 to 6 hours per species-energy combination. That is a total of 16 to 24 hours just for setting up the beam to deliver it to the electronics test chamber. Assuming it takes 3 to 8 hours per electronic board tested, the beam setup time overhead is anywhere from 50% to 800%.

It is essential to mention the iTL schedule at the time to see what impact multiple days of testing would have. Up to 2017, iTL had three primary mandates for the SSC beam time, each assigned about 1/3rd of available the beam time. The first was medical therapy, both proton (200 MeV protons about 1-5% of the therapy time) and neutron (66 MeV protons used to make neutrons, for the rest of the therapy time) therapy was done Mondays to Fridays, about 08:00 to 17:00. Secondly, isotope production was given Monday to Thursday evenings (66 MeV protons used), and finally Nuclear physics experiments were scheduled in a weekend block, from Friday 17:00 to Monday 08:00. For the latter, the energy and ion species used varies from experiment to experiment. For a multi-day slot, SEE testing will have to compete for beam time with nuclear physics experiments, or with medical therapy sessions, assuming the beam is handed back to isotope production every evening. Aligning to current beam usage would significantly improve beam availability and sustainability.

Given the schedule limitations and beam usage profile, a viable option for beam usage must be found. Viability can be achieved if the SEE testing can be done using the beams already available. Slotting in between physics experiments is difficult since the nuclear physics experiments often use ions that would not be useful for electronic testing. Different ions have different penetration depths, in the range of a couple of tens of microns to a few hundred, which is the primary driver in selecting appropriate ions for heavy-ion testing. Taking time from isotope production <sup>1</sup>, is not feasible, as it is a significant source of revenue for iTL [50].

Using proton beams with energies from 66 MeV up to 200 MeV would best fit into the typical iTL beam schedule profile, while also being aligned with proton test guidelines. If proton

<sup>1</sup>iTL labs is the biggest supplier in the southern hemisphere, supplying to over 60 clients, and is the only supplier in the world for <sup>22</sup>Na [50]

tests are done at 200 MeV it would allow for the acceptable practice of estimating heavy-ion device response to be applied to the test data.

## 2.5 Viability of various SEE test locations at iTL

It should be noted that no vaults, nor available space, has been or is currently dedicated to SEE research and testing. Given the variability in experiments allocated to different beam delivery points, a more flexible design can alleviate much of the scheduling limitations, both in beam time slot availability and having the vault available for preparation. The SEE test setup must, therefore, be flexible and mobile in design, to enable easy set up at different beam delivery points. By adopting a flexible design, the availability of a location for SEE testing would be considerably improved.

There are multiple competing factors to be considered when determining the feasibility of doing SEE testing at a specific iTL location. The most important factors include:

- particle energy range available;
- beam geometric profile;
- beam intensity range, both in terms of flux and fluence;
- availability of beam time;
- availability of experimentation area;
- experimental setup lead time;
- experimental setup turnaround time.

*Experimental setup lead time* refers to how long ahead of the intended experiment date the process of installing the beam delivery system must begin, while *experimental setup turnaround time* refers to the time required to make changes to the configuration or DUTs while the experiment is conducted.

For each location identified as a candidate SEE test venue, the advantages and disadvantages will be discussed in terms of the factors as mentioned earlier. A summary of the comparison between location feasibility is given in Table 2.1. The following sections provide additional detail on the characteristics of each candidate beam delivery location.

### 2.5.1 The Proton Therapy Vault

The PTV is located in the medical center at iTL. It was designed for high energy proton therapy and has been used to treat many patients successfully. Since the location is used for medical therapy, the beam needs to be calibrated regularly. The beam delivery system also called the beam nozzle, has been described in detail and characterised for medical therapy use [49].

A proton beam with a nominal energy of 200 MeV is used for therapy. Thus the beam nozzle has been designed to shape a 200 MeV proton beam to the desired proportions. The energy range over which accurate beam characterisation has been done is from 60 MeV to 200 MeV. This very-high-energy proton beam is suitable for SEE testing where a wide range of proton energies is required so that a SEE cross-section of a device can be determined [39].

### 2.5.2 The Neutron Therapy Vault

The NTV is located in the medical center at iTL. It was designed for neutron therapy and has been used to treat many patients. The neutron beam is derived from a 66 MeV proton beam, which is transformed into a neutron beam using a gantry to transport the proton beam to a Lithium target. The gantry is required to set the angle of incidence of the neutron beam onto the patient. Combined with a controllable patient positioning bed, the desired beam entry angle and position can be achieved.

The vault can be operated in a proton beam delivery mode, by bypassing the neutron gantry and delivering the beam directly into the vault, allowing for an in-air beam path length of up to 4 m. The adjustable bed can be used to support the collimator setup and can assist in achieving the required alignment accuracy.

Before 2017 the location was used for medical treatment. Predicting the need for treatment at a future date is difficult since it depends on the time of diagnosis and urgency of treatment to be commenced. As such, it was challenging to schedule this location for SEE testing.

### 2.5.3 The A-line with scattering chamber

The A-line vault was initially designed for nuclear scattering experiments. The scattering chamber is a 1.5 m diameter cylindrical chamber with two rotatable mounting arms. In the centre of the chamber is a height-adjustable scintillation target with a 3 mm hole in the centre. This target is used to verify beam focus and alignment. Both the arms and the target can be adjusted remotely from the data room. After setup is done in the chamber, the lid is closed, and the chamber is evacuated. The pressure in the chamber is pumped down until it is equal with the rest of the beamline pressure, after which the two vacuum valves are opened. The beam can now travel freely down the line to the beam dump at the end of the line. For nuclear scattering experiments, the detectors, scattering target and collimator are mounted on the arms. The arm places the detectors at the required angles from the target, as to observe products from beam-target interactions.

The final beamline elements before the beam enter the scattering chamber are a set of quadrupole focusing magnets and a set of steering magnets. The quadrupole magnets are used to focus the beam on to the target, while the steering magnets can adjust the beam position horizontally and vertically. The quadrupole and steering magnets are used to do final beam focussing, alignment and tuning before an experiment is conducted. When the beam is delivered to the chamber, a manufactured ruby target in the target ladder is used to assist with the beam alignment procedure. The ruby scintillates when the protons impact on it, and by using a camera, the beam can be aligned to pass through the small hole in the centre of the target. At this point, the beam is accurately aligned. The alignment is visually verified using an analogue CCTV-type camera observing the scintillating target through a transparent window in the chamber lid.

The A-line vault was rarely used for nuclear physics research in the period 2007-2015, which meant that during that period, the A-line was the best option from a scheduling point of view. The scattering chamber delivery system also had several positive characteristics relating to the SEE test requirements.



Firstly the chamber has a dual rotating arm assembly that can be controlled remotely, which dramatically simplifies the DUT positioning system requirements that, for the standard A-line setup, reduces to a vertically mounted plate on one of the rotating arms. On this vertical plate the DUTs are mounted. The plate with DUTs mounted can be rotated out of the beam spot during beam calibration and alignment procedures.

Secondly, the remotely controllable alignment procedure will aid to ensure the beam impacts on the correct spot in the DUT plane.

Thirdly, the vault has a multitude of signal cables connected to the iTL data room, making remote monitoring of certain signals possible. The vault also has an Ethernet cable connection to the data room. The latter is useful to interface with monitoring and control equipment.

Due to the mentioned characteristics, this vault and experimental space were previously identified as an option for SEE testing [47]. There are limits to using the A-line chamber for SEE testing in this configuration, as it was designed as a scattering chamber and not for SEE testing. Therefore, the scattering chamber has some characteristics that negatively impact on the design objectives of the beam delivery system.

The first disadvantage is that the chamber was designed to operate with the targets and detectors under vacuum. Thus the chamber must be pumped down to vacuum before the beam can be delivered to the chamber. It also requires all the DUTs to be manufactured to handle vacuum conditions, vacuum connectors to be used to interface to DUTs, and the chamber to be vented and re-pumped if any DUT has to be replaced or inspected during testing. The turnaround time for re-pumping the chamber can be 4-6 hours. All supporting instruments required to monitor and control the DUT must operate over interface wires that are a minimum of 2 m in length, or must be able to operate in a vacuum. In-vacuum operation of the DUTs and related interfacing can reasonably be managed as part of the DUT design cycle, although it would increase the development complexity, time, and cost considerably. A long turnaround time to do any adjustments or replacements to the DUTs severely impact the scheduling options for SEE testing since allowance for significant delays (sometimes overnight) must be built into the allotted beam time.

A second disadvantage is the nature of the beam profile. For beam scattering experiments a pencil beam is typically used. The pencil beam's intensity is too high for SEE testing so the beam must be spread to produce a larger beam spot. Given the maximum of 1.5 m from the DUT to the beam entry point, this relatively short range limits the maximum achievable spot size. With a minimal spread, the beam intensity is also relatively high. A high-intensity beam can induce SEEs at saturated rates during measurements that in turn will cause inaccurate DUT cross-section estimates. To alleviate the high SEE rate, the required beam intensity might be lower than the SSC control system can reliably deliver.

A third disadvantage is the lack of a suitable dosimetry system for proton-based SEE testing. Dosimetry must be associated with up-stream beam current measurements that cannot be monitored by SSC operators during DUT exposure. Beam delivery is manually controlled with an exposure time accuracy in the order of about 1 s that implies a single SEE-count measurement should be at least 100 s long.

Mounting the DUTs within the confines of the chamber is a time consuming and back-breaking endeavour. This process could be more straightforward if the wall section of the

chamber is removed. Unfortunately, due to the chamber size, an overhead crane is required to lift the wall section, making regular removal impractical as it would significantly extend the preparation lead time.

#### 2.5.4 The D-line vault

The D-line vault at iTL is also known as the neutron vault. Here a Li or Be target is used to produce a quasi monoenergetic neutron beam. This setup produces a particular beam spectrum and scattering pattern. By utilising a detector at a specific angle from the target, a reference count can be used as a reasonably accurate indirect dose monitor. The vault has angle indicators to assist with this type of detector setup [62].

The advantage of using a neutron beam is that in addition to SEE testing, displacement damage testing can also be done. Neutrons have been effectively used to get SEE cross-sections and has been proven to produce comparable results to proton beams at energies higher than 30 MeV [63]. Due to minimal scattering of neutron beam by any DUT, multiple DUTs can be tested at the same time under identical beam conditions.

Disadvantages of the neutron beam are that high energy neutrons can activate elements in DUT Printed Circuit Boards (PCBs), which require that DUTs be held until the activity has dropped to acceptable levels before they can be released to the experimenters.

Similar to the NTV, the D-line can be set up in a proton mode, where the Li target is bypassed, and the proton beam exits into the vault. However, for this setup, some modifications to the beamline are required, specifically the addition of a vacuum exit window. The vault can deliver 66 MeV to 200 MeV protons.

#### 2.5.5 The F/G-line vault and S-line vault

The F/G-line and S-line vaults are all designated vaults using specialised detectors and instruments. The S-line houses the K=600 spectrometer that is used in combination with a variety of instruments, detectors and targets to conduct subatomic nuclear physics experiments [64]. The F/G-line houses the AFRODITE detector array [65].

The detectors housed in these locations are sensitive devices and should typically not be exposed to unwanted radiation fields. They also form the backbone of many physics experiments conducted at iTL, making the vaults they are in undesirable locations for SEE testing.

#### 2.5.6 The N-line vault

The N-line vault was originally used for nuclear time-of-flight experiments but has not been actively used in recent years. This location would be an excellent option if funding were available to create a dedicated SEE test facility. The beamline is, however, not in an operational condition. Costly labour and equipment are required to get the line in working condition. For this reason, the N-line was not further considered as a test location option.

### 2.5.7 Comparison of location suitability

Starting with the factors listed at the start of Section 2.5 as comparison facets then quantifying the location characteristics, given in Sections 2.5.1 - 2.5.6, a comparison table was drawn up. The original comparison table is shown in Table 2.1.

Significant changes were made to iTL's operational scope in the 2016-2017 period. Firstly the decision was made to stop all nuclear therapy work at iTL. Even though iTL continued to do bio-medical radiation research, the decision caused the Nuclear Therapy Vault to be much more accessible for SEE testing. SEE testing did not have to compete for time with therapy sessions at the NTV, that became the preferred location for SEE testing during the 2016-2017 period.

In 2018 a programme to install a new 70 MeV cyclotron for radio-isotope production matured to the point that an order for the new cyclotron was placed in 2019. When the cyclotron is acquired, the PTV and NTV will be replaced to house the 70 MeV cyclotron as well as new medical radio-isotope production facilities. The bio-medical radiation research group were moved to the B-line vault in 2019.

These changes have a significant impact on the choice of location for future SEE tests. Given the available information, a revised suitability matrix is shown in Table 2.2.

Location(s)	Beam type	Energy range (MeV)	Advantages	Disadvantages
A-Line	Proton	20 to 200	Stable future location, DUT manipulators	Vacuum, Spreading distance
Proton Therapy Vault		80 to 200	In air, Spreading distance, Dosimetry	Scheduling, Future uncertain
Neutron Therapy Vault		20 to 200	In air, Spreading distance	Scheduling, Future uncertain
Neutron vault (D-line)	Proton / Neutron	50-200	In air, Spreading distance	Physical modifications
AFRODITE vault (F/G-line)	Proton / Ion	50-200	Spreading distance	Unavailable, Physical modifications, Sensitive detectors
K=600 Spectrometer vault (S-line)	Proton / Ion	50-200	Spreading distance	Unavailable, Physical modifications, Sensitive detectors

**Table 2.1:** Summary of evaluation of different SEE testing locations at iTL, valid up to 2017.

Up to 2017, there were some time gaps available during radiation therapy time slots where electronic testing could be done. At the time, there was a decline in therapy patients since other

Location(s)	Beam type	Energy range (MeV)	Advantages	Disadvantages
A-Line	Proton	20 to 200	In-air option, DUT manipulators	Unavailable due to tape station
Proton Therapy Vault		80 to 200	Scheduling, In air, Spreading distance, Dosimetry	Modifications, Unavailable from mid 2019
Neutron Therapy Vault		20 to 200	Scheduling, In air, Spreading distance	Unavailable from mid 2019
Neutron vault (D-line)	Proton / Neutron	50-200	In air, Spreading distance	Physical modifications
AFRODITE vault (F/G-line)	Proton / Ion	50-200	Spreading distance	Unavailable, Physical modifications, Sensitive detectors
K=600 Spectrometer vault (S-line)	Proton / Ion	50-200	Spreading distance	Unavailable, Physical modifications, Sensitive detectors

**Table 2.2:** Summary of evaluation of different SEE testing locations at iTL, valid from 2017.

radiation therapy options have become available at hospitals, and only a few rare cases still require the type of radiation therapy iTL offered. From various discussions with iThemba labs physicists and management, the compromise to share time with medical therapy was reached to try to accommodate electronic testing requests. Nevertheless, some restrictions applied:

- SEE testing must use the 66 MeV proton beam available.
- A maximum test window of roughly 6 hours is available, usually about 10:00 to 16:00.
- Lead time required when requesting a time slot could be from 2 weeks to over a month.

The A-line scattering chamber was identified as the best option for a test location at the time, mainly due to availability. The A-line was not being used often by physics experiments at the time and had an extensive enough area available to do SEE test setups. Additionally, there was some heritage in using the chamber, so all aspects of testing did not require re-evaluation from scratch.

In 2017 the decision was made to end medical therapy at iTL. Restructuring of departments ensued and, as a result, the percentages of time scheduled for nuclear/medical experiments and isotope production changed. For 2018, the split was closer to 50/50, which meant, in essence, there was more time available for experiments. However, the change split only meant that 'parasitic' use of the medical therapy time was not an option for SEE testing anymore.

The A-line, being unused for nuclear research for many years, became the location for housing a tape station in 2017. This change caused the A-line to be occupied by an extensive setup which did not allow for SEE tests to be done there. However, due to the medical therapy being stopped, both the PTV and the NTV became options for SEE locations. The NTV was chosen

as the new SEE location from 2017 based on its availability and ease of use at proton energies from 66 MeV up to 200 MeV.

As described in the preceding paragraphs, between 2007 and 2019, due to the scheduling limitations and location availability, the first SEE tests were done at the A-line, while the following tests were done at the NTV. As a side effect, the changes offered an opportunity to evaluate the flexibility and repeatability of the new SEE test approach under different conditions and at different locations.

## 2.6 Selected international test standards and guidelines

*Standards and test guidelines are typically the result of many years worth of experience from active practitioners in the field. A selection of standards are reviewed in this section to establish the expectation from both users and test facilities as relating to radiation testing.*

There are a few test standards that can be considered as the *key* standards. The current key standards, according to a recent, 2015, presentation by Lauenstein [66], is shown in Table 2.3. The three main organisations responsible for setting the standards are the ESA European Space Components Coordination (ESCC), the USA Department of Defence (DoD), and the Joint Electron Device Engineering Council (JEDEC) Solid State Technology Association.

Standard	Title	Date
JEDEC-JESD57	Test Procedures for the Measurement of SEE in Semiconductor Devices from Heavy-Ion Irradiation [46]	2003
JEDEC-JESD234	Test Standard for the Measurement of Proton Radiation SEE in Electronic Devices [67]	2013
MIL-STD- 750-1	Environmental Test Methods for Semiconductor Devices [68] TM 1017: Neutron irradiation TM 1019: Steady-state total dose irradiation procedure TM 1080: SEB and SEGR	2014
MIL-STD-883	Microcircuits[69] TM 1017: Neutron irradiation TM 1019: Ionizing radiation (total dose) test procedure	2014
ESA-ESCC-25100	SEE Test Method and Guidelines [23]	2014
ESA-ESCC-22900	Total Dose Steady-state Irradiation Test Method [70]	2010

**Table 2.3:** Key space radiation test standards, adapted from [66].

Lauenstein also lists some radiation test guidelines from the American Society for Testing and Materials (ASTM), USA DoD, Sandia National Laboratories (SNL) and NASA. These

should be read in conjunction with the standards as they give practical guidelines and methods to use for test preparation, setup, measurement, reporting, and quality assurance. The list of guidelines is given in Table 2.4. However, it should be noted that since there is constantly new device technology development, the type and impact of radiation interactions with new devices are continuously changing. There is no golden rule as to what exactly to expect from a new device when it is exposed to different types of radiation. This is especially true when COTS components are part of the equation since little to no detailed knowledge of the silicon layout is available to the experimenter.

With the exceptions of MIL-STD-750-1 TM1019 and ESA-ESCC-22900, that covers TID related testing, the standards are all aimed at SEE testing. Aspects of interest, selected comparisons and characteristics that relate to possible testing options at iTL, are discussed in Sections 2.6.1 to 2.6.6. Section 2.6.7 discusses JEDEC Standard (JESD)89A, that is not listed by Lauenstein, but that does contain some useful information regarding SEE testing procedures.

Guideline	Title	Date
ASTM F1192	Standard Guide for the Measurement of Single Event Phenomena (SEP) Induced by Heavy Ion Irradiation of Semiconductor Devices [71]	2011
ASTM F1892	Standard Guide for Ionizing Radiation (Total Dose) Effects Testing of Semiconductor Devices [72]	2012
ASTM F1190	Practice for the Neutron Irradiation of Unbiased Electronic Components [73]	2011
MIL-HDBK-814	Ionizing Dose and Neutron Hardness Assurance Guidelines for Microcircuits and Semiconductor Devices [74]	1994
SNL - SAND2008-6983P	Radiation Hardness Assurance Testing of Microelectronic Devices and Integrated Circuits: Test Guideline for Proton and Heavy Ion SEE Radiation [37]	2008
SNL - SAND2008-6851P	Radiation Hardness Assurance Testing of Microelectronic Devices and Integrated Circuits: Radiation Environments, Physical Mechanisms, and Foundations for Hardness Assurance [32]	2008
NASA/DTRA	Field Programmable Gate Array (FPGA) Single Event Effect (SEE) Radiation Testing (Update [75])	2012

**Table 2.4:** Key space radiation test guidelines, adapted from [66].

### 2.6.1 JEDEC Standard JESD57 - 1996/2003

The standard is titled “Test Procedures for the Measurement of Single-Event Effects in Semiconductor Devices from Heavy Ion Irradiation” [46] and applies to heavy-ion testing.

JESD57 assumes that the facility where testing is done has the ability to:

- mount and position the DUT in vacuum;

- provide heavy-ion dosimetry;
- measure total ionising dose;
- have the required equipment to perform heavy-ion tests.

The standard covers only SEEs resulting from heavy-ion interactions and exclude proton, neutron, and light-ion radiation-induced SEEs.

The aim of heavy-ion testing as per JESD57 is to obtain a cross-section graph. The cross-section, SEE or SEL, per device, with typical units between square brackets, is given as:

$$\sigma [cm^2/device] = \frac{\text{number of events}[\text{dimensionless}]}{\text{fluence}[\text{ions}/cm^2] \times \text{incidence angle compensation}[\text{dimensionless}]} \quad (2.1)$$

or as texts like [22] put it in shorter form, with the same units:

$$\sigma = \frac{N}{f \times \cos \theta} \quad (2.2)$$

It is sometimes required to state the cross-section value in a per-bit unit:  $cm^2/bit$ . This is achieved by just dividing Eq. 2.2 with the total amount of bits in the device.

*The test preparation and procedure guidelines* is given, and most of the information in this part of the standard is thoroughly described by Petersen [22]. Recommended heavy-ion flux is  $1 \times 10^3$  to  $1 \times 10^4$  ions/cm<sup>2</sup>/s for calibration procedures. For DUT testing the flux required typically ranges from  $1 \times 10^2$  to  $1 \times 10^5$  ions/cm<sup>2</sup>/s.

*Energy measurement* is done with surface barrier detectors that should be calibrated once during SEE testing. Heavy-ion LET should be measured with a specific detector for the particular ion in use. An accuracy of 10% from the expected energy value is acceptable. Otherwise, the beam must be re-tuned or the anomaly fixed.

*Beam uniformity* must be measured and adjusted at the start of the test. Adjustments can be done by defocussing techniques and/or thin scattering foils, but must be done by facility personnel. Uniformity should be so that the measurement, done with a scintillating target, is within 10% of the fluence the DUT is exposed to.

*Data collection* should be started with the DUT active before exposure to ensure correct operation. Time recorded beam exposure can then be done. An initial flux of  $1 \times 10^4$  ions/cm<sup>2</sup>/s suggested, then adjusted until an events-per-second rate as expected for the experiment plan is achieved.

The rest of the standard focusses on SEGR testing of discrete Field Effect Transistors (FETs). A similar test procedure to the one mentioned above is suggested, requiring multiple measurements and different LET values using various heavy-ions.

*Report formats* are prescribed at the end of the standard for two report parts: the Test Data Sheet, and the Test Report.

For a full list of contents required in the report documents, [46] should be consulted.

Importantly, the standard does not explain why these two report formats should be followed, and why much of the information is duplicated in both reports.

Furthermore, some useful information is presented in the appendices of [46]. A selection of information from the appendices will be discussed briefly.

*DUT test board/system* is the most important interface to the radiation test chamber for the DUT. It provides mechanical electrical and positioning interfaces. It can be self-contained in-

side the vacuum chamber or partly outside. Interface specifications must be obtained from the facility before test system development is done.

Regarding *DUT test modes*, both static and dynamic test modes should be executed during a test. Dynamic testing helps identify issues that can only occur during operation, i.e. writing a value to a storage element under radiation, while static testing can help identify transients on otherwise stable output pins.

### 2.6.2 JEDEC Standard JESD234 - 2013

The standard is titled: "Test Standard for the Measurement of Proton Radiation Single Event Effects in Electronic Devices" [67].

It covers testing using protons in 40 MeV to 500 MeV range. Indirect proton ionisation will be the dominant charge deposition mechanism for this energy range. However, functional characterisation of the proton SEE rate can be done using proton energies in the range 40 MeV to 100 MeV. Knowledge of the device active die area and any metallic overlays is vital to compensate for beam energy degrading calculations.

The standard references documents from Table 2.3 but also adds the following references to standards:

- ASTM 1192, Standard Guide for the Measurement of Single Event Phenomena (SEP) Induced by Heavy Ion Irradiation of Semiconductor Devices, 2000
- IEC/TS 62396-2, Process Management for Avionics – Atmospheric radiation effects – Part 2: Guidelines for single event effects testing for avionics systems, August 2008
- JEP133C, Guide for the Production and Acquisition of Radiation Hardness-Assured Multichip Modules and Hybrid Microcircuits January 2010

Both proton induced soft errors and hard errors are considered. Soft errors include SEU, MBU, and SET. Hard errors, defined as events that cause permanent damage as well as requiring a power cycle to clear, include SEGR, SEB, SEL, and SEFI. DD and TID effects are not covered by the standard.

High energy proton testing causing SEEs from indirect ionisation is motivated since protons are prevalent in many orbital regimes. Direct proton ionisation is explicitly not covered due to complexities to consider during testing.

SEL is not guaranteed when testing with protons, and when no SEL is observed, the part cannot be considered SEL immune to heavy-ion radiation. When SEL is observed, the threshold proton energy should be identified if possible. SEL is heavily dependent on temperature and bias conditions, so these should also be carefully considered.

Although the standard hints at the possibility of irradiating assemblies, it states that it does not contain guidelines for such tests.

Further, some aspects that must be considered during the planning phase is discussed. Firstly, if any doubt as to the bias effect TID and DD has on the SEE cross-section exist, separate testing must be performed to identify TID and DD dependence. Secondly, test dead-time due to error collection should be considered as part of the cross-section calculations.

Although proton energies below 200 MeV should be adequate for SEU cross-section determination, any mission that cannot tolerate any SEL events should be tested to higher proton



energies. It could also be beneficial to identify any bulge in the cross-section threshold shape as proton energies decrease, that might indicate direct proton ionisation sensitivity which will require further investigation.

The standard defines multiple terms relating to radiation measurements, units, and effects.

Guidelines with regards to the test setup and equipment are made. Many of the aspects covered are general, e.g. remote operation of the test system. However, some specific aspects of proton testing are covered. The following paragraph highlights some of these aspects.

SEEs might not be obvious to the observer. Care must be taken to do different pattern and isolation tests as far as possible. Functionality must continuously be tested to ensure hidden SEL events are caught. Near real-time error, identification is critical in guiding the test procedure.

Flux ranges are typically  $1 \times 10^5$  protons/cm<sup>2</sup>/s to  $1 \times 10^9$  protons/cm<sup>2</sup>/s. A total fluence of about  $1 \times 10^{10}$  protons/cm<sup>2</sup> to  $1 \times 10^{12}$  protons/cm<sup>2</sup>, for soft and hard devices respectively, is suggested.

*Dosimetry* responsibility is mostly placed with the accelerator facility, with scintillators, secondary electron monitors and Faraday cups stated as the three primary dosimetry systems. The standard states that proton beam energy is usually accurate to within  $\pm 10\%$  for most accelerator facilities. Beam verification is done through *golden part* testing and the results are compared to known responses.

*Degrading* of the beam energy is the responsibility of the facility, and the impact on testing as well as the required degrading, peak shift, beam broadening should be discussed with the facility staff and compensated for when reporting test data.

*Test procedures* are provided in the standard. Contrary to the steps of testing given by JEDEC57A, JEDEC234 also provides a test plan guideline with the minimum contents expected listed. The contents are very similar to the *Test Data Sheet* described in Section 2.6.1. The main change is that device information and operating conditions for a specific run is contained in a single *Test Matrix*.

Further on TID and DD effects are discussed similarly to JESD57A. So too, pre-test preparation, and test equipment shielding. For the latter extra attention should be given to neutron field shielding using high hydrogen content materials.

Lid or encapsulation removal is generally not required, specifically for normal incident proton energies above 60 MeV. Facilities usually allow device placement in air for proton energies in range 40 to 500 MeV. However, it is stated that facility procedures are used for corrections to proton beam energy shift and broadening. Packaging and overlay thickness should be determined before tests.

Testing for SEL and SEFI events are described similar to JESD57A, but in more detail. This standard is certainly clearer on some points. Added suggestions include the use of automated SEL protection circuitry that does not prevent SEL events but catches them fast enough to prevent damage to the DUT, responding in the millisecond range to disconnect power. Power can be automatically restored after some charge dissipation has occurred, removing the SEL condition, a 1-second delay is suggested. Latent damage might also occur, so post-irradiation life testing is suggested for SEL sensitive parts.

Typical reporting of the beam, test, and device parameters, both pre- and post-irradiation

is expected. Care should be taken in handling devices. When devices are de-lidded, they can be easily damaged. Many devices are sensitive to electrostatic discharge and materials in the DUT can be activated by the proton irradiation, making the DUT itself radioactive. Handling and transportation of any irradiated DUT should be done in consultation with facility staff and radiation safety officials.

SEE tests usually uses smaller samples to test than TID or DD would use to gain statistical confidence in the responses. For homogeneous lots, a minimum of 5 samples should be tested. If doubt about the homogeneity of a lot exists, enough samples should be tested so that different devices variants can be identified.

A specific test sequence is provided to do destructive testing, i.e. SEL, SEGR, and SEB. The procedure is similar to JESD57A, aiming for  $\pm 10\%$  beam uniformity. However, the suggested flux is of course much higher than for heavy ions, at  $1 \times 10^7$  protons/cm<sup>2</sup>/s to  $1 \times 10^9$  protons/cm<sup>2</sup>/s. The rest of the destructive testing section gives advice on parameter tuning to identify event consistency during a test, as well as options to induce events if they are not visible.

For non-destructive testing, it is recommended that the facility provide the beam at the highest energy required for the test, to minimise TID and DD effects. The facility personnel should also determine beam uniformity and report it. Uniformity variation of  $\pm 10\%$  over the device is usually obtainable. A good starting flux for many devices is  $1 \times 10^7$  to  $1 \times 10^9$  protons/cm<sup>2</sup>.

The DUT should be set up with no undue shadow effects from fixtures or cabling. Care must be taken that support circuitry is shielded, or out of the direct beam, so that no confusion about the source of an observed event is created.

Starting environmental conditions for the DUT is room temperature and minimum supply voltages. Once irradiation starts, the observed error rate should correspond to the expected rate according to the test plan. If the error rate is too low or too high, the flux should be adjusted until the desired error rate is achieved. Irradiation should continue until the desired amount of errors or desired total fluence has been reached. All irradiation time should be recorded.

If non-destructive errors are observed changes to the test setup can be done to measure the device response more completely. These parameters include:

- *Flux change* to obtain statistical data significance, 100 upsets or  $1 \times 10^{10}$  protons/cm<sup>2</sup>/s fluence.
- *Repeat multiple times* to establish repeatability.
- *Angle of incidence change* to grazing angle (85°) and irradiate from back of device to observe any possible variation in response.
- *Change operating parameters*, supply, clock, and input patterns.
- *Change temperature*.
- *Change DUT* to another, same type, device to check inter part variability.
- *Change beam energy*.

However, if no errors are observed the immediately preceding set of parameters can be modified to increase the chance to observe errors. Higher temperature, lower supply voltage, different DUT, angled testing, and higher energies can all be used to help identify the device sensitivity to errors.

### 2.6.3 Test Method Standard MIL-STD-750 - 2013

The document [68] is titled “Test Methods for Semiconductor Devices”, and also covers a range of environmental test other than ionising radiation testing. The standard is divided into six parts.

The *basic standard* covers general definitions, acronyms, and document numbering system. It refers to other applicable USA-DoD standards, i.e. MIL-PRF-19500, as well as part 5 of the standard MIL-STD-750-5.

It further presents temperature and electrical specifications for a DUT during normal and burn-in testing. Neutron irradiation, as well as steady-state total dose irradiation, are classified as destructive tests. The basic standard does not mention or refer to proton or heavy-ion testing.

Part 1A [76] of the specification is titled “Environmental Test Methods for Semiconductor Devices”. It lists 35 different test methods, each as a stand-alone section. The applicable methods for radiation testing are

- 1017.1 Neutron irradiation.
- 1019.5 Steady-state total dose irradiation procedure.
- 1080.1 Single-event burnout and single-event gate rupture.

*Part 1A* refers to many non-governmental publications, with the following applying to radiation effects (adapted from [76]):

- ASTM E263 - Standard Test Method for Measuring Fast-Neutron Flux by Radioactivation of Iron.
- ASTM E264 - Standard Test Method for Measuring Fast-Neutron Flux by Radioactivation of Nickel.
- ASTM E265 - Standard Test Method for Measuring Fast-Neutron Flux by Radioactivation of Sulfur.
- ASTM E666 - Standard Method for Calculation of Absorbed Dose from Gamma or X Radiation.
- ASTM E668 - Standard Practice for the Application of Thermoluminescence-Dosimetry (TLD) Systems for Determining Absorbed Dose in Radiation-Hardness Testing of Electronic Devices.
- ASTM E720 - Standard Guide for Selection of a Set of Neutron-Activation Foils for Determining Neutron Spectra used in Radiation-Hardness Testing of Electronics.
- ASTM E721 - Standard Method for Determining Neutron Energy Spectra with Neutron-Activation Foils for Radiation-Hardness Testing of Electronics.
- ASTM E722 - Standard Practice for Characterising Neutron Energy Fluence Spectra in Terms of an Equivalent Monoenergetic Neutron Fluence for Radiation-Hardness Testing of Electronics.
- ASTM E1249- Minimising Dosimetry Errors in Radiation Hardness Testing of Silicon Electronic Devices.
- ASTM E1250- Standard Method for Application of Ionization Chambers to Assess the Low Energy Gamma Component of Cobalt 60 Irradiators Used in Radiation Hardness Testing of Silicon electronic Devices.
- ASTM 51275- Standard Practice for Use of a Radiochromic Film Dosimetry System.

Part 1A concludes by defining acronyms, terms, destructive and non-destructive tests. As with the parent document methods, 1017 and 1019 is classified as destructive tests. It should be noted that method 1080.1 is not listed in either the destructive or non-destructive classification lists, yet by design, can be destructive if the SEB or SEGR event occurs during the test.

*Method 1017.1* covers device testing in fast neutron fields. Although the method is a radiation effect test, the fast neutron environment is not representative of the space environment. As such, the remaining details of the method is not further considered.

*Method 1019.5* covers testing for TID effects using a  $^{60}\text{Co}$  source. Two parts of the method can be mentioned here. Firstly, the detailed description of the specifications for a Pb/Al container to obtain charged particle equilibrium during TID testing. Secondly, the detailed description of the post-irradiation annealing procedure. Since the focus of this work is on SEE testing the remaining details of the method will not be considered here.

Method 1080.1 covers SEB and SEGR tests for planar vertical power MOSFET devices. It specifies an accelerator as a radiation source. The source should supply ions of sufficient range. Although the minimum range is not specified, detailed analysis and prediction methods are presented to estimate required ranges. The source should also provide ion fluxes greater than  $1 \times 10^5$  ions/cm<sup>2</sup>/s. Devices must be delidded and tested in a vacuum chamber. Detailed test flows and cross-section characterisation techniques are presented. An example test procedure is presented with content specified for the test plan and report.

*Part 5* [77] of the specification is titled "High Reliability Space Application Test Methods for Semiconductor Devices". The document again defines applicable terms and acronyms and refers to a few standards. Importantly, it does not refer to any radiation standard or specification document other than its parent specification [68].

#### 2.6.4 Test Method Standard MIL-STD-883 - 2015

The test method standard [69] is simply titled "Microcircuits". It is an extensive 902 page document covering different aspects of microcircuit test methods. It is similar in format to [68] in defining terms, definitions and acronyms. Due to its vast scope it requires additional definitions on general compliance of parts. Amongst many other referenced documents the following applicable standards are listed in addition to those referred to in MIL-STD-750 (adapted from [69]):

- JEDEC JESD78 - IC Latch-up Test.
- ASTM F526 - Standard Test Method for Measuring Dose for Use in Linear Accelerator Pulsed Radiation Effects Tests.
- ASTM F1192 - Standard Guide for the Measurement of Single Event Phenomena (SEP).
- ASTM F1892 - Standard Guide for Ionizing Radiation (Total Dose) Effects Testing of Semiconductor Devices.

Amongst the extensive set of methods listed the following apply to radiation testing:

- 1017.3 Neutron irradiation.
- 1019.9 Ionizing radiation (total dose) test procedure.
- 1020.1 Dose rate induced latchup test procedure.
- 1021.3 Dose rate upset testing of digital microcircuits.

- 1023.3 Dose rate response of linear microcircuits.
- 1032.1 Package induced soft error test procedure (due to alpha particles).

Only the methods containing significant differences to those described in Section 2.6.3 will be summarised here.

*Method 1017.3* is very similar to Method 1017.1 but applied to microcircuits. The fast neutron environment is not representative of the space environment this research applies to.

*Method 1019.9* is for TID testing and is similar to Method 1019.5. The method lists differentiated tests for different types of microcircuits, and specific focus on Enhanced Low Dose Rate Sensitivity (ELDRS).

*Methods 1020.1, 1021.3, and 1023.3* are all dose rate induced testing and will not be further considered here.

*Method 1032.1* is for soft errors induced from the package, die or die-coat material. The soft error is defined as: “Any error induced by alpha particle impact resulting in either a transient error or an error in data storage witnessed at the DUT’s output”. Accordingly the definition implies only SET and SEFI errors, since any SEE not affecting the output is not considered. The method uses  $^{232}\text{Th}$  as an alpha source. The LEO environment contains an insignificant amount of low energy alpha particles, making this method less applicable to this research.

## 2.6.5 ESCC Basic Specification No. 25100, issue 2 of 2014

The document [23] is titled “Single Event Effects Test Method and Guidelines” and references ESCC Basic Specification No. 21300, ASTM F1192-11, MIL-STD-750 Method 1080, EIA/JEDEC JESD57, EIA/JEDEC JESD89 and EIA/JEDEC JESD234.

Section 2 of the document is of particular importance as it gives updated and clear definitions of terms used in the document and in general in the field of SEE testing.

The requirements presented that pertains to the radiation sources and setups are summarised below (adapted from [23]):

- Radiation source is a proton or heavy-ion particle accelerator beam.
- $\pm 10\%$  uniformity of the radiation fields across the DUT in terms of both fluence and energy.
- Results must report materials causing degrading with appropriate adjustments to calculations.
- Heavy-ion fluxes ranging from  $1 \times 10^1$  to  $1 \times 10^5$  ions/cm<sup>2</sup>/s should be available at the facility.
- For heavy-ion test a DUT vacuum chamber should be supplied by the facility that can hold and position a delidded DUT while shielding it from incoming light.
- Protons energies ranging from 20 to 200 MeV should be supplied.
- Proton beam flux should range from  $1 \times 10^5$  to  $1 \times 10^8$  protons/cm<sup>2</sup>/s.
- 200 MeV incoming beam should not be degraded below 50 MeV, and 60 to 50 MeV incoming beam should not be degraded below 20 MeV.
- For high energy protons, test can be performed in air with the beam normal to the DUT, however effect of angle should be checked.

The specification contains a section specific to low energy proton direct ionisation testing. The low energy proton beam should have an energy of a few MeV and a flux ranging from 100 to  $1 \times 10^8$  protons/cm<sup>2</sup>/s. Delidding the DUT is encouraged, with attention paid to assess the proton energy at the active surface of the device.

*Dosimetry* should be continuous with an accuracy of 10% and the technique used reported. TID must be calculated using:

$$D = F \times LET \times 1.6 \times 10^{-5} \quad (2.3)$$

where D is the dose in *rad*, F is the fluence in *ions/cm<sup>2</sup>* and LET in *MeV/mg/cm<sup>2</sup>*.

The specification further states that the facility is required to have *calibration* data available to the user for the beam delivered, containing the full energy spectrum, composition, flux, fluence and spatial uniformity of the beam.

*SRIM code version 2003* or newer should be used as code to calculate the LET values when using low energy protons or heavy ions, although facility developed codes are also acceptable.

The *temperature* of the DUT should be monitored and recorded.

Guidelines for device preparation for heavy-ion testing is presented, with DUT sample sizes of 3 recommended. Samples should be clearly marked and photographed for traceability to test data.

Electrical and system specifications are given for DUT boards designed for different types of SEE tests.

The *environment* for testing should be chosen for worst case conditions, as applicable to the specific SEE type being tested for. The conditions are specified for SEU, SET, SEL, and SEB and SEGR tests.

In addition the worst case beam conditions are specified for high energy proton beams, non-destructive heavy-ion tests on CMOS logic, heavy-ion SEL tests, and heavy-ion SEB / SEGR tests.

The cross-section for SEEs is represented as:

$$\sigma = \frac{N}{fluence} \quad (2.4)$$

For heavy ion testing the effective LET will be calculated as:

$$LET_{eff} = \frac{LET(normal\ incidence)}{\cos \theta} \quad (2.5)$$

where  $\theta$  is the tilt angle of device from being normal to the beam.

To compensate for the change in fluence due to the tilt angle, the cross-section (compensated) is:

$$\sigma = \frac{N}{fluence \times \cos \theta} \quad (2.6)$$

SEE data should be reported with error bars and with a default confidence level of 95%.

For *documentation*, a test plan template is referenced that should be used when testing to ESCC25100 specifications, as well as specifications, are given for the contents of the test report. For further details [23] should be consulted.

The appendix of the specification gives guidelines for the performance of radiation tests. The guidelines cover test board and cabling issues, design of a device test system and layout

considerations for a test board. Limitations of supplementary radiation sources like  $^{252}\text{Cf}$  and pulsed lasers are covered.

The appendix ends with a guideline to using error bars in reporting the confidence levels of test data, with the required equations and example calculations.

### 2.6.6 ASTM-F1192-11 - 2011

The standard [71] is titled: “ASTM Standard Guide for the Measurement of Single Event Phenomena (SEP) Induced by Heavy Ion Irradiation of Semiconductor Devices” and covers heavy-ion induced SEEs. The heavy-ion test is deemed destructive due to the device being delidded.

The effective cross-section and LET is defined in the same way as equations (2.5) and (2.6). The applicable SEE terms and abbreviations are defined.

*Flux* ranges from  $1 \times 10^2$  to  $1 \times 10^5$  ions/cm<sup>2</sup>/s with a total fluence of at least  $1 \times 10^7$  ions/cm<sup>2</sup> is recommended.

*Accumulated dose* should be considered, but the standard states that the dose damage from heavy-ion tests is typically less than the dose damage due to uniform gamma sources like  $^{60}\text{Co}$ .

*The range* of the ions should be sufficient, although the standard does not specify a minimum range, it mentions that “other requirements specify an ion range of  $>30 \mu\text{m}$ . It further mentions that facilities like the K500 cyclotron at Texas A&M, GANIL and Darmstadt should satisfy all range requirements.

The standard presents an overview of radiation source types to use, including cyclotrons, Van de Graaff accelerators, and alpha emitters.

A typical cyclotron test setup is described in detail, including DUT board mounting, manipulation, vacuum chamber, monitor, energy and dosimetry measurement systems.

*A Test Procedure* consisting of the following steps is described in detail:

- Device Appraisal;
- Pre-Test Procedures;
- Test Plan Preparation;
- Tester Check-Out;
- Dosimetry Checkout;
- Installation and Alignment of Equipment;
- Latchup Monitoring Capability;
- Particle Beam Tuning Procedures;
  - Energy Measurement;
  - Flux Measurement;
  - Beam Uniformity Measurement;
  - Beam Selection.

If none of the expected SEEs are observed, the standard presents the following options to improve the change of observing errors (adapted from [71]):

- increase ion fluence;
- change the beam incidence angle;
- change device bias for better SEU or SEL condition;
- change to another device of the same type;

- change operating parameters;
- change the ion energy;
- change the ion species to obtain a higher LET.

A similar set of steps are presented to reduce the number of unwanted upset if their occurrence hinders the continuation of the test.

*Reporting* should consist of two types of documents, a Test Data Sheet with all the technical details of a specific test run(s), and a Final Test Report containing in preparation documents, calculations, analysed data plots and the full set of test data documents.

### 2.6.7 JEDEC Standard JESD89A - 2006

This standard [78], entitled: “JEDEC Standard: Measurement and Reporting of Alpha Particle and Terrestrial Cosmic Ray-Induced Soft Errors in Semiconductor Devices”, covers the requirements and procedures for Soft Error Rate (SER) testing, which is a subset of SEEs. JESD89A is aimed at the testing required for terrestrial systems. However, some sections apply to SEE testing for space applications. JESD89A covers SET, SEU, SEFI, SEL, MBU but does not include SEGR and SEB. Testing is considered complete if unaccelerated actual use case data is gathered, or if alpha particle, high energy cosmic-radiation, and thermal neutron components are all tested for, under accelerated conditions.

When a quasi-monoenergetic neutron beam is used for accelerated testing, JESD89A states even though methods for SEU cross-section extraction exist, there exist “notable uncertainty in published SEE results”. Therefore JESD89A does not recommend this type of beam for SEU testing until issues with folding methods have been resolved.

### 2.6.8 Discussion on standards and guides

The standards and guides reviewed all have slightly different approaches to set requirements and specifications for radiation testing. This can be expected as each of the documents was created within a specific context by people with different specific experiences in radiation testing.

For the USA-DoD standards, the context is military in nature, with much focus on procedures, documentation specification, and compliance. The nature of the documentation is, therefore, very clear cut in terms of what is allowed and what not. From these documents, the hard limits for acceptable testing practice are obtained. However, the goal of most of the military testing is to *ensure* devices do not fail under the operational conditions they were approved to for. In the context of the document, there is little leeway given to adaptation and self-interpretation. There is also little detail given on example test configurations and practical implementations.

The JESD, JEDEC, and ASTM standards are all clearly industrial in nature. The standards go into much detail regarding technology and fundamental theory driving some of the requirements. It appears that the industry based guides are more written towards enabling the radiation test engineers to understand and conduct the tests successfully the first time. An example of the practicality is the detail in which the heavy-ion test chamber is described in ASTM-F1192-11.



Even allowing for the differences in approaches, it is clear that the standards agree on most of the fundamentals as well as the general requirements of thorough testing. If a permanent SEE test facility is to be developed, the designers should study these standards thoroughly to ensure that the facility will meet their requirements.

None of the standards covers the level to which testing can be adjusted or optimised to minimise test time and preparation effort. For views on this aspect, literature from the active radiation testers, confronted with time and financial budget constraints, have to find ways to obtain acceptable results, given the requirements of their missions. Some examples of new approaches to simplify radiation testing for missions where more risk is allowed was discussed in Section 2.4, specifically [57; 58; 56; 59; 60] all contributing theoretically, while [61; 14] contributed with practical projects showing the simplified method to use proton testing as a proxy for heavy-ion testing.

Since the standards provided limited insight into what the capabilities of accelerator facilities are, versus what they should minimally be, a short review of a selection of proton test facilities is required.

## 2.7 SEE proton test facilities overview

*In this section, a selection of current international facilities available for proton based SEE testing are reviewed, and their characteristics evaluated for similarities with iTL.*

When the standards and guides on proton based radiation testing are considered, there are three proton energy domains of interest: Low energy protons, ranging from a few MeV to roughly 20 MeV; medium energies ranging from roughly 20 MeV to roughly 180 MeV; and high energy protons above 180 MeV. Considering the capabilities of iTL, the beams that can be generated there fall into all of these proton energy categories, making it a prime candidate for developing proton test capabilities.

Some proton testing facilities exist that can produce low energy beams in addition to medium or high energy beams, e.g. RADEF, TRIUMF, and LBNL. The typical setup required for low energy proton testing can be as complicated as heavy-ion testing. Often the DUTs are placed in a vacuum to minimise energy straggling caused by the low energy beam moving through air [79].

For medium energy protons facilities used by NASA in 2016 include (from [29] and E.W. Blackmore, personal communication, May 11, 2020):

- University of California at Davis (UCD) Crocker Nuclear Laboratory (CNL) – 63 MeV.
- Lawrence Berkeley National Laboratories (LBNL) – 55 MeV.
- Texas A & M University (TAMU) – 50 MeV.
- Tri-University Meson Facility (TRIUMF) - 63 MeV.

High energy protons facilities are typically one of three types of facilities: research facility, medical therapy facility, or dedicated radiation facility. RADEF and PIF will be presented as research facilities that through the backing of ESA could create dedicated radiation test facilities.

### 2.7.1 JYFL/RADEF

The Accelerator Laboratory, University of Jyväskylä, Finland (JYFL) is also known as JYFL/RADEF. The facility is ESA supported European Component Irradiation Facilities (ECIF), and the characteristics have been adapted from the following sources: [80; 81; 82; 83; 79]. Even though the facility has heavy-ion radiation capability, only the proton beam capabilities will be considered here. The facility has both low energy and high energy proton beam options.

Low energy proton beam ranges in energy from 0.4 MeV to 8 MeV, and fluxes from  $1 \times 10^6$  protons/cm<sup>2</sup>/s (1 MeV) to  $1 \times 10^8$  protons/cm<sup>2</sup>/s (above 2 MeV). Energy straggling is less than 30 keV up to 3 MeV. Degrading is done using aluminium and a bending magnet. Better than 10% flux/fluence determination and better than 10% beam homogeneity can be achieved. The beam spot on the DUT in vacuum is maximum 5 cm diameter. A large vacuum chamber, 75 cm diameter and with a height of 81 cm is used to mount and maneuver the DUT.

High energy proton beam ranges in energy from 10 MeV to 55 MeV, with fluxes up to roughly  $3 \times 10^8$  protons/cm<sup>2</sup>/s. Beam homogeneity is better than 10% and of Gaussian form with better than 10% flux/fluence determination. The beam spot on the DUT in air is maximum 10 cm diameter. Beam uniformity is achieved through quadrupole and wobbler magnet tuning.

Information on the spot profiles and energy straggling for high energy protons were not in the literature.

### 2.7.2 PSI - PIF

The Proton Irradiation Facility (PIF) at the Paul Scherrer Institute (PSI) is also an ECIF supported by ESA. The facility capabilities have been adapted from [84; 85; 23].

The facility can deliver initial proton beam energies from 74 MeV to 230 MeV and with the added degrader can deliver almost any energy from 6 MeV up to 230 MeV. The maximum beam intensities are from 2 nA (at 230 MeV) up to 5 nA (at 230 MeV).

The beams get spread to a deliver full width half maximum diameter spot size of 10 cm. The dose monitoring is quite accurate at less than 5% error, with a low neutron background level. A mounting frame for test samples is available that is mounted on an XY table and can hold boards up to 25 cm × 25 cm.

### 2.7.3 North American Proton Facilities for Radiation Testing

In a 2016 study by NASA [29], options for proton radiation test facilities were evaluated. The study covered low, medium, and high energy proton facilities. The report details the rationale and requirements for proton testing of electronics. This study was required since IUCF, a major facility used for proton radiation testing, closed in 2014.

For all the facilities listed in Table 2.5, the following minimum requirements were set (adapted from [29]):

- Energy range: 125 MeV to >200 MeV
- Proton flux rates:  $1 \times 10^7$  p/cm<sup>2</sup>/s to  $1 \times 10^9$  p/cm<sup>2</sup>/s
- Test fluences:  $1 \times 10^9$  p/cm<sup>2</sup> to  $1 \times 10^{11}$  p/cm<sup>2</sup>
- Irradiation area: Small (IC ~1 cm) to Large >15 cm × 15 cm

- Beam uniformity: >80%
- Beam structure: Cyclotron preferred (random particle delivery over time), Fixed spot or scatter (random particle delivery over area)

Facility	Type	Hourly rate	Hours/year	Notes
Northwestern Medicine Chicago Proton Center	Cyclotron	TBD	2 hrs weeknights 8-16 hrs Saturdays	230 MeV PBS
Scripps Proton Therapy Center <sup>1</sup>	Cyclotron	<\$1000	Up to 500 hrs	250 MeV PBS
Seattle Proton Center	Cyclotron	TBD	TBD	230 MeV PBS
Hampton University Proton Therapy Institute (HUPTI)	Cyclotron	TBD	TBD weekends (up to 30 hrs?)	230 MeV passive
OKC ProCure Proton Therapy Center Hampton, VA OKC, OK	Cyclotron	\$1000/hr + \$3000 setup	6 hrs Weekdays + 5-8 hrs Saturdays (shared time?)	
University of Florida Health Proton Therapy Institute (UFHPTI)	Cyclotron	TBD	Weekend days up to 300 hours per year	230 MeV passive + PBS
Provision Center for Proton Therapy	Cyclotron	TBD	TBD	230 MeV PBS
Dallas Proton Treatment Center	Cyclotron	TBD	TBD	
University of Maryland Proton Treatment Center	Cyclotron	TBD	TBD	250 MeV PBS
Tri-University Meson Facility (TRIUMF)	Cyclotron	\$750	4x/year	500 MeV
Slater Proton Treatment and Research Center at Loma Linda University Medical Center (LLUMC)	Synchrotron	\$1000	~1000 hrs	250 MeV passive
Mass General Francis H. Burr Proton Therapy (MGH)	Cyclotron	\$650	~800 hours, 12hr weekend days, 3 of 4 weekends, 6 month+ lead time	235 MeV passive + PBS
NASA Space Radiation Lab (NSRL)	Synchrotron	\$4700	~1000 hours	50 - 1500 MeV

**Table 2.5:** North American Proton Facility options (2016) adapted from [29; 45].

The table shows many facilities that meet the requirements. However, some careful planning is required since many of the newer facilities use PBS techniques to create custom beam distribution profiles for medical treatments, which differs from the traditional passive beam spreading technique. An example PBS delivery system and a passive spreading system is shown and described in

Even though this study looks very promising in terms of the number of facilities listed, most of the facilities are medical therapy centres. In an article by Hancock [86], the future of proton therapy centres is seriously questioned. Arguments presented include the inability of

<sup>1</sup>Since the publication of [29] *Scripps Proton Therapy Center* has become *California Protons Cancer Therapy Center*.

many centres to generate the required income to be profitable. This financial challenge faced by medical therapy centres imposes significant risk for sustainable radiation testing options for the North American radiation testing community. The list of facilities in Table 2.5 are examples of the type of facilities of interest to NASA.

### 2.7.3.1 TRIUMF

TRIUMF (Tri-University Meson Facility) in Canada has been developing beamlines for proton and neutron irradiation experiments since 1995. TRIUMF's proton- and neutron irradiation facilities (PIF & NIF) are used by both the Canadian aerospace community and international clients and researchers. Proton beam energy options range from 63 MeV up to 500 MeV, with lower energies produced through using degraders. Both the higher energy and lower energy beams are delivered into the same electronics test area. TRIUMF has multiple beamlines that operate simultaneously allowing for radiation testing while other research experiments are done in parallel [87].

At present TRIUMF PIF & NIF caters for both industry and research, with roughly 80% of the electronics testing time being paid for commercially (\$850-\$950) and the remaining 20% of the time is allotted to approved peer-reviewed research projects. Radiation testing is allotted 1000 hours on average annually. For eight months per year, 1 to 2 weeks are scheduled per month and utilised up to 24 hours per day. TRIUMF users consider it one of the premier proton and neutron test facilities in the world due to its range of energies, versatility and reliability (E.W. Blackmore, personal communication, May 11, 2020).

## 2.8 Overview of SEE rate prediction

*With the details of SEE standards, testing procedures and facilities having been discussed, a short overview of the SEE rate prediction process is required. It is important to understand the context in which testing is done since many test parameters are driven by the type of SEE that is tested for. Knowing the limits to which to test, as well as the expected types of responses, are key drivers for the radiation test design. To this aim, the process of SEE rate prediction is presented in summarised form, since many good extensive explanations on the matter exist in the literature, including but not limited to [22; 88].*

Spacecraft are designed for a specific operational lifetime and to meet performance requirements in terms of executing its intended mission reliably. Designers need to manage the risk of radiation damage to the spacecraft during its lifetime. Consequently, they need to predict the rate of radiation-induced effects the spacecraft might experience.

The SEE rate prediction process can be divided into the following phases:

- Mission modelling;
- Space Environment modelling;
- Device sensitivity modelling;
- SEE rate modelling.

The *Mission modelling* phase involves all the spacecraft mission design information required to establish an operational environment for the device to be tested, usually called the DUT during radiation sensitivity testing. The mission design parameters that are important include:

- mission design lifetime;
- orbit definition;
- spacecraft physical layout;
- spacecraft electrical design;
- spacecraft mechanical design.

The design lifetime and orbit parameters are the primary input used by the space environment models. The physical layout and mechanical design information are used to estimate the amount of shielding the device of interest will have. Finally, the electrical design information and mechanical design affects the electrical and temperature conditions the device of interest will be operating in, that in turn drives the electrical design margins for the test system managing the DUT as well as indicate whether the DUT should be held at a temperature other than ambient, during radiation testing.

The *Space environment modelling* phase uses orbit and lifetime design information as inputs to various space environment models. Since space radiation is due to different radiation sources, different environment models are used to predict the intensity and energy spectrum contribution of a particular source to the device exposure. These generated radiation spectra are in turn used, during the *Device sensitivity modelling* phase as inputs to models aimed to estimate the dose delivered and models aimed to predict the damage caused by different radiation types to the device of interest. In the *Upset rate modelling* phase, the radiation spectra are also used as input to models aimed to predict SEE rates in the device of interest.

Over the years, many different software tools have been developed to assist scientists and spacecraft engineers to model and make rate predictions. Managing, sharing and translating all the different data formats used and generated by different modelling software can be a daunting task. A consortium led by the Royal Belgian Institute for Space Aeronomy (BIRA-IASB) supported by ESA funding developed an online tool by integrating the most popular space weather prediction models and simulation tools into an online web browser accessible software suite called SPace ENVironment Information System (SPENVIS) [88]. For any novice to the radiation environment, SPENVIS provides a one-stop-shop to model exposure levels and predict on-orbit error rates.

However, SPENVIS requires some information regarding the sensitivity of the component (or system) being investigated during the *Device sensitivity modelling* phase. Typically for COTS components an accurate sensitivity model can only be created from terrestrial radiation test data.

## 2.9 A proton-induced SEE test facility for iTL

*Understanding the basic radiation effects and particle beam types, combined with historic ad-hoc tests at iTL set the stage for reviewing the governing standards and guides of proton testing, the characteristics of other proton testing facilities, and how the data generated from terrestrial SEE test is used in SEE rate prediction. In this section, the knowledge is combined to present a viable approach to SEE with practical suggestions to improve on initial attempts.*

### 2.9.1 The standards for SEE testing for COTS-based systems in the South African context

Considering the following question: “What is the bare minimum radiation testing required to enable designers/mission planners to decide on whether a specific component/system will be used in any particular mission?”. It is not an easy question to answer since different missions have different radiation exposure environments. However, if the environment is limited to LEO, then at least the radiation environment scope can be limited. From the literature, as described in the preceding sections, it is clear that protons are the dominant particle to consider, even though high energy Galactic Cosmic Rays (GCRs) are present, their intensity levels are very low.

From the standards, it is clear that although different tests highlight different induced radiation effects, some amount of overlap exists, specifically between high energy proton testing and heavy-ion testing. Proton testing over a representative energy range is considered adequate to characterise a device’s SEU response. If the device does not require a full SEL cross-section analysis, and some amount of risk is acceptable during the mission, effective screening of devices can be done to identify whether the device exhibits any SEL sensitivity. By adding SEL protection circuitry by default to designs the risk of failure due to SEL can be reduced to an expected amount of system downtime due to power cycling events.

Given the variable nature of COTS devices, their relatively short product life cycle times, and the difficulty to procure components from the same batch, simplified radiation test approaches are required. The popularity of CubeSats is also driving simpler radiation testing programmes with faster turnaround times. If the full CubeSat is developed in less than a year, the radiation test programme cannot take many months to complete. The examples given of CubeSat missions using simplified, proton based, radiation testing approaches successfully, further supports the notion of proton based testing for the South African context.

As far as reasonably possible, a test facility within the South African context should aim to adhere to the established international standards governing proton testing, and these include the standards and guidelines set by [23; 67; 39; 37; 75].

### 2.9.2 The viable approach for SEE testing at iTL

The options to consider for SEE testing at iTL, include the beam type, test preparation aspects, test equipment requirements, reporting, and effective test procedures.

The first option to consider is the type of beam that is viable to use at iTL. As discussed in Section 2.5 the most viable option is to use the proton beam at the nominal 66 MeV, and up to 200MeV when the schedule allows. The test location will be dependent on availability. The availability of locations will change through time as long as no dedicated electronics testing location is established. The latter is not feasible, given the small radiation testing community, which lead to the conclusion that a flexible design is required that can be adapted to any of the possible locations that can receive protons. This will allow for medium and high energy proton testing. Based on indirect proton irradiation effects basic mechanisms, the following SEEs can then be tested for:

- SEU with 20 MeV to 200 MeV protons;

- MBU with 20 MeV to 200 MeV protons;
- SET with 20 MeV to 200 MeV protons;
- SEFI with 20 MeV to 200 MeV protons;
- SEL with >180 MeV protons.

The next aspect to consider is the cost of testing. If the cost of testing is too high, radiation testing will stay inaccessible to the South African satellite community. ITL is mandated to do research, which is an advantage for the research community since any approved research can be done effectively free of charge. The challenge is to establish a way to get research approved, which will allow iTL to schedule beam time for testing. As discussed in Section 2.3.1.2, as part of masters students research time was allocated on an ad-hoc basis. The ad-hoc approach is adequate for once-off tests. However, if a radiation test capability is to be established, a more sustainable solution is required. The only option left is to get scheduled beam time on a sustainable basis by applying for beamtime through the annual beam time application process. Starting in 2017, the beamtime application process was followed by the author and collaborators. In two separate applications in 2017 and 2019, three 8-hour shifts and four 8-hour shifts were approved respectively by the iTL Programme Advisory Committee (PAC).

Radiation testing can be accessible to the satellite industry through well-defined research project partnerships between industry and academia. Through partnerships, two options for industry to participate in research are possible. The first is by funding postgraduate students for studies in radiation testing. The second is to sponsor equipment and components so that researchers are enabled to design experiments that will generate publishable data. With well-defined research topics research, outputs can be generated as well as providing radiation response data that is useful to the satellite industry.

### 2.9.3 Affordable development through utilising the available resources at iTL

To develop an SEE test capability affordably, the resources available at iTL should be used as far as reasonably possible. The infrastructure used at accelerator facilities is typically costly. At the start of this work, no funding was available for beamline modifications to the point of establishing a permanent electronics testing area. As such, the flexible design should aim to use available iTL infrastructure, with the fewest possible modifications.

At iTL the following capabilities and infrastructure are already available, and can be used with minor modifications to infrastructure:

- 66 MeV (regularly) or 200 MeV (occasionally) proton beams;
- the proton beam current can be varied from 0.1 nA to a few  $\mu$ A, with energy changes possible in less than 5 minutes;
- the A-line scattering chamber as primary test location option;
- the NTV and PTV as secondary test location options;
- enough physical space to position DUT boards;
- positioning mechanism for DUT boards at the A-line.

In the course of the research and after some experience (see initial A-line experiments in chapter 4) with the infrastructure at iTL, a few changes to the design approach at iTL became

apparent. A summary of those insights and choices are given here, to serve as “previous work” knowledge for the final design process.

### 2.9.3.1 Radiation detection devices overview

One of the challenges is providing accurate dosimetry for the SEE tests. As the A-line calibration experiment showed (discussed in Section 4.1.2), the beam current can vary significantly between the start and end of an exposure run. This varying beam current highlights the importance of having in-situ monitoring of the beam. However, if any in-beam monitoring devices are used, they can affect the beam dispersion and introduce further uncertainties. These effects can be compensated for, but results in an ever-increasing complexity of the delivery system, and its simulation model.

Using Knoll [89] as a reference, some of the more prominent detector types are reviewed: Gas-filled detectors, scintillating detectors and semiconductor diode detectors.

There are three general categories of gas-filled detectors, ion chambers, proportional counters, and Geiger-Mueller counters.

*Ion Chambers* can operate in DC current and pulse counting modes. In current mode, ion chambers can be used for radiation survey instruments, Radiation source calibrators, and measurement of radioactive gasses. Ion chambers are typically relatively large, with gas volumes ranging from a few  $\text{cm}^3$  to thousands of  $\text{cm}^3$ . In pulse mode, ion chambers produce tiny voltage pulses that require sophisticated and expensive pre-amplification stages. Semiconductor diode detectors have replaced pulse-type ion chambers in most applications, except in very specific cases.

*Proportional counters* are a variation of the gassed filled detector working at higher electric fields allowing for a phenomenon called gas multiplication to amplify the ionisation current. They come in many forms, including tissue equivalent-, parallel plate avalanche-, position sensitive-, and multiwire proportional counters. Irrespective of their differences in physical design, proportional counters typically require high-voltage power sources in the order of a few kV to many kV. Due to the complexity of the mechanical design, these detectors are often custom made for fixed installations.

*Geiger-Mueller counters* operate at even higher electric field values than proportional counters, giving rise to a multi-avalanche effect caused by a single ionisation track. This multi-avalanche scenario saturates the detection circuitry resulting in a signal of the same amplitude that is independent of the ion track charge deposited. Unfortunately due to the avalanche conditions, the detectors typically take significant time to disperse the charges formed. Typical Geiger-Mueller counters have maximum count rates in the order of a few kHz. If the time-to-first-count method is applied, the count rate of Geiger-Mueller detectors can be increased to be in the order of  $1 \times 10^5$  Hz.

There is a large variety of *scintillation detector* designs used in nuclear and radiation monitoring applications. Knoll presents a range of inorganic and organic scintillation materials and reviews their response time and light efficiency characteristics. The width of the pulses generated by scintillators can range from less than 2 ns (fast plastic scintillators) to more than 200 ns (some inorganic crystals), in duration. Damage to the scintillation material due to radiation exposure can be observed at different exposure levels for different materials, ranging from as



low 10 Gy to as much as  $1 \times 10^6$  Gy. Scintillators require photomultiplier tubes or photodiodes to convert the light signals into electrical pulses for measurement.

*Semiconductor detectors*, also called solid-state detectors, are very popular due to their relatively smaller size than gas-filled detectors, and their better energy resolution compared to scintillators. Although being a type of diode, in essence, semiconductor detectors come in different varieties, designed to measure radiation in specialised applications. Some varieties of semiconductor detectors include diffused junction detectors and surface barrier detectors. Silicon p-i-n diodes have become popular for use in X-ray spectroscopy and personnel monitors. Due to the relative simple electronic interface and low cost, silicon p-i-n diode based detectors have been used in many different radiation detection applications.

An overview of dosimetry for proton beam testing is given by [90]. Two example setups are presented with associated dosimetry, using either transmission ion chambers (TIC) when the dosimetry is done in air, or secondary emission monitors (SEM) when the dosimetry is done in vacuum. Other methods, including radiosensitive films and position-sensitive TIC and SEM devices, are presented as options to verify beam uniformity.

When considering the results and deductions of the preceding sections, a radiation detector for medium to high energy protons is required that can be used in a mobile and flexible beam delivery configuration. The detector should preferably be small and have a high enough spatial resolution to allow for multiple samples over an active die area. The detector should not require extensive calibration because the test setup should be adaptable to different beam delivery points at iTL. Section 3.3.1 describes the choice of detector for SEE testing at iTL.

#### 2.9.4 Practical suggestion to improve on initial SEE test attempts at iTL

The following set of practical suggestions is presented to improve on the initial SEE attempts at iTL, including the historic test approaches by [47] and [48] as well as the test approaches by Botma, Thesnaar, Smith and Barnard (presented in chapter 4).

- *Change to in-air testing: From the experience of three initial SEE tests at the A-line, testing in a vacuum is not optimal.* Setup of DUT boards take long, and any issues after the chamber have been pumped down results in a 4-6 hour turnaround delay. Utilising medium- to high energy protons makes testing in-air a feasible alternative. Medical therapy uses 200 MeV protons through about 7 meters of air. This change leads to the two in-air experiments done in the A-line vault in 2016, where the essential procedures of in-air SEE testing, using BLM dosimetry, was evaluated and refined.
- *Use passive beam spreading and collimation to create a uniform intensity beam spot.* The focussed pencil beam reaches the chamber with a diameter of 3 mm to 6 mm. The pencil beam is not ideal for creating a uniform beam over a DUT. Initial attempts used the final quadrupole magnets to *de-focus* the beam. The de-focus approach worked to a degree, as mitigation scheme testing was possible, although no accurate dosimetry information was available. The current acted as a reference, but the flux over the die area was a rough guess at best. Borrowing from medical therapy techniques, and descriptions from other facilities, the most reliable beam spreading mechanism uses a passive beam spreading foil. A candidate material for the passive spreading element is lead (or other high-Z

metal) since it provides a high scattering angle to energy loss ratio. Lead (Pb) is a good option since it is affordable, available, relatively safe and easy to work.

- *Develop an accurate, affordable, easy to use dosimetry system for proton-beam based SEE testing.* Having inaccurate dosimetry is problematic. The range of flux used for electronics testing is either much lower or much higher than the typical experiments and setups used at iTL, so no simple off-the-shelf solution was at hand to provide *in-situ dosimetry*, to an accuracy level as prescribed by standards. The requirement of having a flexible design approach that can easily be adapted to different beam delivery points restricts the dosimetry options further. Complicated, bulky equipment requiring accurate alignment and lengthy calibration procedures should be avoided. Given the currents and total fluence required per the expected time of experimental runs, taking scattering and current limits into consideration, a solution of using a BLM device was proposed. Although not designed as a primary dosimetry device, the BLM is simple to use and affordable. There are limits to using the BLM approach, but as stated in Section 4, the dual BLM approach seems to work well. The BLM outputs can be logged, with minor adjustments, using the existing iTL data logging infrastructure. At higher flux levels, saturation occurs in the BLM that needs to be managed. A usable BLM measurement range must be identified. Importantly, the BLM is used as a relative sensor, not as an absolute one. The geometric shape of the beam can be measured by sweeping the sensor horizontally through the beam while using a second identical BLM in a fixed position. The latter acting as a reference measurement to compensate for any current variation during beam spot measurement and during device exposure since the total beam current can not be measured while the beam is delivered to the chamber. The total current is measured, before and after a test run, using an upstream Faraday cup.
- *Use collimators in such a way that they also provide the required beam spot size and simultaneously a shadow area to protect devices currently not in the beam spot.* In order to provide a good flux uniformity over the beam spot, the beam is scattered over a large circular area with a diameter of about 80 cm at 1.4 m from the scattering point. Devices and electronics not supposed to be in the beam should not be damaged while another DUT is in the beam spot. Brass collimators with various apertures can be used to shape the beam as required. With three to four of these collimators in series, a large enough shadow area can be created so that the devices on the positioning system are still mostly protected.
- *Change to multi-DUT test capability:* Testing one DUT, fixed in position, at a time is acceptable for relative mitigation scheme testing, but not good for multi-DUT characterisation, or for effective time usage. In single device tests, when the DUT fails, it needs to be replaced, which takes up valuable test time. A DUT positioning system can be used, holding multiple DUTs to move devices in and out of the beam spot. There is enough physical space at most delivery points for such a system.
- *Use SRIM simulation software for configuration design:* SRIM has been used by many radiation effects researchers to estimate ion distributions and penetration depths being modelled as simple layered geometries. SRIM is the preferred transport code of [23]. Due

to its relative ease of use, SRIM is more accessible to satellite engineers not skilled in the tradition nuclear physics community software tools like GEANT4, FLUKA, and MCNPX.

Following the information gathered in this section, and the implications thereof discussed, the design of a flexible, sustainable, and reliable proton-induced SEE test configuration at iTL can be presented in Chapter 3.

---

## CHAPTER 3

# Exploring a viable, sustainable and flexible SEE test setup for iTL

---

*This chapter presents the conceptual design of the SEE test facility for iTL. It starts by presenting the design drivers and goals, followed by SRIM simulations of a modified beam delivery system at the PTV and A-line vault. A basic contextual analysis of using BLM detectors is conducted before conversion designs for SEE testing of the A-line vault and NTV is presented.*

The design approach developed and refined during this research aimed to accommodate different requirements and limitations by adopting a lean design strategy. The strategy plans to maximise rapid deployment and flexibility of the base design while maintaining a high level of reliability, repeatability and quality of the delivered beam. The rapid deployment is required to enable reasonably fast set up time, while the flexibility is requisite so that the design can be easily adapted to fit the physical constraints in each location. The reliability is needed so that the design approach remains applicable for every beam deliver point or other minor physical limitation variations. Repeatability is required to ensure beam current variation can be monitored, and compensated. Thus, enabling the comparison of test results over multiple test sessions.

### 3.1 SEE Proton Testing Facility Design Drivers and Evolution

As described in Chapter 2, iTL have multiple locations where SEE tests can be conducted. The selection of an appropriate location and the design parameters for the configuration for a specific SEE experiment is driven by the following requirements and limitations (listed in order of importance to the South African context):

- the availability of locations at iTL, based on the beam schedule;
- the availability of iTL, and other, support personnel before and during the test;
- the type of components to be tested;

- the type of SEEs to be observed during the test;
- the particle energy required for the test;
- the particle fluence, or flux, required for the test;
- the beam spot size required to cover the sensitive area of interest on the DUT.

Some of the requirements and limitations might be different for each SEE test and the design approach should be flexible enough to accommodate the variations in requirements.

In addition to the requirements and limitations listed, further, more overarching, goals were pursued. These goals also form part of the design drivers and are:

- adhere to the SEE test requirements by following international SEE test guidelines as far as possible;
- be adaptable, and by implication as uncomplicated as possible, to allow the setup and preparation times at various beam delivery points to be minimised;
- allow for testing of multiple components during one SEE test run in an 8-hour shift (the shortest beam timeslot available);
- operate using 66 MeV protons by default since it is the particle and energy combination most frequently available while providing multiple SEE test scenario options;
- can operate up to 200 MeV protons to allow for SEL sensitivity tests, when the energy option is available;
- use (or re-use) of iTL infrastructure where possible to minimise the development of custom, or once-off, infrastructure;
- provide accurate in-situ dosimetry for SEE tests.

In contrast to the requirements and limitations, the goals listed should be more stable and should be consistent over many SEE tests.

This research had limited funding, specifically in respect of covering new infrastructure development costs at iTL. Given the extremely small local SEE research community, the research and associated system development was, from the start, defined as exploratory in nature.

## 3.2 Simulations of the proton beam for candidate iTL locations

*Firstly, in this section, the use of SRIM is evaluated by simulating the beamline elements in the well-defined PTV beam nozzle. Secondly, SRIM is used to simulate design options for the A-line beam delivery system.*

As preferred by ESCC Basic Specification No. 25100 [23], the beam delivery system can be simulated in SRIM-2013 ([www.srim.org](http://www.srim.org)). Although SRIM cannot handle complex geometries, the simplicity of the design allows that the beam transport can be simulated using only a layered geometry approach.

For example, the layers, material and depth, used for simulating the A-line beam in SRIM are:

- Havar (ICRU-470), 25  $\mu\text{m}$
- Air, Dry (ICRU-104), 150 mm
- Pb, 1 mm
- Air, Dry (ICRU-104), 1.428 m

SRIM simulation results are used to estimate energy spectra as well as beam dispersion quantities at the target DUT position. For the setup in Figure 3.14, assuming a  $3\text{ mm} \times 3\text{ mm}$  Gaussian distributed incoming beam, the SRIM simulated beam dispersion at the target DUT is shown in Figure 3.1.

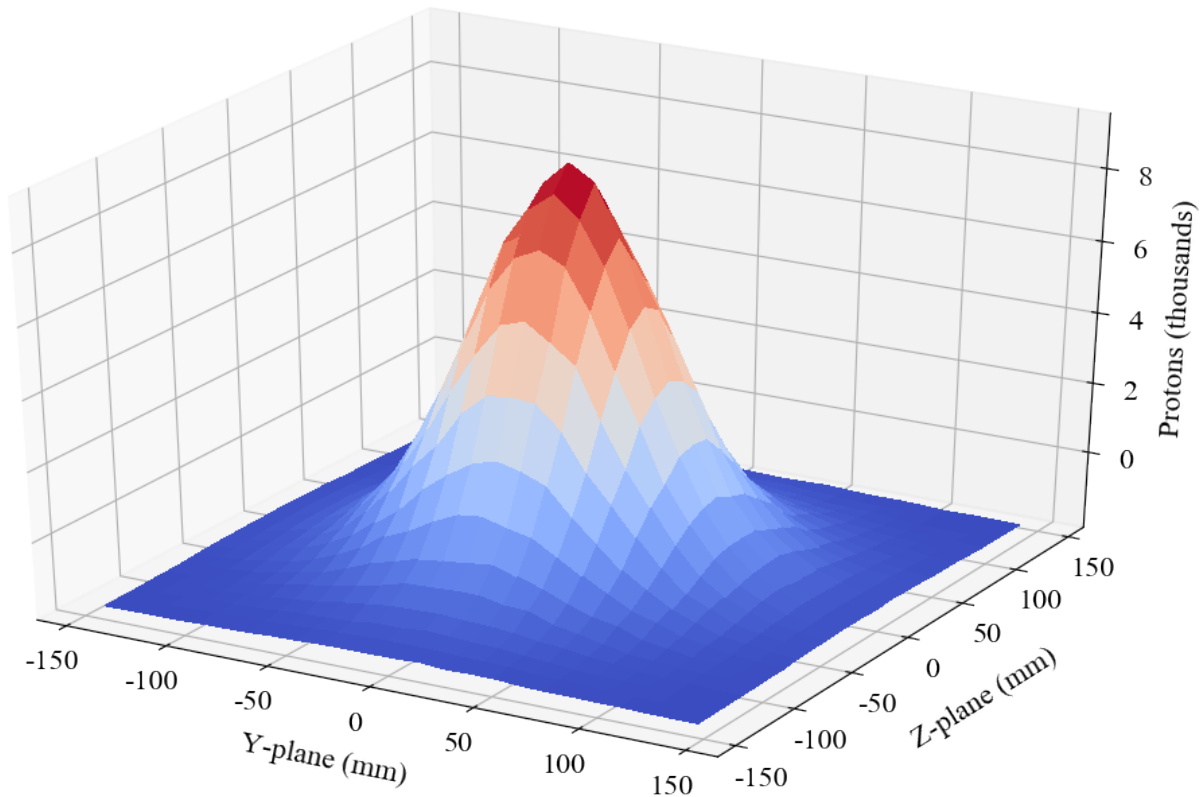


**Figure 3.1:** SRIM simulated beam distribution using at the A-line vault. The simulation used a target distance of 1.428 m from 1 mm Pb scattering sheet, assuming a  $3\text{ mm} \times 3\text{ mm}$  Gaussian distributed incoming beam.

In another case, the SRIM simulations were used to predict the energy spectra due to different degrader thicknesses. As an example, the simulation results of the SEE proton beam delivery system, used for an SEE test in December 2017, requiring multiple test energies, is visualised in Figure 3.2.

### 3.2.1 The Proton Therapy Vault

To understand the limits of SRIM simulations as pertaining to SEE test configurations, simulations of a known beamline delivery system were performed. The model detail of simulations required for SEE testing were investigated. For this purpose, a 200 MeV proton beam was simulated as it passes through the various beam elements in the proton therapy beam nozzle using SRIM 2013 [91]. The PTV was chosen as it had a good description of a proton beam delivery system and the nozzle configuration for the PTV changes very infrequently. Figure 3.3 shows the elements and their geometry used in the simulation. Each of the elements were constructed as layers with the thickness of each layer derived from the specifications of the PTV nozzle as given in [49].

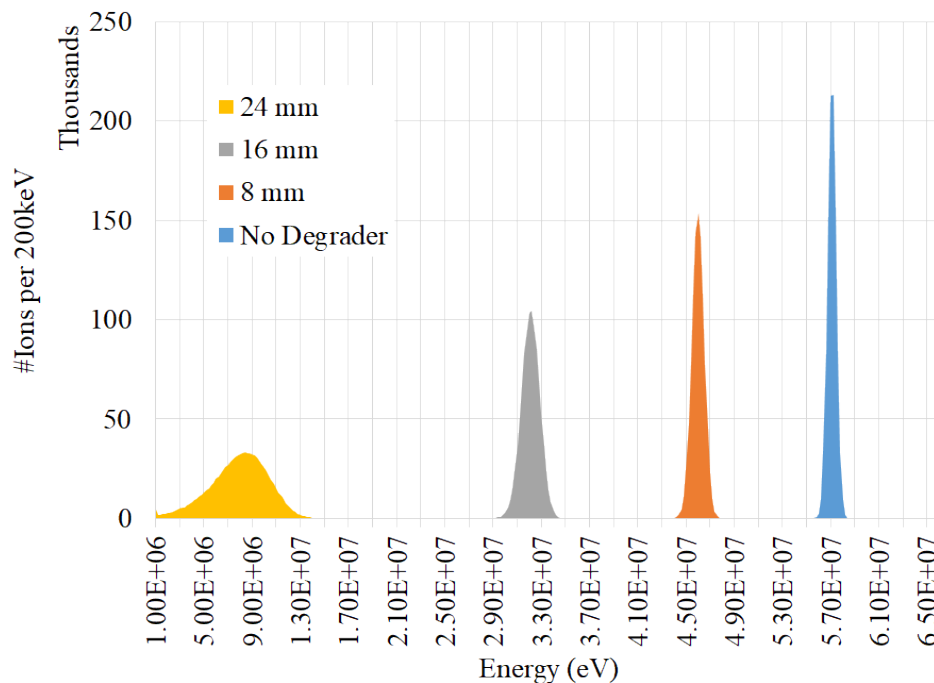


**Figure 3.2:** SRIM simulated energy spectra for various thickness plexiglass degraders after scattering a 66 MeV incoming beam using a 1mm Pb sheet.

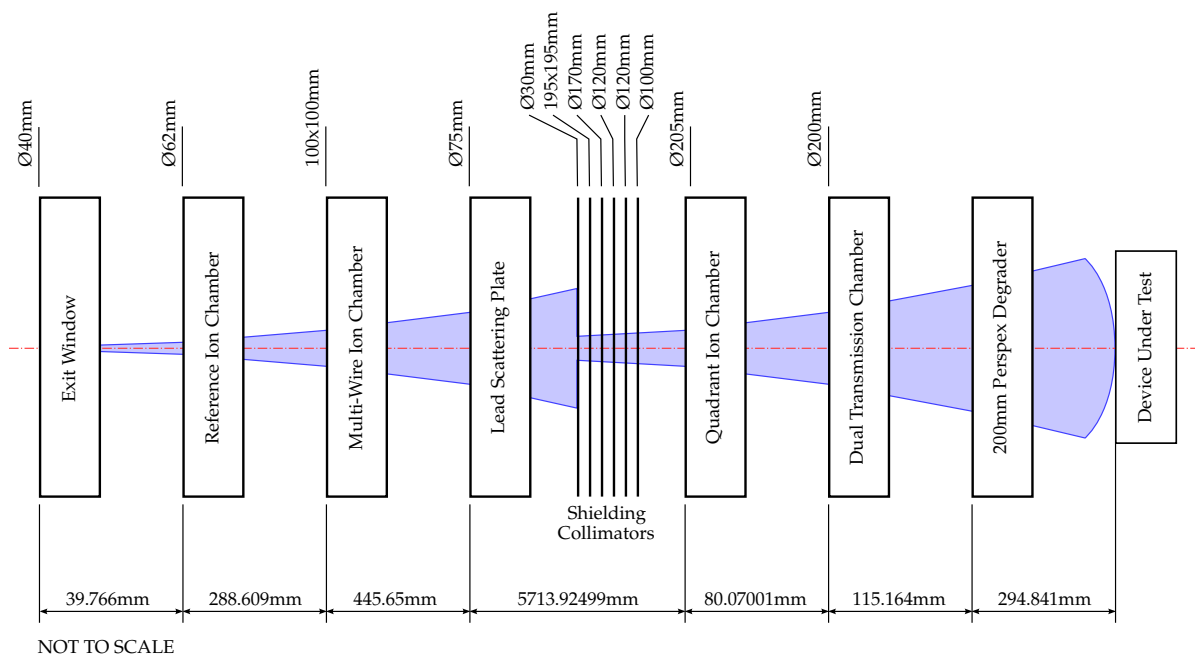


**Figure 3.3:** Simulated elements and geometry of proton treatment nozzle in PTV.

The SRIM input parameters were set to start with a “point beam”, i.e. a beam with all particles originating at 0,0 on the Y-Z plane and having an initial direction parallel with the +X axis. All protons start off being mono-energetic. Originally the first set of simulations were done using  $1 \times 10^5$  particles. However, when the results were analysed, it became clear that more particles were needed in the simulations to achieve the required resolution for accurately determining the beam uniformity. It was decided to increase the number of simulated particles

to  $1 \times 10^6$  particles. The results of the SRIM simulations for the PTV beam nozzle are shown in Figures 3.4 to 3.7. There are two major characteristics of the proton beam under consideration, firstly is the particle energy at the target and secondly the distribution of particles at the target.

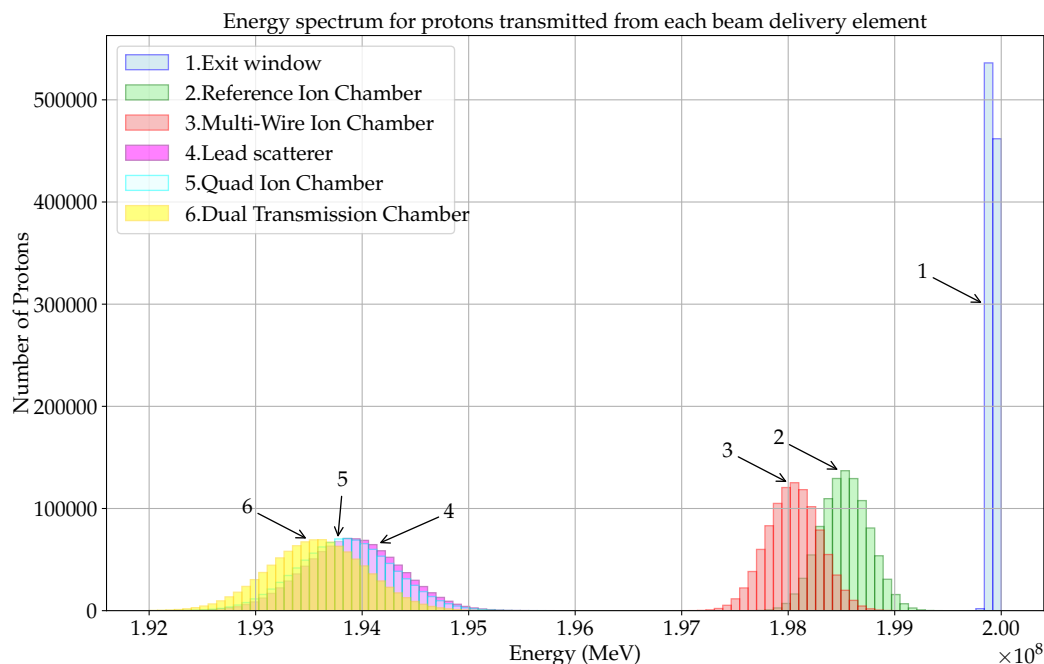


**Figure 3.4:** SRIM simulated energy spectrum of transmitted protons after each of the first six PTV beam nozzle elements at iTL.

Nozzle element	$\mu_{Energy}$ (MeV)	$\sigma_{Energy}$ (eV)	Energy dispersion (eV <sup>2</sup> )
Exit window	199.9169	$3.4116 \times 10^4$	$1.1639 \times 10^9$
Reference Ion Chamber	198.5325	$2.6672 \times 10^5$	$7.1139 \times 10^{10}$
Multi-Wire Ion Chamber	198.0516	$3.0340 \times 10^5$	$9.2054 \times 10^{10}$
Lead sheet	193.9071	$4.6676 \times 10^5$	$2.1787 \times 10^{11}$
Quad Ion Chamber	193.8436	$4.6782 \times 10^5$	$2.1886 \times 10^{11}$
Dual Transmission Chamber	193.5771	$4.7818 \times 10^5$	$2.2865 \times 10^{11}$

**Table 3.1:** Summary of proton energy statistics of 200 MeV proton point-beam after each PTV nozzle element.

When considering the energy of the beam, Figure 3.4 shows that, with a starting value of 200 MeV, the beam energy will spread as it passes through each of the beam nozzle elements. It is assumed for the sake of simplifying the statistical values, that the energy spectrum of the beam at any particular point is of Gaussian shape. Although Figure 3.3 shows a Perspex energy degrader of 200 mm, the degrader width should be chosen so that the required average energy at the DUT can be produced. As the final energy required for a specific test will vary, the beam dispersion is considered only up to the Perspex energy degrader. From the original quasi



mono-energetic beam, the beam energy spreads to a spectrum with mean energy 193.577 MeV and standard deviation of 0.453 MeV after it exists the last beam nozzle element. From the analysis, the two elements contributing most towards the energy degrading end energy spread of the beam are the Reference Ionisation Chamber (RIC) - (2) and the Lead Scattering Plate (LSP) - (4). The simulated values for the mean beam energy and energy spread after each beam element is shown in Table 3.1.

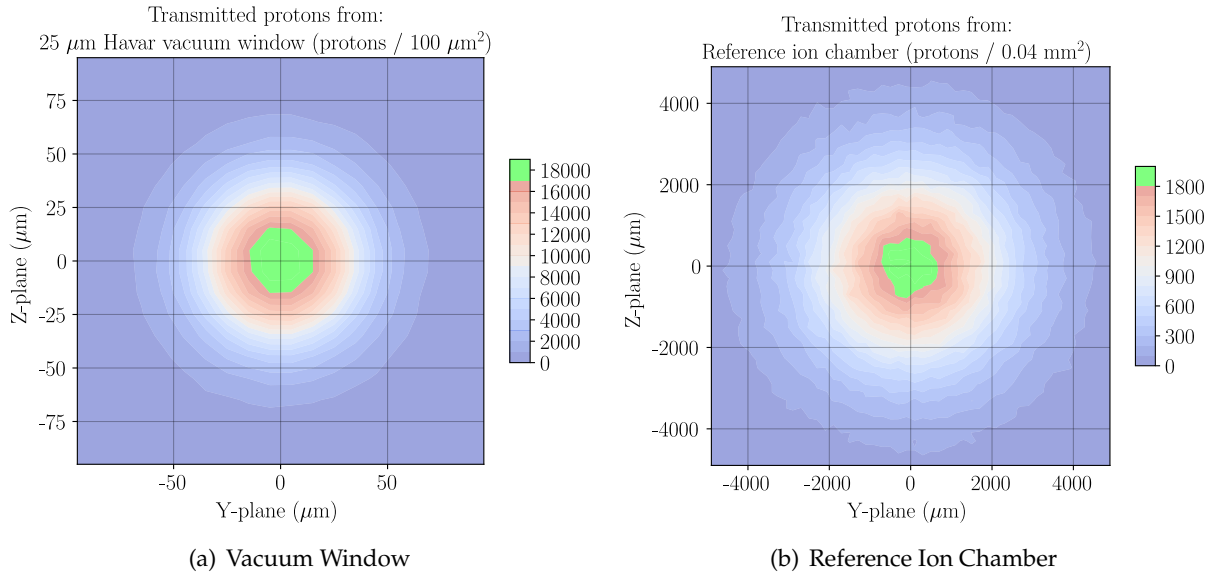


**Figure 3.5:** Beam shape after a) Vacuum Window and b) Reference Ion Chamber. Note the difference in scale of plotted area. Also note the integration area for intensity values.

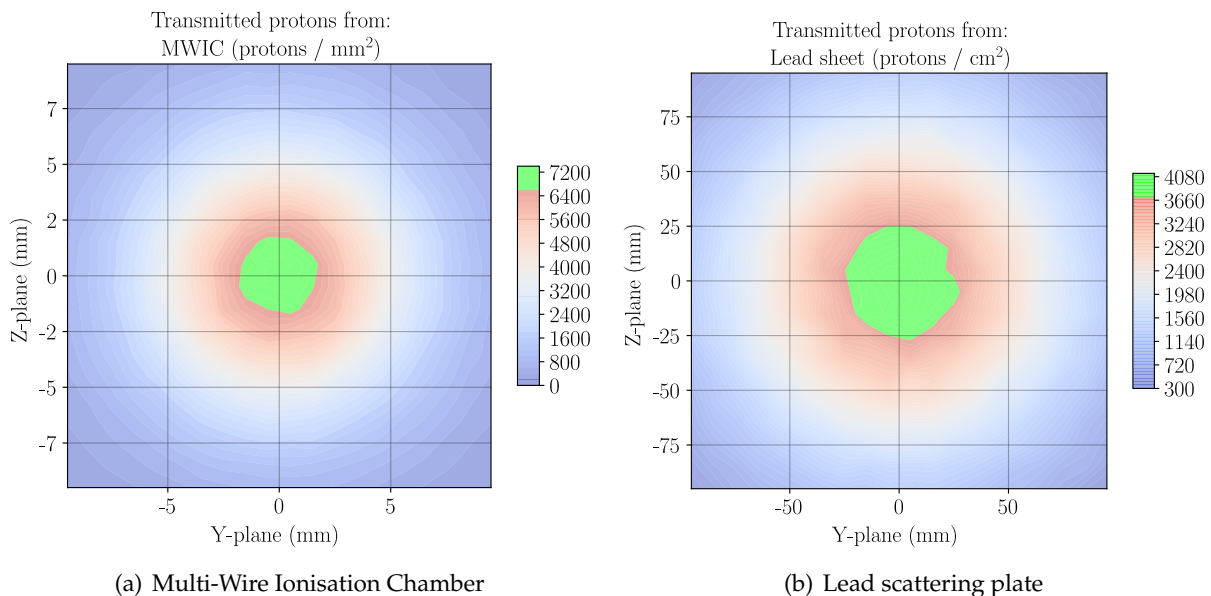


**Figure 3.6:** Beam shape after a) MWIC and b) Lead scattering plate. Note the difference in scale of plotted area, showing the large amount of beam spread due to the lead plate. Also note the difference in integration area for intensity values.

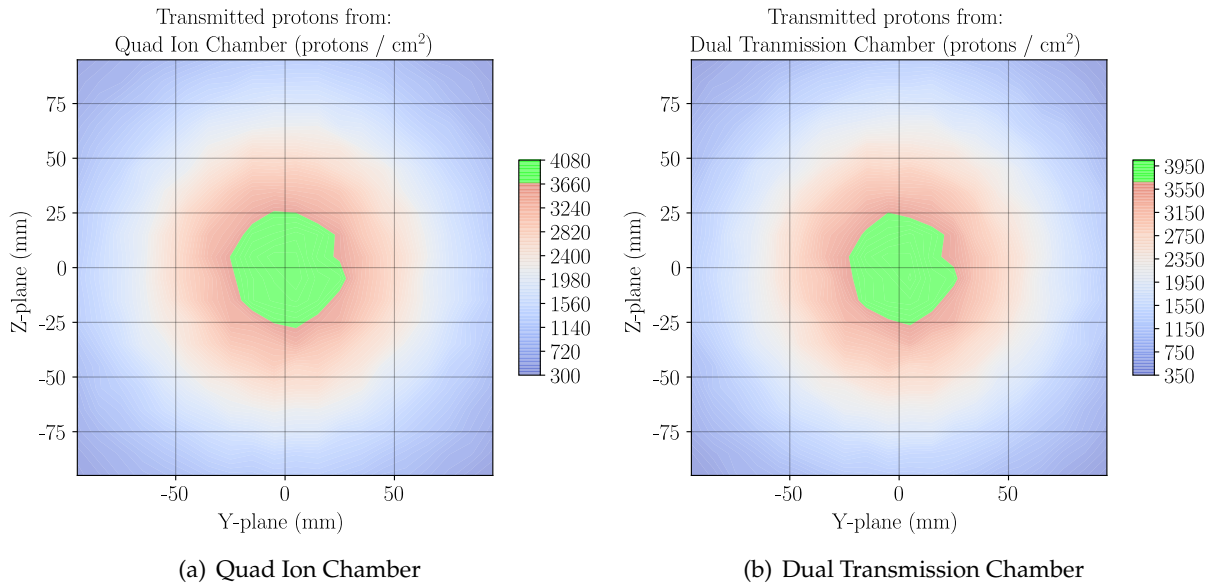


**Figure 3.7:** Beam shape after a) Quad Ion Chamber and b) Dual Transmission Chamber, showing very little effect on the beam profile.

Nozzle element	$\mu_Y$ (Å)	$\mu_Z$ (Å)	$\sigma_Y$ (Å)	$\sigma_Z$ (Å)
Exit window	$-4.087 \times 10^2$	$1.073 \times 10^3$	$7.989 \times 10^5$	$6.791 \times 10^5$
Reference Ion Chamber	$-3.079 \times 10^4$	$-4.490 \times 10^4$	$6.075 \times 10^7$	$5.220 \times 10^7$
Multi-Wire Ion Chamber	$-1.031 \times 10^5$	$-1.363 \times 10^5$	$1.713 \times 10^8$	$1.413 \times 10^8$
Lead sheet	$-1.149 \times 10^6$	$-9.796 \times 10^5$	$1.888 \times 10^9$	$1.496 \times 10^9$
Quad Ion Chamber	$-1.155 \times 10^6$	$-9.846 \times 10^5$	$1.902 \times 10^9$	$1.507 \times 10^9$
Dual Transmission Chamber	$-1.163 \times 10^6$	$-9.908 \times 10^5$	$1.918 \times 10^9$	$1.519 \times 10^9$

**Table 3.2:** Summary of proton distribution statistics of 200 MeV proton point-beam after each PTV nozzle element.

Considering the dispersion achieved, and the beam flux at the DUT, the simulated beam was plotted to show its geometric shape. Figures 3.5 - 3.7 shows the shape of the beam after each beam nozzle element while Table 3.2 summarises the proton distribution statistics. As an illustration of the beam intensity distribution, the protons are integrated over a selected square area. The chosen area is indicated in each figure, and the data is plotted as a contour map. The beam has a central area where the uniformity varies with less than 10% from the maximum intensity, which in each case is indicated with light green. From Figure 3.5(a) it is clear, and expected, that the Exit Window does not disperse the beam significantly, with the area of integration being  $10 \mu\text{m} \times 10 \mu\text{m}$ , or  $100 \mu\text{m}^2$ , in the YZ-plane. The RIC has a significant dispersion effect as is shown in Figure 3.5(b). Note that the YZ-plane scale differs by a factor of 53.33. After the RIC the beam geometry has a dispersion of  $\sigma_Y = 6.075 \text{ mm}$  and  $\sigma_Z = 5.22 \text{ mm}$ .

Figure 3.6 shows the beam shapes after the Multi-Wire Ionisation Chamber (MWIC) and the LSP. The beam shape after the MWIC is very similar in shape to the beam shape after the RIC, however, the distance between the elements results in the beam spreading more. Note that the plot area shown after the MWIC is  $20 \text{ mm} \times 20 \text{ mm}$  in the YZ-plane.

The LSP, however, disperses the beam drastically. The beam is scattered to a much larger

degree by the LSP. This effect is further enhanced by the fact that the air gap between the LSP and the next nozzle element is significant, more than 5.7 m. Note that the plot area shown after the LSP is 200 mm  $\times$  200 mm in the YZ-plane. Most of the collimation elements are also located in this 5.7 m space. The result is that a much flatter beam intensity profile, with only a fraction of the protons that arriving at the next nozzle element. The two nozzle elements that contributed most to the energy degrading as well as the energy spread also contributed most to dispersing the beam.

At this stage, it was noted that the simulations take quite long, sometimes more than six hours per run. To limit further simulation time, the transmitted protons, leaving the final ions chambers, were filtered so that only those with a lateral displacement less than the edges of a 100 mm  $\times$  100 mm box were considered for degrader simulations.

The last two elements' contribution to the scattering of the beam is shown in Figure 3.7. Note that the plot area shown is still 200 mm  $\times$  200 mm in the YZ-plane. The beam shape profile in this area is relatively flat, which is required to give an even dose exposure over the device. At this point, the beam spot has a uniformity with less than 10% variation of roughly 50 mm diameter. The beam spot compares well with the spot sizes reported in [79; 81].

After the 'permanent' beam nozzle elements, different thickness Perspex energy-degrading slabs can be used to degrade the beam energy further. This method provides a convenient and quick way to lower the beam energy incident on the DUT. Compared to changing the cyclotron beam energy, which will require a whole range of re-tuning and calibration procedures for each energy, the aforementioned approach, using the energy-degrading slabs, is preferred. This method makes it possible to simulate the expected beam energy spectrum and beam shape profile using a package like SRIM since the beam elements can be modelled as material layers only. More importantly, the simulation results can be matched to measured values over a representative energy range. Simulation techniques can be used to estimate the energy spectra and beam profiles outside the measurement range, which can result in time and cost savings since re-tuning and calibration cycles will be reduced.

### 3.2.2 Simulating the A-line beam

The first phase of establishing feasibility of in-air testing at the A-line was to use SRIM and simulate a 66 MeV beam to see what energy spectrum and beam profile can be achieved when using a single scattering plate and collimator setup. 66 MeV was used as this is the most readily available beam energy. A single scattering plate configuration was used to keep simulations valid. Collimators are not modelled in the simulation but will be required to shield electronics surrounding DUT.

The type of material and sheet thickness to use for passive beam spreading was investigated through SRIM simulations. The SRIM simulation results for Al and Pb sheets, over a range of thicknesses is summarised in Table 3.3.

Table 3.4 shows extra analysis performed on the simulated results. The first analysis column shows the energy loss as a percentage of the incoming 66 MeV beam. The next column shows the spread factor, which is normalised to 125  $\mu$ m Al. The last column shows the average  $\sigma$  of the particle positions (spread) per the magnitude of energy lost (loss) in units of  $\text{\AA}/\text{eV}$ . The Pb has a significantly higher ratio of the beam being spread versus energy lost.

Material	Thickness ( $\mu\text{m}$ )	$\mu_{\text{Energy}}$ (eV)	$\sigma_{\text{Energy}}$ (eV)	$\sigma_Y$ ( $\text{\AA}$ )	$\sigma_Z$ ( $\text{\AA}$ )
Al	125	$6.521 \times 10^7$	$8.886 \times 10^4$	$2.157 \times 10^7$	$2.103 \times 10^7$
Al	500	$6.441 \times 10^7$	$1.302 \times 10^5$	$3.780 \times 10^7$	$3.707 \times 10^7$
Al	2000	$6.114 \times 10^7$	$2.377 \times 10^5$	$1.054 \times 10^8$	$1.040 \times 10^8$
Pb	500	$6.269 \times 10^7$	$2.191 \times 10^5$	$2.168 \times 10^8$	$1.927 \times 10^8$
Pb	1000	$6.039 \times 10^7$	$3.487 \times 10^5$	$3.099 \times 10^8$	$2.982 \times 10^8$

**Table 3.3:** Summary of proton energy and distribution statistics of 66 MeV proton point-beam passing through Al and Pb scattering sheets of varying thickness and 500 mm air.

It should be noted that spreading efficiency is expected to drop as the material thickness increases due to particle scattering inside the material. The thicker the material, the more chance a particle has of being scattered multiple times in different directions, which on average reduces the overall scatter angle, but the energy loss keeps increasing with each interaction of the particle with the material.

Material	Thickness ( $\mu\text{m}$ )	Energy loss (%)	Energy straggle (%)	Spread factor	Spread / Loss
Al	125	1.200	0.134	1.000	26.894
Al	500	2.409	0.197	1.753	23.546
Al	2000	7.362	0.360	4.885	21.548
Pb	500	5.009	0.332	10.052	61.939
Pb	1000	8.502	0.528	14.369	54.191

**Table 3.4:** Analysis for Al and Pb scattering sheets of varying thickness and 500 mm air. Energy loss is versus 66 MeV, Energy straggle is as a % of 66 MeV, Spread factor is the average position  $\sigma$  vs average 125 $\mu\text{m}$  Al position  $\sigma$ , and Spread/Loss is in  $\text{\AA}/\text{eV}$ .

Gottschalk [92] also showed that high-z materials give the best radial scattering versus energy absorption. Using the SRIM results and guidance from Gottschalk lead (Pb) was chosen as scattering material. By limiting the energy degradation so that the resulting energy spectrum mean is close to 60 MeV, a lead plate thickness of 1 mm was chosen. Given these results, a 1 mm thick lead scattering plate was made up using two layers of a 0.5 mm lead sheet, that was already available.

An experiment was done in the A-line scattering chamber to verify the accuracy of using SRIM simulation results in this context. The experiment and measurement results are discussed in Section 4.1.

### 3.3 Dosimeter selection

*As the results from Section 4.1 will show, a beam monitoring detector was required to provide dosimetry information during beam profile measurements and device exposure. The choice of dosimeter, and its appropriateness for use in a pulsed proton beam is discussed in this section.*

### 3.3.1 BLM device as a dosimeter for SEE testing

A novel approach to beam monitoring was developed for the SEE tests at iTL. Two detectors are used to both profile the beam spot and shadow, and perform in-situ monitoring of the device exposure during SEE testing. This way beam setup can be verified and accurate dosimetry can be achieved while minimising the impact on test time.

The approach uses a beam loss monitor (BLM) [93], which is a p-i-n diode based particle counter device, to do in-situ beam monitoring. The design utilises two of the BLMs, one BLM in-beam at the DUT target distance and one reference BLM on the edge of the scattered beam. Figure 3.14 shows the relative positions of the BLMs. With this configuration, the reference BLM can be used throughout the test to measure the beam current continuously, whereas the in-beam BLM can be remotely moved, both horizontally and vertically, through the beam spot to measure the beam spot profile at the target. By measuring the in-beam BLM count in the beam spot versus the reference BLM count on the periphery of the Gaussian-shaped beam, a reference ratio can be calculated. The ratio is used to calculate the dose received by the DUT after the test. The beam spot uniformity and size is immediately verifiable by plotting the counts from the in-beam BLM versus its position in real-time.

This dosimetry calibration procedure should take less than an hour, leaving more beam time for component exposure. By mounting the BLM on the DUT positioning system, it can be remotely moved out of the beam spot after calibration and SEE testing can begin on the DUTs.

### 3.3.2 Effectiveness of BLM device as a dosimeter in a pulsed proton beam

The BLM device was not designed as a dosimeter. Therefore it is essential to evaluate the effectiveness of using it as a dosimeter in proton beam SEE tests.

Considering the *spatial resolution* for beam spot measurement of the BLM device. The detecting elements of the BLMs are two back-to-back mounted p-i-n diodes with an effective face area of  $7.34 \text{ mm}^2$  ( $2.712 \text{ mm} \times 2.712 \text{ mm}$ ). The size of the detector will ensure that a fine enough measurement can be made over the area of a typical DUT. The required beam spot can be from 10 mm diameter to 80 mm diameter. The active detector area will allow for at least nine non-overlapping measurements over the smallest beam spot, to verify beam uniformity.

Further, the *sensitivity* of the device to detect high-energy protons,  $> 50 \text{ MeV}$ , is expected to be good. It was designed to detect Minimum Ionising Particles (MIPs), typically stray beam particles passing through the beamline walls.

Thirdly, the *measurement bandwidth* of the BLM device is considered. Due to the p-i-n diode having a recovery time of up to 100 ns after a particle strike, the BLM has a measurement limit for particle strike rates of 10 MHz. The proton beam produced by the iTL SSC is a pulsed beam with resonant frequencies ranging from 5 MHz up to 27.5 Mhz. Depending on the beam energy, the limited bandwidth of the BLM can present a problem. The problem is illustrated in Figure 3.8, showing three distinct regions to consider: frequencies below the bandwidth limit; frequencies up to twice the bandwidth limit; and frequencies from  $2\times$  to  $3\times$  the bandwidth limit.

At 66 MeV, the typical operating energy for SEE tests, the cyclotron has a pulse frequency of roughly 16.37 MHz, with proton beam pulses of 3 ns in length. Although these beam pulse

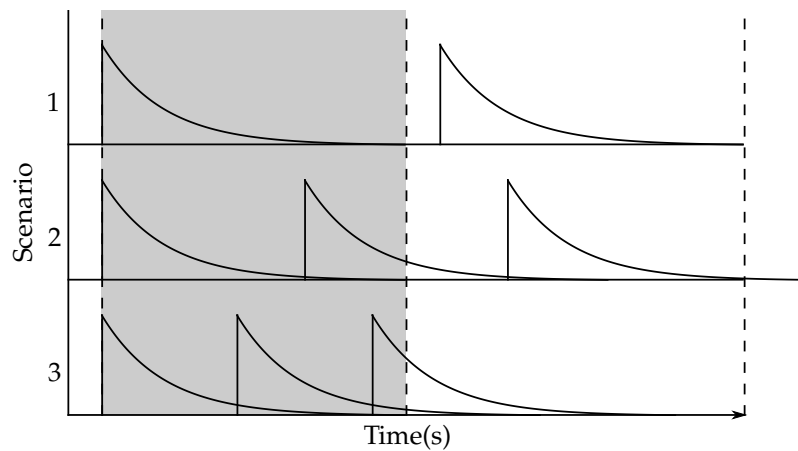


**Figure 3.8:** Illustration of three different scenarios associated with three frequency ranges of SSC beam pulses with BLM sensor recovery window edges shown with dotted lines. Beam frequency, from top to bottom, is:  $<1x$  sensor bandwidth,  $1x - 2x$  sensor bandwidth,  $2x - 3x$  sensor bandwidth.

rates are above the maximum operating frequency for the BLM, the low beam current and passive spreading of the beam mitigate the BLM bandwidth limitation. For the SEE tests, the beam, and therefore the proton bunches are spread out, using the Pb sheet, over a large area to produce a relatively flat central beam spot. If the proton density per bunch, i.e. the beam current, is low enough, the probability of consecutive bunches causing a strike in the small detector area can be reduced to a negligible value.

Next, the effect of *particle density* at the detector on the magnitude of the error in counts is investigated. A simulation was created to investigate the expected effectiveness of using the BLM as a dosimeter in a pulsed beam environment. Based on the probability of protons hitting the target area of the p-i-n diode, the simulation estimates the counting accuracy of the BLM in this context.

The probability of any proton from a single bunch striking the target can be estimated from the simulated distribution of protons at the target using SRIM. It is reasonable to assume that the position of each particle in a bunch is independent of the position of any other particle in the bunch. Therefore the combined result of sequentially simulated independent particles by SRIM should be representative of the particle positions in a bunch. The probability of a proton striking the detector is defined as  $p = P(\text{strike})$ . The value for  $p$  used is the ratio of protons within the detector area divided by the total amount of protons simulated by SRIM:

$$p = P(\text{strike}) = \frac{\text{protons in detector area}}{\text{total amount of protons}} \quad (3.1)$$

With a strike probability defined, a miss probability defined as  $P(\text{miss}) = q = 1 - p$  (a proton whose position falls outside the detector area), and assuming independence between particles in a bunch, the scenario represents a set of Bernoulli trials [94, Chap. 2]. Using  $p$  as defined in (3.1),  $q = 1 - p$ , and  $n$  as the number of protons in a bunch, the probability of the number of protons striking the detector from a single bunch is then:

$$P(k \text{ successes in } n \text{ trials}) = \binom{n}{k} \cdot p^k \cdot q^{n-k} \quad (3.2)$$

or in algorithmic form:

$$P(k \text{ successes in } n \text{ trials}) = \frac{n!}{k! \cdot (n-k)!} \cdot p^k \cdot q^{n-k} \quad (3.3)$$

The number of protons per bunch can be calculated using the beam current, beam frequency and with 1 Coulomb =  $6.241\,509\,75 \times 10^{18}$ :

$$\text{protons per bunch} = \frac{\text{beam current} \cdot 1 \text{ Coulomb}}{\text{beam frequency}} \quad (3.4)$$

The expected amount of counts from the detector is comprised of two sets of counts, 'true' single-strike counts, as well as 'multi'-strike counts. Multi-strike counts are the cases where more than one proton from a single bunch strikes the detector. Now if  $P(k=0)$  and  $P(k=1)$  is calculated, i.e. the probability of *no proton strikes* in a bunch and the probability of *exactly 1 proton strike* in a bunch, then the probability of *more than one proton strikes* from a single bunch  $P(k>1)$  is:

$$P(k > 1) = 1 - (P(k=0) + P(k=1)) \quad (3.5)$$

Using (3.3), (3.4) and (3.5), the probability and expected counts from an ideal detector is calculated over a range of beam currents from 1 nA to 30 nA in steps of 1 nA. The results shown in Figures 3.9 and 3.10 used  $p = 1.007\,61 \times 10^{-4}$  from the SRIM generated data for the geometry.

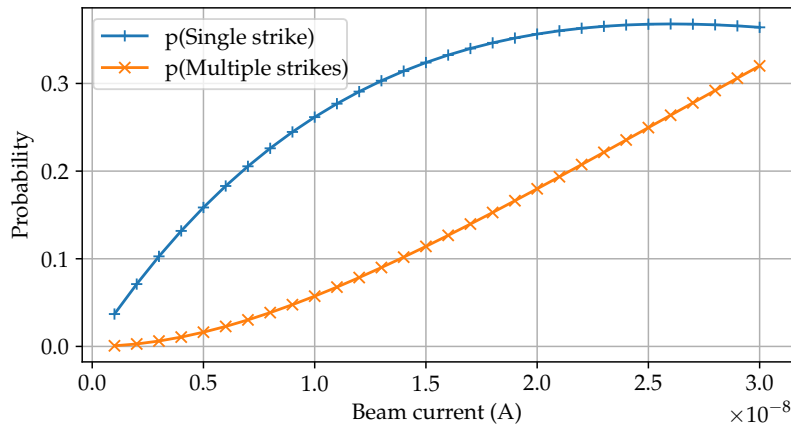


**Figure 3.9:** Probability of proton strikes on the BLM detector area using SRIM data for NTV setup in 2019. The average amount of protons passing through the detector area per  $1 \times 10^6$  simulated protons were 100.761.

At 1 nA, the results show the probability of a single proton strike on the detector is 3.69%, versus the probability of any multi-strike, is 0.07%. The multi-strikes contribute a tiny amount to the events counted. At 5 nA, the probability of single strikes has increased to 15.85% versus multi-strikes' probability of 1.62%. At this point, the multi-strike contribution is 10% of the total and is no longer insignificant. As the current is further increased, the contribution of the multi-strikes increases relative to the single-strike contribution, reaching 32% probability at 30 nA, which is almost the same as the 36.4% probability of single-strikes.

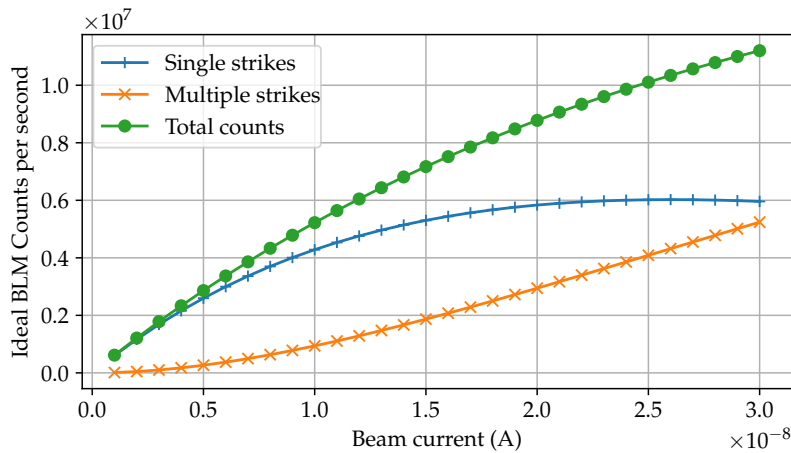


**Figure 3.10:** Expected BLM counts using SRIM data for NTV setup in 2019. The average amount of protons passing through the detector area per  $1 \times 10^6$  simulated protons were 100.761.

From the analysis, the detector counts will have a significant error in representing the beam intensity at currents over 5 nA. These values apply just to the configuration of the beam delivery configuration for the January 2019 setup in the NTV. For other configurations, the amount of beam spread might be different, which will affect the beam distribution at the target, which affects the proton strike probabilities.

The problem with multi-strikes can be mitigated by using the BLM dosimeter only for measurements where the beam current is below 5 nA, put differently, at currents where the probability of multi-strikes is  $10 \times$  less than the single-strike probability.

If the region from 0.1 nA to 1.5 nA is considered, as shown in Figures 3.11 and 3.12, the trends for single-strike and multi-strikes probabilities are quite different. In this region, single-strike probability is the dominant contributor to the total counts. At 1.5 nA the count contribution due to multi-strikes is only 2.93% (0.1595% versus 5.4412%).

For completeness, the actual intensity error magnitude is more than the amount of multi-strike counts. Multi-strikes comprises *all* cases where more than one proton strikes the detector, so some of the multi-strike counts are due to three or more protons striking the detector from one bunch. However, the magnitude of these events is much less than two-proton strikes. If the multi-strike count's contribution is less than 1%, the additional count error will be insignificant.

Lastly, the BLM *directionality* and its filtering of unwanted particles are considered. By utilising the back-to-back diode configuration, the BLM limits the angles at which arriving particles can pass through both p-i-n diodes. Consequently, almost exclusively, only coincident high-energy protons will be the source of generating output pulses. The Si diodes of the BLMs are very inefficient photon detectors with the result that photons will extremely rarely Compton scatter in *both* diodes and cause a coincident event. Neutrons, generated through proton beam interactions with the brass collimators, can only cause BLM counts through indirect ionising mechanisms. Neutrons have a minuscule cross-section to interact with nuclei in the first diode leading to a recoil proton triggering the second diode. Therefore they will contribute negligibly towards BLM counts.

After consideration of the aspects of the BLM it is deemed suitable to use as a dosimetry device in pulsed proton beam SEE tests. Four experiments were conducted to verify the BLM's



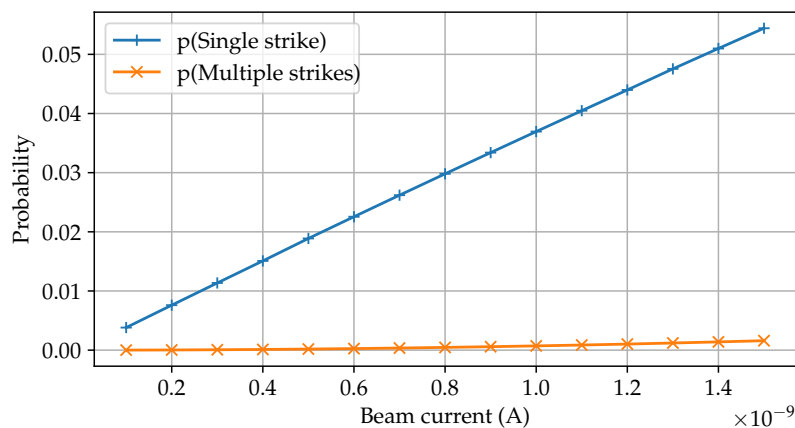


**Figure 3.11:** Probability of proton strikes on the BLM detector area for small beam currents. The average amount of protons passing through the detector area per  $1 \times 10^6$  simulated protons were 100.761.

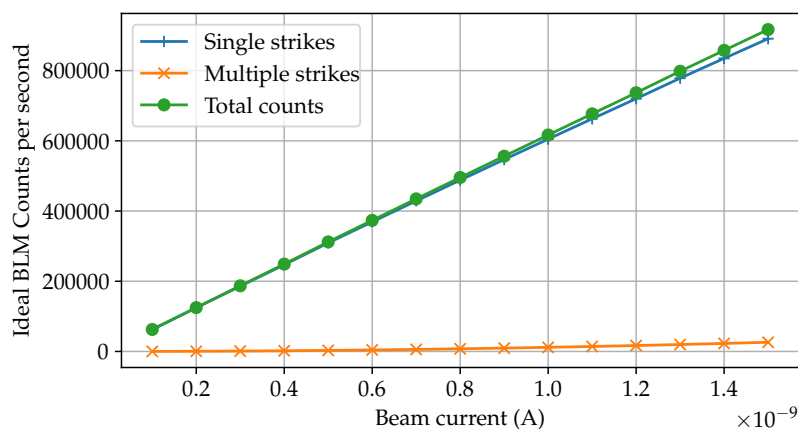


**Figure 3.12:** Expected BLM counts for small beam currents. The average amount of protons passing through the detector area per  $1 \times 10^6$  simulated protons were 100.761.

viability as a dosimeter and the feasibility of using the dual-BLM system for measurement of the beam spot, beam shadow area, and device exposure during testing. The experiments are presented in Sections 4.1, 4.2.1, 4.2.2, and 4.2.3.

### 3.4 Converting the A-line for SEE testing

*From Section 2.9 the first option that will yield the biggest improvement towards enabling SEE testing at iTL, is to create a suitable SEU setup in the A-line.*

The pencil beam (sub 3mm diameter) cannot be used directly to irradiate a device, and the beam must be spread out over a larger area. A sub-optimal beam spreading approach has been used up to December 2015. The final quadrupole magnets, usually used to keep the beam focused, was used to de-focus the beam to an area of approximately 2 cm diameter. Using the de-focused beam results in a beam profile that is not accurately known, and there is no way to measure the beam profile more accurately than visual inspection via a remote camera. Given the dimensions and beam intensity, it is not possible to use available detectors to measure the

beam profile. This scenario required a re-design of the A-line setup for SEE testing.

By using similar principles as applied in the proton vault beam nozzle, a better beam delivery system was designed for the A-line.

In addition to the expected vacuum system modifications, a multi-port vacuum feed-through adapter was designed and manufactured. Standard connectors were used in the feed-through design to keep manufacturing costs affordable.

Summaries of the test configurations for the three initial experiments (see detailed descriptions in Section 4.1.1) are given here for context.

E.J. Thesnaar, Controller Area Network (CAN) controller mitigation - October 2013:

- boards were custom developed FPGA boards for mitigation testing;
- custom vacuum connector had to be made. The design is shown in Figure 3.13;
- experimented with commercial connectors filled with epoxy;
- connectors finally sealed with specialist putty (Presstick);
- board serial port connected using Universal Serial Bus (USB)-Universal Asynchronous Receiver-Transmitter (UART) cable to USB hub;
- USB-to-Ethernet connection used to give access to DUT from the control room.

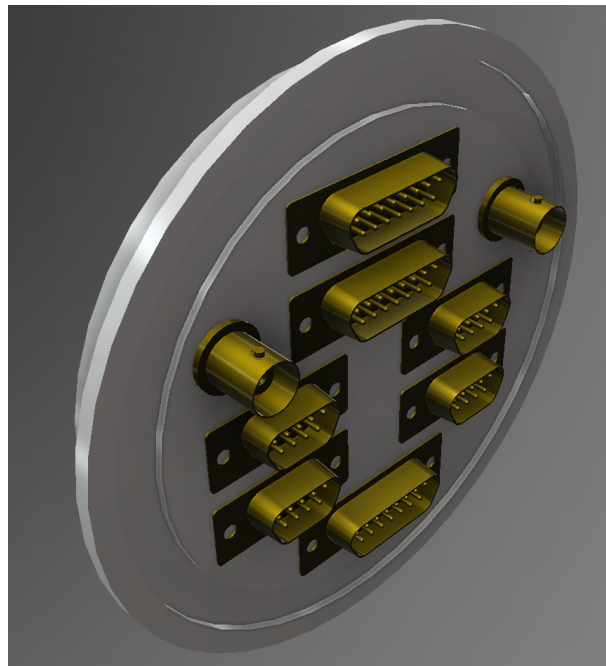


**Figure 3.13:** Rendered 3D model of the vacuum connector for the A-line that includes 2 x analogue signal, 4 x DB-9 digital, and 3 x DB-15 digital interface connectors.

PJ Botma, Cube Computer mitigation - December 2013:

- board was prototype CubeSat onboard computer, not specifically designed for mitigation testing;
- same vacuum connector used as during October 2013;
- same electrical and communication interfaces used the as October 2013.

F. Smith, Xilinx Spartan FPGA - December 2015

- boards were Xilinx Spartan development boards, one DUT and the second, outside the vacuum chamber, used to monitor the DUT;
- same vacuum connector used as during October 2013;
- same electrical and communication interfaces used as during October 2013.

Although the initial three experiments using the magnetic spreading technique to test in vacuum was successful at conducting mitigation tests, the following changes were proposed to optimise the design to be more optimal and suitable for general SEE testing:

- The tests should be done in air to reduce the lead time for physical setups and reduce the turn-around time for manually changing the setup during testing.
- Vacuum windows are required and should be manufactured.
- A passive beam scattering plate should be introduced to produce a more uniform proton field at the DUT.
- Collimators should be used to limit the exposure of the vault and other measuring equipment to the scattered protons.
- To verify the beam profile, a measurement of the beam profile should be done.
- A multi-DUT platform should be built to mount multiple DUTs on, which would further reduce the beam time wasted during tests.

### 3.4.1 Beam delivery and configuration for in-air testing

*Compared to designs for previous SEE tests at the A-line, the major differences for the new design are in-air testing, passive beam spreading, measured uniform (<10% variation) beam exposure, in-situ dosimetry, and multiple remote managed DUTs per test.*

The design of the beam shaping is based on the classical approach of passive beam spreading, as described in [92], and collimating in air. It is also described as a common approach to proton beam test setups in [90]. This approach is similar in concept to the Proton Therapy beamline design at iTL, but with simplifications. Shown in Figure 3.14 is the conceptual design, as applied to the A-line chamber.

In Figure 3.14, the 66 MeV proton beam enters from the left. A 25  $\mu\text{m}$  Havar vacuum window transports the beam from vacuum to air. From there the beam passes through a 1 mm thick Pb scattering sheet. A set of collimators, two, in this case, collimates the beam. The beam can optionally be degraded with a set of degrader sheets ranging from 1 mm to 24 mm thick.

Through the collimators, both a predefined beam spot and a beam shadow area can be achieved. The beam spot ensures that only the DUT is exposed to the protons, whereas the beam shadow protects the surrounding electronics from high levels of exposure during the SEE test. The shadow area allows multiple DUT boards to be mounted on the DUT positioning platform. Thus, multiple devices can be exposed in turn, by remotely moving each DUT board into the beam, reducing the need to enter the vault between test runs.

The original DUT positioning platform design for the A-line vault consists of a rotating table, shown in Figure 3.14, with a back-plate on which multiple DUT can be mounted. The rotational design was chosen since it has a fairly simple drive mechanism, a relatively small footprint, and could fit inside the vacuum chamber of the A-line. The detailed design and manufacture of the table were done in collaboration with the researchers and students from

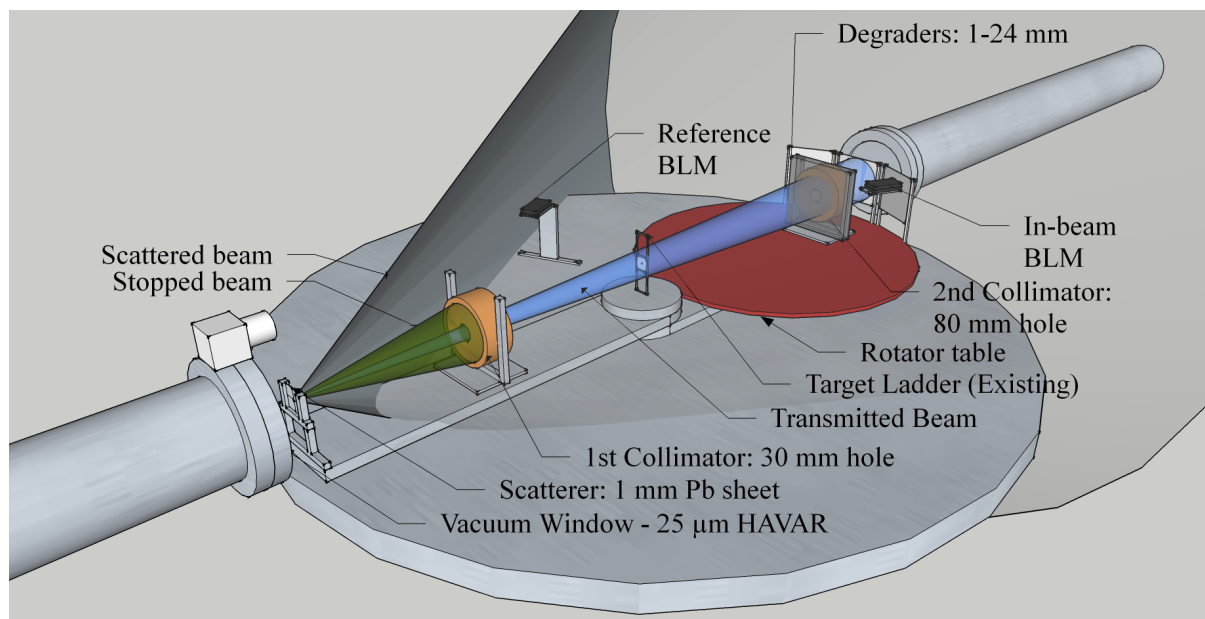


**Figure 3.14:** Conceptual design of SEE proton testing beam delivery system for the A-line showing the elements from beam vacuum window to the DUT, including the BLMs for dosimetry.

Nelson Mandela University and was used in in-vacuum SEE testing in the A-line [95; 96]. A second, linear motion-based, design for a DUT positioning platform was also realised in co-operation with industry partners and students. The linear movement platform, mounted on a rotational arm of the A-line chamber, is shown in Figure 3.15.

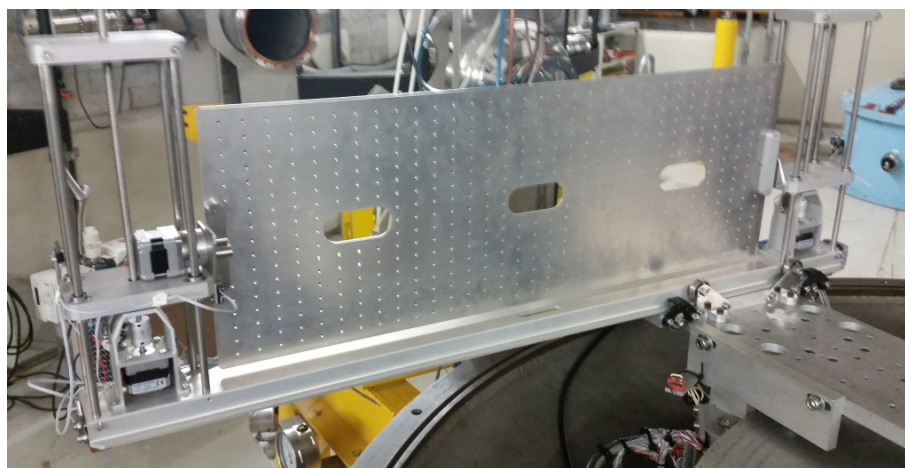


**Figure 3.15:** Remotely controlled DUT positioning platform in the A-line scattering chamber. The platform has mounting space for multiple DUTs and linear horizontal, linear vertical, and rotation movement options. The platform was designed to be mounted on one of the rotatable arms of the A-line scattering chamber.

To degrade the beam during testing, various thicknesses of Poly (methyl methacrylate), more commonly known as Plexiglass, sheets are used. This degrading method is based on the one used in [97]. The Plexiglass is a good degrader material since it has a minimal pro-

ton deflection to energy absorption ratio. Plexiglass is also readily available, affordable and convenient to machine.

### 3.4.2 Vacuum window design

The vacuum window must maintain the high vacuum of the beamline while allowing the proton beam to exit into the air. As the protons pass through the vacuum window material, they will be scattered to a degree. The aim is thus to choose a material that is strong enough to handle the pressure differential while not being too thick and scatter the beam too much. The material must also be durable to minimise maintenance and re-manufacture time. There were two candidate materials, each in two thicknesses. The first material is the same material used in the PTV beam delivery system, Havar (ICRU-470). The Havar used in the PTV is 25  $\mu\text{m}$  thick. There was also 6  $\mu\text{m}$  Havar available in storage at iTL. Havar has good qualities, including high strength, high corrosion resistance, and it is non-magnetic. From previous good experience at iTL 50  $\mu\text{m}$  and 90  $\mu\text{m}$  Kapton (ICRU-179) was also suggested as candidate material for the vacuum windows by iTL staff.

The strength of the various material options had to be verified. The thinner 6  $\mu\text{m}$  Havar would cause less beam deflection and energy loss, as discussed in the following paragraphs, so it was investigated as an option. Being much thinner than the 25  $\mu\text{m}$  reference, it was important to test if the material could withstand the required operational vacuum pressure. Two 88 mm-diameter, to match the beamline diameter, vacuum window holders were manufactured. Two 6  $\mu\text{m}$  Havar foil windows were prepared and assembled into the holders. Both assemblies were tested on a vacuum test rig, and both failed before the required pressure was reached. The 6  $\mu\text{m}$  Havar was not strong enough for the size of the vacuum window used, i.e. 88 mm-diameter. This result suggested that for the 25  $\mu\text{m}$  Havar evaluation, the vacuum window diameter be reduced to 50 mm. To validate that the 90  $\mu\text{m}$  Kapton is strong enough when used, a 88 mm-diameter film was also prepared, and vacuum tested. The Kapton passed the vacuum tests and remained an option for the vacuum windows.

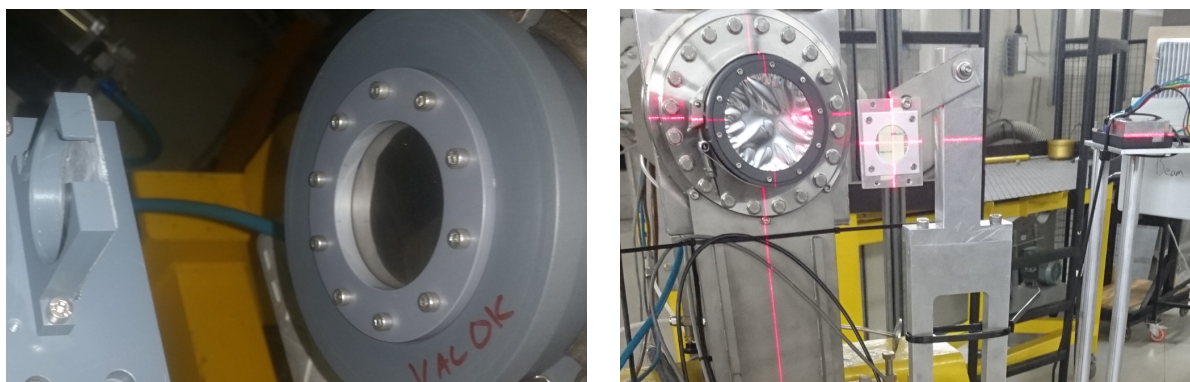
Since the amount of beam deflection and energy loss caused by the vacuum window is important, SRIM simulations were done using 25  $\mu\text{m}$  Havar reference, 6  $\mu\text{m}$  Havar, 50  $\mu\text{m}$  Kapton, and 90  $\mu\text{m}$  Kapton to compare the expected amount of proton scattering for each. The simulation setup consisted of the vacuum window material followed by 1400 mm of air, which corresponds roughly to the available space for the setup in the A-line vault. The transmitted protons were inspected with regards to the average energy loss, the  $3\sigma$  width of the energy distribution as well as the Y- and Z- axes  $3\sigma$  lateral position of the transmitted protons. The results of the simulation is summarised in Table 3.5. From a scattering point of view, the Kapton seems a good option.

However, when localised heating due to a focused beam is considered, the Kapton is less suited. The focused beam upstream would degrade the Kapton over time, weakening it, possibly leading to explosive venting of the vacuum line. Explosive venting, in turn, can lead to costly damage to the turbo vacuum pumps used in the beamline. The Kapton options should only be used in the downstream window where the beam would be scattered to create a sustainable solution, requiring the minimum amount of maintenance and re-manufacture.

Material and thickness ( $\mu\text{m}$ )	Avg. proton energy (MeV)	$3\sigma$ energy (MeV)	$3\sigma$ y-position (mm)	$3\sigma$ z-position (mm)
Havar 25	64.364	0.3859	24.26	23.71
Havar 6	64.471	0.3726	23.72	21.81
Kapton 50	64.438	0.3733	16.94	17.54
Kapton 90	64.385	0.3797	20.05	19.60

**Table 3.5:** SRIM results: Vacuum window material + 1.4 m Air(ICRU-104) effects on 66 MeV protons.

In the interest of long term reliability, the choice for downstream window was 88 mm diameter 25  $\mu\text{m}$  Havar foil and for the upstream window 50 mm diameter 25  $\mu\text{m}$  Havar foil. The mechanical design of the windows was done by iTL staff since they are familiar with the design constraints for vacuum adapters and windows. Both the vacuum windows passed vacuum pre-testing with no concerns. The vacuum windows are shown mounted to the beamline in Figures 3.16(a) and 3.16(b).



(a) Pb sheet for passive spreading (left) and manufactured upstream vacuum window (right). (b) Manufactured downstream vacuum window (left), second scintillating target, and in-beam BLM.

**Figure 3.16:** Beam line elements at (a) upstream and (b) downstream positions on beamline, mounted and being aligned for A-line in-air profile measurements.

The dimensions of the two collimators used will be determined by the beam spot and shadow requirements for a given SEE test. For a feasible setup, two collimator sizes were chosen out of a set of 50 mm thick brass collimators with an outer diameter of 120 mm, one with a 30 mm diameter hole, the second with a 80 mm diameter hole. If the first collimator is placed 325 mm from the Pb spreader, the second collimator can be placed at 1300 mm. A beam spot of roughly 86 mm can be achieved using this example configuration, with a shadow area of roughly 517 mm diameter.

### 3.4.3 Dosimeter positioning

The dual-BLM dosimetry system requires the BLM devices to be placed according to their function. The reference BLM should be mounted in a fixed position relative to the beam and beam spreader. Preferably the reference BLM should be mounted so that no other element is obscuring the spread beam from the Pb sheet. To allow for the largest operational range, the reference

BLM should be mounted so that a count rate of 500 pulses/second to 1000 pulses/second is produced during beam spot profile measurements. Lower count rates will create unacceptable uncertainty in the beam current measurements. Having a count rate of 1000 pulses/second will also allow for the beam current to be increased up to  $80 \times$  during SEE testing, without causing significant BLM saturation effects. The in-beam BLM should be mounted on the DUT positioning platform. The platform is used to move the BLM through the beam spot to measure the beam spot profile.

#### 3.4.4 A-line in-air configuration summary

Combining all the required elements, the design for an A-line SEE test setup consists of:

- A 25  $\mu\text{m}$  Havar vacuum window, 50 mm diameter.
- A 1 mm lead scattering plate 50 mm  $\times$  50 mm, mounted on a rotating arm.
- A primary brass collimator, to create a shadow area and limit exposure to DUTs not in the beam spot.
- A central scintillating target on a moveable ladder, used for alignment of the pencil beam.
- A second brass collimator, to create the required beam spot size on the DUT.
- A second scintillating target mounted on the DUT positioning platform, for alignment of the pencil beam.
- A rotating or linear DUT positioning platform, to move the second scintillating target, in-beam BLM and DUTs.
- A degrader sheet stand to hold various perspex sheets for energy degrading.
- One fixed (reference) BLM and one DUT positioning platform mounted (in-beam) BLM for dosimetry.
- A 25  $\mu\text{m}$  Havar vacuum window, 88 mm diameter, over beam dump pipe.

The dual-BLM dosimeter design was verified through an experiment conducted in the A-line, as described in Section 4.1.2. Unfortunately due to availability limitations, an opportunity to use the A-line for an in-air SEE test could not be realised. The test design was also applied to the NTV, as discussed in the next section.

### 3.5 Converting the NTV for SEE testing

In 2017 the A-line scattering chamber became unavailable for SEE testing due to a long term tape station experiment being conducted at that location. A different location for SEE testing had to be identified. Initially, the N-line was considered, but it would have required some infrastructure upgrades and re-installations to get the beam delivery point in an operational state. Funding and time limitations prohibited such developments at the time. However, due to the termination of medical therapy services at iTL, the PTV and NTV vaults became more attractive options from a scheduling point of view.

The PTV was still being used regularly for biomedical research. For electronics testing, it is required that some of the beam delivery instruments be removed to allow for unmodified passive spread beam conditions. These instruments require extensive alignment procedures

when re-installed. Consequently, the PTV was not considered as the primary SEE test location at the time.

In contrast to the PTV, the NTV was an excellent option since very few experiments were scheduled there and the environment allowed for a custom beam delivery configuration to be erected. A design methodology, similar to the one used for the A-line experiments, was followed for the NTV beam delivery system.

### 3.5.1 Proton beam delivery to NTV

Instead of bending into the gantry, the proton beam is delivered straight into the NTV vault. This delivery is achieved by deactivating the applicable bending magnet and removing the tilt angle indicator assembly.

With the bend magnet deactivated, the proton beam passes through a pre-existing 25  $\mu\text{m}$  Havar vacuum exit window into the vault. The gantry can be rotated to have the least amount of interference with the beam delivery system. Additionally, the patient bed can be used as an assembly platform for the beam delivery system, or be moved to allow for a support structure to be placed in the vault. The conceptual design of the beam delivery system for SEE testing in the NTV is shown in Figure 3.17.

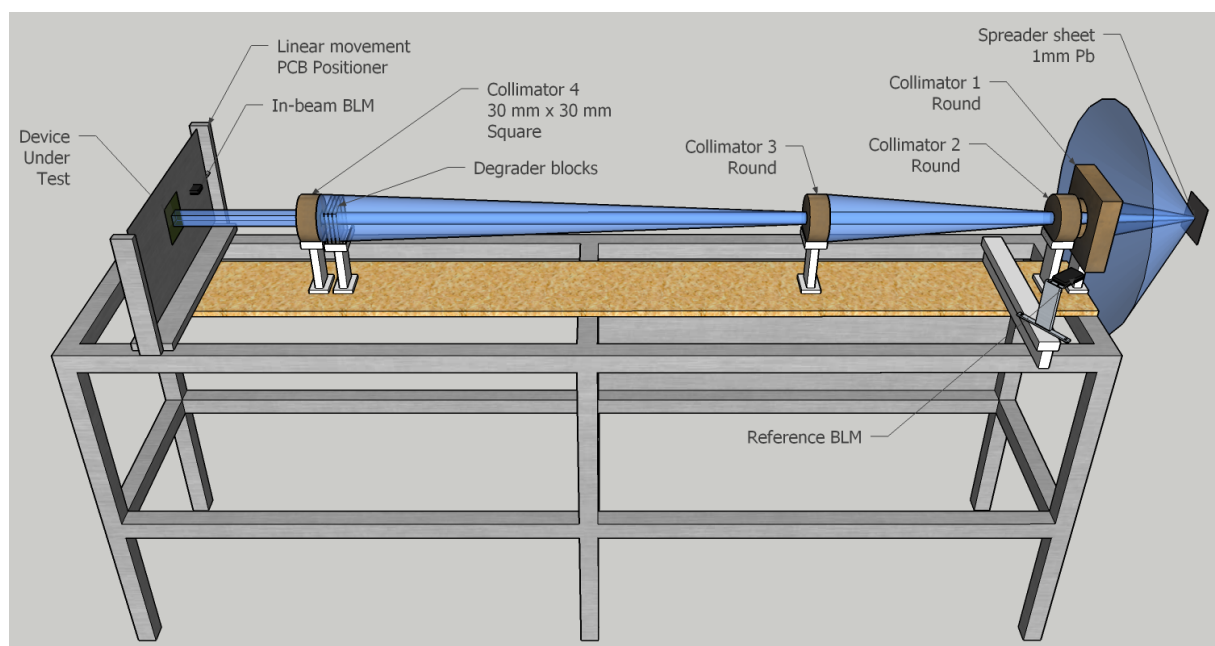


**Figure 3.17:** Conceptual beam delivery design for SEE testing in Neutron Vault. Configuration uses linear movement DUT positioner platform with four collimators. Beam profile and reference current measurements are similar to the A-line design.

The design of the beam delivery system in the NTV follows the A-line design. The beam is passively spread using a Pb sheet after exiting the beamline via a 25  $\mu\text{m}$  Havar vacuum window. Since the nominal test energy at the NTV is 66 MeV, the same thickness of lead is used as the passive beam spreading element. In contrast to the A-line configuration, the NTV has more space for a longer beam path to allow the beam to spread out more.



For the NTV experiments, one primary goal is to do an SEE experiment with the new configuration and dosimetry system. Therefore the beam should be formed to create both a beam spot and an adequate shadow area around the beam spot.

### 3.5.2 Beam, spot, and shadow forming

The beam spot should be large enough to ensure a reasonably uniform particle distribution across the area of interest on the DUT, while the beam shadow area should be large enough to cover the whole DUT positioning platform.

Before the optimal collimator positions can be calculated, the minimum required distance from the Pb sheet to the DUT target must be determined. SRIM is used to simulate the beam spread, similar to the approach used for the A-line setup. A practical setup distance is determined using a uniformity variance limit of 10% over the minimum required spot size. If the required uniformity cannot be achieved using the maximum practical distance available in the vault, the Pb sheet thickness must be increased to create a greater beam spread.

A set of collimators are used to form the beam to achieve the required spot and shadow sizes. Various collimators, mainly used in PTV configurations were available. Given the available space, the size of the DUT position platform, and the collimator options available, the optimal mix of collimators can be chosen. As a first-order approach, a simple geometric analysis was done to determine the collimator positions. The generic geometry of a configuration, using four collimators, is shown in Figure 3.18.

The geometric analysis was done manually, the first time. A Python script was written to assist with the geometric analysis for future configurations. A generic approach to the script design was taken. The script is driven via a Graphical User Interface (GUI). Input parameters required by the script are:

- size and shape of the beam spot;
- distance to next collimator;
- outside diameter of next collimator;
- hole diameter of next collimator;
- amount of collimator overlap required.

To determine optimal placement the dimensional limitations must be considered. Firstly, the distance from the Pb sheet ( $d_5$  in Figure 3.18) to the target has a hard upper limit, since is directly dependent on the available space in the vault. The lower limit for  $d_5$  is determined by the beam uniformity required over the spot size, as calculated using the preceding SRIM simulation. Secondly, the shadow area ( $b_5$  in Figure 3.18) has a hard lower limit, since it is defined by the size and movement range of the DUT positioner platform. Thirdly, the spot size ( $a_5$  in Figure 3.18) has a hard lower limit, since it is directly dependent the DUT size. The spot size often has an upper limit too, due to the location of support electronics around the DUT, specifically, if the DUT is a single IC on a test PCB. Thus, for the configuration shown in Figure 3.18 the following is defined:

$$d_5 \equiv \text{distance to target} \quad (3.6)$$

$$b_5 \equiv \text{beam shadow size} \quad (3.7)$$

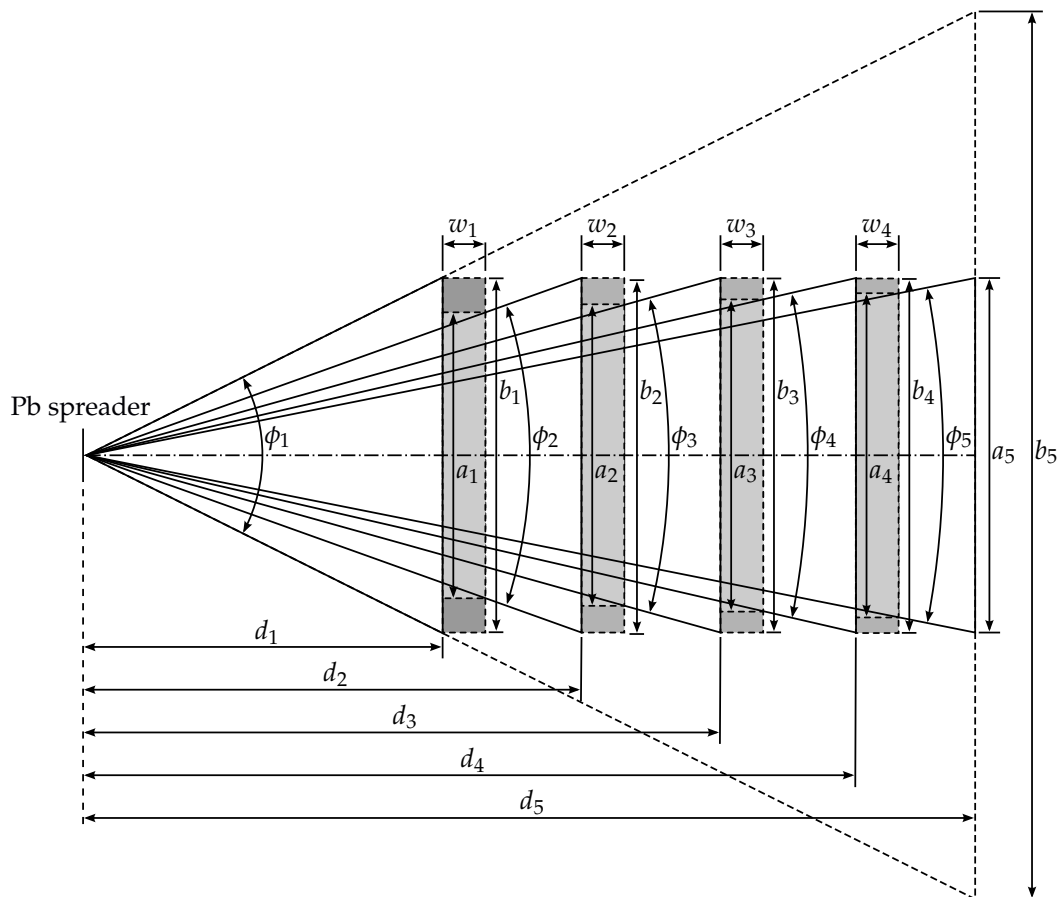


**Figure 3.18:** Diagram for the generic geometry of the collimator configuration. The collimator dimensions ( $a, b, w$ ), distances ( $d$ ), spreader distance to target ( $d_5$ ), and the spot ( $a_5$ ) and shadow ( $b_5$ ) diameters are indicated. From these parameters the optimal collimator placement can be calculated.

$$a_5 \equiv \text{beam spot size} \quad (3.8)$$

The collimator positions can be calculated starting either from the Pb sheet side, using the shadow size as the primary driver, or from the DUT side, using the spot size as the primary driver. However, if the positions are calculated using only one limitation, either the other limitation is not achieved, or the setup becomes impractical. The optimal solution can be found by calculating collimator distances simultaneously, starting from both the Pb sheet side and the DUT side.

Using the simultaneous calculation sequence, the positions for collimators 1 and 4 are calculated first using equations 3.9 to 3.11. Next, the position range of collimators 2 and 3 are calculated. The range is the difference between the positions of collimators 2 and 3 as calculated from the two starting points.

Working from the Pb sheet side

$$\phi_1 = \arctan\left(\frac{b_5}{d_5}\right) \quad (3.9)$$

and

$$d_1 = \frac{b_1}{\tan(\phi_1)} \quad (3.10)$$

substituting 3.9 in 3.10, gives

$$d_1 = \frac{b_1}{\tan(\arctan(\frac{b_5}{d_5}))} = \frac{b_1 \times d_5}{b_5} \quad (3.11)$$

Next, using similar steps, we have in turn

$$d_{2_{pb}} = \frac{(d_1 + w_1) \times b_2}{a_1} \quad (3.12)$$

$$d_{3_{pb}} = \frac{(d_2 + w_2) \times b_3}{a_2} \quad (3.13)$$

$$d_{4_{pb}} = \frac{(d_3 + w_3) \times b_4}{a_3} \quad (3.14)$$

Working from the DUT side, we have in turn

$$d_{4_{DUT}} = \frac{a_4 \times d_5}{a_5} - w_4 \quad (3.15)$$

$$d_{3_{DUT}} = \frac{a_3 \times d_4}{a_4} - w_3 \quad (3.16)$$

$$d_{2_{DUT}} = \frac{a_2 \times d_3}{a_3} - w_2 \quad (3.17)$$

To ensure some minimal overlap between collimators is possible, the condition  $d_{4_{DUT}} < d_{4_{pb}}$  must hold. If  $d_{4_{DUT}} > d_{4_{pb}}$  a continuous shadow cannot be created using only four collimators, and an extra collimator must be added.

### 3.5.3 DUT beam energy degrading

Since the beam is generated using a SSC and is delivered to the test area using a beamline that includes multiple focus magnets and bending magnets, changing the energy of the delivered protons is no simple matter. Firstly the SSC has to be adjusted to deliver the beam at the new energy. Changing the beam energy also means adjusting and fine-tuning the control parameters of each of the active beam elements along the beamline. This process can take anywhere from one to four hours, depending on the number of active elements involved. A more sensible approach to beam energy management is to deliver the highest required beam energy to the test area, and then to degrade the beam to the required level using energy degrader sheets.

Similar to the reasoning behind choosing Pb as material for the beam spreader element, Plexiglass was chosen as the preferred energy degrader material. Plexiglass (also known as Perspex, Lucite, Acrylite) and other plastics are commonly used in nuclear beam delivery systems to moderate the proton beam [49; 98; 92]. For efficient energy degrading, the beam should lose the maximum amount of energy while being deflected the least amount, while passing through a unit of mass of the material.

Less dense materials typically have this property compared to more dense materials [92]. Plexiglass is readily available in various thickness sheets. For SEE testing purposes a set of Plexiglass squares were cut from larger sheets. The options available at iTL at the time was: 2 mm, 3 mm, 6 mm, 8 mm, 10 mm, 12 mm, 30 mm.

A custom 3D-printed holder was designed and printed, that could be fitted to a 3D-printed collimator stand foot piece. The holder can accommodate 100 mm × 100 mm Perspex square sheets. With limited development time available, the holder was designed to be manually operated. To adjust the thickness of the Perspex energy degrader, different combinations of a set of Perspex sheets, each of different thickness, can be placed in the holder. The sheets are held in place by a simple clamping screw. The foot piece, holder and plexiglass sheet assembly constitutes the energy degrader unit.

### 3.5.4 Beam dosimetry, monitoring, and exposure control

For acceptable SEE testing, accurate beam dosimetry, monitoring and control is required. In contrast to the A-line scenario, the NTV is equipped with a dosimetry control system that was used during neutron therapy. However, since the gantry is bypassed during SEE testing, the primary dose monitors cannot be effectively used. Since the beam is not passing through the gantry system as designed, its dosimetry system cannot reliably be calibrated.

Consequently, an alternative dosimetry and beam monitoring system must be utilised for SEE tests. For this purpose, a similar approach to the A-line dosimetry and beam monitoring is taken. The dual-BLM design is used, where one BLM acts as the beam current reference monitor and the other is used for determining the beam profile in the DUT plane. Even though this placement of the reference BLM is different relative to its placement in the A-line configuration, the same general simulation and measurement approach is taken, i.e. the expected beam intensity at the BLM position can be simulated using SRIM, and the primary purpose of the reference BLM is still to monitor the relative beam current during DUT exposure.

The reference BLM is placed outside the shadow area created by the collimators, but relatively close to the Pb sheet to minimise its measurement uncertainties. The spread beam is expected to have a Gaussian beam shape, as simulated using SRIM. By placing the BLM this far outside the beam centre, the expected count rate is significantly reduced. Although this approach reduces the risk that the BLM will saturate, there is a risk that its count rate can be too low. To compensate for this, the BLM is placed much closer to the Pb sheet, increasing the effective detector area. In this position, due to the directionality of the BLM device, scattered or secondary radiation emitted from the collimators should not affect it. Even though the reference BLM would be in the tail of the Gaussian spread beam, its count rate will have a fixed ratio compared to the count rate in the centre of the beam spot.

The in-beam BLM is used to measure the beam spot and shadow profiles. As in the case of the A-line configuration, the in-beam BLM is mounted on the DUT positioning platform. Since the in-beam BLM, is in the same plane as the mounted DUTs, it can accurately measure the beam spot incident on the DUTs.

To measure the profile of the beam spot, the in-beam BLM will be moved through the beam spot, first in a horizontal, and second in a vertical line. Due to the control options available for the DUT positioning platform, the BLM cannot be moved through the spot at a constant rate slow enough to take sensible measurements. The BLM will instead be moved in set increments and be kept in a stationary position between steps for a long enough period so that multiple samples of the beam intensity can be taken at that point. For shadow profile measurements,

the in-beam BLM is only moved in a horizontal line due to the limited movement range the DUT positioning platform has in the vertical plane.

Both of the BLM units must be interfaced to the same counting instrument so that concurrent samples can be taken. This combination will eliminate the need to synchronise the two BLM data streams afterwards.

For timing control of the beam, the existing dose monitoring system can be used in an open-loop mode. By setting the dose monitor to the maximum threshold, the timer control of the dose monitoring system can be used to control the DUT exposure times accurately. The timer system can also be run in open-loop mode, which can be useful for certain SEE experiments.

### 3.5.5 DUT positioning and interfacing

For the NTV experiments the linear movement DUT positioner platform, shown in Figure 3.15, is used. The movement of the platform is controlled using an embedded controller. The controller is connected via a wire harness to the platform. The length of the wire allows the controller to be placed out of the beam, behind lead shielding. The platform itself contains only mechanical limit switches and stepper motors, as far as electronics are concerned, and should be immune to dose effects or single event effects from the proton beam.

The platform controller communicates to the control room using a Local Area Network (LAN) connection via Ethernet cable. Control software on a Personal Computer (PC) is used to control the movement of the platform. Figure 3.19 shows the user interface. Since the platform does not have absolute position feedback, home position calibration is provided using the limit switches. After calibration, the platform can be moved to the required position.

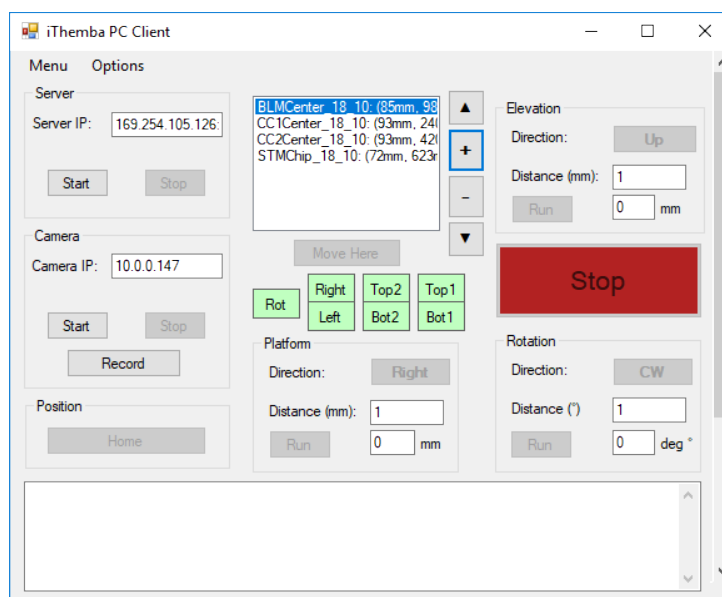


**Figure 3.19:** User interface software for the linear movement DUT position platform for SEE testing in the NTV. User control is available for manual movement, set and use of pre-defined positions, and camera recording.

The reference BLM, and all the DUTs that will be irradiated is mounted on the platform's mounting plate. Each device's position can be recorded using the user interface, which allows for fast re-positioning during tests.

An Ethernet switch is provided for high-speed data connection to the control room for all the DUTs. All the DUT interface cables are routed next to the platform mounting plate to their respective support electronics. The support electronics, the Ethernet switch and all the required power supplies are placed behind the same shielding used for the platform controller.

Finally, a camera, either Ethernet-based or Closed Circuit Television (CCTV) based, is used to monitor the DUT platform movement from the control room. The video stream serves as a visual confirmation that the platform is moving to the correct positions during testing.

---

## CHAPTER 4

# Implementations of a SEE test environment at iTL

---

*The proton-induced SEE test environment was developed and implemented over a series of experiments from 2013 to 2019. Given the original goals, the implementations used as much of the iTL infrastructure as possible, to minimise the effort to create a sustainable SEE test environment. This chapter will present the experiments conducted to verify and refine the various design elements of a proton based SEE test at iTL.*

The first approach was to use the A-line scattering chamber with magnetic beam spreading in vacuum, which evolved into passive beam spreading in air, as detailed in the following sections. The evolutionary step to in-air testing occurred through experience gained while testing at the A-line vault. With typical beam scheduling and location availability challenges, three tests at the NTV presented the opportunity to evolve the test techniques and configurations further to be sustainable, flexible, reliable and repeatable.

### 4.1 Experimental Verification at A-line

#### 4.1.1 Magnetic spreading of the proton beam

As described in Section 3.4, the modifications to the A-line scattering chamber comprised two designs. The first design utilised the magnetic beam spreading approach in vacuum. The following sections will detail the experiments conducted to investigate the feasibility of this approach.

##### 4.1.1.1 Experimental design for verifying magnetic beam spreading and in-vacuum testing

The following goals were set for the experiment:

- Must use the existing A-line infrastructure as far as possible

- Verify the quality of the beam spot generated using quadrupole de-focus technique
- Realise a usable beam for comparison of mitigation techniques for 4 separate SEE experiments by Botma, Thesnaar, Naudé and Smith respectively.
- Investigate the effect of spreading the beam using a 1mm Pb sheet with no collimators (set after the first two of the aforementioned three SEE tests were completed)

**4.1.1.1.1 Mechanical configuration** The mechanical configuration used the existing A-line mechanical infrastructure consisting of the vacuum chamber, two moveable arms, a moveable scintillating target, patch cable panels, and a CCTV camera mounted outside the vacuum chamber. The modifications made to the infrastructure included a custom made vacuum connector, two fixed mounting stands, one each for the DUT and the Pb sheet.

The DUT was mounted on one of the rotating arms, as far away from the beam entry point as possible. Power and interfacing wires were connected from the DUT to the vacuum side of the vacuum connector panel. At this time no multi-DUT mounting platform existed, and this configuration limited the SEE test to have only one DUT inside the vacuum chamber at a time.

After the first three SEE experiments, a second scintillating target and the Pb sheet was added. The secondary scintillating target was mounted to the side of the DUT to assist with alignment measurements. The Pb sheet was mounted on the second rotating arm, as close as possible to the beam entry point. As part of the test preparations, the DUT and scintillating target was aligned to the centre of the beamline using a cross-hair laser level. Figure 4.1 shows most of the final configuration of the fourth test.

All the support electronics required for the SEE tests were placed outside the vacuum chamber, as far upstream from the beam entry point as possible. The upstream distance to the control electronics ranged from 0 m to about 1 m, resulting in interface cables ranging in length from 3 m to 5 m. After the DUT and other components were installed, the final steps are to close the vacuum chamber and pump it down to vacuum.

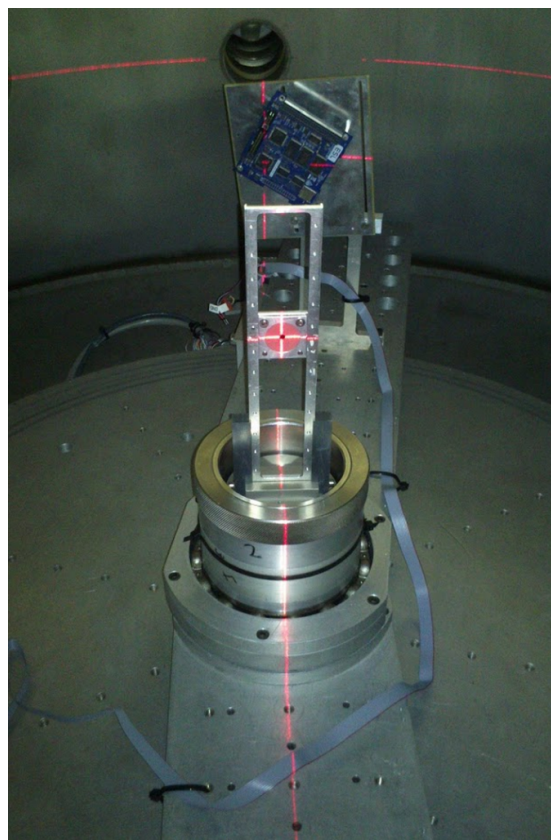
**4.1.1.1.2 Electrical interfaces** Interface cables to power, control and monitor the DUT were connected from the support electronics via the vacuum connector to the DUT. The support electronics were powered from the existing clean main supply in the vault, while an existing Ethernet connection was used to communicate with the DUT support electronics from the data room.

The control units, situated in the data room, were used to remotely control the movement of the rotating arms and the centre scintillating target ladder. The CCTV camera was connected to the control room using an existing coaxial, analogue signal cable.

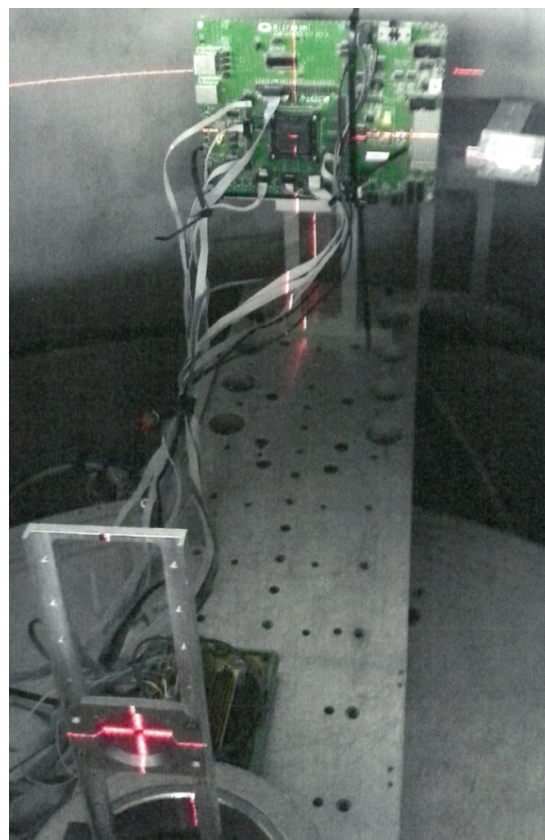
**4.1.1.1.3 Beam configuration, alignment and intensity** Beam delivery was done in two phases. First, the beam was aligned using the central scintillating target only. The DUT is moved out of the beam path to a 90 deg position, perpendicular to the beam path. This calibration procedure also aims to give the DUT the minimum amount of unwanted beam exposure.

First, the beam was focussed and positioned in the centre of the target in the centre of the chamber. Then the beam position at the far end of the chamber was verified using the secondary scintillating target. With the beam thus aligned, the beam was defocused using the





(a) CubeComputer alignment setup



(b) FPGA development board alignment setup

**Figure 4.1:** Configuration setup for a) Botma’s 2013, and b) Smith’s 2015 SEE tests with the central scintillation target in its ladder, and the mounted DUT boards shown. The laser cross-hairs used during alignment is visible on both the central target and DUT boards. For b) the second scintillation target mounted to the right of the DUT board is visible as well as the support electronics placed inside the chamber mounted behind the ladder on the rotating arm.

two quadrupole magnets nearest the chamber. Using this method the beam could be spread over an area of about  $10\text{ mm} \times 10\text{ mm}$  at the central target position. This amount of beam spread increases to an spot of about  $20\text{ mm} \times 20\text{ mm}$  at the DUT position.

A beam current of  $1\text{ nA}$  was chosen to do the alignment and spot forming. Based on previous experience of iTL staff, the  $1\text{ nA}$  beam current was deemed high enough that a stable current could be supplied by the SSC while minimising the levels of exposure to the DUT.

The beam intensity was open-loop controlled from the data room. Before each exposure session, the control room was tasked to set the beam current to the desired intensity. The beam on/off control to the A-line chamber was manually done from a data room terminal by the researchers and iTL staff. This method resulted in a beam exposure time resolution of roughly  $1\text{ s}$ . After each exposure, the control room was asked to verify the beam current to ensure that no significant shift in current occurred during exposure.

#### 4.1.1.2 SEE electronics and software preparations

Several SEE tests were planned and conducted at the A-line vault from 2013 to 2015. This experiment aimed to support SEE tests that were conducted by different researchers. An in-vacuum

configuration was selected for the tests as described in Section 3.4. The DUT electronics consisted of four separate SEE tests, conducted in three separate test sessions. The first two tests used the same custom hardware, and the third used different custom hardware and the last used commercially available development hardware.

**4.1.1.2.1 CAN controller and soft-core processor:** The first experiment, on 30 October 2013, was part of Thesnaar's research and the complete test logs are given in Appendix F of [55]. In summary, the aim of his SEE test was to compare the sensitivity of an unmitigated CAN controller versus a mitigated CAN controller. To allow for custom targeted mitigation to be applied to the CAN controller design it was implemented in a non-volatile FPGA on a custom-build board. The FPGA board was specifically developed to allow for SEE testing. Both the unmitigated and mitigated design were programmed into the FPGA to be irradiated at the same time. This approach eliminates any SEE cross-section difference that might exist between the different COTS samples. By testing both designs at once, the overall test time should also be minimised. A second student also prepared for a mitigated versus unmitigated processor design test using the same electronics and approach as Thesnaar. For both of these experiments, a reference unmitigated controller design was programmed on a support board placed outside the vacuum chamber.

**4.1.1.2.2 CubeComputer:** Botma developed a CubeSat onboard computer and applied a range of standard mitigation techniques to his design [26]. However, due to time limitations, his design could not be tested as part of his graduate studies. He did, however, conduct a SEE test of his design on 26 November 2013 to verify the effectiveness of his applied techniques. His electronics comprised the CubeComputer board that was monitored and controlled from a controller unit outside the vacuum chamber. For the SEE tests the CubeComputer was programmed to execute a suite of elementary software tests. The software exercised and checked the various memories and executed calculation sequences to exercise the computational units, while monitoring system health. All the software tests were custom developed and implemented in an Operating System (OS)-less software framework.

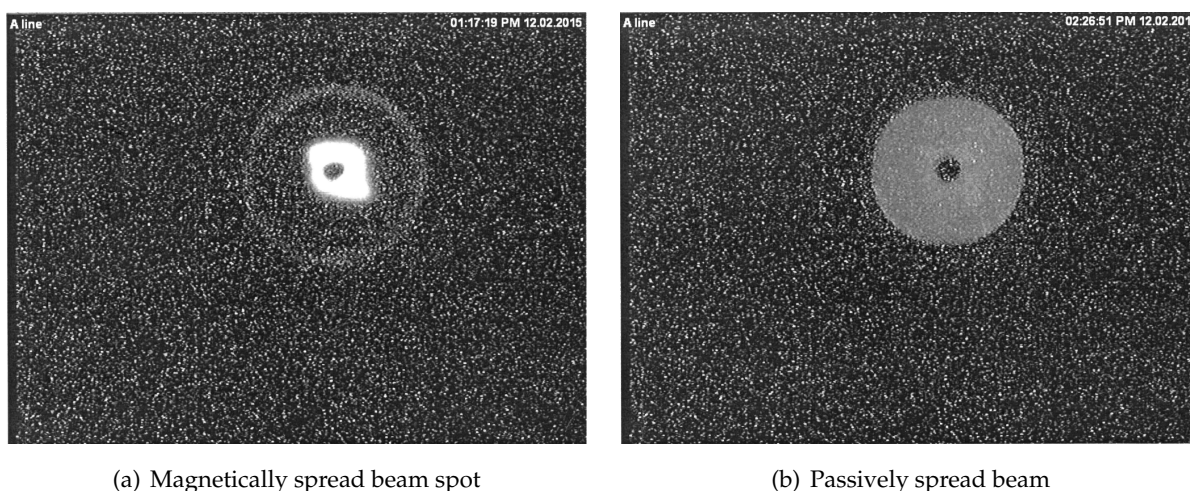
**4.1.1.2.3 Dual modular redundant SET suppression:** Smith developed novel dual modular redundant SET suppression techniques [99; 100; 27] that in theory improved on current designs. The SEE test of December 2015 was aimed at verifying the effectiveness of his SET suppression technique. His electronics comprised of an FPGA board, shown in Figure 4.1(b), programmed with both mitigated and unmitigated designs. His DUT was monitored and controlled using support electronics. Due to cable length limits, some of the support electronics were placed inside the vacuum chamber.

#### 4.1.1.3 Measurements

Since the A-line configuration did not include an accurate dosimetry system, the measurements as pertaining to the beam delivery are limited. Summaries of the SEE tests results are presented, giving context to the successes and failures of the overall test procedures.

**4.1.1.3.1 Beam delivery:** For all four experiments, the beam alignment and defocusing were done using a 2 nA 66 MeV proton beam and the central scintillation target on the ladder. For the first three tests, the beam was assumed to be delivered precisely in the centre of the beamline. After the third test, it was decided to add a second scintillation target close to the DUT to verify the beam alignment more accurately. With the second scintillation target added it was noticed that the beam was not delivered precisely in the middle of the beamline. The small offset position was noted and the DUT was re-positioned to be in the centre of the beam spot.

The typical beam spot generated using the magnetic defocus technique is shown in Figure 4.2(a). The scintillating target can be seen, having a diameter of 25 mm, the centre hole with a diameter of 3 mm, and the spot with an approximate diameter of 10 mm. The fourth test was also the first time the Pb sheet was used to investigate the passive beam spreading technique in this context. A significantly improved uniform distribution over the scintillation target of the passively spread beam is shown in Figure 4.2(b).



(a) Magnetically spread beam spot

(b) Passively spread beam

**Figure 4.2:** The resulting beam spot as indicated by the scintillation target using (a) the magnetic spreading technique, and (b) passive spreading.

Table 4.1 shows a list of exposure times, summarised from [55], to illustrate the typical exposure times obtained correlated to the effects observed.

Start time	Stop time	Exposure duration	Beam current	Effects observed
16:48:02	16:48:29	00:00:27	0.1 nA	No scattered protons measured
16:52:34	16:54:34	00:02:00	0.1 nA	No SEE observed
16:56:00	16:58:00	00:02:00	0.1 nA	Single digit SEUs observed and mitigated
17:00:59	17:03:00	00:02:01	0.1 nA	Single digit SEUs observed and mitigated
17:06:30	17:08:30	00:02:00	0.1 nA	Single digit SEUs observed and mitigated
17:11:30	17:13:30	00:02:00	0.2 nA	Hundreds of SEUs observed and mitigated

**Table 4.1:** Beam activation times, exposure duration, and effects observed at iTL A-line vault experiment on 2013/10/13.

The setup allowed the beam intensity and shape to remain reasonably constant between exposure runs, allowing the comparison of results from different runs throughout the day.

**4.1.1.3.2 CAN controller and soft-core processor:** Core-current supply increased from 11 mA at start of test to 26 mA. From [21] this increase in core-current supply is a good indication of the amount of TID received by the device. The main supply current to the board also increased from 190 mA to 245 mA. Thesnaar, however, did not fully investigate the reason for this excessive increase in board current, nor was this current mentioned in post-irradiation electrical tests. The temperatures on the board stayed stable, rising only a fraction of a degree during the duration of the tests.

From the measurements, it can be seen that an extremely low intensity beam of 0.1 nA was used for most of the exposures. The low intensity was used to limit the exposure rate until it could be established that the DUT and monitoring equipment can handle the resulting error rates. If the DUT showed low SEE rates, the current would be increased in subsequent runs to increase the error rates and thus minimise the overall beam time used.

**4.1.1.3.3 CubeComputer:** For the processor system, the memory management using Error Detection and Correction (EDAC) worked as expected. The board regularly experienced unknown reset events during exposure, that limited the running time of the system and consequently the watchdog implementation, to catch code stalls, could not be tested successfully. These reset events, combined with the fact that 66 MeV protons typically do not cause a significant amount of SELs, meant the SEL detection circuitry on the board was also not thoroughly tested.

A post-test investigation into the nature of the reset events revealed that it was probably due to a faulty power supply unit which caused the DUT board to go into brown-out states when it started consuming any appreciable amount of current. However, with mitigation applied, the board's SEU rate due to medium energy protons was positive. The results showed that the system could be successfully operated in LEO environments from a SEU point of view.

**4.1.1.3.4 Dual modular redundant SET suppression:** The test was conducted with a testing window that opened after 12:00 and lasted until 15:00. The response of the FPGA system was positive. Since the aim was to verify FPGA design techniques to mitigate SETs in reprogrammable circuits, the relative performance of the DUT board, with and without mitigation was of relevance.

SEU induction was attempted using 3 beam delivery scenarios:

- No obstacle in beam path scenario. The beam is directly onto the DUT showing some SEUs in response.
- With the centre target in the beam scenario, showing SEUs, but fewer.
- With passive beam spreading using 1 mm Pb sheet scenario, showing no SEUs. This may be due to the much lower flux.

After initial checks, the first two listed beam scenarios were repeated until the device failed. The aim was to generate enough error statistics for the SEE test.

#### 4.1.1.4 Results from experiment(s)

The four experiments done in this development phase were very exploratory, especially from a beam delivery point of view. Although iTL staff is experienced in using high energy particle

beams to conduct nuclear physics experiments, they were not experienced in using the beam for applications like SEE testing. *It was a learning experience, for the author and the other researchers involved, to plan, prepare and approach SEE testing sessions.* The next two sections will summarise and discuss the positive and negative results obtained.

*Positive* outcomes to note from the experiment are:

- In the magnetic beam spreading scenario, there are no obstacles in the beam path and no proton energy loss is incurred, resulting in the full 66 MeV reaches the DUT.
- Quadrupole magnets are present close to most of the beam delivery points. Therefore the magnetic spreading technique can be replicated at these points, making the beam delivery design very flexible.
- In support of research and student projects, beam time allotment was very flexible and accommodating to the changes and limitations inherent in student projects.
- No pre-simulation of the beam is required since spot forming and alignment is done in the same procedure and verified visually via a CCTV-type camera.
- The beam alignment procedure using two scintillation targets resulted in accurate and fast alignment of the elements relative to the beam centre line.
- A good beam intensity level for beam alignment was identified to be roughly 1 nA.
- Easy and reliable DUT positioning from the data room using controllable arms.
- Activating the beam is easy and can achieve one-second accuracy using manual switching control on the PC in the data room.
- The beam intensity can be easily adjusted via the control room, and it takes roughly two minutes to change the beam current to the required level.
- Relative measurements between mitigated and unmitigated parts are possible since beam spot shape, and therefore the associated exposure rate stays fairly constant throughout the tests.
- With proper planning and preparation, a subset of 66 MeV proton based SEE tests can be successfully executed at the A-line scattering chamber.
- The passive beam spreading technique showed promise to be further investigated. When applied, the technique resulted in the scintillation target showing an even illumination over its full area.
- Actual exposure time of the DUTs was reasonably short, as little as 3 hours while still producing the desired results.

*Negative* outcomes to note from the experiment are:

- Ad-hoc beam scheduling is not sustainable; an excessive amount of time was used to liaise with the beam schedule manager. A more managed scheduling process should be sought and followed.
- Doing SEE testing in a vacuum is problematic and results in long lead times to allow time for pumping the chamber to vacuum.
- Special preparation of DUT boards were required to allow for their use in a vacuum environment.
- Vacuum connectors for signal interfacing with the DUT boards were problematic. A generic set of vacuum connectors are prohibitively expensive to be used in manufacturing a generic solution. A lower-cost alternative design works but is not a sustainable option.

- Vacuum system and chamber preparation require many hours of support from iTL staff.
- Irregular use of A-line and chamber resulted in the readiness testing of many support systems before they were used.
- No in-situ dosimetry measurement system is present. Since the beam current varied significantly during tests, current setting verification requests to the control room are required after each run.
- A CCTV-type camera is required for successful alignment and spot forming.

When analysing the test procedures followed, it became clear that a more sustainable way of scheduling tests was required. However, until a deep enough understanding of what future testing would require was gained, ad-hoc scheduling would still be required.

The test infrastructure worked well and simplified testing in many ways. However, the length of preparation and turnaround time was prohibitive to effective use of the available test time. A fresh approach to the beam delivery configuration was required. Three main changes were considered: to change to passive beam spreading; to move to in-air testing; to add a beam intensity monitoring and profile measurement system of some kind. These changes aim to solve the problems with effective time use and the uncertainty in exposure rates the DUTs experience.

#### 4.1.2 Passive spreading of the proton beam

The magnetic beam spreading approach using quadrupole magnets, as described in Section 3.4 has some shortcomings. Given the limitations of the existing infrastructure, magnetic spreading will not meet the beam spot uniformity requirement for SEE test, set in Section 1.

As an alternative to magnetic beam spreading, passive beam spreading, as motivated and described in Section 3.4.1, was chosen as an alternative option. Given the challenges faced with working in a vacuum environment during the magnetic spreading experiment, it was also decided to conduct the SEE testing in air. Section 4.1.2.1.4 described the use of SRIM to simulate how the proton beam will spread through a Haver-Air-Pb-Air layered geometry. With the beam being spread over a larger area, and more predictably and stably, the BLM dosimetry approach, as described in Section 3.3, could be employed to measure the proton flux.

An experiment was designed to verify the accuracy of the in-air SRIM simulated beam profile while simultaneously verifying the effectiveness of employing the BLM based dosimetry system.

##### 4.1.2.1 Experimental design for verifying SRIM beam simulations and BLM based dosimetry

The following goals were set for the experiment:

- verify in-air test methodology, compared to the in-vacuum testing;
- verify SRIM simulation accuracy, compared to the measured data;
- verify BLM as dosimetry system, compared to previous approaches.

**4.1.2.1.1 Mechanical configuration** The infrastructure at the A-line vault had to be slightly modified to test in air. Most of the modifications related to the vacuum system for the scat-

tering chamber. Usually, the vacuum is maintained from the beamline through the scattering chamber and into the beam dump, with a vacuum valve placed immediately before and after the scattering chamber. For in-air testing, the beam will have to exit via a vacuum window into the air before reaching the DUT. The optimal option is to place the vacuum window at the entry coupling to the scattering chamber to derive the most benefit from working in-air. However, the vacuum window will not fit with the current couplings in place.

In order to make space for the vacuum window, either other couplings have to be manufactured to adapt to the new spacing requirement, or the scattering chamber wall section must be removed entirely. The latter option is much easier to do than the manufacturing of custom coupling pieces. When working in air, the chamber walls have no functionality, and consequently, the scattering chamber wall section was removed. The removal of the chamber wall section exposes the beam entry and exit ports. These ports must be capped with vacuum windows. Two 25  $\mu\text{m}$  Havar vacuum windows were designed (as described in Section 3.4.2), manufactured, and installed. One window at the beam entry point and the other at the beam exit point towards the beam dump.

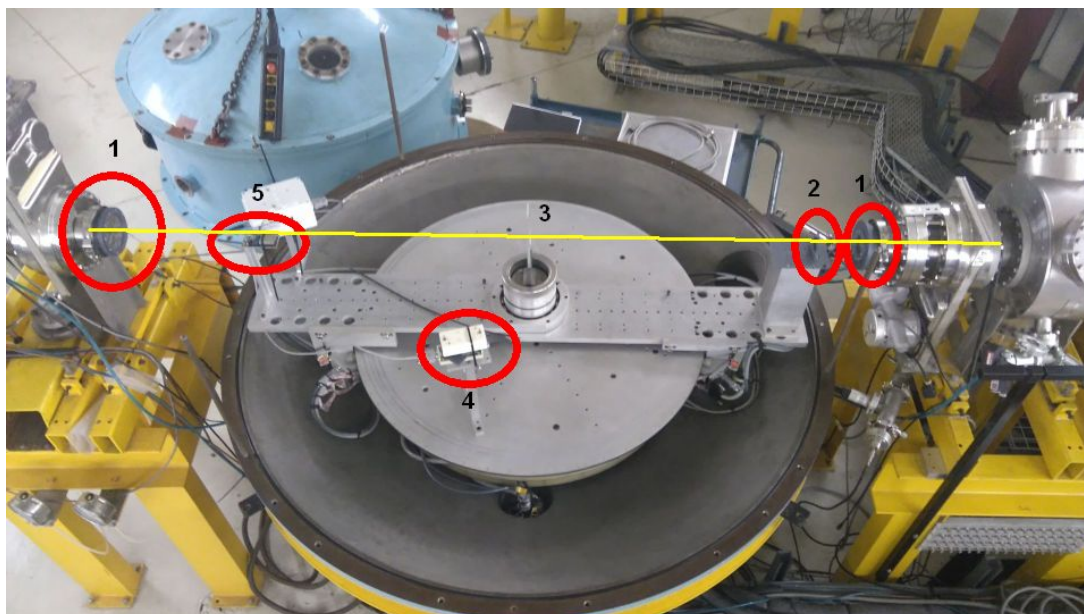
When the full scattering chamber is used, the vacuum in the chamber is created using a vacuum pump connected to the centre of the chamber. However, when the wall section is removed, and the vacuum windows are installed, there are two short sections of beamline that is not connected to any vacuum pump. These sections must be pumped down to the required low pressure to allow the vacuum valves isolating these sections from the rest of the beamline to open. Thus, it was necessary to connect two portable vacuum pumps to these short sections to pump them down. The temporary pumps were manually controlled since they could not easily be integrated into the central, automated vacuum control system.

The impact of these vacuum system modifications on the timeline for test preparation severely in two ways. Firstly a workforce and extra time are required to install the vacuum windows and pumps physically. Secondly, the short beamline sections have to be pumped down at least one day before the SEE tests to verify that the vacuum system is fully functional.

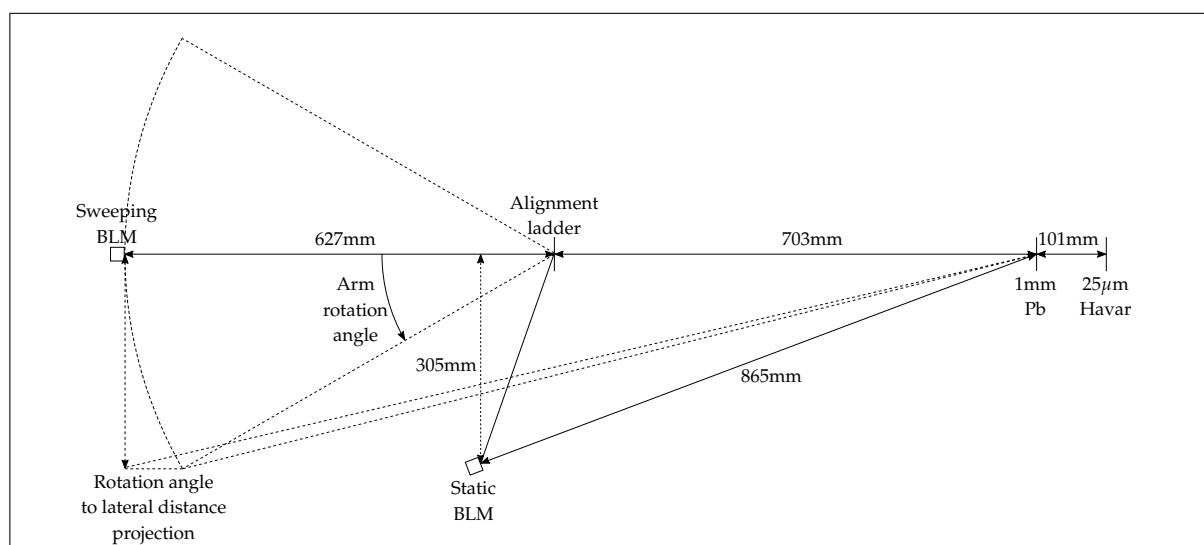
In the in-air configuration, the floor section of the scattering chamber was still available to use, and most of the advantages of the A-line mechanical infrastructure was retained. The Pb sheet, used to spread the beam, was mounted on one of the controllable arms so that it could be moved out of the beam during the beam alignment procedure. To characterise the created beam profile, a reference BLM at a fixed angle, and a moving in-beam BLM setup was used. The monitor BLM was mounted in a fixed position to the scattering chamber floor section while the in-beam BLM was mounted on the second of the controllable arms. The in-beam BLM could thus be moved in a horizontal arc through the formed beam. This configuration, shown in Figure 4.3, is identical to the conceptual design of the modified A-line test setup as shown in Figure 3.14 except for the two collimators and the DUT rotator table, which was not required.

Figure 4.4 shows the measured distances between the mechanical elements of the beam delivery system. These distances are used when the raw data from the BLM monitors are adjusted for comparison to the simulated values.

The support electronics were all placed next to the scattering chamber on the floor, about 1 m below the chamber floor section, and as far as possible behind the beam spreading point. Due to the placement position of the support electronics, no additional shielding was used to



**Figure 4.3:** Configuration setup for beam profile characterisation measurements at the A-line vault. Proton beam direction is from right-to-left. The following elements are indicated: 1) Vacuum windows, 2) Pb sheet, 3) Scintillating alignment ladder, 4) Fixed BLM monitor, 5) Sweeping, in-beam BLM monitor.



**Figure 4.4:** Geometry of the setup for beam characterisation measurements at the A-line vault.

shield it from scattered radiation.

**4.1.2.1.2 BLM electrical interface** The experiment used two BLM detectors for dosimetry. These detectors had to interface with the existing iTL Data Acquisition (DAQ) system. It was decided to use the DAQ hardware already set up in the spectrometer vault. Cable connections from the BLM detectors to the DAQ hardware was required. This was achieved by using the existing signal cabling between the A-line vault and the data room, as well as the existing signal cabling between the data room and the spectrometer vault. It was only necessary to connect the signal cables from the A-line vault to the spectrometer vault using their respective



patch boxes in the data room, and a patch cable. Since the total signal path was close to 200 m, the signal quality was checked at the input to the DAQ hardware using an oscilloscope. The received signals looked good with no discernible noise. Low noise levels indicated that all the cabling and connections seemed to be well-matched and in good condition. No additional amplification of the BLM detector output signals were required.

**4.1.2.1.3 Beam configuration, alignment and intensity** The experiment was designed to use a 66 MeV proton beam to allow for beam scheduling constraints. The beam is transported from vacuum to air through the 25  $\mu\text{m}$  vacuum window. Next, the beam passes through air for a short distance, about 100 mm, before being scattered by a 1 mm Pb sheet. From here the spread beam is transported through 1.428 m of air before reaching the DUT position.

Beam alignment was done with the in-beam BLM and the Pb sheet moved out of the beam. The scintillating ruby target was used to indicate the position of the beam. By using visual feedback from the CCTV camera in the control room to tune the Y-Z beam-steering magnets, the pencil beam was positioned in the centre of the ruby. With the beam aligned, the Pb sheet was moved into the beam while the in-beam BLM was placed at the beam spot centre.

At this point, the optimal beam intensity for the experiment had to be established. The optimal beam current was found by reducing the current until the in-beam BLM measurements seemed to give a linear response to current changes. This linear response region was found to be at a beam current of about 0.2 nA and below. Based on these observations, it was decided to conduct the beam profile measurement at a nominal beam current of 0.2 nA. It should be noted that although the in-beam BLM had a significant non-linear response above 0.5 nA, the monitor BLM had a somewhat linear, although noisy, response over the same range of beam currents.

Operating the cyclotron at such a low current can cause significant beam current drift to occur. The drift is due to how current control is done in the iTL cyclotron. Current control is achieved by controlling the opening between slits, and at low currents, any small parameter variation in the SSC can cause the beam position to move slightly with regards to the slit opening. The smallest of beam movements can cause a significant relative change in output current for extremely low currents. Using the monitor BLM was a crucial requirement to allow for a useful measurement of the beam profile.

**4.1.2.1.4 Simulations** SRIM simulations were done before the setup to estimate the beam distribution using the passive beam spreading approach. The geometry of the devices were similar to the geometry shown in 4.4, but final setup measurements were not available yet. The following estimated distances were used in the SRIM simulations:

- from Havar to Pb spreader = 150 mm;
- from Pb spreader to centre scintillating target = 808 mm;
- from scintillating target to BLM = 620 mm.

The resulting beam distribution for a 66 MeV proton beam is shown in Figure 4.5. The expected beam spot, with uniformity varying less than 10%, is roughly 40 mm diameter. The proton beam was assumed to be a point beam for all the SRIM simulations of this experiment, which should result in a more conservative estimate of the achieved beam spot size (this as-

sumption is proven in the more extensive SRIM simulations for the 200 MeV NTV experiment presented in Section 4.2.2.

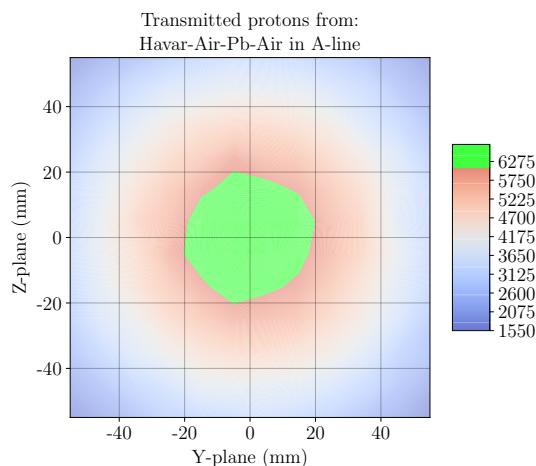


**Figure 4.5:** SRIM simulated beam spot intensity for 66 MeV protons in A-line configuration using 25  $\mu\text{m}$  Havar, 150 mm air, 1 mm Pb spreader, and 1.428 m air. Light green area indicates uniformity with less than 10% variation. Proton intensity values are per 100  $\text{mm}^2$ .

When a small cross-section detector like the BLM is moved through the beam, measuring the beam profile, a “slice” of the beam distribution is measured. By filtering the SRIM generated particle data, an estimated slice can be produced. Figure 4.6 shows the filtered slices representing the expected profile measurements. The horizontal and vertical values with fitted Gaussian functions are shown. The fitted Gaussian functions have  $\sigma = 92.44$  mm and  $\sigma = 93.24$  mm respectively for the horizontal and vertical profiles.

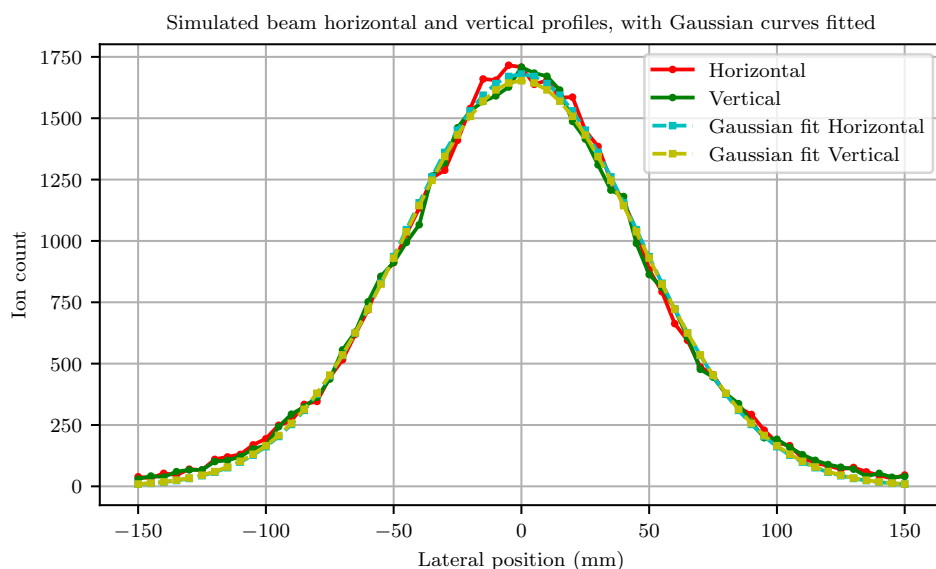


**Figure 4.6:** SRIM simulated beam profiles with fitted Gaussian functions for 66 MeV protons in A-line configuration using 25  $\mu\text{m}$  Havar, 150 mm air, 1 mm Pb spreader, and 1.428 m air. The data points represent 5 mm x 5 mm areas.

It should be noted that the data shown in Figure 4.6 is averaged over a  $5\text{ mm} \times 5\text{ mm}$  area and not the effective area of the BLM. Averaging was done because the averaging over the BLM area only produced data with a large variance. The large variance is due to the relative small amounts of protons per BLM area when the SRIM input data contains only  $1 \times 10^6$  particles. Simulating with more particles becomes impractical as the simulations already take a few hours to complete using  $1 \times 10^6$  particles. By averaging over a larger area, a smoother, more representative profile is produced. The real BLM values can be estimated by multiplying the magnitude of the data points in Figure 4.6 with the ratio of the BLM effective area to the  $25\text{ mm}^2$  area.

The maximum arm rotation angle from the centre for the measurements was chosen as  $15^\circ$ . SRIM geometry produces simulation results for particle distributions in a plane. However, with this geometry, the detector will be moving in an arc as the arm is rotated. It is prudent to investigate the maximum error that is caused by misaligned geometry. To this end, a simulation of the beam distribution, in a plane at a perpendicular distance from the centre scintillating target of  $598.874\text{ mm}$ , was performed.

The results of the simulation is shown in Figures 4.7 and 4.8. Only the tails of the proton distributions are shown. The tails are where the concern of introducing an error due to the arc-motion of the rotating arm lies. The figures show both the horizontal and vertical simulation values, to ensure that no unsymmetrical issue is missed. There is no significant difference between the distributions at the two planes. The small difference is expected since the distance difference between the planes is only  $21.128\text{ mm}$  over a total distance of  $1.428\text{ m}$ , that is only  $1.47\%$  of the total distance.

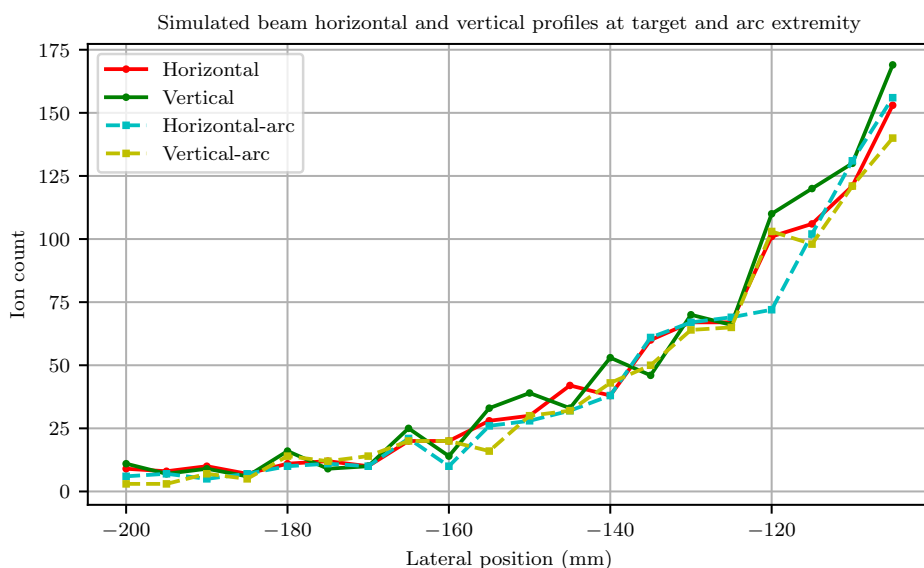


**Figure 4.7:** SRIM simulated beam profiles at target plane and arc extremity plane for  $66\text{ MeV}$  protons in A-line. Only the negative lateral distance tail of the distribution is shown. Data points represent  $5\text{ mm} \times 5\text{ mm}$  areas.

The simulation results are positive and show that the setup should be acceptable to evaluate the accuracy of the SRIM simulations and use of the dual-BLM dosimetry system.

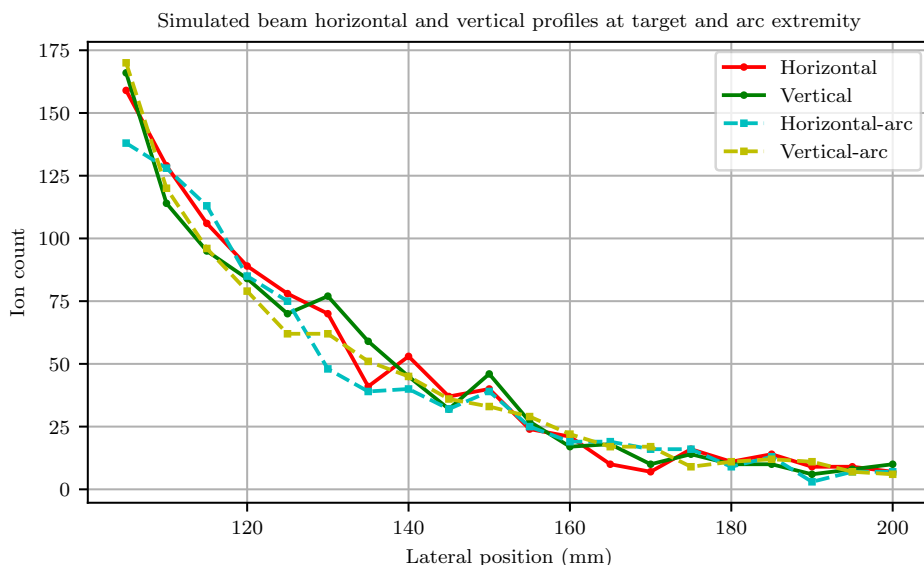


**Figure 4.8:** SRIM simulated beam profiles at target plane and arc extremity plane for 66 MeV protons in A-line. Only the positive lateral distance tail of the distribution is shown. Data points represent 5 mm x 5 mm areas.

#### 4.1.2.2 Measurements

Initially, only one beam profile measurement session was planned. Unfortunately, in the final minutes of preparation before the experiment started, the control electronics for the moveable arms failed. Inspection from support engineers determined that no quick fix was possible before the experimentation time window ended. Due to the electronics failure, only a minimal number of measurement positions for the in-beam BLM was possible. These positions were manually set up between each measurement and is listed in Table 4.2 with the corresponding mean in-beam BLM and reference BLM count values.

Lateral position	Normalised count/sec
0 mm	826063
63.5 mm (left)	514944.837
127 mm (left)	34398.425
220 mm (left)	146

**Table 4.2:** Normalised In-beam BLM pulse counts for each lateral position during iTL A-line vault experiment on 2016/06/09.

Notwithstanding the non-ideal test conditions, valuable measurements were obtained. The first set of raw measurements is shown in Figure 4.9, and it highlights some issues that need to be considered when measuring beam profiles.

Firstly it illustrates the process of finding the optimal beam current to use for the measurement, as described in the previous section. The leftmost part of the graph shows the beam switched on with an intensity of 1 nA, followed by 0.5 nA and 0.2 nA respectively. It is clear that the in-beam BLM was either saturating or working in a highly non-linear region at 1 nA since halving the beam intensity to 0.5 nA did not halve the measurement, as it did on the reference

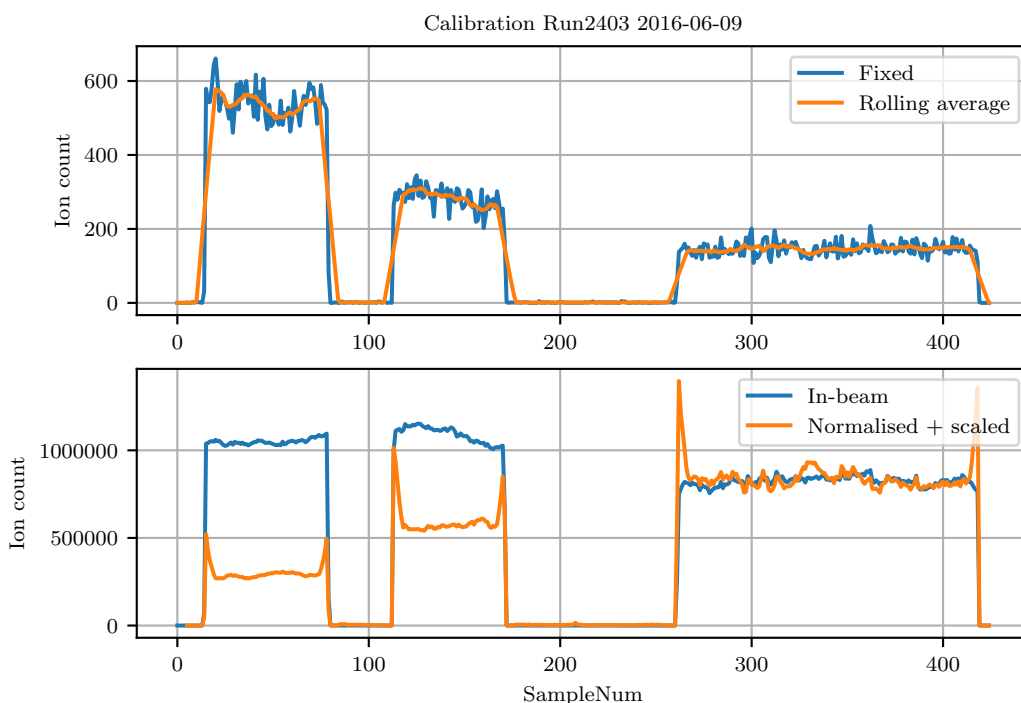


**Figure 4.9:** Raw measurements to determine optimal beam intensity for A-line profile beam profile measurement. The ‘horns’ are a side effect of smoothing, using a windowed rolling mean and normalising the data using the reference BLM values.

BLM. However, when the intensity was further lowered to 0.2 nA, the in-beam measurement dropped by an appreciable amount. Although it could not for sure be said that the BLM was operating in a linear region, there was enough observable range to allow a more detailed analysis of the data after the experiment. At 0.2 nA the beam intensity was also very close to the lower operational limit of the SSC. At this point, it was decided to do the profile measurement at 0.2 nA to optimise the use of the available beam time for the experiment.

Measurement of the beam profile was done at four positions, with the in-beam BLM moved manually to each position. Due to the setup and time constraints, the only sensible option was moving the BLM in the area left of the beam centreline. The measured data points were mirrored to the right side of the centreline to allow for a Gaussian fit on the data.

A Gaussian fit for the data samples is also shown in Figure 4.10. With  $\sigma = 57.16$  mm, the fitted Gaussian did not agree well with the expected  $\sigma$  from the SRIM simulations in Section 4.1.2.1.4. The simulated data, as discussed in 3.2.2 and shown in Figure 4.6 assumed certain distances for the setup. Accurate measurements of the configuration distances were taken and the SRIM simulations were performed again. The distances used were (also shown in Figure 4.4:

- from Havar to Pb spreader = 97 mm;
- from Pb spreader to centre scintillating target = 715 mm;
- from scintillating target to BLM = 620 mm.

The new SRIM results was also fitted with a Gaussian function, which had a mean Y-

position of 0.1329 mm and  $\sigma = 58.96$  mm, that agrees very well with the measured  $\sigma = 57.16$  mm. Since the profile data is only for the one side of the beam profile, the symmetry of the beam profile could not be verified with this experiment. However, the data indicated that this measurement approach could be successful and accurate enough. When combined with the need for a higher resolution profile measurement, there was enough motivation to schedule a second test session.

In preparation for the second session, a workaround for the arm control electronics was implemented, allowing the arm to be remotely controlled for the measurement.

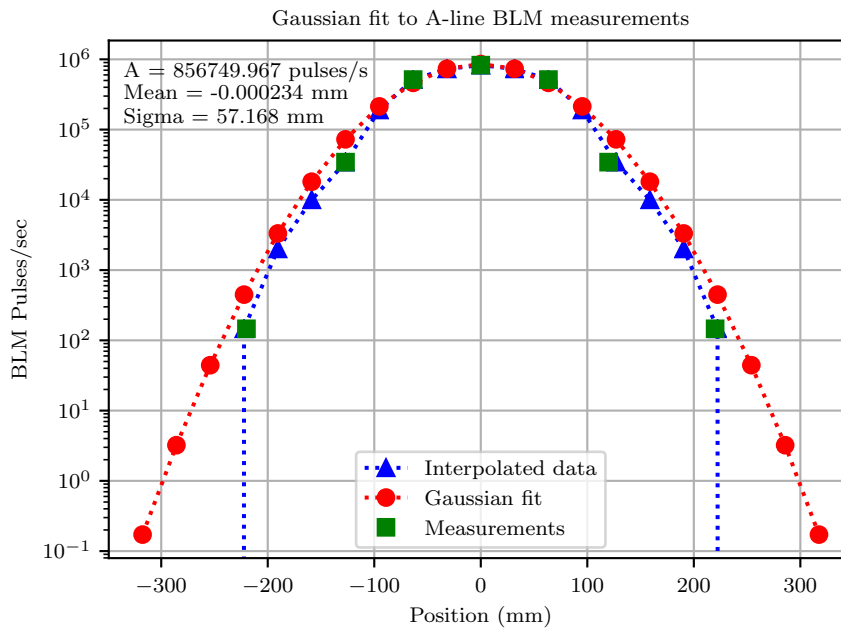


**Figure 4.10:** First profile measurements with interpolated (and mirrored) data points, and the Gaussian function fit to the dataset.

The results of the second measurement were much more definitive. With the ability to accurately control the rotating arms remotely, the profile could be measured in steps of 5mm horizontal distances on the projected DUT plane. Measurements were made at 65 separate positions, from  $-161$  mm to  $161$  mm. The central beam spot area, from  $-20$  mm to  $20$  mm, was sampled twice.

The raw data from both the in-beam BLM as well as the monitor BLM is shown in Figures 4.11 and 4.12 respectively. There was a significant drift in the beam current during the measurements. Consequently, the in-beam BLM counts can not be used directly to compare against the simulated beam profile. The in-beam measurements were normalised using the ratio of corresponding monitor BLM measurement relative to the average current for the entire 2837 samples to compensate for the current drift,  $t$ , i.e.

$$BLM_{monitor_{avg}} = \frac{\sum_{n=1}^{2837} BLM_{monitor_n}}{2837} \quad (4.1)$$

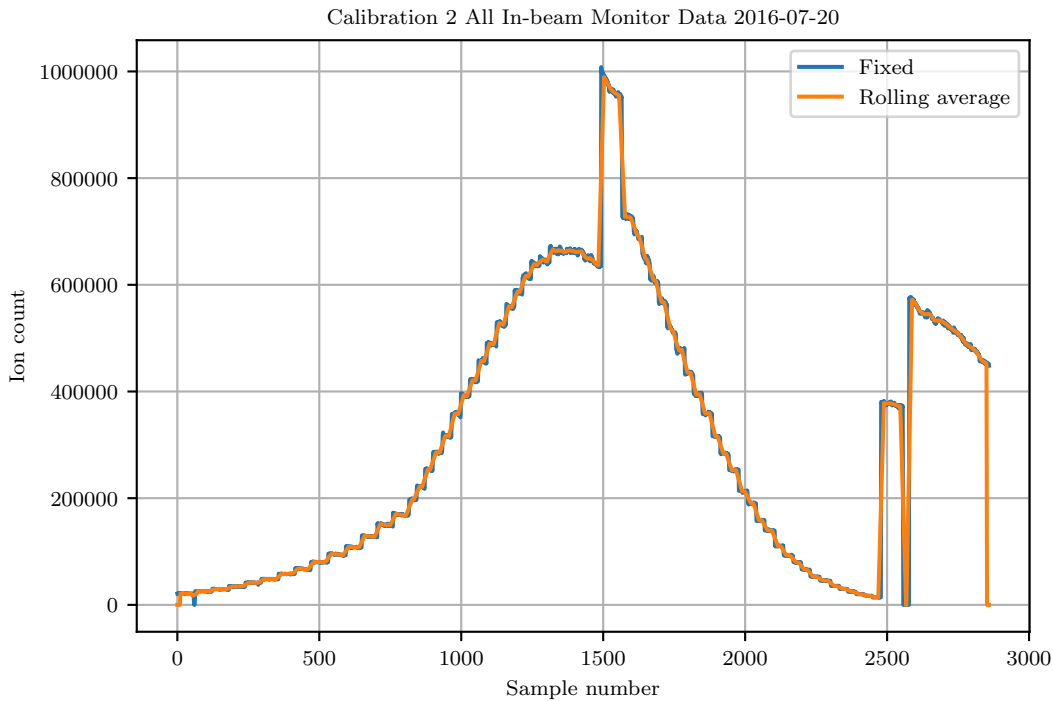


**Figure 4.11:** In-beam BLM data over all runs. Even though the general Gaussian shape is visible, there is clearly some shift in intensity present as the measurements progress.

$$BLM_{in-beam_n} = BLM_{monitor_{avg}} \times \frac{BLM_{in-beam_n}}{BLM_{monitor_n}} \quad (4.2)$$

where  $n$  is the sample number.

The normalised results were fit with a Gaussian function of the form

$$Ae^{-\frac{(x-\mu)^2}{2\sigma^2}} \quad (4.3)$$

where  $A$  is the amplitude,  $\mu$  is the mean, and  $\sigma$  is the standard deviation of the distribution. The function parameters were calculated using the `curve_fit` function from Python's Scipy package, producing  $A = 704\,968.588$  counts,  $\mu = 6.906$  mm, and  $\sigma = 55.86$  mm. Compared to the SRIM simulated beam particle distribution using accurate distances for the configuration of the first experiment, there is good agreement with an only a 3.1 mm, or 5.25% difference between the simulated and measured Gaussian. The Gaussian fit to the measured data is shown in Figure 4.13.

It must be noted that some variability should be expected in the beam intensity. The level of variability is apparent when analysing the data of the two sample sets of the central beam region, shown in Figure 4.14.

The small difference in mean Y-position, between the measured and simulated values, is due to the offset in beam position on exiting the vacuum window, which is a setup accuracy issue. Given the alignment procedure limitations combined with the experimental setup, this magnitude of inaccuracy is acceptable. Since the two Gaussian functions agree well, it can be

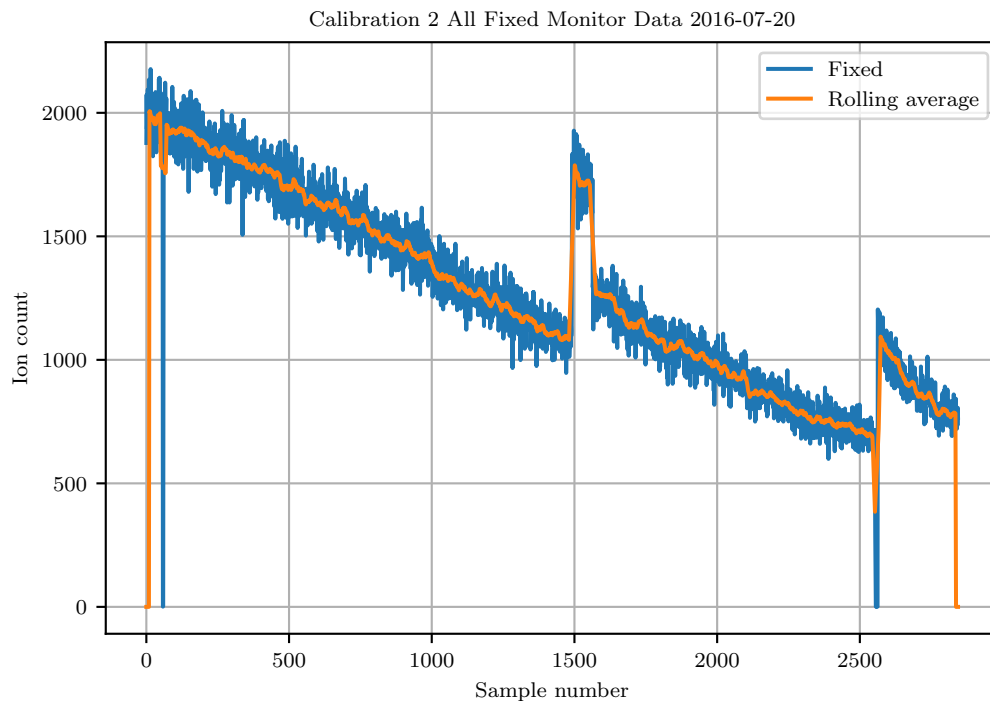


**Figure 4.12:** Fixed BLM data over all runs. Shift of beam current is clearly visible. Beam current was set to 2 nA by control room at the start of the measurements. The jumps in beam current is when the control room was asked to set the current again to 0.12 nA, 0.2 nA, and 0.13 nA respectively from samples 1500 to 1600.

deduced that the two BLM devices produced consistent, reliable measurement data, with a detection efficiency that stays constant throughout an SEE test.

#### 4.1.2.3 Results from experiment(s)

The aims as set out in Section 4.1.2.1 were all met with the results obtained from the two measurement sessions. The positive and negative results from the experiments are presented in the following paragraphs.

Positive outcomes to note from the experiment are:

- The mechanical modifications to the A-line infrastructure, to enable in-air testing, were successful.
- Successful beam alignment, spreading, and determining the optimal beam intensity for profile measurements was demonstrated.
- Successful BLM interfacing to existing iTL DAQ infrastructure was demonstrated.
- The advantages of changing to in-air testing was demonstrated as:
  - No custom vacuum connector required for interfacing to DUT electronics,
  - Preparation and installation time of DUT and support electronics reduced due to easy access to the workspace.
  - Reduction in turn-around time for adjustments to the configuration, specifically when manual repositioning of in-beam BLM was required,



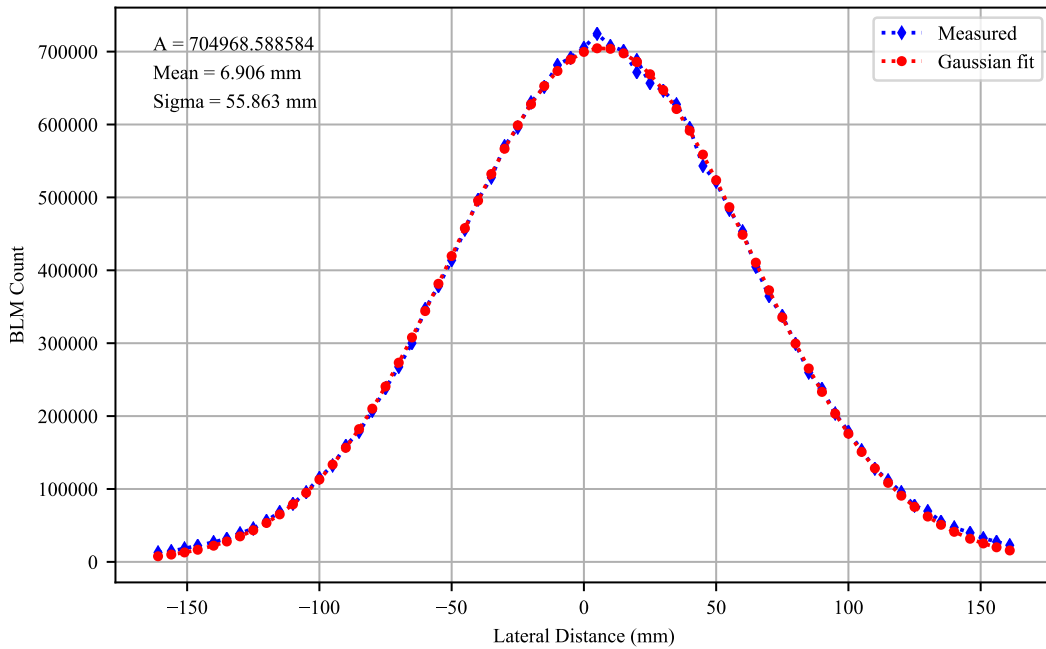


Figure 4.13: Gaussian fit of measured data from calibration run 2.

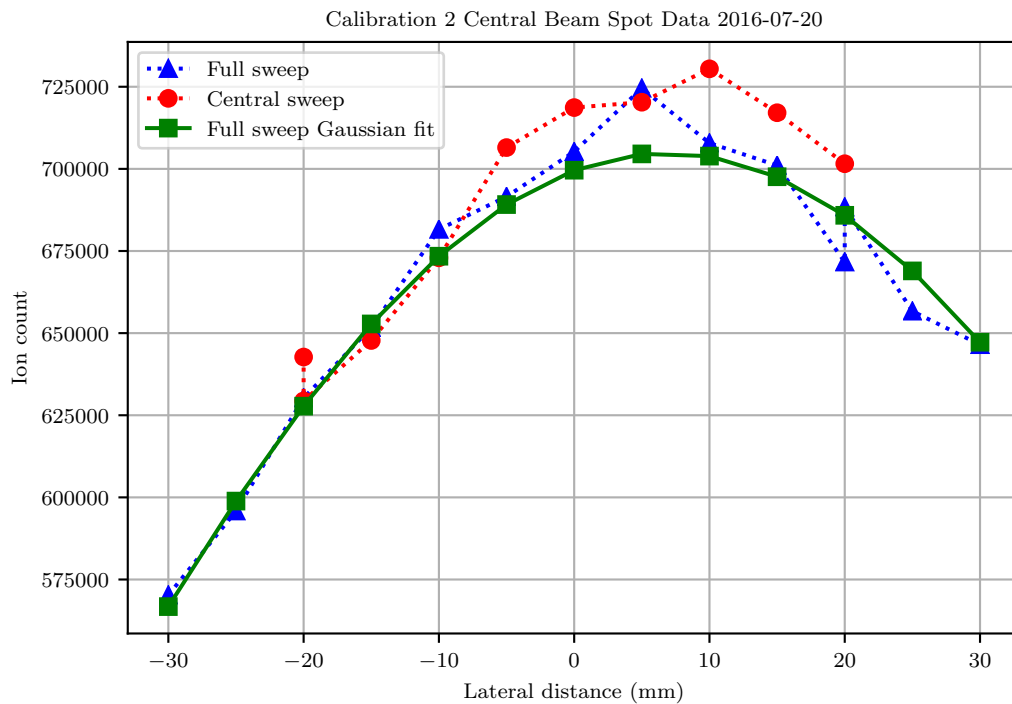


Figure 4.14: Central beam spot measurements with fitted Gaussian from full width data.

- The time required for beam profile measurement preceding an SEE test was established as roughly 2860 samples that equates to 47.66 minutes and is sufficiently short.

- The dual BLM based dosimetry approach produced accurate relative beam profile measurements that agree well with the SRIM simulated beam profile.

*Negative* outcomes to note from the experiment are:

- The time required to make the required modifications to the vacuum lines was significant and added at least three days to the preparation time.
- The dependence on ageing A-line control infrastructure was detrimental as the breakage resulted in significant downtime, sub-optimal measurements, the addition of an extra measurement session, and inconvenient workarounds to produce useful measurements.
- The lack of any data interface to the control infrastructure resulted in all position commands being manually set and logged. This shortcoming increases the complexity of executing a profile measurement as values must be double-checked to avoid command and transcription errors.

After initial verification of the advantages gained through using passive beam spreading in combination with the dual BLM based dosimetry, the use of collimators to create the required beam spot size and shadow area needed investigation. The next phase was planned for execution in the A-line vault. However, due to the installation of a tape station at the A-line, a new location for SEE testing was needed. The current author proposed that either the PTV, NTV or the decommissioned N-line. After some deliberation with iTL staff, the N-line was initially chosen.

An analysis of the required infrastructure to commission the N-line was done and proposed to iTL management. Unfortunately due to time and staff constraints, the needed modifications could not be implemented before a next round of SEE testing was due. The next option, based mainly on availability, was to use the NTV.

## 4.2 Experimental Verification at NTV

As the NTV was chosen based mainly on availability, some effort was required to modify the NTV environment so allow for SEE testing. Various elements of the original A-line design approach still required verification. Three experiments were designed and conducted at the NTV from 2017 to 2019 to evaluate and further develop the SEE testing techniques.

### 4.2.1 66 MeV proton beam in air, December 2017

An experiment was designed to verify the beam spot geometry and uniformity with collimators used to shape the scattered beam. The calibration procedure, designed to precede the SEE tests, was also verified. This experiment was performed using a 66 MeV beam in the Neutron therapy vault.

#### 4.2.1.1 Experimental design for verifying SRIM beam simulations, setup geometry and dosimetry

The following goals were set for the NTV experiment:

- verify in-air test methodology at NTV;

- verify SRIM simulation accuracy compared to the measured data for the NTV configuration;
- verify BLM as dosimetry system at NTV;
- verify the quality of the beam spot and shadow areas, created using a series of collimators;
- verify the quality and ease of use of the 3D-printed collimator stands;
- verify the use of energy degrading sheets to enable SEE measurements over a range of energies.

**4.2.1.1.1 Mechanical configuration** The diagram for the mechanical configuration for the 66 MeV experiments at the NTV is shown in Figure 4.15. The conceptual design, as described in Section 3.5, is used as a guideline to implement the mechanical beam delivery configuration.

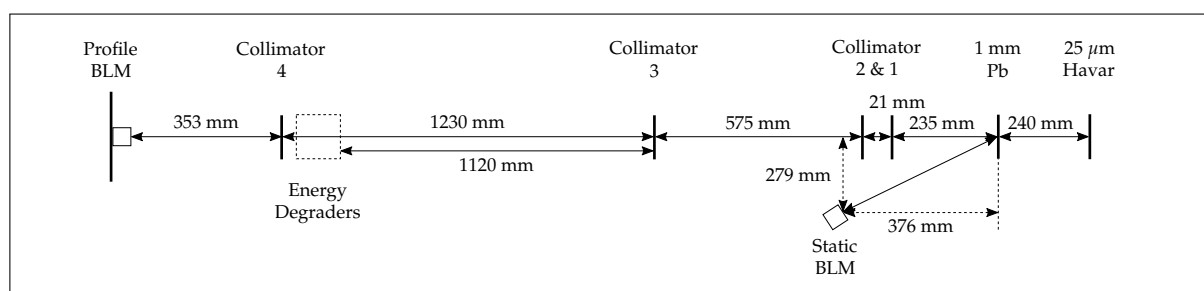


**Figure 4.15:** Geometry of the collimator and BLM configuration for 66 MeV SEE tests at the NTV.

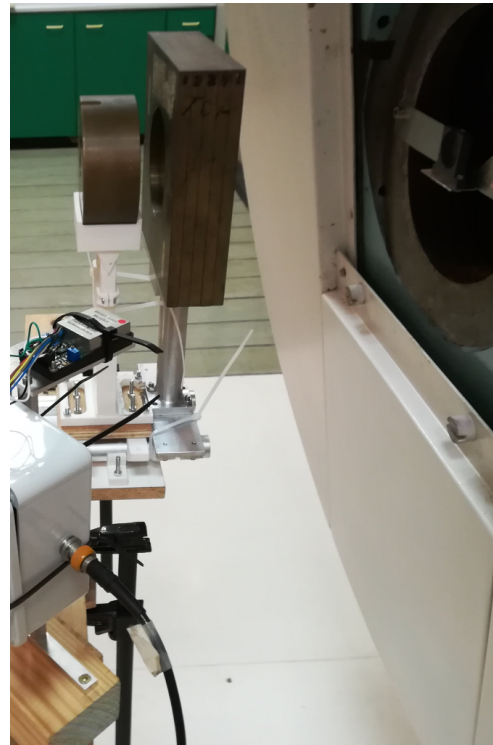
Firstly the beam needs to be transferred to air. At the NTV there already is a Havar vacuum window in place, shown in Figure 4.16(a). The window was not used during neutron therapy as the proton beam is diverted to the gantry using a beam bending magnet. For these experiments, the beam bending magnet is disabled to allow the proton beam to pass straight through to the vacuum window and the vault behind.

Shortly after the beam exits the vacuum window, the 1 mm Pb sheet is installed to spread the beam. Due to the size of the vault, a distance of up to 4 m is available between the spreader and the DUT positioning platform. However, based on the wooden patient bed's dimensions, and mounting options on it, the DUT distance was chosen to be 2805 mm. After the Pb sheet, the first two collimators are positioned fairly close to the Pb sheet. To the side of the first collimator, the reference BLM is mounted, as shown in Figure 4.16(b). The complete SEE test setup in the NTV is shown in Figure 4.17.

In between the spreader and the DUT positioning platform, the collimators are placed. The collimators should form the beam spot and the desired shadow area. The placements position of the collimators were calculated using the first approximation geometric line-of-sight approach, as described in Section 3.5. The collimators were placed on the 3D-printed collimator stands which in turn were mounted on the alignment rails. Alignment of collimators was done with the aid of laser levels and the adjustable 3D-printed collimator stands. The collimator placement planning was done using a spreadsheet, and the original values used are listed in Table 4.3.



(a) Havar exit window with protective carbon cap in the background, the 1 mm Pb sheet mounted across the opening, and collimator 1 and 2 in the foreground.



(b) From right to left the 1 mm Pb sheet, collimator 1 and collimator 2. The current reference BLM is visible in the foreground.

**Figure 4.16:** Configuration details of beam delivery system for 66 MeV SEE test at NTV.

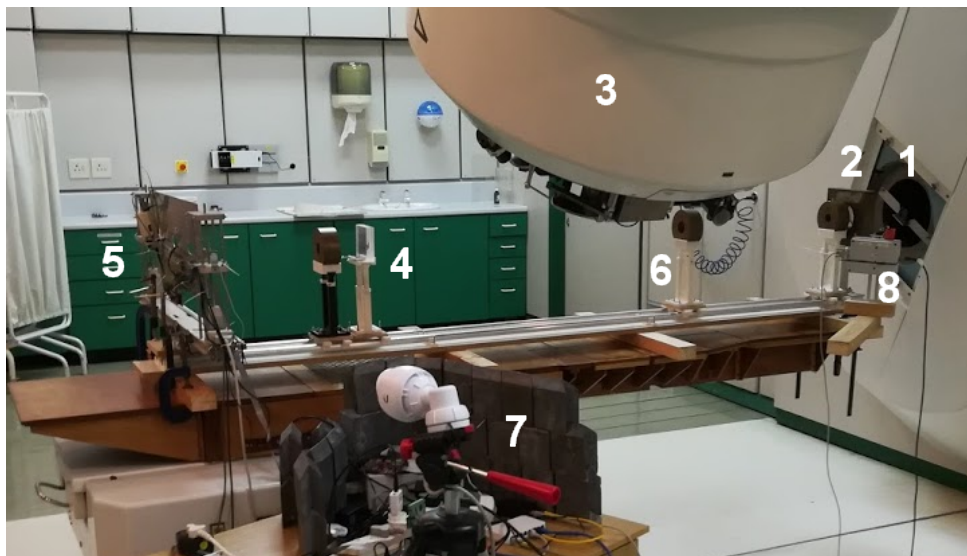


**Figure 4.17:** Configuration setup for beam profile characterisation measurements and SEE tests at the NTV. The beam enters from the right passing through the Pb sheet (1), three collimators (2)(6), the degrader sheets and the fourth collimator (4), before reaching the DUT mounted on the positioning platform (5). The therapy gantry (3), lead shielding for support electronics (7), and reference BLM (8) is also visible.

Beam Element	Distance from Pb (mm)	Body dia. (mm)	Aperture dia. (mm)	Collimator Thickness (mm)	Theta (Radians)	Spot dia. (mm)	Shadow dia. (mm)
Collimator 1	111	200	100	50	$6.802 \times 10^{-1}$	108	4207
Collimator 2	174	120	30	50	$3.007 \times 10^{-1}$	108	1612
Collimator 3	806	120	40	50	$6.682 \times 10^{-2}$	108	347
Collimator 4	2313	120	30	50	$2.334 \times 10^{-2}$	33	121
DUT	2600	30	-	-	$6.346 \times 10^{-3}$	-	-

**Table 4.3:** Inputs and calculated results for collimator placement for NTV experiment on 2017/12/19. DUT distance, spot diameter, and collimator dimensions are all inputs.

The values chosen for the distance to the DUT and shadow size were estimates, as these could only be measured when the mounting track was placed on the patient bed. The spot diameter was chosen as 33 mm to ensure full coverage of the relevant electronics of both DUT boards. The rest of the input values are the dimensions of the chosen collimators. The resulting positions for the collimators are shown in the distance column of Table 4.3. By choosing a smaller aperture for the second collimator, the third collimator can be placed closer to the centre of the distance between collimator two and collimator four.

Collimator 1 could not be placed as close to the Pb sheet as originally planned. The minimum sensible setup distance was determined to be 235 mm, that resulted in a knock-on effect in the collimator positions. During the alignment procedure, collimators 1-4 were therefore slightly adjusted to their final positions of 235 mm, 306 mm, 931 mm, and 2211 mm respectively. However, the impact of the changes on the test was small, as it only increased the spot diameter by roughly 1.3 mm and increased the distance to the DUT by 14 mm. The position calculations assumed minimal overlap of 10% between the preceding collimator's aperture edge and the following collimator's outer diameter. These calculations resulted in a sub-optimal shadow intensity that is discussed in more detail in Section 4.2.1.3.

For this experiment, the linear movement DUT positioning platform was used and is shown mounted in place in Figure 4.18. The motivations for using the linear movement platform was first, to simplify the calculations required to verify the beam profile measurements, and secondly, to verify the operational characteristics of the linear movement platform.

The fixed reference BLM was mounted on a stand, relatively close to the spreader, on an extension piece. The in-beam BLM was mounted on the DUT positioning platform.

The energy degrader unit was placed just up-stream from the fourth collimator, and its position was measured from the upstream edge to the third collimator. It was oriented so that the sheets are clamped to the upstream edge of the holder, which also simplifies the layer configuration for the SRIM simulations for the different degrader options chosen.

A low wall of lead blocks was packed onto the wooden table to provide some shielding to the support electronics. All the support electronics were placed behind this lead, as viewed from the beam entry and spreading point.

**4.2.1.1.2 Experiment electrical interfaces** Electrical interfaces were needed for the BLMs, the DUT positioning platform, the CCTV camera, and the DUT boards. Power was provided

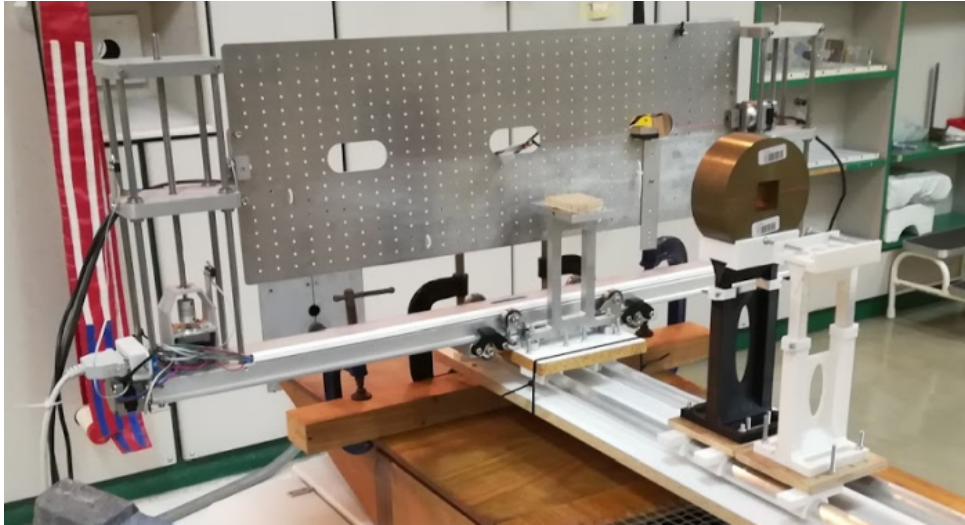


**Figure 4.18:** The linear movement positioning platform mounted on the support rails with the mounted in-beam BLM, fourth collimator, and degrader sheet holder visible.

to the electronics from the available wall sockets.

For the BLM interface, the existing coaxial cables were used to transport the BLM signals to the neutron therapy control room. At the control room the BLM signals were captured using a customised instrumentation rack connected to the iTL DAQ system.

For the DUT positioning platform the existing Ethernet connection to the control room was used. In the vault, the platform's embedded controller is connected to a network switch, which is in turn connected to the control room's Ethernet cable. In the control room, the cable was connected to another network switch to which the laptop, with the control software for the platform, was connected.

No custom connectors were required to interface the BLMs and the positioning platform, as all the cables, switches, and patch panels uses standard Bayonet Neill–Concelman (BNC) and 8 position 8 contact (8P8C) connectors. Using standard connectors significantly lowered the cost and time required to test and implement the setup.

**4.2.1.1.3 Beam configuration, alignment and intensity** The planned beam for the experiment is a 66 MeV proton beam with an intensity of between 0.2 nA and 30 nA. The DUT electronics required, based on the largest package size, a beam spot size of roughly 20 mm diameter. As the DUT and the BLM would both be mounted on the positioning platform, a shadow needs to be created so that the DUT does not get overexposed to the protons during the beam profile measurements.

Beam alignment cannot be done other than verifying that the beam spot is as uniform as expected. Therefore the experiment relied on the beam to be aligned to the accuracy the cyclotron control system can provide. Given the fact the beamline is straight, with no bends, from the SSC, it can be assumed that the beam alignment would be reasonably good.

Similarly, the beam intensity would be controlled from the cyclotron control room. The beam current is set to the required level and delivered to the vault. During the beam delivery to the neutron therapy vault, there can be no direct beam intensity measurements. Thus the

reference BLM will be monitored to verify the beam intensity indirectly during exposure runs.

Activation control of the beam during the experiment was done using the Dose Monitor and Control (DMC) system of the NTV vault. The DMC was operated in timer mode allowing for devices to be exposed for pre-determined times. The DMC was operated by the experimenters, and DMC timer values could be changed during the experimentation session.

#### 4.2.1.2 Simulations

With the configuration designed, SRIM simulations can be done to verify the feasibility of the configuration to produce the required uniformity over the beam spot. SRIM simulation results can also indicate the expected energy spectra when varying thickness degraders are used. For the SRIM simulations the configuration is modelled as layered materials, similar to the PTV simulations and A-line experiment.

To estimate the thickness of degraders required, SRIM was used to generate a table of ranges of protons with energies up to 66 MeV. An initial SRIM simulation with no degraders showed that the Havar, Pb sheet and Air layers, will reduce the beam energy to a mean value of 56.958 MeV. The SRIM simulations give a projected range in Plexiglass for 55 MeV and 60 MeV protons of 23.10 mm and 27.02 mm respectively. Thus the maximum thickness degrader to use would be less than 27.03 mm. A set of degrader thicknesses, based on the available degrader sheets, were used to simulate the energy spectra for the experiment. Table 4.4 shows the simulation results for  $1 \times 10^5$  protons.

Thickness	$\mu_{Energy}$ (eV)	$\sigma_{Energy}$ (eV)
0	$5.696 \times 10^7$	$4.286 \times 10^5$
2	$5.435 \times 10^7$	$4.462 \times 10^5$
3	$5.300 \times 10^7$	$5.544 \times 10^5$
6	$4.881 \times 10^7$	$5.999 \times 10^5$
8	$4.583 \times 10^7$	$6.301 \times 10^5$
10	$4.271 \times 10^7$	$6.978 \times 10^5$
12	$3.938 \times 10^7$	$7.535 \times 10^5$
16	$3.192 \times 10^7$	$9.070 \times 10^5$
19	$2.523 \times 10^7$	$1.079 \times 10^6$
22	$1.658 \times 10^7$	$1.434 \times 10^6$

**Table 4.4:** Beam energy mean ( $\mu_{Energy}$ ) and energy standard deviation ( $\sigma_{Energy}$ ) from SRIM simulation results for varying thickness degraders for NTV experiment on 2017/12/19.

Using each of the degrader options, from Table 4.4, during the experiment, a good set of data points can be generated over the energy range of 16.5 MeV to 54.3 MeV. For many digital electronic circuits, this range of proton energies should be sufficient to show the devices SEE sensitivity cross-section. There is, however, a concern that the 16.5 MeV lower limit might not be low enough to estimate the threshold energy for the cross-section function to a reasonable accuracy. In order to mitigate this, it was decided to simulate a 24 mm degrader as part of the final simulation set. From SRIM simulation the expected energy after the 24 mm degrader will have a mean value of 7.79 MeV with  $\sigma_{Energy} = 2.38$  MeV.

It was also estimated that to measure the device response at each of these energies will take longer than the allotted experimentation time. Aiming for a balance between having enough energy levels while limiting the experimental time to a reasonable amount, a reduced number of four energy levels was chosen for this experiment. Table 4.5 shows the final sets of layers and thicknesses used for the SRIM simulation using  $1e+6$  protons.

Material	No degrader	8 mm degrader	16 mm degrader	24 mm degrader
HAVAR (ICRU-470)	25 $\mu\text{m}$	25 $\mu\text{m}$	25 $\mu\text{m}$	25 $\mu\text{m}$
Air, Dry (ICRU-104)	240 mm	240 mm	240 mm	240 mm
Pb	1 mm	1 mm	1 mm	1 mm
Air, Dry (ICRU-104)	2564 mm	2101 mm	2101 mm	2101 mm
Plexiglass	-	8 mm	16 mm	24 mm
Air, Dry (ICRU-104)	-	455 mm	447 mm	439 mm
Total thickness	2805.0025 mm	2805.0025 mm	2805.0025 mm	2805.0025 mm

**Table 4.5:** SRIM layer material stack and thickness configuration for beam spot simulation of NTV experiment on 2017/12/19.

As with the A-line experiment, the case can be made whether a more realistic beam model should be used as input to the SRIM simulations, instead of the “point beam” model which models a mono-energetic parallel beam positioned at the X-Y-Z origin, in the positive X direction. For the NTV experiment both the point beam and a beam with a Gaussian distribution ( $\sigma = 3$  mm) was used for the SRIM simulations.

Figures 4.19, 4.20, 4.21, and 4.22 shows the SRIM simulation results for the beam spot intensity for each of the scenarios listed in Table 4.5, for both the point beam case and the Gaussian distribution case. In the graphs, the proton intensity shown is the amount of transmitted protons integrated over an area of  $10 \text{ mm} \times 10 \text{ mm}$  ( $100 \text{ mm}^2$ ).

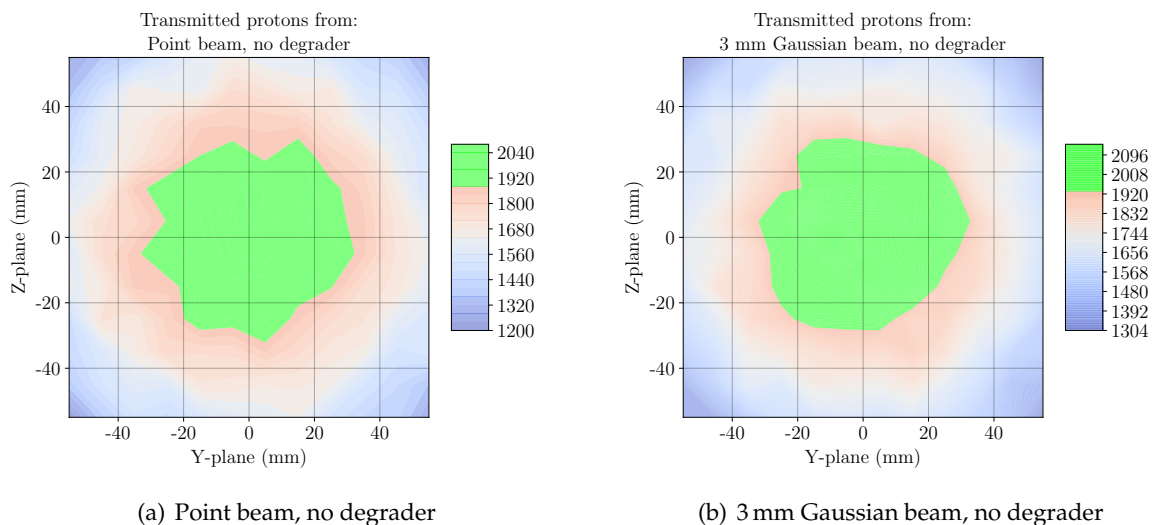


**Figure 4.19:** SRIM simulated beam spot intensity for 66 MeV protons, from (a) Point beam source and (b) 3 mm Gaussian beam, in NTV configuration. Light green area indicates uniformity with less than 10% variation. Proton intensity values are per  $100 \text{ mm}^2$ .



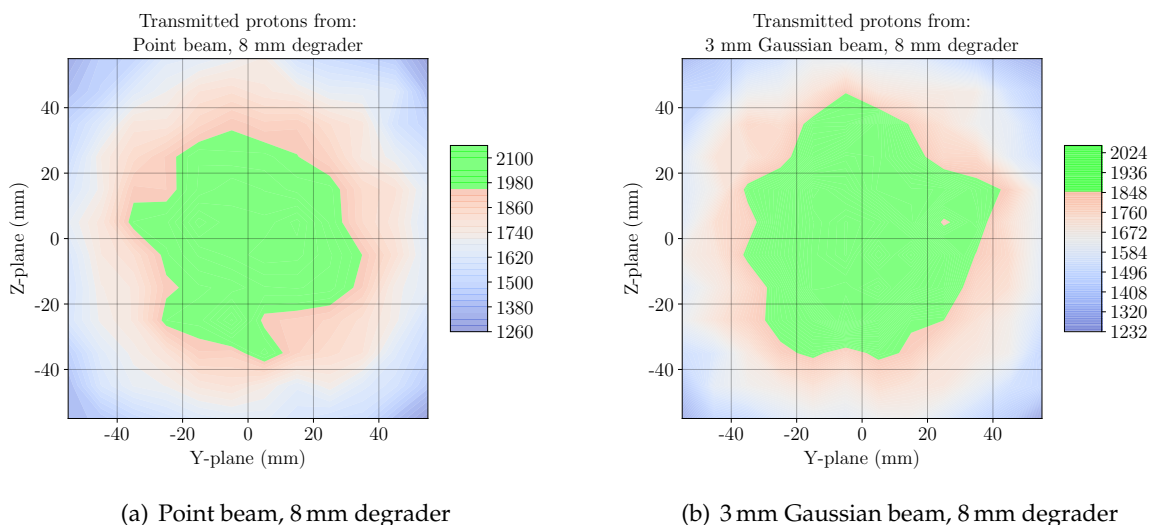


**Figure 4.20:** SRIM simulated beam spot intensity for 66 MeV protons, from (a) Point beam source and (b) 3 mm Gaussian beam, in NTV configuration using 8 mm energy degrader. Light green area indicates uniformity with less than 10% variation. Proton intensity values are per 100 mm<sup>2</sup>.

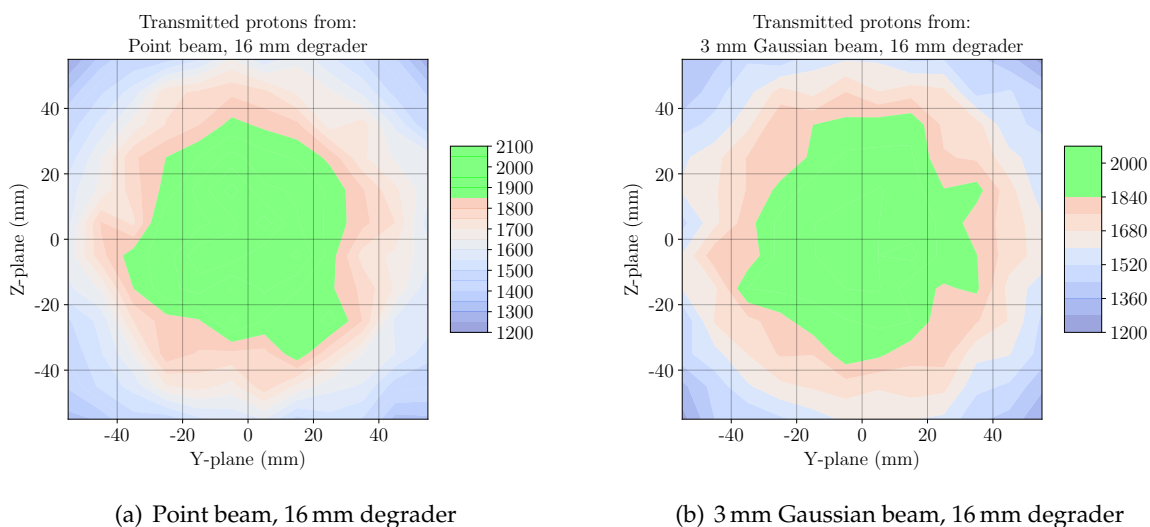


**Figure 4.21:** SRIM simulated beam spot intensity for 66 MeV protons, from (a) Point beam source and (b) 3 mm Gaussian beam, in NTV configuration using 16 mm energy degrader. Light green area indicates uniformity with less than 10% variation. Proton intensity values are per 100 mm<sup>2</sup>.

In all cases the required beam uniformity over the central 20 mm  $\times$  20 mm square area was achieved. In each case, adding a thicker degrader does cause the beam to spread out more. However, the amount of added spread is relatively small.

A further notable consideration is the relative runtimes for the different scenario simulations. In the case of using a point beam configuration versus using a 3 mm Gaussian beam input, for the 24 mm degrader scenario, the runtime for simulating 50000 protons increased from 00:24:21 to 02:25:44, a factor of 5.98 more, which is a substantial increase.

Considering the relatively small impact the more realistic beam distribution had on the results, there is an unacceptably large increase in simulation runtime associated with the sim-

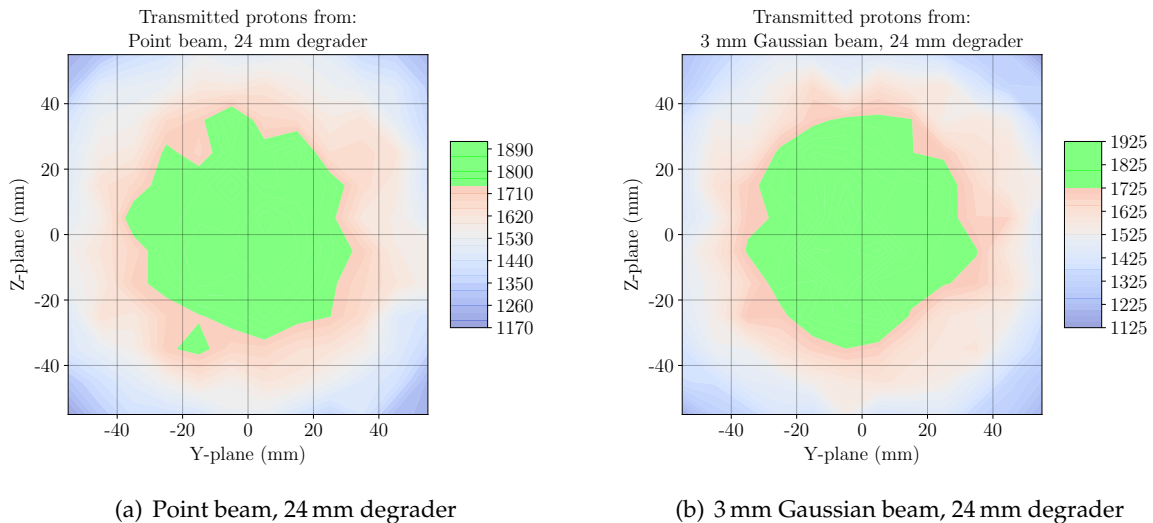


**Figure 4.22:** SRIM simulated beam spot intensity for 66 MeV protons, from (a) Point beam source and (b) 3 mm Gaussian beam, in NTV configuration using 24 mm energy degrader. Light green area indicates uniformity with less than 10% variation. Proton intensity values are per  $100 \text{ mm}^2$ .

ulation. Combining the significantly longer runtime with the observation that in each case, the simplified point beam model produced a more conservative estimate of the beam uniformity, it can be justified to use the simplified point beam model for similar future beam simulations.

Additionally, the simulations are useful to choose a starting beam current for the beam spot profile measurements. Using the simulation data from the “No degrader” case, using the point beam model, a maximum proton density of  $2055 \text{ protons/cm}^2$  is obtained per  $1 \times 10^6$  protons simulated. Calculating the amount of protons striking the BLM area,  $2.712 \text{ mm} \times 2.712 \text{ mm}$ , assuming  $6.241 509 \times 10^{18} \text{ protons/s}$  as 1 Ampere of beam current, gives  $9.433 672 7 \times 10^{14} \text{ protons/s}$ . To limit the count rate to less than  $1 \times 10^6 \text{ protons/s}$ , the required beam current for the beam spot profile measurement should be no more than 1 nA.

#### 4.2.1.3 Measurements

To measure the complete beam profile the following measurements were planned: The in-beam BLM is horizontally moved from the movement limit of the DUT positioning platform (630 mm) through the beam spot centre (113 mm) to its origin (0 mm). The in-beam BLM is then vertically moved from 30 mm above the beam spot centre to 30 mm below the beam spot centre. At each position, a minimum of five measurements is taken, to help keep the data consistent.

The beam intensity was monitored using the reference BLM during device exposure to allow compensation for any beam instability during device exposure. The analysis of time usage during profile measurement as well as SEE testing is presented.

**4.2.1.3.1 Beam intensity selection for profile measurement** From the SRIM prediction in Section 4.2.1.2, the optimal beam intensity should be about 1 nA in order to keep the in-beam BLM rate below  $1 \times 10^6 \text{ counts/s}$ . Using a similar approach to the procedure followed at previous tests in the A-line, the optimal beam intensity, for the beam spot and shadow measurements, was also determined experimentally. The in-beam BLM was centered in the planned

beam spot and the beam intensity was lowered while observing the BLM response. The full measurements from the first part of this process is shown in Figure 4.23, where the beam was lowered to 5.6 nA from the initial 10 nA. Table 4.6 show the averaged count values for the in-beam BLM as the beam intensity was lowered from 10 nA. The table also shows the calculated ratio between the beam current and BLM count. The data is from the four calibration runs, run 26-29, shown in Figures 4.23, 4.24, 4.25, and 4.27.

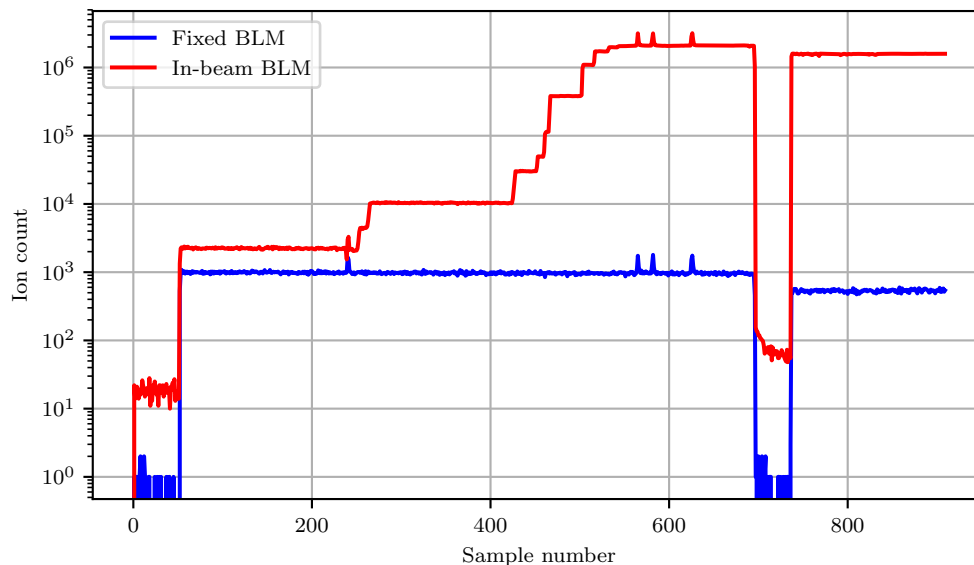


**Figure 4.23:** NTV beam calibration measurement. First the in-beam BLM is moved to the spot centre, reaching it at about 550 seconds in a 10 nA beam. At 696 seconds into the run, the beam intensity was lowered to 5.6 nA.

Beam current	Reference BLM rate	CC ratio (Ref)	In-beam BLM rate	CC ratio (In-beam)
10 nA	991/s	99.10	$2.128 \times 10^6$ /s	$0.212 \times 10^6$
5.6 nA	533/s	95.18	$1.579 \times 10^6$ /s	$0.280 \times 10^6$
2.2 nA	210/s	95.45	$0.862 \times 10^6$ /s	$0.392 \times 10^6$
1 nA	124/s	124.00	$0.557 \times 10^6$ /s	$0.557 \times 10^6$

**Table 4.6:** BLM measurements for beam intensity calibration at iTL neutron therapy vault experiment on 2017/12/19. CC ratio is the Current-to-Count ratio and for each BLM it is calculated by dividing the beam current (in nA) into the count value.

The Current-to-Count (CC)-ratio stays relatively constant for the reference BLM, indicating consistency in the measurements. Note that for the last entry, 1 nA, the reference BLM was moved a little closer to the lead sheet to get a slightly higher count. For the in-beam BLM the ratio is not constant, but increase as the beam current is lowered. This change indicates that the BLM measures more accurately with a lower beam intensity, which aligns with the theoretical development for the expected multi-particle strike probabilities explored in Section 3.3.2.

**4.2.1.3.2 Wide-beam horizontal beam spot and shadow profile** With the beam at 5.6 nA, the first beam profile was attempted. Figure 4.24 shows the in-beam and reference BLM measurements. The in-beam BLM was moved horizontally from the centre position to the leftmost limit at 0 mm, samples 0 to 303, then back through the centre position to 30 mm right of centre, sample 596. The BLM was moved back to the centre and then right to the rightmost limit at 663 mm, sample 1360. The DUT platform was moved in steps of 10 mm for the wide-beam measurements to limit the measuring time.

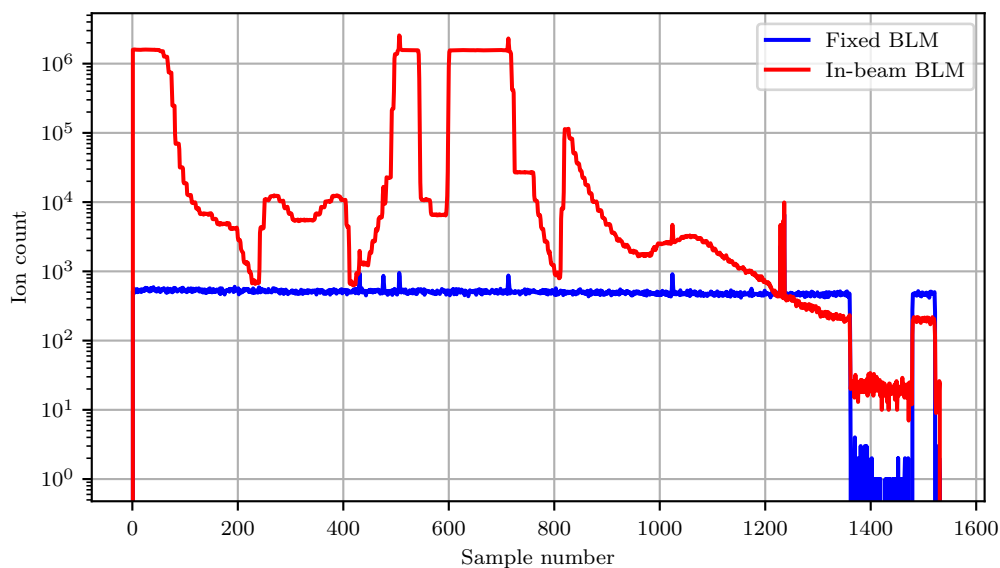


**Figure 4.24:** First horizontal wide-beam profile measurement before aligning the data with the position information. The data During this run it was noted that the maximum measurements were saturated, prompting a second measurement at a lower beam intensity.

The shadow created could not be measured entirely due to the BLM being mounted off centre on the DUT positioning platform to allow for the DUT to be mounted to the BLM's left. The wide-profile could be measured up to 113 mm left and up to 663 mm right of the spot centre.

From the raw data, the general shape of the beam spot looks good, specifically in terms of the spot size. However, it is also clear that some amount of saturation is occurring in the beam spot area. With this level of saturation, significant deviations from the desired uniformity in intensity may be obscured within this region. Consequently, another measurement with the beam intensity lowered to 2.2 nA was done.

The second wide-beam profile measurement is shown in Figure 4.25. With the maximum intensity measurement being well below the saturation point, any deviations in intensity over the beam spot area should be visible. The beam shadow area has a similar shape to the one measured at 5.6 nA (Figure 4.24). From inspection of the two measurements, the quality of the shadow area can be characterised.

The raw data of Figure 4.25 must be matched with the position logs of the DUT platform to characterise the beam spot and shadow. Since the BLM monitoring system and the DUT

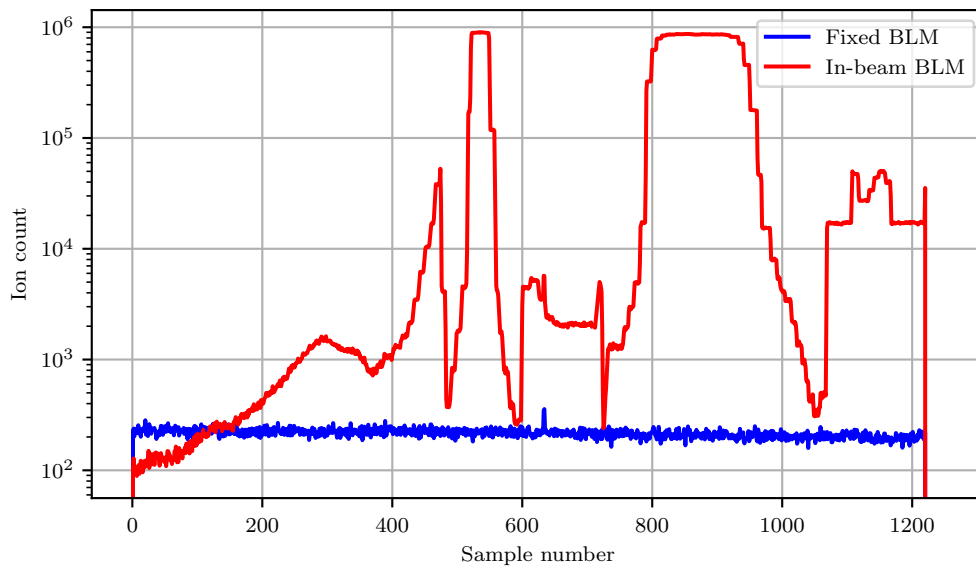


**Figure 4.25:** Second horizontal wide-beam profile measurement. With a lower (2.2 nA) intensity, unsaturated maximum values are produced. Note the data is not aligned with position information.

positioning platform has two separate logging instruments, the data synchronisation must be done, manually, post-test. The position synchronised beam intensity data is shown in Figure 4.26. The beam spot and shadow area can now be evaluated as a function of the DUT platform position.

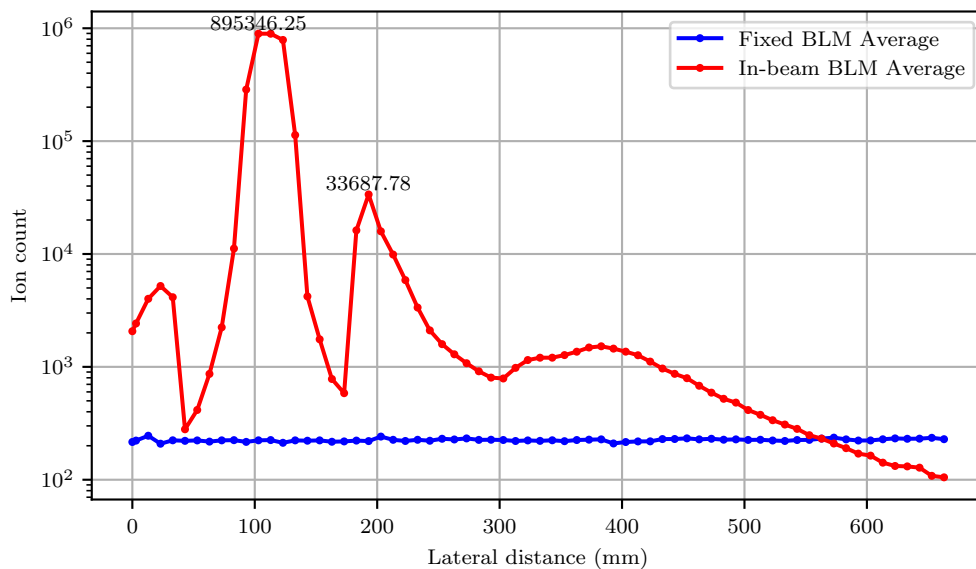


**Figure 4.26:** Position aligned data of the second horizontal wide-beam profile measurement. The beam spot centre is aligned with the 113 mm position on the positioning platform.

Regarding the beam spot, from the wide-beam measurements, it can be estimated to be

about 20 mm wide horizontally, centred at 113 mm. For the most part, the beam shadow has an intensity well below 1% of the central beam spot intensity. The implication is that components that are placed in the beam shadow should have an exposure that is 100 times lower than the maximum in the beam centre. It should be noted that for a small region, with a width of about 30 mm (from 173 mm to 203 mm), the beam shadow intensity rose above 1% to about 3.76% of the maximum at the centre of this region. The reason for this higher than expected intensity was due to the collimators not being positioned with enough overlap. The original software routines were erroneously written to calculate the collimator positions with minimal overlap between collimators. Due to the angle of the spreading beam moving through the collimators, this positioning resulted in the beam only passing through a part of the 50 mm thick brass of the collimators, instead of through the full 50 mm.

After the December 2017 experiment, the collimator position calculating software was adjusted to make sure that the overlap is calculated so that the beam will always pass through a minimum of 50 mm brass.

**4.2.1.3.3 Beam spot profile** For the beam spot profile measurement the beam intensity was further lowered to 1 nA. A finer position resolution was required for an accurate beam spot measurement. With the BLM's active area having side lengths of 2.712 mm, the DUT platform was moved in steps of 2 mm to ensure that the measurements overlap. The beam spot area was measured in one run. First by moving the DUT platform horizontally from 200 mm to 145 mm (in 5 mm steps) then from 145 mm to 83 mm at a constant vertical position of 88 mm. Followed by moving the DUT platform vertically from 56 mm to 118 mm at a constant horizontal position of 113 mm. The uncorrelated BLM data is shown in Figure 4.27.

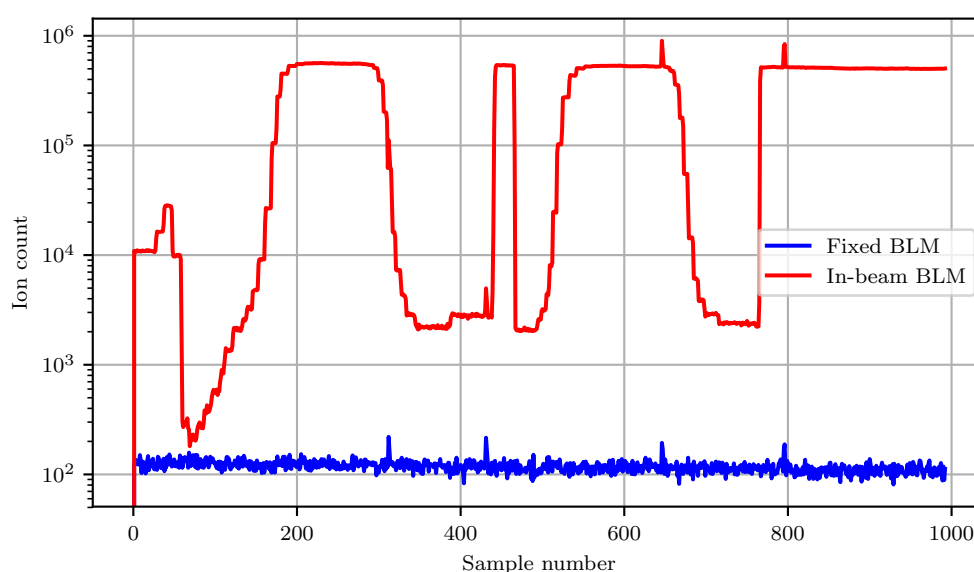


**Figure 4.27:** Central beam profile measurement in both horizontal and vertical planes with the beam current at 1 nA. Note the data is not aligned with position information.

After correlating the raw data with the DUT platform positions, further analysis becomes possible. Considering the horizontal profile, shown in Figure 4.28. The horizontal edges of the spot are reasonably sharp, falling from 450900 down to 4790 in 10 mm on the one side and from 507946 to 4260 in 12 mm on the other. The minimum intensity measured in this area is at 175 mm (62 mm from the centre point) with a value of only 212, a factor of 2657 times lower than at the centre of the beam. The spike in intensity in the shadow area can also be observed in better detail, rising to a maximum of 27751 at 190 mm, a factor of only 20.3 times lower than at the centre of the beam.

The vertical profile edges are consistent with the horizontal profile edges, dropping from 505164 to 4390 in 12 mm on one side and from 473661 to 3774 in 12 mm on the other side.

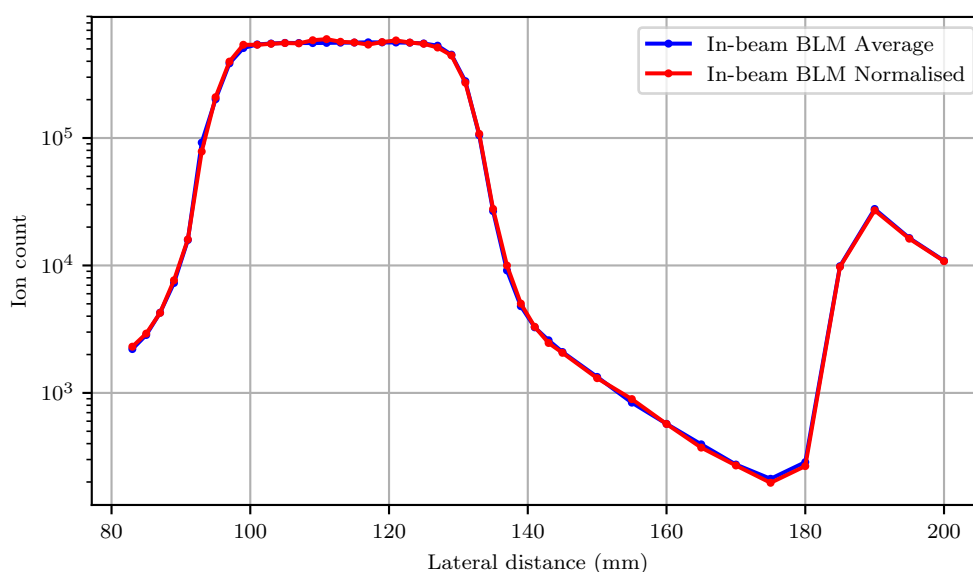


**Figure 4.28:** Central beam horizontal profile, averaged and normalised. Data is normalised to the average reference BLM count for the horizontal measurement. Standard deviation error bars are not shown as they are  $< 1\%$  of the data value. The beam spot centre is aligned with the 113 mm lateral distance point.

By analysing the uniformity of the beam, the actual beam spot size can be determined by applying the requirement of less than 10% variation in intensity over the beam spot. Figures 4.28 and 4.29 show the raw and normalized BLM values for the horizontal and vertical profiles respectively. Given that some variations are visible in the current reference BLM values of Figure 4.27, it is prudent to rather work with the ratio of the in-beam BLM value versus the reference BLM value. The ratios for the horizontal profile as well as the vertical profile are plotted versus the lateral distance from the beam centre point in Figure 4.30.

The resulting beam spot is uniform with less than 10% variance from 101 mm to 127 mm, a width of 26 mm in the horizontal direction, and from 74 mm to 100 mm, also a width of 26 mm in the vertical direction. The final collimator had a square hole of 30 mm  $\times$  30 mm, indicating that there probably occurred some beam reflection from the aperture walls.

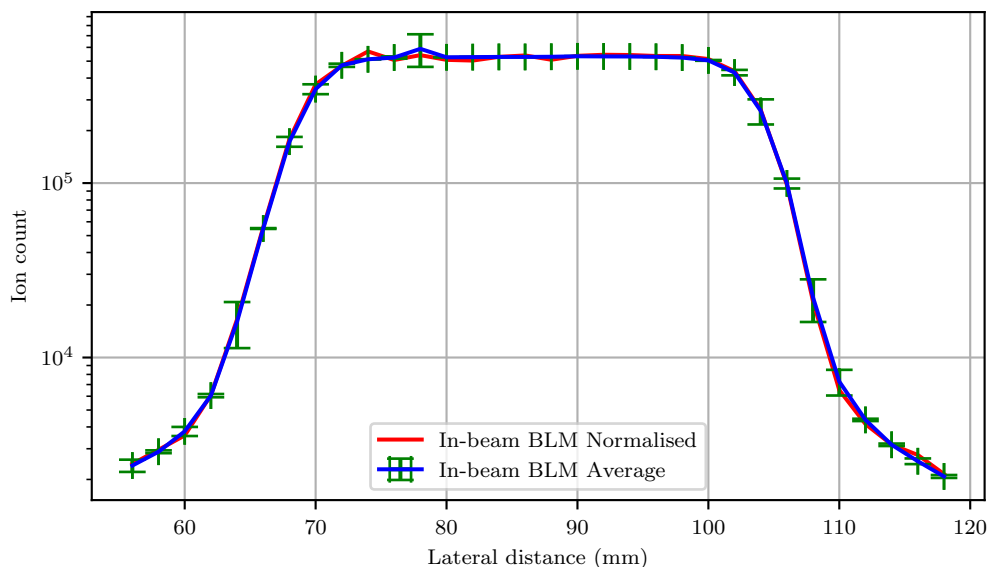


**Figure 4.29:** Central beam vertical profile, averaged and normalised. Data is normalised to the average reference BLM count for the vertical measurement. Standard deviation error bars are shown. The beam spot centre is aligned with the 86 mm lateral distance point.

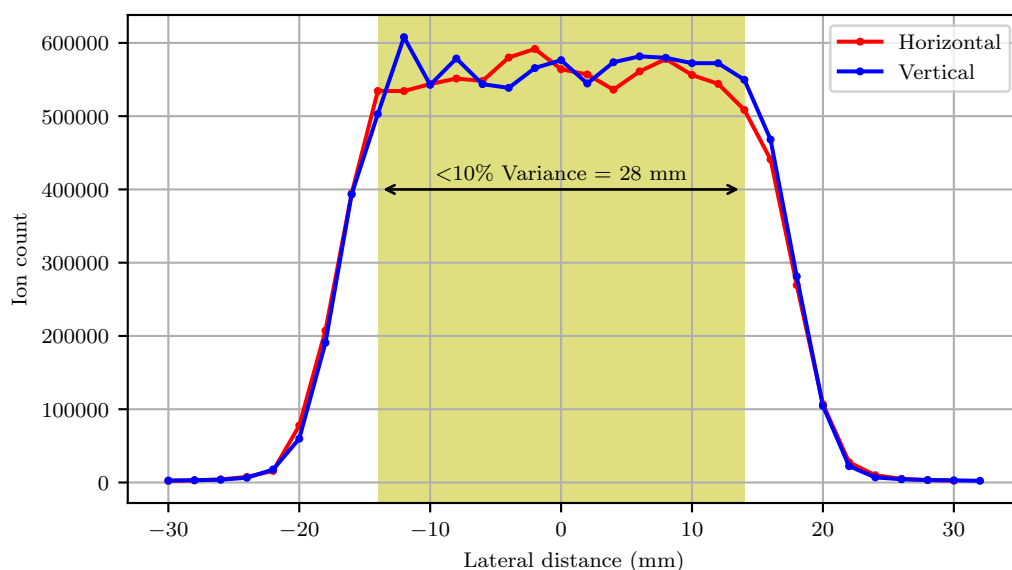


**Figure 4.30:** Normalised horizontal and vertical central beam spot profile showing good uniformity of the beam over the beam spot. Y-axis is ratio of in-beam BLM count to reference BLM count. Centre position (0 mm) corresponds to horizontal position 113 mm and vertical position 86 mm in Figures 4.28 and 4.29.

**4.2.1.3.4 SEE testing of electronics and beam utilisation** A critical part of the viability of an SEE test design is the effective beam time usage during a test. The effective usage of the beam can be evaluated using the test logs to identify the amount of time spent on different activities. Table 4.7 shows the approximate times spent on different activities during the test window. The



test logs (fully transcribed in [101]) did not contain accurate time information for all activities and some of the times are estimated based on BLM and positioning platform logs.

Activity	Time used
Test window	08:00:00
Beam current changes	00:20:00
DAQ setup and verification	00:35:00
Beam on for profile measurement	01:13:51
Dosimetry maintenance	02:20:00
Beam on DUT #1	00:16:30
Beam on DUT #2	00:32:54
Beam on DUT #3	00:13:51
DUT maintenance	01:20:00
Beam current changes	00:10:00
Test setup maintenance	01:05:00

**Table 4.7:** Summary of activities and approximate time spent thereon during SEE test window in iTL NTV, December 2017.

The analysis shows that roughly half of the time was spent on the beam profiling, with effective beam usage during profiling being roughly 27.4%. During the beam profiling process, specific events contributed to the resulting time usage. This experiment was the first at the NTV for SEE testing. There was uncertainty regarding the placement for the reference BLM. The initial position was too far away from the beam spreader resulting in very low beam reference counts. Subsequently the reference BLM was moved closer to the spreader, that took some time. Due to the location of the NTV and its previous function as therapy station, the DAQ interface had to be custom set up for the test. A few minutes were spent to ensure that the measurements by the DAQ were consistent with the manually observed rates from the BLM devices. As the beam profile for this configuration that creates a beam spot as well as a required beam shadow has not been measured before, the beam profile measurements were done twice to ensure good data was gathered.

The effective beam usage for SEE testing is only about 29%. One contributing factor to inefficient time usage was the way the DUT positioning platform was utilised. Even though it can mount several boards at once, it was decided to mount only one board at a time, since the beam shadow quality would be verified after the tests. The resulting time usage to replace a damaged DUT and to change to a different DUT was significant. It must be noted that due to safety procedures, there is a waiting time after beam exposure before personnel can enter the vault to allow for generated neutrons to be absorbed.

Time planning before the test is critical. Without such planning, the time utilisation would have been much worse. However, planning has limits since not all events can be foreseen. In the case of this experiment, the first DUTs (SRAM) observed during testing did not produce enough SEUs. During the 15 minutes of exposure at 66 MeV with currents ranging from 10 nA to 30 nA only a few SEUs were observed. The device response prompted the researchers to rather to switch to the second type of DUT (FPGA) hoping it would be more sensitive to SEUs. It turned out to be the case as statistically significant amounts of SEUs were observed using the 66 MeV beam at 10 nA and 20 nA. The successful induction of SEUs further prompted the researchers to continue with the planned energy degraded measurements, that was done using

8 mm, 16 mm, and 24 mm degraders. Since the degraders had to be changed manually, this process also used some of the time.

#### 4.2.1.4 Results from experiment(s)

*Overall the design approach taken is deemed successful.* There is however room for improvement, specifically in effective use of time and improving the planning that would allow for a test procedure that can more readily adapt to unforeseen events during testing.

*Positive* outcomes to note from the experiment are:

- BLM dosimetry approach worked as expected. Similar BLM positioning and DAQ interfacing was used as in the in-air A-line experiment.
- Beam uniformity could be verified through horizontal and vertical beam intensity profile measurements.
- Beam delivery configuration with collimators produced the required beam spot of 28 mm size, having uniformity varying by less than 10%.
- Beam delivery configuration with collimators produced an adequate shadow area with a maximum intensity of 3.7% of the beam centre intensity.
- SEE tests were successfully conducted on two different DUTs using this configuration.
- In-air testing approach was successful in providing a usable and accessible experimental environment for researchers to conduct proton-beam based SEE experiments. See [101] for a detailed analysis of the SEE response of the FPGA tested.

*Negative* outcomes to note from the experiment are:

- Verification of the SRIM simulations were limited. Beam spreading aspects could be verified, while beam intensity aspects could not be accurately verified.
- Beam energies could not be verified directly as no energy measurement equipment was part of the experiment. The energies seem to be degraded as expected, resulting in a measured cross-section curve [101].
- The use of the wooden patient bed, as an “optical bench”, was adequate, but extra time was spent to get the positioning and alignment of the collimators accurate. The main reason for added complexity and effort is how much the wooden bench bends under the weight of the collimators and their supporting elements.
- Separate DAQ and positioning platform data logging required manual correlation of beam intensity data with measurement position data to calculate beam profiles.
- Due to the extensive profile measurements and some inefficient procedures, the effective time used for SEE testing was only 13.1% of the total test window time.

#### 4.2.2 200 MeV proton beam in air, October 2018

During iTL beam time application rounds (end of 2017) a proposal for three 8-hour sessions to do SEE tests at 66 MeV were made to the iTL PAC. As part of the PAC feedback, it was proposed to expand the proton SEEs testing to 200 MeV. Given the difficulty to schedule a 200 MeV shift, the author planned for research into the feasibility of 200 MeV SEE testing for some future date. Additionally, there was a need to test specific CubeSat electronics under higher energy conditions, since they showed undesired responses in orbit.

Earlier in 2018, a specific CubeSat onboard computer started exhibiting responses in-orbit that were consistent with micro-latchup behaviour. The board would start drawing a higher amount of current than usual, but not enough to trigger the external SEL protection circuitry, causing the component's temperature to rise appreciably. The system would otherwise keep on functioning normally. After a power reset, the board would exhibit normal current consumption and temperature levels. The on-board computer design is described in [26] and was previously tested at iTL using 66 MeV protons as described in 4.1. During the previous tests some SEUs were observed, but no SELs were observed. The previous test result was not unexpected, as 66 MeV protons only induces SEL in the most sensitive of devices. Testing the same design using 200 MeV protons should shed more light on whether radiation-induced micro-latchup is the mechanism causing the in-orbit observed responses.

It was decided to plan for testing other CubeSat subsystems as well to improve the beam utilisation. If the CubeComputer tests do not use all the time available during the test window, the other subsystems can be tested. The other systems contained different untested microcontroller than the one used in CubeComputer. Consequently, the tests should also provide at least a relative performance indication of the new candidate microcontroller. Additionally, the subsystems contained two camera sensors than can be tested if time allows.

Given the PAC feedback, stated requirements and research need, there was sufficient motivation to schedule a 200 MeV SEE test for October 2018. This test was planned to coincide with other experiments done by the biomedical radiation research team since they required the SSC to provide 200 MeV protons delivered to the PTV. The NTV was available for the SEE tests at that time. Switching the same beam to the NTV is a straight forward procedure taking only about 10-20 minutes.

#### 4.2.2.1 Experimental design for 200 MeV proton-based SEE test

Building on the success of the in-air SEE experiment of December 2017, this experiment will follow similar design procedures. Where applicable the improvements made, as well as the required adjustments made due to the much higher beam energy involved, will be discussed.

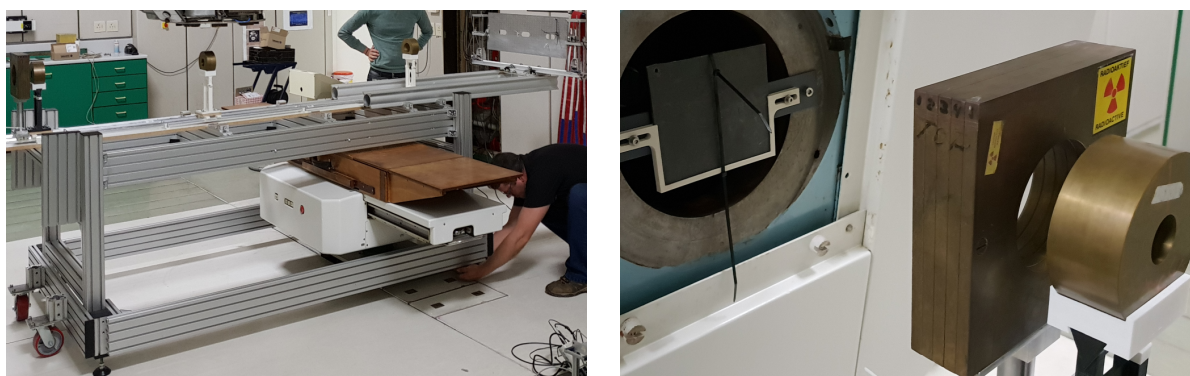
The experiment aims to verifying SRIM beam simulations, setup geometry and dosimetry for a 200 MeV proton-based SEE test. Additionally, the experiment is investigating the response of several CubeSat boards to much higher energy particles.

The following goals were set for the experiment:

- verify in-air test methodology at 200 MeV, compared to the previous 66 MeV tests;
- verify SRIM simulation accuracy, compared to the measured BLM data;
- verify BLM as dosimetry system at 200 MeV, compared to the previous 66 MeV tests;
- verify the quality of the beam spot and shadow areas, compared to the previous 66 MeV tests;
- verify the creation of a larger beam spot, of at least 60 mm diameter, at the target to enable whole board testing of CubeSat subsystems;
- conduct a SEE test on CubeSat electronics, aiming to reproduce similar responses from the DUT as observed in space;
- conduct a similar SEE test on candidate spacecraft electronics, and produce responses to compare against future on-orbit data;

- identify if other responses can be observed using 200 MeV, than what was observed at 66 MeV.

**4.2.2.1.1 Mechanical configuration** The mechanical configuration for the October 2018 SEE test at the NTV followed the same basic design as described in Section 3.5. One major change to the design hardware was the use of the support structure, originally from a PRaVDA experiment, as alignment bench for the configuration elements. The bench is shown in Figure 4.31(a). It is constructed of Aluminium extrusion channels and is assembled using typical industrial modular fixture components. The bench is fitted with wheels for easy relocation and adjustable feet for levelling and limited height adjustment.



(a) The current author levelling the PRaVDA bench during preparation. The linear DUT positioning platform can be seen mounted on the right end of the bench. (b) 3.46 mm Pb sheet mounted in holder to the left, with collimators 1 and 2 to the right.

**Figure 4.31:** Details of mechanical configuration elements for the 200 MeV proton test October 2018 in NTV.

Due to the portability and modularity of its design, the bench made positioning and alignment of the DUT positioning platform, collimators and BLMs much easier and faster. For example, to fit into the available space, the one support beam of the PRaVDA bench had to be removed, to allow the bench to be placed over the wooden patient bed, then replaced to stiffen the structure. This task could easily be accomplished by one person in roughly ten minutes. Mounting and aligning the DUT platform, collimators, and BLMs was simplified since the bench provides a flat, stiff reference surface. In contrast to the previous SEE test, no height re-adjustments were required when setting up the collimator stands.

The collimator selection and positions were pre-calculated based on the spot requirement and size limitations of the vault and PRaVDA bench. The inputs and collimator positions calculated are shown in Figure 4.32. During alignment, the collimators were slightly adjusted in an attempt to get a better quality shadow while maintaining a large spot size. The collimators were adjusted until the laser crosshairs were obscured midway into the ring thickness of the collimator. This method is limited as the laser tripod cannot be placed exactly at the same position as the Pb sheet, causing the angles to be slightly different.

After setup the final measurements of the collimator and BLM positions were taken and the geometry is shown in Figure 4.33. The final position of the fourth collimator differed slightly

Collimator	Inner (mm)	Outer (mm)	Thick (mm)	Position (mm)
Col 1	100	200	50	470.0
Col 2	35	120	50	624.0
Col 3	40	120	50	2310.9/1335.0
Col 4	60	120	50	2770.0

**Figure 4.32:** Python script inputs and calculated results for collimator placement for the 2018 200 MeV SEE test at NTV. DUT distance, spot diameter, shadow diameter and collimator dimensions are all inputs. The position values to the right of the window are the calculated results.

from the planned position, being placed at 2662 mm instead of at 2770 mm. The third collimator was still within the planned range of 1335 mm to 2310 mm, being placed at 1384 mm.

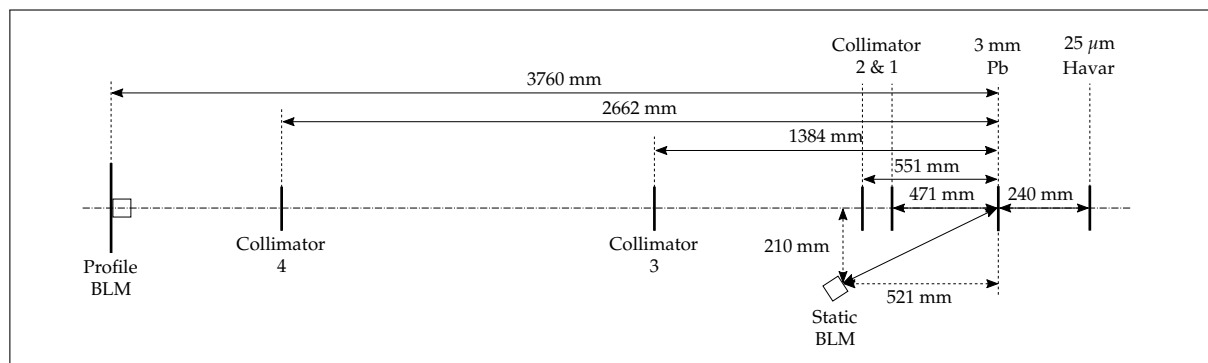


**Figure 4.33:** Geometry of the collimator and BLM configuration for 200 MeV SEE tests at the NTV.

A second significant change to the mechanical configuration was the use of a 3.46 mm Pb sheet (shown mounted in Figure 4.31(b)) as the passive beam spreader element instead of the 1 mm sheet used for the previous 66 MeV experiments. Section 4.2.2.2 explains in detail how the simulations were done to inform the sheet thickness selection. In the final configuration, a Pb sheet of thickness 3.46 mm was used as there was no 3 mm sheet immediately available, and since the 3.46 mm sheet is also used in another iTL area, it was decided not to modify the sheet by rolling it out to a 3 mm thickness.

**4.2.2.1.2 Electrical interfaces** Due to staff changes and the requirements for the high-speed counting of the BLM pulses for the SEE experiment's beam profile measurement, versus the typical detector interfacing, the standard iTL system could not be reconfigured and used for this SEE test. To interface with the BLMs, a new approach was taken, which involved the use of a different, newer DAQ system from iTL. Unfortunately, the new DAQ system could not be configured to measure pulse rates above 100 kHz. A pre-scaler was added to allow for 20x

higher rates, up to about 2 MHz, to be measured. The BLM pulses were transmitted via 50 m coaxial signal cables to the NTV control room where the signals were sampled using the DAQ.

Following the approach used in the previous SEE test at the NTV, the same interfaces were used for the DUT positioning platform and the CCTV camera, i.e. LAN network cables and analogue signal cables respectively.

**4.2.2.1.3 Beam configuration, alignment and intensity** Since the 200 MeV proton beam is spread differently than the 66 MeV proton beam, SRIM simulations were used to assist in selecting an appropriate thickness Pb sheet. One limiting factor for the beam delivery configuration, is the maximum distance from where the beam is spread, to where the DUT can be placed. Keeping the dimensions of the vault and the PRaVDA bench in mind, the maximum achievable distance was estimated to be around 4 m.

The 4 m maximum distance guided the choices for the SRIM simulation layers, which are similar to the layers listed in Table 4.5. The major change was the layer thickness of the last 'Air' layer (No degrader option), which was increased from 2564 mm to 3750 mm.

The minimum thickness Pb sheet that would give the required beam spot uniformity of less than 10% variance given the maximum beam spreading distance was determined by starting with a 1 mm sheet and increasing the thickness by 1 mm for each simulation. The result of the simulations indicated that a Pb sheet of minimum 3 mm would be required.

As with previous measurements, the beam intensity will be lowered from a saturated level until a linear region is reached. From the SRIM simulations the proton flux due to a specific beam current is estimated to be  $1.957 \times 10^7$  protons/cm<sup>2</sup>/nA. After adjusting for the BLM sensitive area, a beam current of 0.5 nA should be sufficient for the beam spot profile measurement. At 0.5 nA the SSC beam current is high enough to be fairly stable, while the expected BLM measurement rate of  $8.52 \times 10^5$  counts/sec should be well within its linear response region.

#### 4.2.2.2 Simulations

Moving from 66 MeV protons to 200 MeV protons has a significant impact on how the beam is effected by the Pb passive spreader. With much more energy at 200 MeV, the protons are not deflected as much as the 66 MeV protons are. Given that the SEE test is being done at the same location, i.e. the NTV, the physical size of the vault limits the path length of the dispersed beam that can be achieved to about 4 m. Two questions are raised at this point. Firstly: How big can the beam spot be if the configuration allows the beam to travel the full 4 m before reaching the DUT? Secondly: To what degree thicker Pb sheets will disperse the beam? A resulting question following on the second one is: How much energy is lost by the protons, due to passing through the thicker Pb sheets?

A series of SRIM simulations were done to answer these two questions. The first simulation set used a 1 mm Pb sheet and compared the beam dispersion at 2.8 m versus at 4 m. The second set compared the beam dispersion over the same two distances but used an increased Pb sheet thickness of 2 mm. The final simulation used 3 mm Pb and a distance of 4 m. At this point, no more simulations of thicker Pb sheets were done, as the amount of beam energy loss was increasing significantly. The dispersion results of the simulations are shown in Figures 4.34,

4.35, and 4.36. No normal distribution function fits were done to the results at this point, as the raw simulated data showed the differences clearly.

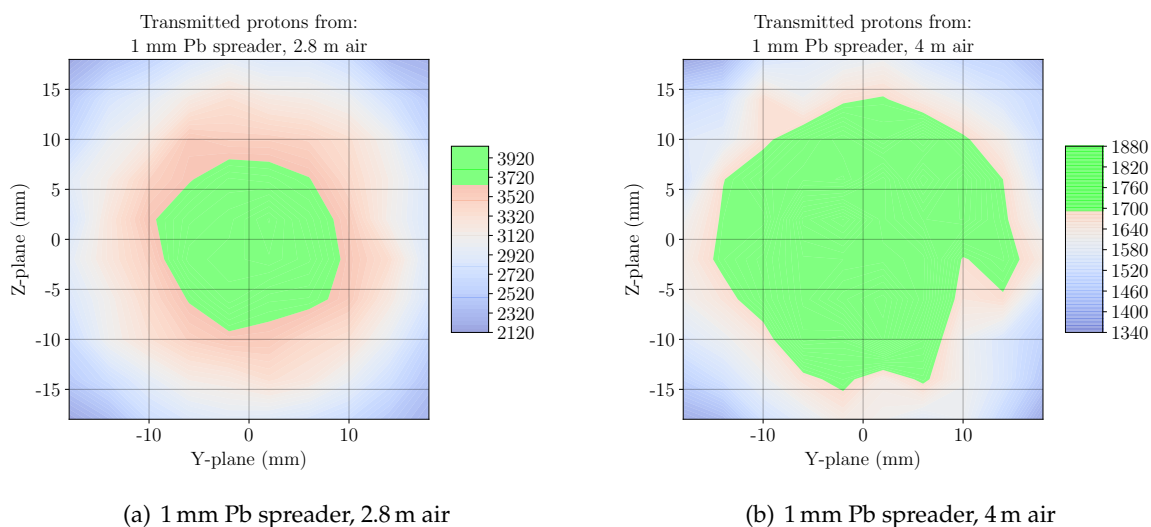


**Figure 4.34:** SRIM simulated beam spot intensity for 200 MeV protons, with a) 2.8 m air b) 4 m air, in NTV configuration using 1 mm Pb spreader. Light green area indicates uniformity with less than 10% variation. Proton intensity values are per  $16\text{ mm}^2$ .

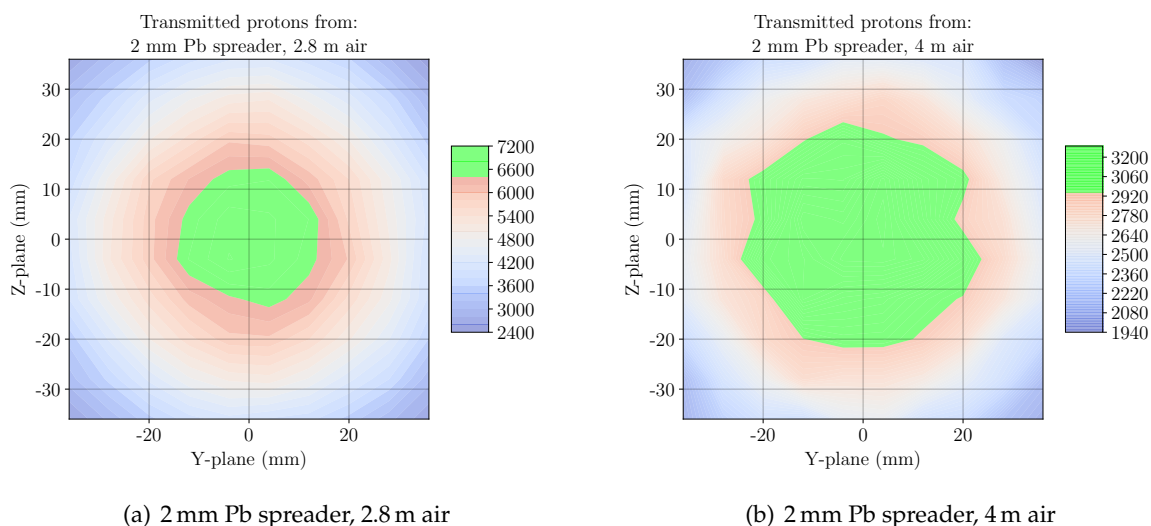


**Figure 4.35:** SRIM simulated beam spot intensity for 200 MeV protons, with a) 2.8 m air b) 4 m air, in NTV configuration using 2 mm Pb spreader. Note that the axis scales are larger here than for the 1 mm Pb simulations. Light green area indicates uniformity with less than 10% variation. Proton intensity values are per  $64\text{ mm}^2$ .

As expected, in both comparisons the beam is dispersed more if given a longer path to the DUT, increasing the spot diameter from roughly 16 mm to about 28 mm, and from roughly 28 mm to about 44 mm, for the 1 mm Pb and 2 mm Pb cases respectively. If the goal was to achieve a beam spot diameter of 30 mm, the 2 mm Pb over 4 m would have sufficed. However,

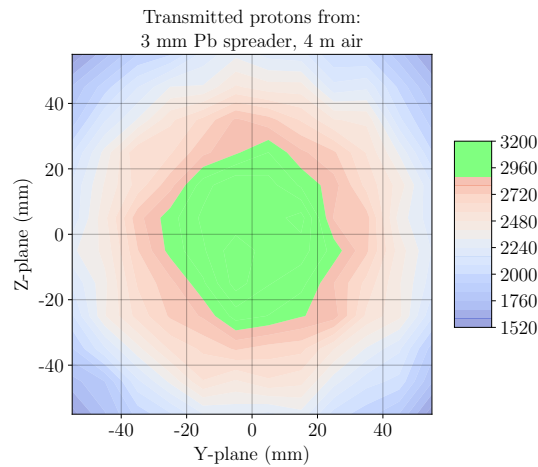


**Figure 4.36:** SRIM simulated beam spot intensity for 200 MeV protons, with 4 m air, in NTV configuration using 3 mm Pb spreader. Note that the axis scales are larger here than for the 1 mm Pb and 2 mm Pb simulations. Light green area indicates uniformity with less than 10% variation. Proton intensity values are per  $100 \text{ mm}^2$ .

one aim of the experiment was to create a beam spot to cover a complete CubeSat board, that can be up to  $100 \text{ mm} \times 100 \text{ mm}$ . With the 3 mm Pb sheet dispersed over a distance of 4 m, a beam spot diameter of about 54 mm can be achieved.

The characteristics of the beam energy distribution arriving at the DUT is summarised in Table 4.8. From a nominal 200 MeV energy, the energy loss increases to a significant 4.95% when 3 mm Pb is used. The difference in beam energy between the shorter and longer distances is very similar for both 1 mm Pb and 2 mm Pb cases and is in the order of 570 keV.

Pb thickness (mm)	Distance to DUT(mm)	Energy $\mu$ (MeV)	Energy $\sigma$ (keV)	Energy loss %
1	2805.025	195.982	384.814	2.00
1	3987.025	195.413	408.336	2.29
2	2805.025	193.339	515.156	3.33
2	3987.025	192.765	560.918	3.61
3	3987.025	190.094	670.308	4.95

**Table 4.8:** Mean, standard deviation and mean loss % of beam energy distributions for different thickness Pb sheets and different distances to DUT for SEE experiment at iTL NTV in October 2018.

Another way to visualise the distribution data is to make a horizontal slice through the centre of the beam spot. For this data, a 5 mm thick slice was chosen and averaged over 5 mm intervals. This gives the expected proton count per  $5 \text{ mm} \times 5 \text{ mm}$  area. A summary of the averaged SRIM simulation data is shown in Figure 4.37, for the 1 mm, 2 mm and 3 mm cases. Since the SRIM simulations were configured only to simulate  $1 \times 10^6$  protons, the distribution of the particles seems somewhat noisy. The noisiness is an expected artefact resulting from the limited amount of particles used during data binning. By fitting a Gaussian distribution curve to the data, a better indication of the real distribution is obtained. The fitted Gaussian distributions functions are shown in Figure 4.37.



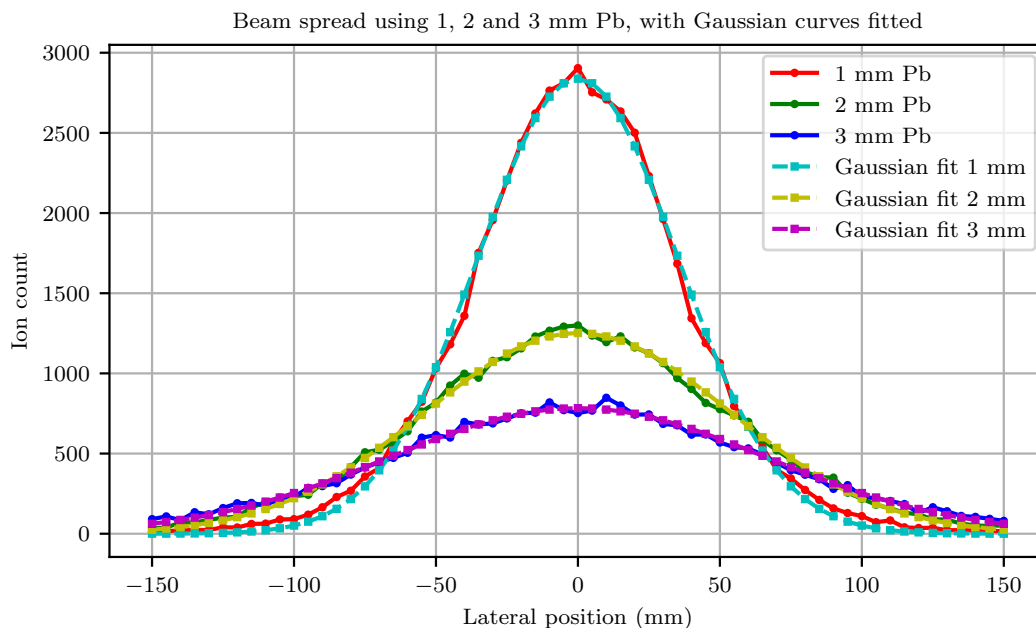


**Figure 4.37:** 5 mm×5 mm averaged centre slice of SRIM simulated beam spot intensity for 200 MeV protons, in NTV configuration using 1 mm, 2 mm and 3 mm Pb spreader over 4 m distance. Gaussian curve fitting for each case also shown.

By using the fitted Gaussian distribution functions more accurate estimates of the beam spot size can be achieved compared to inspection of the SRIM simulation data. For a 1 mm Pb sheet, a spot size of required uniformity with diameter just more than 30 mm can be obtained, (Ion count of 2808 maximum and 2568 at  $\pm 15$  mm). For 2 mm Pb the spot diameter increases to almost 50 mm (Ion count of 1252 maximum, 1123 at  $\pm 25$  mm), and for 3 mm Pb to just over 60 mm (Ion count of 782 maximum and 706 at  $\pm 25$  mm).

#### 4.2.2.3 Measurements

Due to the delay in receiving the beam at the start of the test session combined with vacuum leak issues later during the test, it was decided not to do the shadow measurement to save time and allow for electronics to be tested. Additionally, with three DUTs mounted, there was limited movement available before the platform would move the adjacent DUT into the beam spot during profile measurement. If the DUT is moved into the beam spot, it will receive a large amount of unwanted additional dose. The shadow exposure levels would instead be estimated by using the in-beam measurements while a DUT was exposed to the beam. Having multiple DUTs would cause the in-beam BLM to be at different positions in the shadow, giving some indication of the shadow exposure levels.

**4.2.2.3.1 Beam intensity selection for profile measurement** Based on the SRIM simulation results, a profile measuring current of 5 nA was planned, however at 200 MeV the beam tends to be less stable at lower beam currents. It was therefore decided to start with a more stable 10 nA beam current. A horizontal beam profile was measured, averaged, correlated with the positioning platform movement, and corrected for the  $20\times$  pre-scaler used for the in-beam

BLM, is shown in Figure 4.38. The profile was measured from  $-80$  mm to  $60$  mm (relative to spot centre at  $98$  mm) in steps of  $10$  mm.

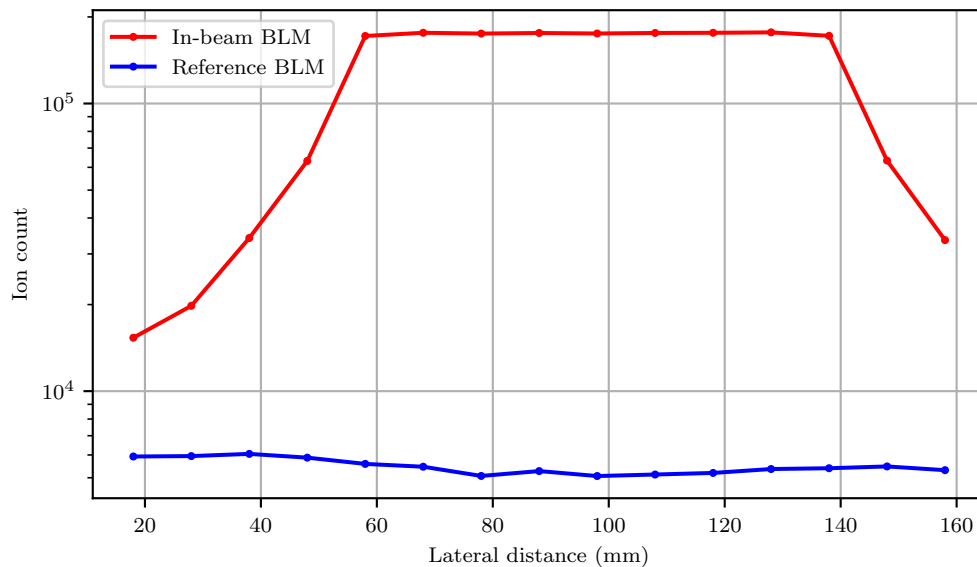


**Figure 4.38:** Horizontal beam spot profile measurement of  $200$  MeV proton beam at  $10$  nA. In-beam BLM values corrected for  $20\times$  pre-scaler used. Estimated beam spot diameter of  $80$  mm, but saturation of in-beam BLM makes estimate inaccurate.

It seems as if the in-beam BLM measurement saturates at a value of just under  $180\,000$  counts/s. The raw sampled data can be inspected to verify if saturation occurred, and is shown in Figure 4.39. The raw measurements indeed show that the in-beam values saturate when comparing them to the maximum data spikes of the reference BLM values. It should be noted how noisy the measurements are compared to the previous experiment at the NTV in 2017. Since both the in-beam and reference measurements show similar relative up-and-down movement at the same sample times, it is concluded that the ‘noise’ source is not due to physical noise in the signals. Consequently, it must be assumed that the noise is an artefact caused by incorrect DAQ settings, or it is a relatively true representation of the beam current fluctuations as produced by the SSC system.

In response to the measurements observed at  $10$  nA, the beam current was lowered and measured at  $5$  nA,  $1$  nA and finally  $0.5$  nA. The ratios between the reference BLM and in-beam BLM measurements are  $33.67$  for  $10$  nA,  $54.11$  for  $5$  nA,  $177.95$  for  $1$  nA, and  $276.36$  for  $0.5$  nA. At  $5$  nA the in-beam BLM still showed the same saturated maximum values as at  $10$  nA. At  $1$  nA the maximum in-beam values started to lower from the saturated levels. At  $0.5$  nA the maximum values were well below the saturate levels and it was decided not to try with a lower, and possibly more unstable, beam current.

**4.2.2.3.2 Horizontal and vertical beam spot profile measurement** A horizontal profile measurement, from  $-60$  mm to  $30$  mm (relative to spot centre at  $98$  mm) in steps of  $10$  mm, and from  $30$  mm to  $50$  mm in steps of  $2$  mm, was made and the data is shown in Figure 4.40. Similarly,

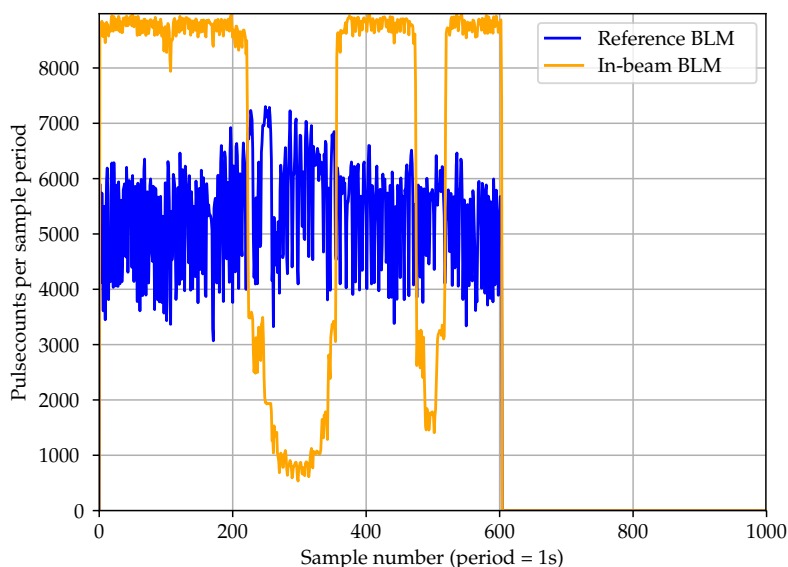


**Figure 4.39:** Raw per second sampled data from in-beam and reference BLMs. The in-beam BLM measurement seems to saturate at 9000 counts (20x pre-scaler used). The in-beam and reference data are both fairly noisy with the reference values changing by more than  $\pm 20\%$ .

a vertical profile was measured from  $-50$  mm to  $60$  mm (relative to spot centre at  $85$  mm) in steps of  $10$  mm and is shown in Figure 4.41.

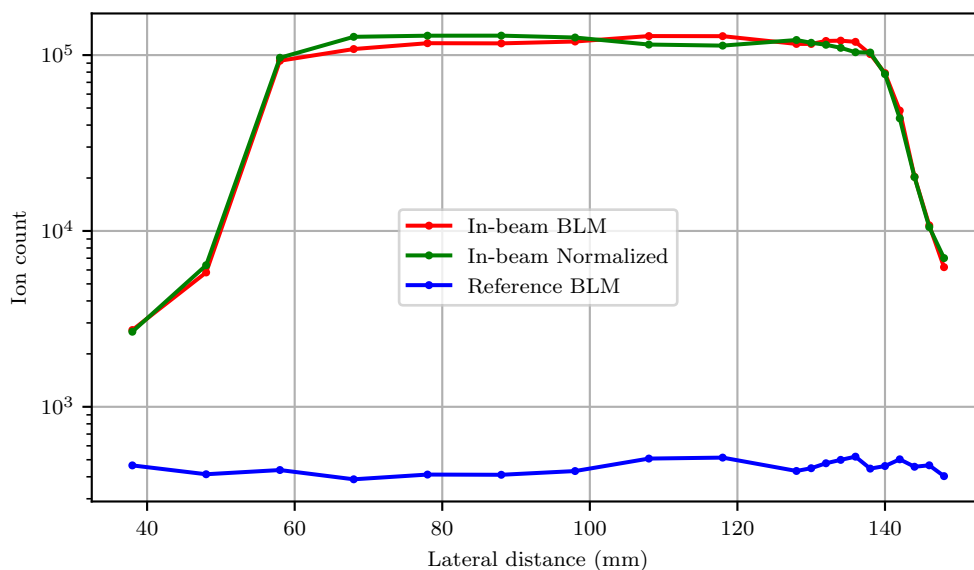


**Figure 4.40:** Horizontal profile measurement showing the in-beam BLM, normalised in-beam BLM (to reference) and reference BLM values. Beam current is  $0.5$  nA and the values are averaged and correlated to the positioning platform data.

The data for the horizontal and vertical measurement were translated to be aligned with the beam spot centre positions, normalised to the reference BLM values, and shown together

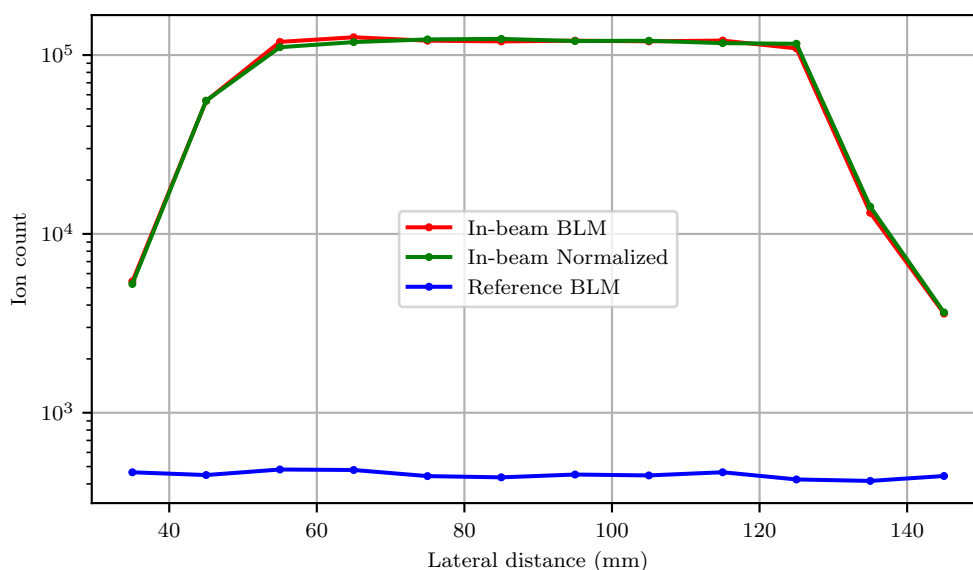


**Figure 4.41:** Vertical profile measurement showing the in-beam, normalised (to reference) and reference BLM values. Beam current at 0.5 nA.

in Figure 4.42. From the measurements, a beam spot diameter of 64 mm is achieved with this configuration, but this beam spot size must be put in context.

During the original in-air experiments in the A-line vault, the Gaussian distribution of the 66 MeV beam was simulated using SRIM and measured using the dual-BLM dosimeter approach. However, the Gaussian distribution was not rechecked at the previous 66 MeV NTV experiment. In moving to the much higher energy 200 MeV protons, the SRIM simulations, the collimator placement and the dual-BLM system might produce different results. The SRIM simulations for this experiment, described in Section 4.2.2.2, indicated that a beam spot diameter of about 54 mm can be achieved with this experiment. However, as stated in Section 4.2.2.1.1, a thicker 3.46 mm Pb sheet was used that would disperse the beam more than the simulated 3 mm Pb sheet would. The simulations also assumed a point beam is entering the vault rather than a Gaussian distributed beam (typically 3 mm - 6 mm diameter). Finally, the fourth collimator was chosen with an aperture of 60 mm, to make the beam spot large enough to cover the whole CubeSat board. From the collimator geometry calculations, the beam spot was estimated to be 80 mm maximum. With the context presented, the achieved beam spot can now be further analysed.

The area of the beam spot adhering to the uniformity requirement exceeds the estimated spot area size by about 18%, due to the 15% thicker Pb sheet used. Although the beam dispersion has a non-linear relationship to the thickness of the spreading material, the magnitude of the measured difference in beam spot size is within acceptable limits, and still smaller than the maximum allowable size due to the fourth collimator. The effect of the fourth collimator aperture size is also visible in Figure 4.42, as the steep edges of the beam spot is roughly 80 mm to 90 mm diameter. The dosimetry measurements produced values that are expected and within reasonable levels of variation.

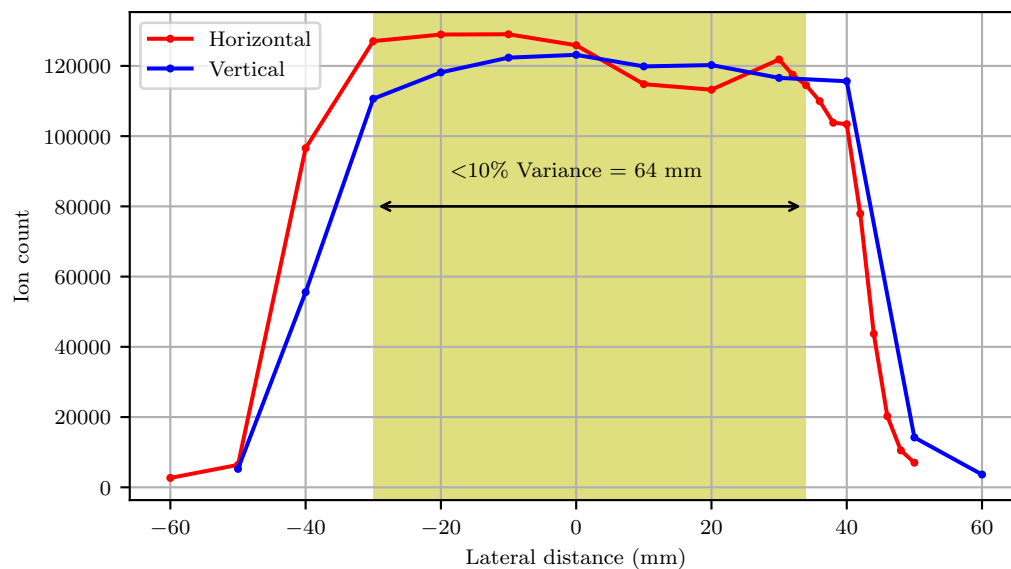


**Figure 4.42:** Combined horizontal and vertical beam spot profile measurements, both normalised to the reference BLM values. Beam current at 0.5 nA.

**4.2.2.3.3 Beam shadow profile measurement** As stated in the introduction of this section, the shadow profile was not accurately measured due to time constraints during the test window. By using the in-beam BLM measurements when it is positioned in the shadow during DUT exposure showed that the shadow levels are much lower than in the beam spot, they were even lower than the previous 66 MeV test in the NTV. The shadow intensity ranged between 0.137 % to 0.742 % and the values for some runs are listed in Table 4.9.

Run #	Beam current (SSC)	Reference BLM count rate	In-beam BLM count rate	BLM Ratio	Shadow %	Notes
2	5.0	3201.0	$1.730 \times 10^5$	54.1		BLM in spot
3	1.0	762.8	$1.357 \times 10^5$	178.0		BLM in spot
4	0.5	399.6	$1.101 \times 10^5$	275.5		BLM in spot
7	0.1	103.3	$0.548 \times 10^5$	530.7		BLM in spot
16	0.5	307.0	203.9	0.664	0.185	
17	0.5	276.6	186.0	0.672	0.169	
20	0.5	262.8	176.1	0.670	0.160	
21	0.5	273.2	182.0	0.666	0.165	
23	0.5	250.5	670.1	2.675	0.609	
24	0.5	216.3	717.2	3.315	0.651	
25	0.5	241.7	816.7	3.380	0.742	
26	0.5	239.9	647.3	2.698	0.588	
27	0.5	243.8	162.4	0.666	0.147	
28	0.5	224.5	151.2	0.673	0.137	

**Table 4.9:** Measurements of the beam shadow during device exposure using 200 MeV protons, at iTL NTV, October 2018. Only relevant runs are listed. The shadow percentage is derived as the shadow count as a percentage of the center spot count.

Although a full shadow was not measured, these measurement points are sufficient to indicate that a good quality shadow was formed.

**4.2.2.3.4 SEE testing of electronics and beam utilisation** As stated in the aims of this experiment, CubeSat electronics were tested to observe their response to 200 MeV protons, specifically the sensitivity to micro-latchups. Two versions of the computer were available for testing. The only difference between the two versions was the SRAM components used. Three other CubeSat subsystem boards were also available for testing.

In an attempt to improve on the effective beam utilisation the DUTs were grouped into two groups of three boards, that will result in just one change of DUTs during the SEE test. The first group comprised the two different CubeComputers and a star camera prototype without its imaging sensor. The second group of components comprised a star camera prototype with an image sensor, and the IR camera prototype and a third CubeComputer. Since it was the second test using the NTV configuration, there was more certainty about the quality of the shadow which allowed for multiple boards mounted at once on the DUT positioning platform.

With multiple boards on the DUT platform, any board could be quickly moved into the beam spot. This option was used several times to allow for irradiated boards to be checked for errors using remote readout routines. While the irradiated board was checked (and positioned in the beam shadow area), one of the other DUTs was irradiated. This process was repeated until all the DUTs either failed entirely or enough statistical data was gathered.

Similar to the previous NTV experiment, an analysis of the beam time usage was done as is shown in Table 4.10.

Activity	Time used
Test window	08:00:00
DAQ setup and verification	00:09:00
Beam current changes	00:03:00
Beam on for profile measurement	00:30:20
Beam on DUT #1	00:13:52
Beam on DUT #2	00:29:16
Beam on DUT #3	00:13:00
Beam on DUT #4	00:25:00
Beam on DUT #5	00:11:49
Beam on DUT #6	00:06:00
DUT maintenance	01:27:00
Beam current changes	00:20:00
Test management	03:12:00

**Table 4.10:** Summary of activities and approximate time spent thereon during SEE test window in iTL NTV, October 2018.

The analysis shows that much more time was spent testing electronics compared to the previous NTV experiment, which is expected since the beam profile measurement process was known, and only the essential profile measurements were done. Beam usage during profile measurements was 79% of the 42 minutes duration.

The SEE test time usage did not change much in terms of the percentage of the test time used and was effectively 25% usage. However, due to the much faster profile measurement,

the overall effective active beamtime used for SEE testing rose to 22.53% from 13% during the previous experiment.

During this experiment, accurate logs regarding test events and decisions were kept, which assured that decisions during the test were clearly stated and that accurate analysis of effective time usage was possible.

Time was lost due to problems with the beamline, specifically a small vacuum leak at one of the beamline components. This leak caused the safety system to shut down the beam to the NTV several times before a solution could be implemented by iTL staff. Some of the time lost due to the beamline problems were added to the test window time. The final test window time available was 41 minutes less than the planned 8 hours.

The response of the electronics to the 200 MeV protons was monitored using custom-developed software for each different type of board tested. Measurements taken included current monitoring of the DUT during exposure (SEL and micro-latchup monitoring), validation of stored data and system operation (SEU,SEFI monitoring) and quality of images from camera sensors (SEU and DD monitoring). Unfortunately, the full analysis of the results has not been published yet, as such only selected results will be presented.

#### 4.2.2.4 Results from experiment(s)

*Overall, most of the goals of the experiment were achieved.* The major goal of successfully detecting micro-latchups in the CubeComputer was achieved, that validates the necessity to *also* test candidate spacecraft electronics using 200 MeV protons. One goal that was not achieved was a detailed beam shadow measurement, as discussed in Section 4.2.2.3.

*Positive* outcomes to note from the experiment are:

- The 200 MeV was successfully dispersed to create the required beam spot diameter using a 3.46 mm Pb sheet and the associated collimator placements.
- A successful profile measurement of the 200 MeV proton beam was made using the dual-BLM method combined with a new DAQ system.
- The measured profile is adequately comparable with the simulated SRIM uniformity, and compares well with the designed maximum allowable spot size.
- An alternative to measuring the full shadow was used, saving significant time while still producing adequate data to estimate the quality of the created beam shadow.
- Radiation-induced phenomena observed on-orbit for a specific COTS based CubeComputer was recreated using the 200 MeV proton beam at iTL, that allowed researchers test the efficacy of the SEL protection circuitry and accurately identify the current consumption levels for micro-latchup conditions for the CubeComputer design.
- New candidate space electronics were successfully tested. The processor showed much lower SEU rates compared to the CubeComputer. More importantly, no micro-latchups were observed in the candidate COTS processor.
- In one of the camera sensors, SEUs and possible DD was observed. A few single dead pixels were observed with only minimal exposure to the beam, ruling out total dose damage as a possible cause.
- The other camera sensor produced good quality images, with the expected SEU induced noise, but during data readout, kept crashing. The cause of the crashes must still be

identified.

*Negative* outcomes to note from the experiment are:

- New DAQ logging of the BLM signals, proved to be cumbersome, and not reliable. The DAQ system crashed at least two times, which could be attributed to the custom setup that was done for this test.
- The in-beam absolute measurements did not match the expected flux levels at the beam centre. It is unclear why there is such a large disparity. It might be due to the scaling setup required to ensure the DAQ system does not saturate.
- The variation in current measurements of the delivered beam was more than expected. Levels changed by more than 20% in many cases. However, it seems to change from sample to sample, which usually would indicate that some statistical effect might be involved. However, here the % change in measurement stays large at low rates (250 counts/s to 500 counts/s) and at high rates (4000 counts/s to 7000 counts/s), that indicates it is an accurate measurement of a less stable beam current.
- The average current level drifted somewhat during the profile measurements but not nearly as much as the during the A-line profile measurements. The result is negative in terms of the quality of the beam at 200 MeV. However, in terms of monitoring the beam current, the result is positive. The change in beam current during device exposure can be compensated for in dose calculations.

### 4.2.3 66 MeV proton beam in air, January 2019

In January 2019 a second 66 MeV experiment was scheduled to be conducted in the NTV. The motivation for the specific scheduling was due to a masters student requiring SEE test data for his research into SEE characterisation of a microprocessor. This experiment also provided the opportunity to evaluate a new data acquisition design, that would be independent of the iTL infrastructure.

#### 4.2.3.1 Experimental design for verifying SRIM beam simulations, setup geometry and dosimetry

From the user community the requirements for the SEE test was the following:

- SEU sensitivity test of an embedded processor.
- Create a beam spot for a 10 mm × 10 mm processor die.

The following goals were set for the experiment based on the user requirements and improvement of the test capability:

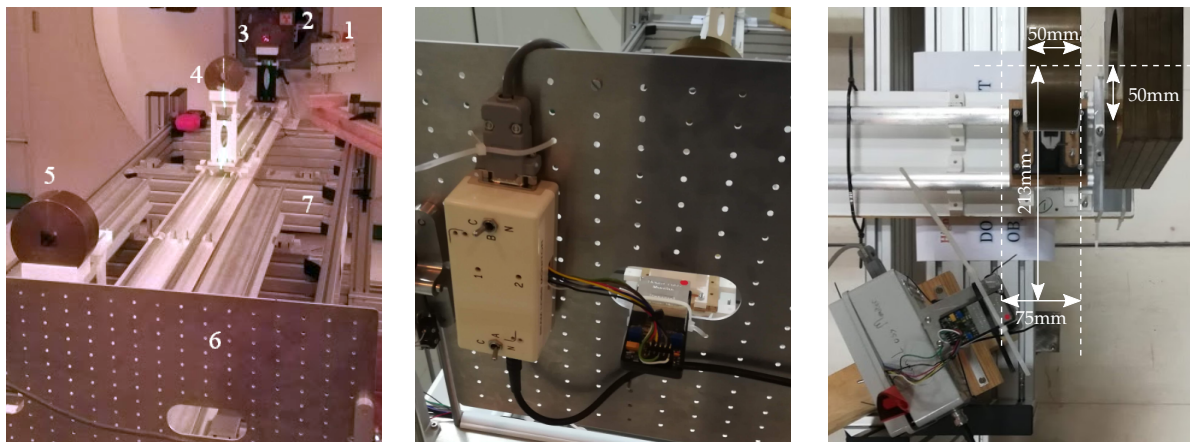
- Use a 66 MeV proton beam to induce SEEs.
- Create a uniform beam spot of 30 mm × 30 mm.
- Measure the beam spot profile using the new independent DAQ interface to the BLMs.
- Create a better quality shadow compared to the 2017 NTV 66 MeV experiment and measure the shadow intensity profile.

**4.2.3.1.1 Mechanical configuration** The mechanical configuration for the January 2019 experiment was a combination of the December 2017 and October 2018 experiments. The PRaVDA



bench was used as a mounting platform. A 1 mm Pb sheet was used as passive beam spreader followed by a set of four collimators to form the beam spot and shadow area. The configuration after setup is shown in Figure 4.43(a).

In Figure 4.43(b) the in-beam BLM is shown with its calibration box, mounted in its typical position on the DUT positioning platform. Figure 4.43(c) shows how the position of the reference BLM can be verified using photographs of the configuration.



(a) Configuration elements: (1) Reference BLM, (2) Pb sheet, (3) Collimators 1 and 2, (4) Collimator 3, (5) Collimator 4, (6) DUT positioning platform, (7) PRaVDA bench.

(b) In-beam BLM and its calibration box mounted to the DUT positioning platform

(c) Reference BLM position for 66 MeV SEE tests at the NTV, January 2019. Good photos of the configuration help to verify measurements.

**Figure 4.43:** Detail of configuration elements for 66 MeV experiment in iTL NTV, January 2019.

The collimator aperture sizes 20 mm, 35 mm and 25 mm(square) and their positions were calculated in the same way as the position calculations for the October 2018 NTV experiment. A screenshot of the calculated values as produced by the Python script is shown in Figure 4.44. The final measured positions of the configuration elements is shown in Figure 4.45.

By aiming for the best possible overlap between collimators, there is a small difference from the calculated positions compared to the placed collimators. Collimator 2 is 60 mm closer to collimator 1, and collimator 4 is 40 mm closer to the DUT. Collimator 3 was placed so that the overlaps from collimators 2 to 3, and from collimators 3 to 4 is roughly the same.

**4.2.3.1.2 BLM electrical interface** The electrical interface architecture for the experiment remained the same, with one exception, as for the 2017 and 2018 NTV SEE experiments. For the 2019 experiment a new FPGA based custom designed BLM signal logging unit was employed in parallel to the iTL mobile DAQ option.

The logger design is based on the Xilinx Artix-7 FPGA combined with signal conditioning electronics. A prototype logger with signal conditioning electronics was built by an undergrad student as part of his project work in 2018. The original design used a micro-processor based design and had some limitations. Its maximum count rate for BLM pulses was only up to about 600 kHz. This count rate is not high enough since the BLMs can output pulses up to a rate of 10 MHz.

Collimator Type	Inner (mm)	Outer (mm)	Thick (mm)	Position (mm)
Col 1	100	200	50	272.4
Col 2	20	120	50	386.9
Col 3	35	120	50	2621.5/522.4
Col 4	25	120	50	2747.3

**Figure 4.44:** Python script inputs and calculated results for collimator placement for the 2019 66 MeV SEE test at NTV. DUT distance, spot diameter, shadow diameter and collimator dimensions are all inputs. The position values to the right of the window are the calculated results.

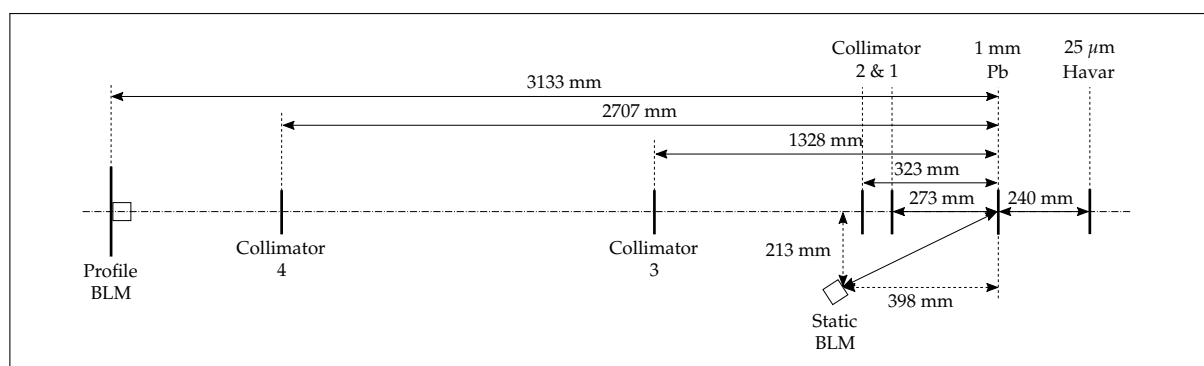


**Figure 4.45:** Geometry of the collimator and BLM configuration for 66 MeV SEE tests at the NTV, January 2019.

The author modified the design by replacing the microprocessor with an Arty development board from Xilinx. This change enabled pulses of up to 10 MHz to be measured on two simultaneously sampled channels. The BLM signals were distributed to the logger using the same coaxial cables as with previous experiments. The prototype signal conditioning circuit and Arty development board, as used, is shown in Figure 4.46.

**4.2.3.1.3 Beam configuration, alignment and intensity** The beam energy is chosen to be 66 MeV since it meets the requirements and can be readily scheduled. Since the configuration is very similar to the 2017 66 MeV experiment the beam intensity for profile measurements was chosen to be in a similar range, i.e. 1 nA to 10 nA. For the electronics, the maximum beam intensity chosen was 30 nA, as this is the highest intensity used on electronics in previous tests while still providing sensible measurements.

#### 4.2.3.2 Simulations

Given that the beam configuration was very similar to the previous 66 MeV experiment, it was decided that no beam dispersion simulations were needed in preparation for this experiment.

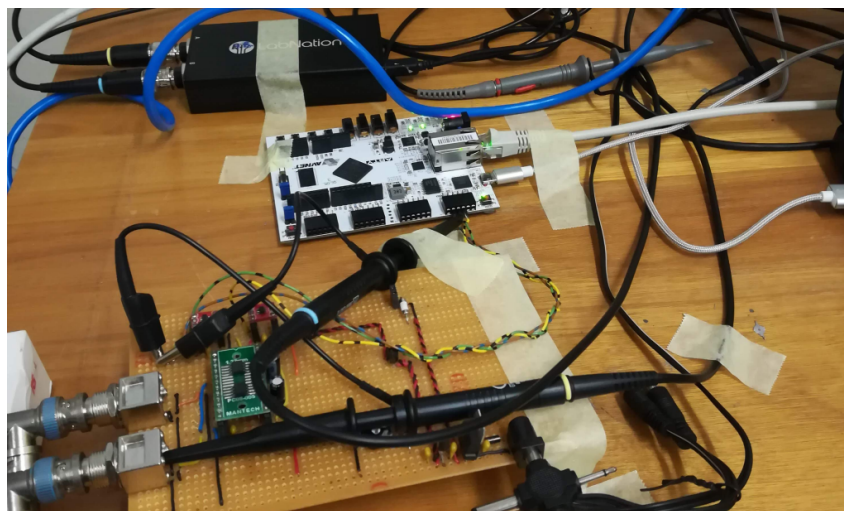


**Figure 4.46:** The new prototype BLM pulse logger using prototype signal conditioning circuitry and an Arty development board.

The results from the simulations done for the 2017 experiment would still be applicable to this experiment. In fact, the beam path is slightly longer, by 308 mm, so the uniformity of the beam is expected to be slightly better.

#### 4.2.3.3 Measurements

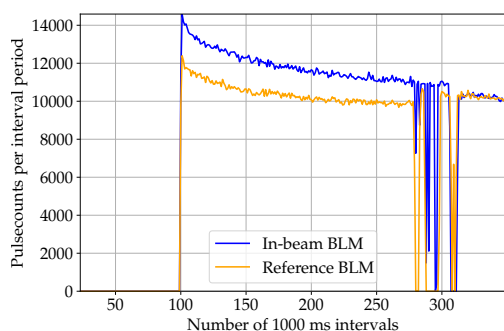
Adopting similar procedures for this experiment as with previous SEE experiments at NTV, the sequence of measurements was as follows:

- Measure BLM calibration values and noise levels.
- Determine intensity setting for profile measurements by starting with a saturated level and lowering the beam intensity until a linear region is reached.
- Perform a beam spot profile measurement in small (preferable 2 mm) steps both horizontal and vertical planes.
- Perform a wide beam profile measurement in larger (maximum 20 mm) steps in the horizontal plane.
- Monitor both BLMs continuously to measure beam drift during device exposure and detect beam anomalies.

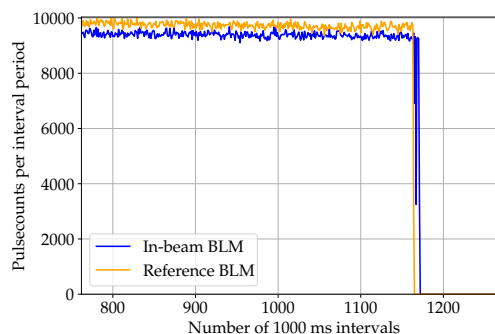
**4.2.3.3.1 Calibration of BLMs before irradiation** The operation manual [93] for the BLM devices provides a calibration procedure to ensure the correct sensitivity level. During calibration, the circuit should be tuned to output a pulse rate of roughly 10 KHz. This procedure is done for each of the device's calibration channels. After calibration, the device should be sensitive enough to generate pulses due to MIP interactions while rejecting noise effectively giving an expected spurious count rate in the order of single pulses per second. Since an approach was taken to measure the BLM signals continuously, it was possible to verify the calibration procedure and the device's noise floor.

Figure 4.47 shows the output pulse rates of the BLMs in calibration mode. It should be noted that the calibration procedure was completed the day before and that these measurements

were taken to verify the calibration values. An unexpected anomaly can be seen in Figure 4.47(a), where the pulse rates are exhibiting a non-linear decrease from an initial higher rate. At 300 seconds, the calibration channels were switched from channel A to channel B for each BLM. Figure 4.47(b) shows the calibrate mode steady-state pulse rates. It seems steady state was reached after 800 seconds. The behaviour was unexpected, but the same trend is visible in both BLM outputs, indicating that it is indeed due to a BLM start-up transient, and not due to an anomaly in the data logger. Although not shown here, the noise floor for the devices was observed to be in the range of 1 to 3 pulses per second.



(a) In-beam and reference BLM pulse rates showing decreasing transient behaviour immediately after start-up.



(b) In-beam and reference BLM pulse rates showing steady state values after roughly 800 seconds.

**Figure 4.47:** BLM calibration pulse counts showing (a) a settling period at start-up, and (b) a stable calibration count rate, for 66 MeV experiment in iTL NTV, January 2019.

**4.2.3.3.2 Determining beam intensity for profile measurement** As stated, the approach taken to establish a good intensity for profile measurement is to start with a higher beam intensity and adjust it lower until a linear region for measurement is reached. For this experiment the beam current was started at 15 nA then reduced to 10 nA, 5 nA and finally 2 nA. The the average values and ratio of in-beam BLM average value to reference BLM average value is given in Table 4.11.

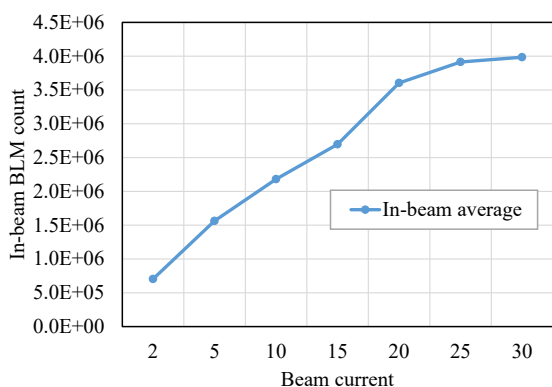
Current (nA)	In-beam average	Reference average	Ratio (In-beam/Reference)
2	$7.042 \times 10^5$	$0.461 \times 10^3$	$1.526 \times 10^3$
5	$1.640 \times 10^6$	$1.241 \times 10^3$	$1.320 \times 10^3$
5	$1.564 \times 10^6$	$1.188 \times 10^3$	$1.315 \times 10^3$
5	$1.255 \times 10^6$	$0.987 \times 10^3$	$1.271 \times 10^3$
10	$2.182 \times 10^6$	$2.162 \times 10^3$	$1.008 \times 10^3$
15	$2.697 \times 10^6$	$3.288 \times 10^3$	$0.820 \times 10^3$
20	$3.604 \times 10^6$	$4.272 \times 10^3$	$0.843 \times 10^3$
25	$3.914 \times 10^6$	$5.811 \times 10^3$	$0.673 \times 10^3$
30	$3.985 \times 10^6$	$6.358 \times 10^3$	$0.626 \times 10^3$

**Table 4.11:** Beam intensity averages and ratios for beam currents ranging from 5 nA to 30 nA for January 2019 experiment.

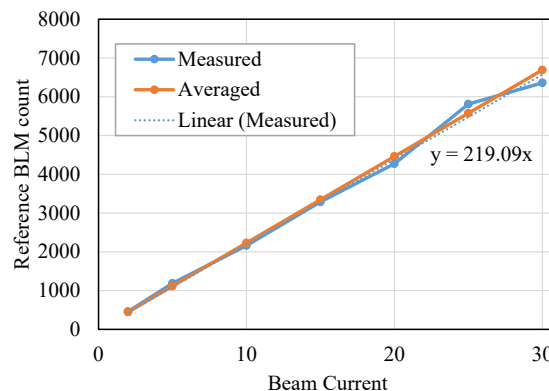
During the intensity determination steps, some insight into the relationships between the measured values and the theoretically expected beam intensities was gained. With the new DAQ option, BLM data were sampled at rates much higher than the 2 MHz previously achieved. The measurements listed in Table 4.11 showed rates up to almost 4 MHz, allowing for a broader range of the measured data to be evaluated.

The first insight gained was that the reference BLM is measuring the beam intensity at its position with a linear response. This relationship is shown in Figure 4.48(b), where a linear function was fit to the measured and averaged data.

The measured data is the time-averaged values for the reference BLM, while the ‘averaged’ dataset represents the average estimate of the true beam current. To estimate the reference count rate to beam current ratio accurately, the average ratio of all the BLM rate to beam current ratios, at each current level, is calculated and the measured rate is normalised to that average. This estimation is required since the actual beam current is not known during irradiation. Before a run, the SSC control room staff accurately sets the beam to the requested intensity before delivering the beam to the vault. However, as soon as the beam is delivered, the beam intensity is effectively controlled in an open-loop fashion, since there is no more accurate feedback to keep the beam intensity constant. Consequently, the real beam current is estimated by assuming the first few data points measured by the BLMs corresponds to the beam current delivered. The last-mentioned assumption does not always hold true, as can be seen in the variation of the average reference BLM values for the three separate 5 nA runs listed in Table 4.11.



(a) In-beam BLM average values as a function of the beam current supplied. Significant saturation of the measurement starts occurring above 15 nA.



(b) Reference BLM average values as a function of the beam current supplied. The relationship is very close to perfectly linear, as expected. Linear function fit to the measured data is shown.

**Figure 4.48:** Reference BLM to beam current over a range of currents.

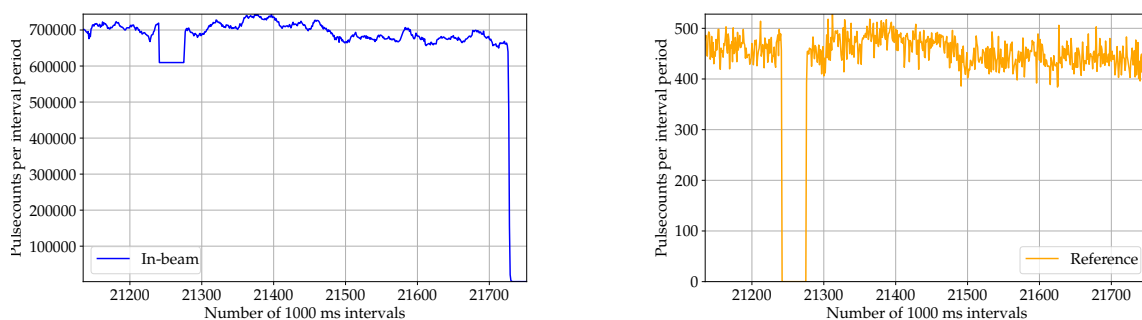
Although the linear response of the reference BLM was assumed in earlier experiments, this experiment provided a broad enough range of data that the fact could be proven. Since the response is linear, only two calibration points relating the count rate of the reference BLM to the actual beam current is needed to establish an accurate reference to normalise the in-beam profile measurements, that allows for beam intensity drift compensation to be applied. The linear response also allows for accurate monitoring of beam current drift during the exposure

of devices, allowing for accurate device exposure estimates, assuming that the beam intensity is known at the DUT.

The second insight is the implication of the non-linear response of the in-beam count rate to the increase in beam current. This response is not unexpected as it has been observed in previous experiments. Given the excellent resolution and range of the measured data, a more detailed understanding of the response is possible. The theoretical development in Section 3.3.2 predicted that the small area sensors exposed to the pulsed beam would respond in a non-linear way as the current is increased. More precisely, the response should follow the shape of two combined binomial distributions. The measured in-beam BLM rates have the same shape as the estimated curve, shown in Figure 3.9. However, the magnitudes of the two curves do not match.

The mismatch could be due to the effective sensitivity of the BLMs to detect each 66 MeV proton, coupled with the masking of successive proton strikes due to the limited bandwidth of the BLM devices, as explained in Section 3.3.2.

**4.2.3.3.3 Determining beam current intensity variation and stability before profile measurement** The graphs of Figure 4.49 are shown in linear scale to better see the stability of the beam. For the in-beam rates the range is from maximum 744 051 counts/second to minimum 649 898 counts/second, a change of  $\pm 6.754\%$  (13.5% variation). For the reference values the range is from maximum 528 counts/second to a minimum 384 counts/second, change of  $\pm 15.789\%$  (31.57% variation).



(a) In-beam BLM stability measurement showing some drift over a period of roughly 10 minutes.

(b) Reference BLM stability measurement showing significant variation and a similar drift pattern to the in-beam values over a period of roughly 10 minutes.

**Figure 4.49:** Beam intensity measurements showing beam stability for (a) the in-beam BLM only, and (b) the reference BLM only, at 2 nA for 66 MeV experiment in iTL NTV, January 2019.

Knowing the magnitude of the expected beam current drift and beam current variations, help to inform the researchers conducting an SEE experiment to make better on-the-fly decisions during testing. It is important to identify severe beam current anomalies, as they can confuse individual test results, cause unplanned damage to DUT electronics, or result in beam time being wasted. For many COTS electronics SEE experiments, the required exposure rates and levels cannot be accurately predicted. Therefore the researchers must adjust the beam

current and exposure times on-the-fly during tests, aiming for the best conditions to induce the right amount of errors. The ‘right’ amount is challenging to define, as its value varies from device to device. The required amount of errors is usually driven by three main factors namely: generating enough errors for acceptable statistical analysis of the DUT response; generating errors at a sensible rate to enable extraction of error data from the DUT; and ensuring that the DUT electronics are exposed to enough particles in the available test time while not being exposed to too many particles and being affected by TID effects.

**4.2.3.3.4 Determining the beam spot profile** Similar to previous experiments, the beam spot profile was measured by moving the in-beam BLM first horizontally, then vertically through the beam spot. This procedure was repeated after the wide beam profile was measured. Figure 4.50 shows the four measured profiles, translated so the beam spot centre corresponds to the 0 mm position.

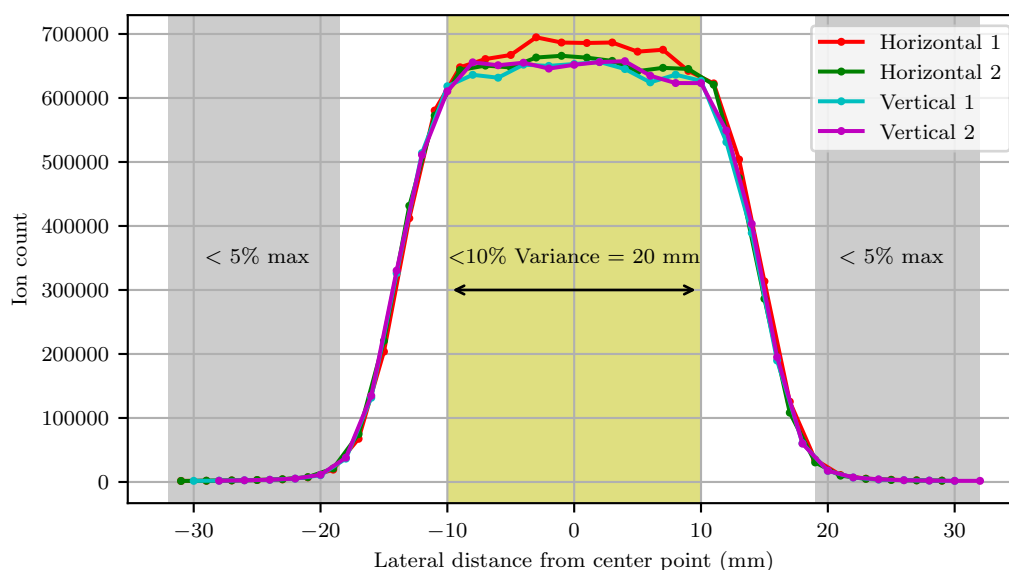


**Figure 4.50:** Combined central profile - Raw in-beam BLM values (this is true dose over spot) - 2 nA.

From the profile measurements the achieved beam spot, meeting the uniformity requirement, is 20 mm diameter. The intensity starts to drop sharply 10 mm from the beam spot centre and reaches an intensity of less than 5% of the maximum at 18 mm. The spot diameter is less than the design value, but still significantly more than the required 10 mm × 10 mm.

**4.2.3.3.5 Determining the wide beam profile and beam shadow intensity** Similar to the previous 66 MeV experiment in the NTV, the wide beam profile was measured by moving the in-beam BLM through the beam horizontally as far as possible without compromising mounted DUT electronics through unwanted exposure. The results of the wide beam profile measurement are shown in Figure 4.51.

The intensity drops to a rate of 7426 counts/second (1.21%) and 32 962 counts/second (5.37%) at 20 mm left and right of the beam spot respectively. At ± 40 mm the intensity has dropped

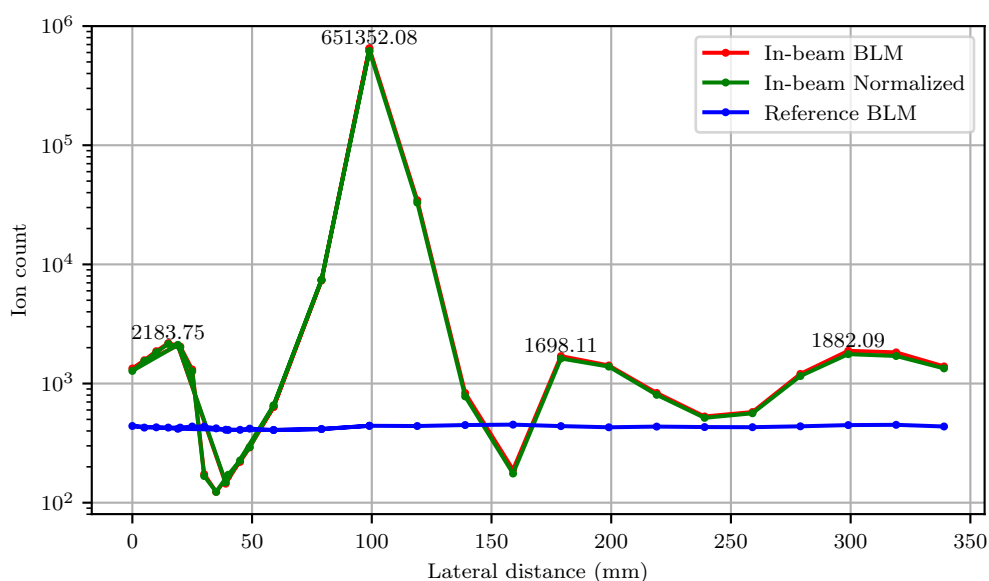


**Figure 4.51:** Wide horizontal profile - Raw in-beam BLM and reference BLM values - 2 nA.

to 655 counts/second (0.11%) and 779 counts/second (0.13%). As the distance from the centre increases, the intensity varies and rises no more than 0.35% of the centre intensity at any point. This shows that a shadow intensity achieved was 10 times better than the 3.7% achieved at the 66 MeV experiment in December 2017.

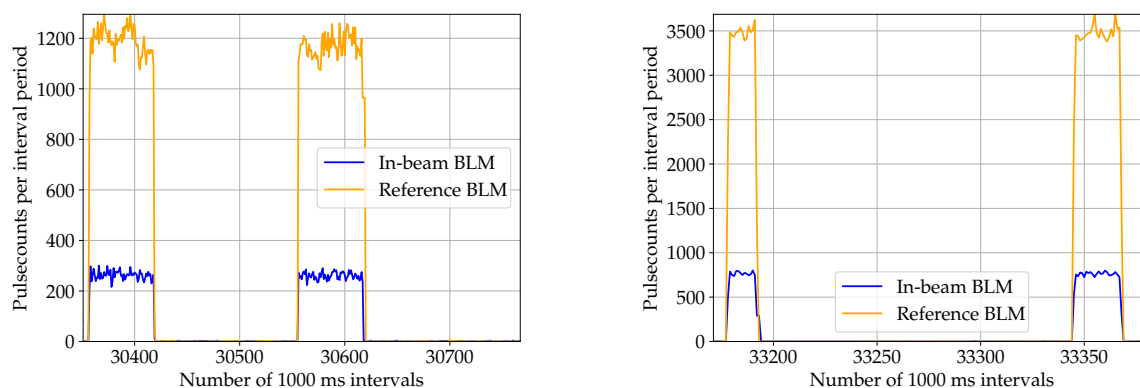
**4.2.3.3.6 Monitoring beam current drift during device exposure** Similar to the previous experiments, the quality of the delivered beam was monitored throughout the experiment. With the new DAQ prototype, more data was sampled than in the previous experiments, that allowed for a more detailed analysis of the beam quality.

The first important facet of the measurements is the amount of beam variability and beam drift present. Two example runs are shown in Figure 4.52. The variation in the beam intensity is up to  $\pm 10\%$  between samples, much better than the previous test at 200 MeV. There is, however, still a reasonable amount of drift present during exposure, as was evident at the start of the experiment and shown in Figure 4.49. The use of the reference BLM is again proven to be indispensable if accurate doses and dose rates are to be calculated. The assumed beam current received from the SSC is not adequate.

When considering the 5 nA and 15 nA runs one difference is observable compared to the 200 MeV beam, that is the beam is much more stable as the current is significantly increased. These observations suggest that for the next 200 nA configuration the option of spreading the beam more should be investigated as it would allow for a slightly higher beam current to be used during testing, which in turn would result in a more stable beam.

**4.2.3.3.7 Level of latent radiation between exposures** The high energy protons from the beam activate some of the material it interacts with, especially the brass collimators used to block most of the dispersed beam. It is important to know the level of latent radiation due to activated material, as it can also induce errors into the DUT electronics positioned in the beam



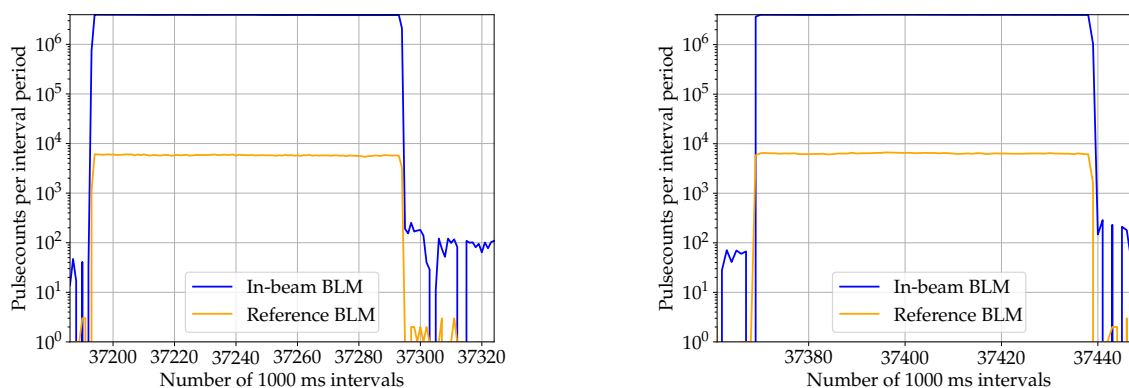


(a) Two 5 nA runs show there are some beam drift and variation present. The exposure duty cycle, of roughly 30%, for this microprocessor experiment, is also evident.

(b) Two 15 nA runs show there is some beam drift and variation present. The exposure duty cycle, of roughly 15%, is much shorter compared to the 5 nA runs.

**Figure 4.52:** Monitored beam intensity using both BLMs during device exposure.

spot while the beam is off. It also informs the researchers of the level of radiation present in the vault immediately after the beam is switched off, that in turns drive the 'cool down' time researchers should wait before entering the vault for any configuration adjustments or DUT replacements. Figures 4.53(a) and 4.53(b) shows the level of radiation immediately after beam switch off for a 25 nA and a 30 nA run.



(a) Monitored latent radiation during 25 nA run.

(b) Monitored latent radiation during 30 nA run.

**Figure 4.53:** Latent radiation level immediately after beam is switch off at the end of a device exposure.

In both cases the BLM counts are about 200 counts/second immediately after switch off, dropping to about 100 counts/second within 10 seconds. From other runs and samples it was determined that the count rate drops to about 30 counts/second after about 200 seconds, and to below 10 counts/second after about 1000 seconds.

**4.2.3.3.8 SEE testing of electronics and beam utilisation** The electronics tested was an Intel Atom processor with the details described in [102]. Only one board was available for testing.

After beam profile measurements were done, the board was placed in the beam spot and irradiated. Due to the nature of the test software and test board used, the only reliably observable radiation-induced effect during testing was SEFI events.

The approach taken was to irradiate the board until a SEFI occurred. The beam would then be switched off, and the board would be power cycled to restore functionality. The device SEFI cross-section was calculated by Malinda [102] for cache on as  $4.46 \times 10^{-10}$  and  $4.52 \times 10^{-10}$  and for cache off as  $2.40 \times 10^{-10}$  and  $4.84 \times 10^{-10}$ . Total fluence was calculated using the BLM logged data and amounted to  $5.622 \times 10^{10}$  protons/cm<sup>2</sup> for the cache on tests and  $2.825 \times 10^{10}$  protons/cm<sup>2</sup> for the cache off tests. The fluence levels were reached using different beam intensities over a total exposure time of 2896 seconds (48 minutes and 16 seconds).

The device exposure time accounts for 25.4% of the SEE experiment time of 11820 seconds (14:42 to 17:59), or 18.49% of the total experiment window. The beam utilisation is in line with previous experiments. The total time spent on beam profile measurements amounted to 84 minutes or 32.18% of the total test window time of 4 hours 21 minutes. Although a full 8 hours was scheduled for the test window, due to a faulty Faraday cup in the beamline followed by an RF trip of the SSC there was a maintenance delay of 4 hours 49 minutes in the middle of the beam profile measurements. The more significant percentage of time spent on beam profile measurements was due to the results from the previous experiments (sections 4.2.1 and 4.2.2) indicating that more thorough measurements of certain aspects of the beam and BLMs before and during beam profiling (as described in the preceding sections).

#### 4.2.3.4 Results from experiment(s)

*All the goals set for the experiment was achieved.* The beam monitoring system worked well and produced detailed data about the beam that was helpful in identifying the beam quality as well as a previously unknown transient “warm-up” response from the BLM devices. The beam spot was well formed and the beam shadow was better than in previous experiments.

*Positive* outcomes to note from the experiment are:

- The new prototype BLM pulse logger works much better than the previous DAQ solutions since it was designed to count accurately at high pulse rates.
- The BLM calibration values and noise levels were measured explicitly. The transient behaviour of the BLM device was identified, and future experimenters should note the settling time to reduce the chance of measurement error. The noise level was observed as being less than at the 200 MeV test but is still significant enough to motivate that the reference BLM should be sampled continuously.
- A detailed BLM response versus beam intensity was measured by starting with a saturated level and lowering the beam intensity until a linear region is reached. The linear region is required for accurate beam profile measurement. Through the detailed measurements, the BLM device’s response could be compared to its theoretically expected response. The shape of the response curves was fairly similar, but the magnitudes differed.
- A successful beam spot profile measurement in small (preferable 2 mm) steps both horizontal and vertical planes was performed.
- A successful wide beam profile measurement in larger (maximum 20 mm) steps in the horizontal plane was performed, showing that a beam shadow with a maximum intensity

of 0.35%, which is even better than the shadow created for the 200 MeV test.

- Both BLMs were continuously measuring beam drift during device exposure and to detect beam anomalies. The beam drift information can be used to correct dose calculations.
- The configuration created an environment in which an embedded processor could be successfully tested to identify its sensitivity to 66 MeV protons. Given the nature of the electronics tested the most prominent effect observed during testing was SEFI events.
- The BLM logs produced, indicated a total fluence of  $8.447 \times 10^{10}$  protons/cm<sup>2</sup> delivered in just over 48 minutes of exposure. Maximum flux was  $1.29 \times 10^8$  protons/cm<sup>2</sup>/s at 30 nA.

*Negative* outcomes to note from the experiment are:

- The new FPGA based DAQ unit is still only a rough prototype. Some development is required to produce an advanced prototype with all signal conditioning circuits on a single PCB.
- The disparity in magnitude of the measured beam intensity still raises a question regarding the sensitivity of the BLM to protons with energies ranging from 66 MeV to 200 MeV.
- Non-optimal utilisation of scheduled beamtime due to only one DUT available for testing. This problem can be addressed by better coordination between researchers that will allow for combined tests to be planned.

### 4.3 Results summary

*The viability of a SEE test environment at iTL has been proven.* The environment was proven to be accessible, flexible, reliable, repeatable and sustainable. After four successful experiments, one at the A-line vault, followed by three at the NTV the procedures for effective setup and testing has been refined.

The SRIM simulation approach to design and plan the configuration for a setup was proven to be adequate and accurate. By using a passive beam spreading in air technique, the A-line experiment showed the Gaussian shape of the simulated beam, and measured beam matched well, which validated the passive beam spreading in-air choice for the design.

The good match further indicated that the choice of dual-BLM dosimetry system was valid. The results proved that the BLMs produced consistent data as long as the beam intensity is well chosen for profile measurements.

Beam spot and beam shadow profiles were measured in three experiments at the NTV. The measurements showed that the beam spot had the required size and uniformity, while the created beam shadow's intensity was no more than 0.35% of the beam spot intensity.

The results proved that the followed test procedures work, not only for 66MeV protons but due to the October 2018 test opportunity, for 200MeV protons as well. Thus the test regime covered both medium and high energy protons. With passive spreader and degraders added energies from 7.7 MeV to 190 MeV were used to test SEEs in various electronic circuits.

Through the beam profile measurements, the beam's stability and drift during device exposure monitored and characterised. The in-situ reference BLM measurement is crucial to calculate the device exposure levels accurately.

With each SEE experiment, the effective time usage was calculated. Beam utilisation was optimised through adjusting the beam profile measurement processes and effective use of multiple DUTs on the positioning platform. The platform's use was validated as it allowed both the in-beam BLM and multiple DUTs to be remotely moved for profile measurements and into the beam spot for SEE testing.

By implication this test procedure and planning approach should work for any proton energy and most proton beam delivery points that iTL SSC can provide. The results also prove successful detection and monitoring of multiple types of SEEs, specifically SEUs, SET, micro-SEs, and SEFIs.

---

# CHAPTER 5

## Conclusions

---

*This chapter will consider the context, background, design and implementation of a viable SEE test environment at iTL. Conclusions are drawn based on the experience gained and results obtained from multiple SEE test experiments.*

### 5.1 Conclusion from conducted research

A new proton induced SEE test facility has been designed, implemented, and tested at iTL. The design approach and implementation of the the facility was proven to work at two different iTL delivery points i.e. the A-line vault scattering chamber and the NTV. The facility was proven at 66 MeV and 200 MeV energies with and without energy degrading elements.

The design aims, as stated in Section 3.1, were all achieved. Experiments showed that a 20 mm to 64 mm diameter beam spot with a variation in its uniformity of less than 10% could be achieved using passive beam spreading and collimation. A beam shadow, large enough to contain multiple DUTs, with a maximum intensity of less than 0.35% of the central beam intensity was achieved. Additionally, the beam spot and dosimetry calibration procedure can be done in as little as 30 minutes.

Both the beam spot and shadow characteristics were simulated using SRIM, and the beam measurements proved that the simple geometry approach is accurate and representative of the beam delivery configuration used.

The novel dosimetry system using two BLM devices for dosimetry was verified, firstly through simulation and secondly through four experiments, one in the A-line vault and three in the NTV. The dosimetry system provides an adaptable, fast, accurate and repeatable means of verifying the beam profile before SEE tests, as well as monitoring a relative proton flux during DUT exposure. Although absolute dosimetry cannot be measured until the BLM devices have been calibrated against a calibrated detector, with the theoretical derivations, the required correction factors can be applied to produce representative dosimetry values.

The procedures to apply for and effectively use beam time at iTL for SEE testing was verified and was compiled into a practical user guide for SEE researchers (refer to Appendix A). The guide is also applicable to iTL staff to assist future researchers in preparing and specifying requirements for SEE tests.

These experiments were not only used to validate the SEE test setups, but also to provide opportunity for researchers to conduct SEE research. By combining the beam forming and dosimetry experiments with SEE in electronics research, the iTL facility was made significantly more accessible to South African SEE researchers. This accessibility produced data that enabled researchers to produce five masters theses [55; 96; 95; 101; 102], two journal publications [99; 100] and at least three conference publications [27; 15; 30].

In the course of the beam delivery development experiments, the SEE facility was used by South African researchers to:

- accurately test the effectiveness of mitigation techniques applied on a CubeSat OBC;
- successfully provided a degraded energy environment for FPGA device characterisation;
- evaluate SET mitigation techniques applied in Xilinx and Microsemi FPGAs;
- recreate and observe similar device behaviour as observed with on-orbit devices;
- screened candidate spacecraft processors and imaging sensors;
- and investigate failure modes and sensitivity of an embedded Intel Atom processor.

The application of test experience at iTL and the basic understanding of SEE mechanisms in proton beams effectively assisted researchers to conduct SEE experiments with success. Enabled by this research, this facility is the first high-energy proton-induced SEE testing facility on the African continent, and in the southern hemisphere. The following subsections will discuss in more detail the conclusions drawn on different aspects of the SEE test environment.

### 5.1.1 SRIM simulation to design configuration

SRIM was used to simulate the beam distribution and energy degradation for each of the in-air experiments. It was chosen due to its simplicity both in configuration and output. Having only a layered geometry to work with, limited the complexity of components used in the beam delivery system. The simple geometry was advantageous since it forced the design of the beamforming elements to be of reasonably simple geometry.

Adding the simplifying assumption that the collimators do not contribute much to changing the uniformity of the beam spot, they can be ignored for purposes of determining if the uniformity of the beam will be good enough over the required beam spot area. Having a simple geometry, of a Havar vacuum window, beam spreader sheet, air, and degrader sheets (when applicable), made the configuration of the SRIM input simple.

The statistical nature of the interactions can cause anomalies during a simulation, so it is advised that simulations are run at least twice, using different random number seeds to ensure that the results consistent. When degraders are added, the SRIM simulation slows down significantly, and the long runtime for simulation should be planned for.

If only energy distribution is of concern, simulations of  $1 \times 10^5$  protons should be sufficient to see the general distribution at the target. However, when beam uniformity is simulated, simulations of  $1 \times 10^5$  protons produce areas in the beam spot with densities varying significantly

due to the statistical distribution. By using  $1 \times 10^6$  protons, simulations produce densities that can be averaged over a small enough area, typically  $25 \text{ mm}^2$  to  $100 \text{ mm}^2$  to produce a sufficient visual presentation of the area meeting the uniformity criteria.

Care must be taken when a SRIM simulation is configured since the graphical user interface has peculiarities. It was found to be more reliable to edit the configuration input files directly in a text editor, as fewer mistakes and unit conversion problems would occur. The strict text-based format of the output files also allows for relatively easy scripting to analyse and visualise the output data.

*The SRIM software produced accurate results with minimal effort and only a limited knowledge of nuclear transport codes. This result is useful since many students and engineers that are and would be involved SEE testing, have the same limited knowledge. The software would still be beneficial to them for basic analysis and planning of experiments.*

### 5.1.2 Dual-BLM dosimetry system

A viable SEE test environment at iTL required a unique dosimetry solution to meet the design criteria. The criterium of adaptability was the primary driver for using a dosimetry system that requires minimal mechanical setup and the least support electronics. Also, a reasonable spatial resolution was required. As dosimetry solution, two BLM devices were used in a combined configuration. One BLM was used as a remotely movable in-beam detector to measure the beam profile, while the second BLM was used as a static reference detector to monitor beam intensity during device exposure.

The BLM devices chosen provided a simple electrical interface and a sensitive area of  $7.355 \text{ mm}^2$ . The detector area was adequate for all of the beam spot size required as it allowed for a linear resolution at least  $7 \times$  better than the spot size. The BLM devices require no special environment to work effectively and could be mounted on the same positioning platform as the DUT, taking up minimal space. The reference BLM was mounted on a simple vertical stand supported by wooden struts.

These devices, and how they are used in the configuration, make the setup extraordinarily portable and adaptable to the physical limitations any of the beam delivery locations. The support electronics required in the vault consist only of a power supply unit. The signals produced by the BLMs were successfully transmitted via coaxial cable up to roughly 200 m to the various DAQ instruments used.

The concern about detector saturation was adequately analysed and theoretically characterised for the pulsed beam environment. The BLM should be operated in the linear region of its response to intensity. The beam delivery configuration geometry is such that a low enough beam intensity can be created at the beam spot to ensure that the BLM is operating in the linear region. By using two BLMs, it is easier to identify when the BLM devices are entering the linear region during beam profile measurement.

All four in-air experiments used the same two BLMs in the dual-BLM configuration to do dosimetry during DUT exposure, and to take beam profile measurements. The BLM datasheet states at least 1 MGray tolerance to TID, which implies that the same two BLM devices should last for many SEE tests.

Interfacing to the BLMs was done using iTL DAQ equipment. For the A-line, it was noted that the measurement saturated at a count rate just over 1.1 MHz. The DAQ used, was the default system used in the K600 vault, set up to do high-frequency pulse counting. Since the BLM has an effective bandwidth of up to 10 MHz, it could only have been the DAQ equipment causing the saturation. Subsequent tests at the NTV produced mixed results. For the December 2017 test, a similar DAQ system was used. The front end electronics was custom configured and set up at the NTV control room, with the data being logged using the central data logging system. This time the saturation count rate was just over 2.1 MHz. For the last two experiments at the NTV a newer DAQ front-end system from iTL was used. The newer system caused some problems to configure and operate at the required count rates, resulting in more time spent in test preparation. The incoming signal from the in-beam BLM had to be scaled down significantly ( $20\times$ ) to ensure that the DAQ count rate did not saturate. The iTL DAQ solution could not be optimally configured for use in the SEE test environment using the dual-BLM configuration.

The current author decided to develop a backup DAQ solution, and it was used, in prototype form, during the final NTV experiment in January 2019. The new system was tested to operate successfully at count rates up to 10 MHz. During the beam measurements, a slow saturating plateau was observed at around 4 MHz. However, the response shape resembles the theoretical response expected (compare Figure 3.10 with Figure 4.48(a)). The result indicates that the DAQ is not the limiting factor, but that the saturating response is due to the saturation effect of multiple protons from the same bunch in the beam impact the detector's active area. It is important to note that the value of saturation is  $2.5\times$  lower than the expected count rate from the theoretical calculations. This discrepancy can be due to two effects that were not accounted for during the theoretical calculations, the counting efficiency of the detector for high energy protons, and the bunch masking that can occur due to the beam pulse frequency being higher than the BLM bandwidth.

Fortunately, the saturation effect is mitigated in the way beam profile measurements are done. The reference BLM is not affected, as the count rate on it is usually well below 10 KHz. The effect on the in-beam BLM is mitigated by reducing the beam current to an intensity level low enough so that the BLM response can be approximated to be linear (see Figure 3.12) during profile measurements. The total particle rate at the target can be effectively calculated using the particle density at the target from SRIM calculations, the beam current supplied, and compensating for beam variance using the reference BLM measurements.

*The dual-BLM system proved to be successful in providing a means to measure and verify the beam spot profile and beam shadow profile. The same configuration also provides a means to monitor the beam stability and current drift during device exposure allowing for accurate dosimetry calculations.*

### 5.1.3 Quality and repeatability of the beamforming configuration

The SEE test environment must deliver a predictable beam distribution while allowing for short preparation times and require minimal logistic support to be sustainable. *The passive beam spreading approach, using collimators to form the beam spot and shadow area, and degrader sheet for energy degradation provided, a predictable beam distribution meeting the beam quality requirements for SEE testing.*



The first experiment in the A-line showed that the passive beam spreading using a Pb sheet produced a beam distribution that was accurately predicted using SRIM code (see Figure 4.13). By keeping the configuration simple and adding multiple standardised and available collimators, a uniform beam spot size (varying by less than 10%) and an adequately low-intensity shadow area were created for the three SEE experiments in the NTV.

Due to its uncomplicated design, setting up the beam delivery system is relatively fast. Alignment of elements are not overly critical, and accuracies to 1 mm in position are adequate. Standard tripod-based laser cross-hairs are adequate to achieve the required alignment accuracy. The configuration has been done for beam path lengths ranging from 1.4 m to 4 m.

All the collimators were available, as well as various thickness Pb sheets. The degrader sheets were cut from available larger sheets. No portable mounting rail was available, so one was manufactured using a pressed wood sheet and two aluminium pipes, supported by 3D-printed foot pieces. Similarly, stands were required that would fit the mounting rail and the 120 mm diameter, 50 mm thick brass collimator blocks. The stands were also 3D-printed and height-adjustable. The same stands and mounting rail were used for all three experiments in the NTV.

The addition of the PRaVDA bench made the configuration even more portable and easy to set up. In order to set up, the bench is positioned and aligned with the centre of the beam then levelled using water levels and laser cross-hairs. The manufactured mounting rail is placed on the bench, and the collimator stand heights are adjusted to align the collimators to the beam centre. To adjust the collimator distances from the beam spreader, they can be slid along the mounting rail and maintain alignment with the beam. The DUT positioning platform and the reference BLM are then added to the PRaVDA bench to complete the beam delivery configuration, apart from the Pb sheet.

For the A-line, a separate existing stand was used to mount the 1 mm Pb sheet. At the NTV the Pb sheets were placed in a 3D-printed sheet frame that was bolted to the gantry where the beam exited via the Havar vacuum window. Since the beam is a pencil beam before passing through the Pb sheet, only very rough alignment of the sheet is required. It has to be mounted perpendicular to the beam, and the beam can pass through any point on the sheet, as long as it is not closer than roughly 10 mm from the sheet's edges. Depending on the physical details of the beam delivery point, the Pb sheet might require a custom frame or stand to be mounted. However, the custom frame or stand can be easily 3D-printed.

The configuration was proven to be robust through using both a 66 MeV and a 200 MeV incoming proton beam at the NTV. By using the optional degrader sheets beam energies from 7.7 MeV to 190 MeV was delivered to electronics tested for SEE response. The configuration was easily adapted to the medium energy proton and high energy proton regimes, as well as to the change in beam spot size requirement (20 mm to 60 mm diameter). During the profile measurements and SEE tests, the proton intensity was adjusted producing a stable proton flux (at 66 MeV with <10% drift) at the target ranging from  $2.15 \times 10^6$  protons/cm<sup>2</sup>/s to  $1.29 \times 10^8$  protons/cm<sup>2</sup>/s.

### 5.1.4 Multiple device option using the DUT position platform

Arguably the biggest challenge for accessibility is to get a SEE test scheduled. By limiting a SEE test session to 8 hours, the same duration as the shortest schedulable SSC beam time slot, the highest probability of getting a beam time slot is ensured.

One way to reduce the time required for SEE testing is to have the option of testing more than one DUT during a session. If the DUTs are replaced manually during a test, turnaround times can be up to 90 minutes, as experienced in the first NTV experiment. The support staff and researchers are exposed to additional radiation during the manual DUT exchange, since the collimators usually have some latent secondary radiation due to being activated. It was a significant improvement to have the option to move multiple DUTs into the beam spot remotely. The nature of proton irradiation, coupled explicitly with the creation of a beam shadow area, makes it feasible to place multiple DUT on a DUT positioning platform.

Two DUT positioning platforms were manufactured in collaboration both with academia and industry. The operational requirements were specified by the author. The first platform, built by Nelson Mandela University (NMU), was designed to fit inside the A-line scattering chamber. The second platform, built by student interns at a commercial space systems company, was designed as a linear platform. Both platforms had mounting surfaces large enough to accommodate at least three boards of the size 25.4 cm × 25.4 cm as specified by [23].

*The effectiveness of using the positioning platform was demonstrated in every NTV experiment.* In the 200 MeV experiment, the platform was particularly useful to allow switching between subsystems being irradiated. This capability saved a significant amount of time since the micro-latchups require the DUT to be power cycled, after which the board preparation takes a minute or two. In this time the platform was moved to irradiate another DUT.

*The positioning platform was also proven as an essential component to measure the beam spot and shadow profile.* Since the in-beam is mounted to the same positioning platform as the DUTs, only one control interface is required for all BLM and DUT movement and positioning. The dual-purpose use of the platform saved more time since there was no need to manually switch between a beam profile measurement setup and a DUT exposure setup.

### 5.1.5 Efficient use of beam time and application for beam time

Previous ad-hoc student projects were accommodated by iTL, but such an approach is not sustainable over more extended periods. *Effective beam time utilisation was a priority goal in establishing a sustainable solution to SEE testing.* As state in the preceding paragraphs, the SEE test was limited to be completed in an 8-hour timeslot to match the minimum schedulable beam time slot. Effective beam utilisation depended on multiple aspects, some controllable, and some not. The controllable aspects included effective procedures for beam profile measurements, pre-mounting and management of multiple DUTs, and proper test planning. Uncontrollable aspects include device sensitivity and instrument, equipment, or device failure. The impact of unforeseen effects or failures can be severe. The best strategy used to minimise the time lost due to failures was to have spare equipment, instruments, and DUTs ready for replacement.

The overall beam time utilisation was improved from the first test in the NTV, where only 13.1% of the 8-hour window was active beam time on a DUT, to the second test at the NTV

using 22.53% of the test window for active beam time on a DUT. It is unlikely that the effective beam utilisation will rise much higher than 25 % to 30 %. The reason for this upper limit is the nature of the devices currently being tested. The DUTs are mainly complex processors and SPCs, that require sophisticated test software with readout procedures that often should be done while the device is being irradiated.

The beam profile measurement was effectively done in 30 minutes during the 200 MeV NTV test of October 2018. By shortening the beam profile measurement time, more time is available for DUT testing.

In 2017 and 2019, the author and collaborators applied for SEE test beam time following the same procedure as all other SSC beam time applications. Proposals were submitted to the iTL PAC and presented at the annual beam time application meeting. In 2017 the three 8-hour shifts applied for were granted, and in 2019 another four 8-hour shifts were granted. The successful granting of test time shows that the international PAC and iTL management believe the research conducted and the continued improvement of the SEE test environment is worthwhile.

## 5.2 Limitations

The SEE test environment developed at iTL has limitations. As discussed in the introduction, this development of this SEE test capability had no official budget, except for a few thousand rands for basic research material. The nature of the accelerator environment is that any modifications to the beamline are usually costly. As such, the SEE environment was developed using the available infrastructure at iTL, with some minor relatively inexpensive additions to improve the options available for creating an adaptable beam delivery system. With no official budget, no expensive state of the art dosimetry system could be acquired, neither could a dedicated permanent test environment be built. The following paragraphs will discuss the limitations of the design, implementation, and procedures as applied to the SEE test environment.

The adaptability of the setup is limited to an area that can provide a beam path of at least 1.4 m when using 66 MeV protons and roughly 2 m when using 200 MeV protons. These lengths are not absolute minimums, but working with shorter distances will either severely limit the maximum uniform spot size achievable, or the maximum energy deliverable to the DUT. It is a physical limitation due to the amount of beam spread a sheet of material can cause. In areas with less than 2 m space is used, the PRaVDA bench will not fit in the space. Of course, a custom setup with a custom mounted rail can then be used, but it will incur costs and require significant labour time to manufacture and install.

The effective measurement range of the BLM devices is limited to the bandwidth of the device. Although procedures were developed to operate the BLM in an acceptable range, they are limited in their application scope. Beam intensity anomalies were observed in some measurements (refer to the spikes in intensity in Figure 4.27). With a limit on the beam intensity the BLM can be used at, some beam anomalies might not be observable.

The sensitivity of the BLM devices to medium and high energy protons are still unknown. A dedicated calibration measurement is required to establish the sensitivity of the BLM. An opportunity for this calibration against a small Faraday cup, as part of an SEE test, was scheduled

for December 2019. However, due to power grid interruptions experienced in South Africa during the first two week of December, iTL could not operate at that time, and the test slot was postponed to the end of January 2020.

The current DAQ solution for the BLM signals is not sustainable. The typical instruments used at iTL is not well suited for the high pulse rates generated by the BLM devices in this application. The FPGA based solution developed by the author provides a way to accurately sample the BLM signals up to the maximum BLM bandwidth of 10 MHz. The DAQ solution needs to be further developed into a more robust advanced prototype.

The energy profile of the beam at the target has not been verified through measurement. Although the exact energy distribution is unknown, it becomes only important when the proton energy is lowered to the point where direct proton ionisation starts to contribute significantly to the SEE rates. When using medium energy protons (above 20 MeV) and high energy protons, the LET of protons in silicon is relatively constant throughout the thickness of a DUT. Relatively small changes in energy (up to a couple of MeV) should not affect the device response appreciably. If lower energy proton tests are to be done more regularly, some energy distribution measurement should be done for verification.

The simplified model used for the SRIM simulations cannot account for complex geometry beam interactions. The way the beam is effected by the inner edges of the collimators is not modelled. From the literature on proton therapy beams, some intensity “horns” should be expected along the collimator edge. Even with some intensity increase on the edge of the beam spot, the effect on the testing is limited. Usually, the beam spot is chosen to be reasonably larger than the active silicon area (or die size) of the DUT. Therefore, the higher intensity “horns” would fall outside the die area.

### 5.3 Future work

Based on literature summarised in chapter 2, observations during the experiments described in chapter 4, as well as feedback received from the iTL PAC, there is a large scope for future development and research. A selection of feasible short and medium term options are:

- *Energy sensitivity and detection efficiency characterisation of the BLM devices for energies from 5 MeV to 200 MeV protons.* If the detector efficiency is known for a particular energy, accurate dose to target DUTs can be directly measured instead of being deduced from indirect relative measurements. The first attempt to characterise the BLM was planned for December 2019, and will most likely be conducted during the next SEE test opportunity in January 2020.
- *Automated system for changing degrader sheets.* The manual change of degrader sheets exposes staff to unnecessary radiation. An automated sheet changer was developed by an undergraduate student and the prototype delivered in December 2019. The automated sheet changer is remotely controllable via Ethernet and has no semiconductor-based sensors, making it extremely robust to radiation-induced damage. It is planned to use the prototype in the next SEE test scheduled for January 2020.
- *Automated process for beam profile measurement.* Currently, the positioning platform can only be controlled in an open-loop mode since it has no position feedback sensors. Pos-

sible solutions exist in stepper motor drivers than can control and detect stepper motor slippage. The drawback of these drivers is that they must be installed relatively close to the positioning platform, roughly 2 m from it, to allow the drivers to be shielded during testing. Other non-semiconductor sensing option could also be explored to provide position feedback. Combined with the position feedback, software should be developed to conduct an automated beam profile measurement. It should allow for identical measurement time intervals at each BLM position that would simplify beam shape analysis significantly. Currently, the positioning platform software and BLM pulse logging software are two separate systems, which should be combined to allow for accurate correlated logging of beam intensity measurements with BLM position measurements. Real-time feedback of the beam shape will allow researchers to respond immediately and correct anomalies in the beam profile. The combined solution should be integrated into the existing iTL data capturing infrastructure to centralise maintenance of the system.

- *Expanding test capability at iTL to include proton-beam based testing for direct ionising effects.* If the SSC is configured for lower energy proton beam delivery (less than 66 MeV) then direct proton-induced ionising effects can be investigated by degrading the beam using the same degrading sheets used in the current SEE test configurations. Lower initial energy will reduce the energy spread significantly allowing for adequate beam conditions to differentiate between the contributions of direct ionisation and indirect ionisation induced errors.
- *Expanding test capability at iTL to include neutron beam based testing.* iTL already has the capability to produce high quality monoenergetic neutron beams [103]. Using the monoenergetic beams could provide more research opportunities regarding RHA issues with COTS electronics for space applications.
- *Expanding test capability at iTL to include heavy-ion beam based testing.* iTL can produce a range of heavy-ion beams, as discussed in Section 2.3.2. Currently, the logistics of creating ion beams, other than protons, for experiments lasting for one to two 8-hour shifts are undesirable. However, new developments at iTL might significantly change the dynamics of scheduling ion beams at iTL. A new 70 MeV cyclotron has been ordered and is to be installed at iTL over the next three years [54]. The cyclotron will provide proton beams for medical isotope production that will free up a significant amount of beam time on the K=200 SSC. Due to more nuclear research opportunities, it is expected that different ion beams will be generated more regularly. Some of these beams can afford the opportunity to conduct heavy-ion based SEE research at iTL.
- *Investigate and monitor the background radiation environment at iTL for proton and neutron exposure.* Due to the production of neutrons when using high energy proton beams for SEE testing [104], the background radiation outside the beam spot area needs to be investigated further to include the characterisation of the neutron field specifically.
- *Absolute calibration of BLM against a calibrated ion chamber or Faraday cup.* Since the BLMs saturates at higher rates there is still some uncertainty to the absolute accuracy of the devices. A comparison of the BLM measurements against a calibrated beam monitor device should be made over a range of energies and fluences.

# APPENDICES

---

# APPENDIX A

## iTL SEE Test Guide

---

The scope of this guide is to assist researchers, who would like to perform proton based Single-Event Effect (SEE) testing on electronics using the facilities available at iThemba LABS (iTL). The document covers information regarding location preparation for tests and operational details at different locations. All activities related to SEE tests should be recorded to serve as a reference for future research.

### A.1 iThemba LABS application for beam time

As with most large accelerator facilities, iTL beam application process is mainly governed using a Programme Advisory Committee (PAC) approach. As of 2017, PAC meetings are held once a year to evaluate proposed experiments and beamtime requests. Application for beamtime via the PAC should be done only after consultation with iTL staff as an iTL liaison is required. Beamtime might have been allocated to SEE testing for the period in question from previous PAC applications. SEE tests should be planned and applied for at least a year in advance to have the best chance of success.

### A.2 iThemba LABS liaisons as of January 2020

Beam scheduling:

- Matthis Wiedeking - HOD Sub-atomic physics, beam schedule manager

A-line, D-Line, S-line vaults

- Ricky Smit - Researcher
- Retief Neveling - Researcher

B-Line (Proton line for Radiation Biophysics - to be commissioned in 2020)

- Evan de Kock - Researcher
- Julyan Symonds - Researcher

- Jaime Nieto Camero - Researcher

### A.3 Physical / Mechanical Set-up

The physical set-up will differ slightly depending on the vault to be used for SEE testing. The common elements of the set-up as well as the changes for some locations are detailed in the following sections.

#### A.3.1 Test setup and common elements

The test design aims to have a set-up that is as uncomplicated as possible, while maintaining the required test accuracy. The baseline accuracy requirements are based on the following standards:

- JEDEC Standard JESD 234 - 2013 [67]
- ESCC Basic Specification No. 25100, issue 2 of 2014 [23]

The design approach should be adaptable to most of iTL beam delivery points with minimal physical modifications.

##### A.3.1.1 Proton beam energy selection

It is assumed that the proton beam is delivered to a test location by the accelerator operators. The beam energy is pre-determined through the beamtime application process and in consultation with iTL staff. Up to 2020, the proton energy most common available was 66 MeV. However, proton beams with particle energies of up to 200 MeV are possible.

The particular energy required for a SEE test is dependent on the type of SEE to be observed as well as the type of components tested. It is recommended that research into the expected response of the DUT is conducted before a beam energy is selected. The design allows for degrading of the delivered beam, and the highest required energy should be selected as the delivered beam energy.

##### A.3.1.2 Conceptual design overview

Figure A.1 shows the elements present in the default SEE test configuration.

1. HAVAR vacuum exit window
2. Air gap to spreader sheet
3. Beam spreader sheet
4. Air gap to DUT
5. Collimators
6. Degradation plate
7. DUT positioning platform with DUTs and in-beam BLM
8. Current reference BLM



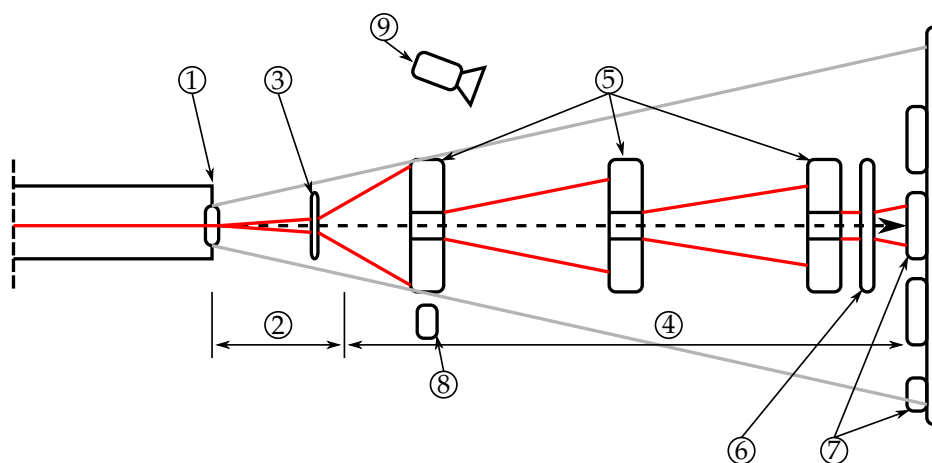


**Figure A.1:** Conceptual test set-up diagram. Set-up seen from above.

### 9. IP/CCTV camera

The elements shown in Figure A.1 has the following definitions, descriptions and requirements:

1. The beam exits through a vacuum window, typically made of 25  $\mu\text{m}$  HAVAR. A window will either be in place, be available, or can be manufactured to install for the specific beam end.
2. The air gap to the spreader sheet is dependent on the vault used but can range from 50 mm up to 1 m.
3. The beam spreader sheet is made from Pb. It should be easily removable if the alignment of the pencil-beam is required prior to the SEE test. The sheet should be positioned as close as feasible to the vacuum window while still allowing the first collimator to be placed relatively close after the spreader sheet. The thickness of the sheet is determined by the beam spot size required, the beam energy, and the physical space available at the location.
4. The minimum air gap to the DUT is determined using SRIM. A more detailed discussion on this simulation is given in section A.3.1.3.
5. The collimators are used to provide a beam spot and beam shadow (around the beam spot area). The distance of the collimators from the spreader sheet (or exit window), and between collimators, should be calculated using the python application available from A. Barnard for that purpose. The python application implements the method discussed in section 3.5.2.
6. A set of various thickness degrader sheets is available, that is used to degrade the beam energy. SRIM software should be used to determine the total thickness of the sheets required for each degraded energy. The software will also indicate the expected energy spread, as well as spatial spread, introduced by the degrader. See section 4.2.1.2 for an example of this method applied. As of December 2019, a prototype automated sheet changer is available that should be commissioned in 2020.

7. The DUT positioning platform is used to hold multiple DUTs and one BLM. It can be remotely operated. All DUT and BLM positions should be calibrated prior to testing. The central beam profile should be measured using the BLM on the positioning platform, at the start of an SEE test session.
8. The current reference BLM is used to monitor the relative beam current during exposure. It should be calibrated using the beam current measurement at the start of the profile measuring procedure and can be verified using the beam current measurement immediately following profile measurement. Beam current measurements should be provided by accelerator operators.
9. The IP/CCTV camera is used to visually verify that the DUT positioning platform moves as expected between different device exposures.

### A.3.1.3 Calculating DUT distance from vacuum window

Depending on the beam energy and device sensitive area, the minimum required distance to the DUT must be calculated. To do the calculation, the SRIM software simulation package should be used. A base SRIM configuration file is given in Appendix B. The layers in the SRIM configuration file are:

- HAVAR - usually  $25\mu\text{m}$
- Air gap to spreader sheet - depends on vault, should be measured.
- Pb spreader - 1mm
- Air gap to DUT from spreader - depends on vault, should be measured.

The process to calculate distance consists of the following steps:

1. Choose a convenient air gap to DUT, taking physical space in vault into account.
  - For A-line on moveable arms this distance is about 1.4m.
  - For Neutron Therapy vault this distance can be up to 3m.
2. Set up SRIM with the given and chosen layers' thickness.
3. Simulate at least  $1 \times 10^6$  particles at the intended energy. The simulation should take about 3 hrs on 3 GHz laptop computer (SRIM-2013 executes single threaded).
4. Use analysis software like SSSM ([http://www.ujfi.fei.stuba.sk/srim\\_support/SRIM\\_support.zip](http://www.ujfi.fei.stuba.sk/srim_support/SRIM_support.zip)) or a python script available from A. Barnard ([srim\\_transmit\\_plot\\_contour.py](#)) to:
  - Verify that beam uniformity over sensitive chip area is at the required level, typically  $<10\%$ .
  - If uniformity requirement is not met, try adjusting one of the following parameters until analysis yields acceptable results:
    - Increase air gap to DUT if possible, which will only reduce the flux at the DUT.
    - Increase thickness of Pb scattering disc, which will decrease the beam energy and flux at the DUT.

Once the distance is calculated, set up the DUT positioning platform to the required distance. If the exact distance cannot be achieved during the setup, measure the actual set-up distance for use in the post-test analysis.

#### A.3.1.4 Calculating degrader thickness required

Use the method proposed by Gottschalk [92] to calculate degrader thickness required. A set of degraders (100 mm x 100 mm square), with the following thicknesses are available:

- 2 mm, 3 mm, 6 mm, 8 mm, 10 mm, 12 mm, 30 mm

If degraders of the required thickness are not available, either prepare degraders or liaise with iTL staff to prepare the required degrader sheets. Typically Poly(methyl methacrylate), also known as Plexiglass or Perspex, with composition  $(C_5O_2H_8)_n$  is used as the degrader material.

#### A.3.1.5 Calculating collimator set-up distances

The collimators are used to create a beam spot as well as a beam shadow area. The beam spot should cover the DUT sensitive area with some margin (at least 5 mm). The beam shadow should cover the DUTs mounted on the DUT positioning platform so that they are mostly protected from the beam while not being tested. Use the python script available from A. Barnard ([colcalculator.py](#)) to get an optimal collimator spacing.

#### A.3.1.6 Positioning the current reference BLM

The current reference BLM is in a fixed position during SEE testing. It should be positioned to give a reading of at least 250 counts/second while the calibration BLM reading is below the saturated level in the beam center ( $< 8 \times 10^5$  counts/second).

#### A.3.1.7 Alignment

The best alignment method depends on the beam delivery point that will be used for the SEE tests. Photographs of the final set-up should be taken for reporting and post-test analysis.

**A.3.1.7.1 A-line** If the A-line is used, the ruby target with ladder should be used to verify beam alignment prior to starting the test. In this case, both the DUT positioning platform, as well as the Pb spreader is mounted on a rotating arm and moved perpendicular to the beam. After alignment is confirmed the arms can be rotated back into the beam. The rest of the mechanical set-up should preferably be aligned, using a laser level or similar tool, with the ruby and beam pipe.

**A.3.1.7.2 Neutron therapy vault** If the neutron therapy vault is used than the reference laser crosshairs in the vault can be used to aid alignment.

### A.3.2 Preparing the A-line vault

A-line vault has the following characteristics to keep in mind before testing:

- There are two movable arms to assist in moving DUT positioning platform out of beam while aligning the beam.
- To move the arms of the scattering chamber, the arm controls in the data room must be used. Pre-check all relevant position settings prior to testing.
- Maximum distance DUT positioning platform can be placed from the vacuum window is approximately 1.4m.
- Vacuum windows are available and must be fitted to beam end.
- Vacuum pumps and needed pipes must also be fitted. These pumps need to be manually operated. The procedure for pumping down the pumps should be checked with iTL vacuum system technicians. Ample preparation time for vacuum system modifications should be allowed.
- Stands for the Pb spreader sheet, current reference BLM, and the collimators are available and should be fitted to the arms and platform.
- The DUT positioning platform has mounting holes designed to fit on the moveable arm.
- Previous beam profile results for an A-line set-up is presented in section 4.1.2.

### A.3.3 Preparing the N-line vault

N-line vault is non-operational at the time the current version of the document was created.

### A.3.4 Preparing the Proton therapy vault

The information in this section is given as a reference on how to approach testing in the new B-line (to be commissioned in 2020) since the PTV was decommissioned at the end of 2019. The new B-line will be similar in design to the old PTV line.

For a complete description of the PTV beam delivery system, the document by E.A. de Kock, "Specification of the proton treatment nozzle in vault BG1 at iThemba LABS" (2007) should be consulted. The suggested changes to the default beam delivery set-up are:

- The MWIC immediately following the vacuum window is removed.
- The beam position control for the Y-Z magnets is removed.
- The 0.5mm Pb scattering disc is replaced with the 1 mm Pb spreading sheet.
- The carbon wedges are kept in the fully open position.
- A beam blocker is placed at the wall before entering the final beam delivery section.
- The rail adapter is placed on the rails between the scattering disc and the occluding ring assembly.

- DUT positioning platform is fitted to the rail adapter in front of the occluding ring assembly.
- The collimator stands are fitted to the rail adapter.
- The current reference BLM is fitted to the rail adapter using the offset extension.
- The IP camera is fitted using the camera adapter.

These changes are suggestions as no validating SEE test has been performed at the PTV up to the time this document was created.

### **A.3.5 Preparing the Neutron therapy vault**

The information in this section is given as a reference on how to approach testing in the D-line since the NTV was decommissioned at the end of 2019. The environment is similar, except for the therapy components that were present in the NTV.

The specific changes to the default beam delivery set-up are:

- The bending magnet is disconnected by accelerator control.
- Multiple options are available for mounting the rail adapter:
  - on the patient wooden bench, which is moved in-line and as close as possible to beam exit point. Dec 2017 SEE tests.
  - on the PRaVDA support structure. Oct 2018 , Jan 2019 SEE tests.
- DUT positioning platform is fitted at the end of the rail adapter.
- The collimator stands are fitted to the rail adapter.
- The current reference BLM is fitted to the rail adapter using the offset extension.
- The IP/CCTV camera is fitted using the camera adapter on tripod.
- Previous beam profile results and SEE test information for a NTV set-up is presented in sections 4.2.1.3, 4.2.2.3, and 4.2.3.3.

### **A.3.6 Preparing the D-line vault**

In November 2019 the D-line was considered as location for an SEE test. The following preparations and suggestions to modify the beam delivery system are:

- Remove any target used for neutron beam generation.
- Disconnect the final bending magnet, allowing the proton beam to continue into the D-line vault and not be diverted to the beam dump.
- Fit the vacuum exit window to the beamline end.
- Use the 1 mm beam spreader sheet on a custom stand (to be manufactured).

- Use the PRaVDA bench as structural support for the rail adapter.
- All the beamline elements following the beam spreader sheet are fitted to the rail adapter, similar to the NTV configuration. These elements include: Four collimators, reference BLM, and DUT positioning platform with mounted in-beam BLM and DUTs.
- The IP/CCTV camera is fitted using the camera adapter on a tripod.

These changes are suggestions as no validating SEE test has been performed at the PTV up to the time this document was created.

### A.3.7 Preparing the S-line vault

In November 2019 the S-line was considered as location for an SEE test. The following preparations and suggestions to modify the beam delivery system are:

- Remove any targets and detectors in the beamline upstream from the spectrometer.
- Move the spectrometer to a position perpendicular to the beamline.
- Add a vacuum window to the beamline end (to be manufactured).
- Use the 1 mm beam spreader sheet on a custom stand (to be manufactured).
- Use the PRaVDA bench as structural support for the rail adapter.
- All the beamline elements following the beam spreader sheet are fitted to the rail adapter, similar to the NTV configuration. These elements include: Four collimators, reference BLM, and DUT positioning platform with mounted in-beam BLM and DUTs.
- The IP/CCTV camera is fitted using the camera adapter on a tripod.

These changes are suggestions as no validating SEE test has been performed at the PTV up to the time this document was created.

## A.4 Electrical/Communication set-up

This section describes the electrical set-up for all the support electronics, communication systems and cameras.

### A.4.1 Power supply

Power mains are available in all vaults. Clean power should be used where needed for instrumentation or measuring equipment. Power supplies for the Ethernet switch, USB interface board, IP/CCTV camera and DUT positioning platform are available and should be used. It is recommended that at least one backup of each power supply is available.

#### A.4.2 Communication / Data interfaces

It is recommended that all experiment data be placed on an Ethernet interface and connect via the Ethernet switch to a host PC/Laptop in the control/data room/area. It is recommended that at least one Ethernet switch backup is available.

#### A.4.3 Beam Line Monitors

Before using the BLM devices, they should be calibrated as per the user manual instructions. The manual can be found online at <http://www.bergoz.com/en/blm>. Additionally, the devices should be allowed to stabilise after switching on power (see section 4.2.3.3 for more details).

The set-up of the cabling should be organised in consultation with iTL staff well in advance of the test.

Depending on the vault used, the coaxial data cables are set up differently:

- When using the A-line, the BLMs can be connected to coaxial data cables via a patch panel in the vault and the data room, to the K600 logging systems maintained by iTL. If suitable logging equipment is available, it can be connected to the signals in the data room.
- When using the Neutron Therapy vault, cables must be laid from the vault to the vault control room. This distance is about 55-60 meters. From the control room signals can be connected to logging equipment.
- B-line and D-line connections should be similar to A-line.
- S-line connections can be made directly to K600 logging systems as they are in the same vault.

On receiving BLM data from iTL, users should check whether the BLM rates are given as raw count rates or if they have been converted to a more convenient unit, e.g. per  $cm^2$ . If no conversion was done the active BLM area can be assumed to be  $7.34\text{ mm}^2$  for conversion calculations.

#### A.4.4 DUT positioning platform and Camera

There are two DUT positioning platform options, a circular rotating positioning platform developed by NMU researchers, and a linear positioning platform developed by Space Advisory Company. Software for remote control of the latter is available from A. Barnard.

The IP-camera should be mounted on a tripod as far upstream as possible. This positioning will minimise scattered radiation exposure to the camera. Software for the camera is bundled with the linear positioning platform system. Alternatively, a CCTV camera with an analogue monitor can be used. For the latter, an extra coaxial signal cable will be required.

### **A.4.5 USB devices via Raspberry Pi**

A Raspberry Pi Single Board Computer is available that is connected to the Ethernet network. The RPi runs Raspbian with *VirtualHere server* and *VirtualHere client* that supports virtualisation of USB interfaces.



---

# APPENDIX B

## Example SRIM Configuration File - TRIM.IN

---

```

==> SRIM-2013.00 This file controls TRIM Calculations.
Ion: Z1 , M1, Energy (keV), Angle,Number,Bragg Corr,AutoSave Number.
    1  1.008      66000      0 999999      1  10000
Cascades(1=No;2=Full;3=Sputt;4-5=Ions;6-7=Neutrons), Random Number Seed, Reminders
                                1                                0      0
Diskfiles (0=no,1=yes): Ranges, Backscatt, Transmit, Sputtered, Collisions(1=Ion;2=
    Ion+Recoils), Special EXYZ.txt file
                                0      1      1      1      0
                                                0

Target material : Number of Elements & Layers
"H (66000)_ITL_NV_3135_Dec2019      "      17      4
PlotType (0-5); Plot Depths: Xmin, Xmax(Ang.) [=0 0 for Viewing Full Target]
    0      0      3.376025E+10

Target Elements:   Z   Mass (amu)
Atom 1 = C =      6  12.011
Atom 2 = Cr =     24  51.996
Atom 3 = Mn =     25  54.938
Atom 4 = Fe =     26  55.847
Atom 5 = Co =     27  58.933
Atom 6 = Ni =     28   58.69
Atom 7 = Mo =     42  95.94
Atom 8 = W =      74 183.85
Atom 9 = C =      6  12.011
Atom 10 = O =     8  15.999
Atom 11 = N =     7  14.007
Atom 12 = Ar =           18  39.948
Atom 13 = Pb =           82 207.19
Atom 14 = C =     6  12.011
Atom 15 = O =     8  15.999

```

```

Atom 16 = N =          7  14.007
Atom 17 = Ar =          18  39.948
Layer   Layer Name /           Width Density      C(6)  Cr(24)  Mn(25)  Fe(26)
      Co(27) Ni(28) Mo(42)  W(74)   C(6)   O(8)   N(7)  Ar(18)  Pb(82)  C(6)
      O(8)   N(7)  Ar(18)
Numb.   Description           (Ang) (g/cm3)   Stoich  Stoich  Stoich  Stoich
      Stoich Stoich Stoich  Stoich  Stoich  Stoich  Stoich  Stoich  Stoich  Stoich
      Stoich Stoich Stoich
1       "Havar (ICRU-470)"      250000  8.3 .009648 .222858 .016874 .181139
      .417828 .128336 .014494 .008824      0      0      0      0      0      0
      0      0      0      0
2       "Air, Dry (ICRU-104)"    2400000000 .00120484      0      0
      0      0      0      0      0      0 .00015 .210756 .784423 .004671
      0      0      0      0      0
3       "Pb"                    10000000 11.3437      0      0      0      0
      0      0      0      0      0      0      0      1      0      0
      0      0
4       "Air, Dry (ICRU-104)"    25639999389.6484 .00120484      0      0
      0      0      0      0      0      0      0      0      0      0
      0 .000124 .231781 .755268 .012827
0 Target layer phases (0=Solid, 1=Gas)
0 1 0 1
Target Compound Corrections (Bragg)
1 1 1 1
Individual target atom displacement energies (eV)
      28      25      25      25      25      25      25      25      28      28
      28      5      25      28      28      28      5
Individual target atom lattice binding energies (eV)
      3      3      3      3      3      3      3      3      3      3
      3      1      3      3      3      3      1
Individual target atom surface binding energies (eV)
      7.41      4.12      2.98      4.34      4.43      4.46      6.83      8.68      7.41      2
      2      2      2.03      7.41      2      2      2
Stopping Power Version (1=2011, 0=2011)
0

```

---

## References

---

- [1] Clark, J., Koopmans, C., Hof, B., Knee, P., Lieshout, R., Simmonds, P. and Wokke, F.: Assessing the full effects of public investment in space. *Space Policy*, vol. 30, no. 3, pp. 121–134, aug 2014. ISSN 0265-9646.  
Available at: <https://www.sciencedirect.com/science/article/pii/S0265964614000071> 1
- [2] Murphy, T.: 40 Years After the First Cell Phone Call: Who Is Inventing Tomorrow's Future? *IEEE Consumer Electronics Magazine*, vol. 2, no. 4, pp. 44–46, oct 2013. ISSN 2162-2248.  
Available at: <http://ieeexplore.ieee.org/document/6633068/> 1.1.1
- [3] Stern, S.A.: THE LOW-COST TICKET TO SPACE. *Scientific American*, vol. 308, no. 4, pp. 68–73, 2013.  
Available at: <https://www.jstor.org/stable/pdf/26018069.pdf?refreqid=excelsior%3A96ebc3b0cd54ed69cb70ad8228bf1608> 1.1.1
- [4] Messier, D.: Spaceflight, NanoRacks Team Up on CubeSat Launches. 2014.  
Available at: <http://www.parabolicarc.com/2014/01/09/spaceflight-nanoracks-team-cubesat-launches/> 1.1.1
- [5] Ryan, K.J.: Elon Musk Made Space More Affordable. These Entrepreneurs Want to Make It a Trillion-Dollar Industry. 2018.  
Available at: <https://www.inc.com/kevin-j-ryan/space-travel-trillion-dollar-industry-future-of-everything.html> 1.1.1
- [6] Mabrouk, E.: What are SmallSats and CubeSats? 2015.  
Available at: <https://www.nasa.gov/content/what-are-smallsats-and-cubesats> 1.1.1
- [7] Heidt, H., Puig-Suari, J., Moore, A., Nakasuka, S. and Twiggs, R.: CubeSat: A New Generation of Picosatellite for Education and Industry Low-Cost Space Experimentation. In: *AIAA/USU Conference on Small Satellites*. aug 2000.  
Available at: <https://digitalcommons.usu.edu/smallsat/2000/All2000/32> 1.1.1
- [8] Swartwout, M.: CubeSat Database. 2018.  
Available at: <https://sites.google.com/a/slu.edu/swartwout/home/cubesat-database> 1.1.1, 1.1.1

- [9] Swartwout, M.: Cheaper by the dozen: The avalanche of rideshares in the 21st century. In: *IEEE Aerospace Conference Proceedings*, pp. 1–12. IEEE, mar 2013. ISBN 9781467318112. ISSN 1095323X. Available at: <http://ieeexplore.ieee.org/document/6497182/> 1.1.1
- [10] Klofas, B.: CubeSat Communications Table version 16. Tech. Rep., Private, 2018. Available at: <https://www.klofas.com/comm-table/table.pdf> 1.1.1
- [11] Lee, S., Hutputanasin, A., Toorian, A., Lan, W., Munacata, R., Carnahan, J., Pignatelli, D. and Mehrparvar, A.: CubeSat Design Specification Rev. 13. Tech. Rep., Cal Poly SLO, 2014. Available at: <https://static1.squarespace.com/static/5418c831e4b0fa4ecac1bacd/t/56e9b62337013b6c063a655a/1458157095454/cds{ }rev13{ }final2.pdf> 1.1.1
- [12] ISIS-Innovative Solutions In Space | The nanosatellite specialist. 2018. Available at: <https://www.isispace.nl/> 1.1.1
- [13] NASA: Edison Demonstration of Smallsat Networks. Tech. Rep., National Aeronautics and Space Administration, 2015. Available at: <https://www.nasa.gov/sites/default/files/atoms/files/edsn{ }fact{ }sheet{ }02nov2015.pdf> 1.1.1, 1.1
- [14] Reddell, B.D., Bailey, C.R., O'Neill, P.M., Nguyen, K.V., Wheeler, S.A., Gaza, R., Patel, C., Cooper, J., Kalb, T., Beach, E. and Mason, L.: Compendium of single event effects test results for commercial-off-the-shelf and standard electronics for low earth orbit and deep space applications. In: *IEEE Radiation Effects Data Workshop*, vol. 2017-July. Institute of Electrical and Electronics Engineers Inc., nov 2017. ISBN 9781509046478. 1.1.2, 2.4.1, 2.6.8
- [15] Barnard, A. and Nwosa, C.: COTS Based On-Board-Computer on South Africa's Sumbandilasat: A Radiation and In-Orbit Performance Analysis. In: *2011 IEEE Radiation Effects Data Workshop*, pp. 1–4. IEEE, jul 2010. ISBN 978-1-4577-1281-4. ISSN 2154-0519. Available at: <http://ieeexplore.ieee.org/lpdocs/epic03/wrapper.htm?arnumber=6062529> 1.1.2, 1.2, 1.2, 5, 2.1.1, 5.1
- [16] Manjoo, K. and Magagula, G.: SUMBANDILASAT-LEADING THE WAY FOR FUTURE SATELLITE PROGRAMMES. In: *62nd International Astronautical Congress*, 1. Cape Town, 2011. Available at: <https://iafastro.directory/iac/archive/tree/IAC-11/B4/1/IAC-11,B4,1,2,x11640.brief.pdf> 1.1.2
- [17] Sierawski, B.D., Warren, K.M., Sternberg, A.L., Austin, R.A., Trippe, J.M., McCurdy, M.W., Reed, R.A., Weller, R.A., Alles, M.L., Schrimpf, R.D., Massengill, L.W., Fleetwood, D.M., Monteiro, A., Buxton, G.W., Brandenburg, J.C., Fisher, W.B. and Davis, R.: CubeSats and Crowd-Sourced Monitoring for Single Event Effects Hardness Assurance. *IEEE Transactions on Nuclear Science*, vol. 64, no. 1, pp. 293–300, jan 2017. ISSN 0018-9499. Available at: <http://ieeexplore.ieee.org/document/7755840/> 1.1.2, 2.1.1
- [18] Oyewole, S.: Space Research and Development in Africa. *Astropolitics*, vol. 15, no. 2, pp. 185–208, may 2017. ISSN 1477-7622. Available at: <https://www.tandfonline.com/doi/full/10.1080/14777622.2017.1339254> 1.2
- [19] Milne, G., Schoonwinkel, A., du Plessis, J., Mostert, S., Steyn, W., vd Westhuizen, K., vd Merwe, D., Grobler, H., Koekemoer, J. and Steenkamp, N.: SUNSAT - Launch and First Six Month's Orbital Performance. In: *AIAA/USU Conference on Small Satellites*. aug 1999. Available at: <https://digitalcommons.usu.edu/smallsat/1999/all11999/4> 1.2

- [20] Steyn, W., van Zyl, R., Inggs, M. and Cilliers, P.: Current and future small satellite projects in South Africa. In: *2013 IEEE International Geoscience and Remote Sensing Symposium - IGARSS*, pp. 1294–1297. IEEE, jul 2013. ISBN 978-1-4799-1114-1.  
Available at: <http://ieeexplore.ieee.org/document/6723018/> 1.2
- [21] Barnard, A. and Steyn, W.: Low cost TID testing of COTS components. In: *2007 9th European Conference on Radiation and Its Effects on Components and Systems*, pp. 1–4. IEEE, sep 2007. ISBN 978-1-4244-1704-9.  
Available at: <http://ieeexplore.ieee.org/document/5205562/> 1.2, 1.2.1, 2.3.1.1, 4.1.1.3.2
- [22] Petersen, E.: *Single event effects in aerospace*. Wiley-IEEE Press, 2011. ISBN 9780470767498. 1.2.1, 2.1, 2.1.1, 2.6.1, 2.6.1, 2.8
- [23] ECSS: *Single Event Effects Test Method and Guidelines - ESCC Basic Specification No . 25100 Issue 2*. ESA Requirements and Standards Division, 2014. 1.2.2, 2.1.1, 2.2, 2.6, 2.6.5, 2.6.5, 2.7.2, 2.9.1, 2.9.4, 3.2, 5.1.4, A.3.1
- [24] Srour, J.R. and Palko, J.W.: Displacement damage effects in irradiated semiconductor devices. *IEEE Transactions on Nuclear Science*, vol. 60, no. 3, pp. 1740–1766, 2013. ISSN 00189499. 1.2.2
- [25] Felix, J.A., Schwank, J.R., Shaneyfelt, M.R., Baggio, J., Paillet, P., Ferlet-Cavrois, V., Dodd, P.E., Girard, S. and Blackmore, E.W.: Test procedures for proton-induced single event latchup in space environments. *IEEE Transactions on Nuclear Science*, vol. 55, no. 4, pp. 2161–2165, aug 2008. ISSN 00189499. 1.2.2
- [26] Botma, P.J., Barnard, A. and Steyn, W.H.: Low cost fault tolerant techniques for nano/pico-satellite applications. In: *IEEE AFRICON Conference*, pp. 1–5. IEEE, sep 2013. ISBN 9781467359405. ISSN 21530033.  
Available at: <http://ieeexplore.ieee.org/lpdocs/epic03/wrapper.htm?arnumber=6757859> 1.2.2, 4.1.1.2.2, 4.2.2
- [27] Smith, F. and Gaffoor, S.: An amalgamation of hardening methods for single event upset mitigation in memory elements. In: *2016 16th European Conference on Radiation and Its Effects on Components and Systems (RADECS)*, pp. 1–4. IEEE, sep 2016. ISBN 978-1-5090-4366-8.  
Available at: <http://ieeexplore.ieee.org/document/8093150/> 1.2.2, 4.1.1.2.3, 5.1
- [28] Virtanen, A.: Facilities and Radiation Test Methods. In: *Proceedings of 10th International Workshop on Radiation Effects on Semiconductor Devices for Space Applications*, pp. 90–95. 2013. 1.2.3
- [29] Turflinger, T., Haas, T., George, J., Moss, S., Davis, S. and Guertin, S.: Team Update on North American Proton Facilities for Radiation Testing Kenneth A. LaBel-NASA/GSFC. Tech. Rep., NASA, 2016.  
Available at: <https://ntrs.nasa.gov/search.jsp?R=20170001454> 1.2.3, 2.2, 2.7, 2.7.3, 2.5, 1
- [30] Barnard, A., Smit, F., Neveling, R. and Steyn, W.: SEE Proton Testing Facility at iThemba LABS. In: *2018 18th European Conference on Radiation and Its Effects on Components and Systems (RADECS)*. Institute of Electrical and Electronics Engineers Inc., Göteborg, Sweden, 2018. 6, 5.1
- [31] Wertz, J.R. and Larson, W.J.: *Space mission analysis and design*. Microcosm, 1999. ISBN 9780792359012. 2.1

- [32] Schwank, J.R., Shaneyfelt, M.R. and Dodd, P.E.: Radiation Hardness Assurance Testing of Microelectronic Devices and Integrated Circuits: Radiation Environments, Physical Mechanisms, and Foundations for Hardness Assurance. *IEEE Transactions on Nuclear Science*, vol. 60, no. 3, pp. 2074–2100, jun 2013. ISSN 0018-9499.  
Available at: <http://ieeexplore.ieee.org/lpdocs/epic03/wrapper.htm?arnumber=6515710> 2.1, 2.6
- [33] Velazco, R., McMorro, D. and Estela, J. (eds.): *Radiation effects on integrated circuits and systems for space applications*. Springer Nature Switzerland AG, 2019. ISBN 9783030046590.  
Available at: <https://doi.org/10.1007/978-3-030-04660-6> 2.1.1
- [34] Sexton, F.W.: Destructive single-event effects in semiconductor devices and ICs. *IEEE Transactions on Nuclear Science*, vol. 50 III, no. 3, pp. 603–621, jun 2003. ISSN 00189499. 2.1.1
- [35] Bhuvu, B.L., Tam, N., Massengill, L.W., Ball, D., Chatterjee, I., McCurdy, M. and Alles, M.L.: Multi-Cell Soft Errors at Advanced Technology Nodes. *IEEE Transactions on Nuclear Science*, vol. 62, no. 6, pp. 2585–2591, dec 2015. ISSN 00189499. 2.1.1
- [36] Koga, R. and Kolasinski, W.A.: Heavy ion induced snapback in CMOS devices. *IEEE Transactions on Nuclear Science*, vol. 36, no. 6, pp. 2367–2374, 1989. ISSN 15581578. 2.1.1
- [37] Schwank, J.R., Shaneyfelt, M.R. and Dodd, P.E.: Radiation Hardness Assurance Testing of Micro-electronic Devices and Integrated Circuits: Test Guideline for Proton and Heavy Ion Single-Event Effects. *IEEE Transactions on Nuclear Science*, vol. 60, no. 3, pp. 2101–2118, jun 2013. ISSN 0018-9499.  
Available at: <http://ieeexplore.ieee.org/document/6530784/> 2.1.1, 2.4.1, 2.6, 2.9.1
- [38] Bernard, F., Petit, S. and Courtade, S.: Ionizing doses and displacement damage testing of COTS CMOS imagers. In: *International Conference on Space Optics*, p. 102. SPIE-Intl Soc Optical Eng, nov 2008. ISBN 9781510616219. ISSN 1996756X. 2.1.1
- [39] Schwank, J.R., Shaneyfelt, M.R., Ferlet-Cavrois, V., Dodd, P.E., Blackmore, E.W., Pellish, J.A., Rodbell, K.P., Heidel, D.F., Marshall, P.W., LaBel, K.A., Gouker, P.M., Tam, N., Wong, R., Wen, S.-J., Reed, R.A., Dalton, S.M. and Swanson, S.E.: Hardness Assurance Testing for Proton Direct Ionization Effects. *IEEE Transactions on Nuclear Science*, vol. 59, no. 4, pp. 1197–1202, aug 2012. ISSN 0018-9499.  
Available at: <http://ieeexplore.ieee.org/lpdocs/epic03/wrapper.htm?arnumber=6127925> 2.2, 2.5.1, 2.9.1
- [40] Peggs, S.: THE EUROPEAN SPALLATION SOURCE. In: *Proceedings of IPAC2011, San Sebastián, Spain*. 2011.  
Available at: <http://accelconf.web.cern.ch/accelconf/ipac2011/papers/fryba01.pdf> 2.2
- [41] Wei, J., Chen, H., Chen, Y., Chen, Y., Chi, Y., Deng, C., Dong, H., Dong, L., Fang, S., Feng, J., Fu, S., He, L., He, W., Heng, Y., Huang, K., Jia, X., Kang, W., Kong, X., Li, J., Liang, T., Lin, G., Liu, Z., Ouyang, H., Qin, Q., Qu, H., Shi, C., Sun, H., Tang, J., Tao, J., Wang, C., Wang, F., Wang, D., Wang, Q., Wang, S., Wei, T., Xi, J., Xu, T., Xu, Z., Yin, W., Yin, X., Zhang, J., Zhang, Z., Zhang, Z., Zhou, M. and Zhu, T.: China Spallation Neutron Source: Design, R&D, and outlook. *Nuclear Instruments and Methods in Physics Research, Section A: Accelerators, Spectrometers, Detectors and Associated Equipment*, vol. 600, no. 1, pp. 10–13, feb 2009. ISSN 01689002. 2.2

- [42] Borcea, C., Cennini, P., Dahlfors, M., Ferrari, A., Garcia-Muñoz, G., Haefner, P., Herrera-Martínez, A., Kadi, Y., Lacoste, V., Radermacher, E., Saldaña, F., Vlachoudis, V., Zanini, L., Rubbia, C., Buono, S., Dangendorf, V., Nolte, R. and Weierganz, M.: Results from the commissioning of the n\_TOF spallation neutron source at CERN. *Nuclear Instruments and Methods in Physics Research, Section A: Accelerators, Spectrometers, Detectors and Associated Equipment*, vol. 513, no. 3, pp. 524–537, nov 2003. ISSN 01689002. 2.2
- [43] Mansur, L.K., Gabriel, T.A., Haines, J.R. and Lousteau, D.C.: R&D for the Spallation Neutron Source mercury target. *Journal of Nuclear Materials*, vol. 296, no. 1-3, pp. 1–16, jul 2001. ISSN 00223115. 2.2
- [44] Baba, M., Takada, M., Iwasaki, T., Matsuyama, S., Nakamura, T., Ohguchi, H., Nakao, T., Sanami, T. and Hirakawa, N.: Development of monoenergetic neutron calibration fields between 8 keV and 15 MeV. *Nuclear Instruments and Methods in Physics Research, Section A: Accelerators, Spectrometers, Detectors and Associated Equipment*, vol. 376, no. 1, pp. 115–123, jun 1996. ISSN 01689002. 2.2
- [45] PTCOG - Facilities in Operation. 2019.  
Available at: [pt](#) 2.2, 2.5
- [46] JEDEC Solid State Technology Association: EIA/JEDEC Standard 57: Test Procedure for the Management of Single Event Effects in Semiconductor Devices from Heavy Ion Irradiation. dec 1996.  
Available at: <https://www.jedec.org/sites/default/files/docs/jesd57.pdf> 2.2, 2.6, 2.6.1, 2.6.1
- [47] Berner, H.: *The selection and single event upset testing of a DSP processor for a LEO satellite (MSc thesis)*. University of Stellenbosch, 2002.  
Available at: <http://hdl.handle.net/10019.1/53171> 2.3.1.2, 2.3.2.1, 2.5.3, 2.9.4
- [48] Van der Horst, J.G.: *Radiation tolerant implementation of a soft-core processor for space applications (MSc thesis)*. March. University of Stellenbosch, 2007.  
Available at: <http://hdl.handle.net/10019.1/1857> 2.3.1.2, 2.3.2.1, 2.9.4
- [49] de Kock, E.A.: Specification of the proton treatment nozzle in vault BG1 at iThemba LABS. Tech. Rep., iThemba Labs, 2007. 2.3.1.2, 2.5.1, 3.2.1, 3.5.3
- [50] About iThemba LABS. 2019.  
Available at: <https://tlabs.ac.za/about/> 2.3.2, 2.4.1, 1
- [51] Conradie, J.L., Celliers, P.J., Crafford, J.P.A., Delsink, J.L.G., De Villiers, J.G., Du Plessis, .H., Fenemore, R.E.F., Fourie, D.T., Kormany, Z., Manjoo, Y.E., Muller, G.S., Price, G.S., Rohwer, P.F., Sharpey-Schafer, J.F., Steyn, G.F., Van Der Walt, J.T., Van Der Walt, T.N. and Van Niekerk, M.J.: CYCLOTRONS AT ITHEMBA LABS. In: *Proc. of the XVII Int. Conf. on Cycl. and Their Appl.*, pp. 105–109. Tokyo, Japan, 2004.  
Available at: <http://accelconf.web.cern.ch/AccelConf/c04/data/CYC2004{ }papers/20A2.pdf> 2.3.2
- [52] Conradie, J.L., Celliers, P.J., De Villiers, J.G., Delsink, J.L.G., Du Plessis, H., Du Toit, J.H., Fenemore, R.E.F., Fourie, D.T., Kohler, I.H., Lussi, C., Mansfield, P.T., Mostert, H., Muller, G.S., Price, G.S., Rohwer, P.F., Sakildien, M., Thomae, R.W., Van Niekerk, M.J., Van Schalkwyk, P.A., Dietrich, J., Weis, T., Adam, S., Goetz, D. and Schmelzbach, P.A.: IMPROVEMENTS TO THE ITHEMBA LABS CYCLOTRON FACILITIES. In: *Proc. of the XVIII Int. Conf. on Cycl. and Their Appl.*, pp. 140–142. Giardini Naxos, Italy, 2007.  
Available at: <http://www.ghga.com/accelsoft>. 2.3.2

- [53] iThemba LABS Cyclotron Parameters. 2019.  
Available at: <https://tlabs.ac.za/cyclotron-parameters/> 2.3.2
- [54] Conradie, J.L., Anthony, L.S., Baard, S., Bark, R.A., Barnard, A.H., Broodryk, J.I., Cornell, J.C., De Villiers, J.G., Du Plessis, H., Duckitt, W., Fourie, D.T., Gardiner, P., Hogan, M.E., Kohler, I.H., Lussi, C., Mcalister, R.H., Mira, J., Mostert, H.W., Nemulodi, F., Sakildien, M., Steyn, G.F., Stodart, N., Thomae, R.W., Van Niekerk, M.J., Schalkwyk, P.A.V., Andrighetto, A., Monetti, A., Prete, G. and Rossignoli, M.: New Developments at iThemba LABS. In: *Proceedings of Cyclotrons 2016*, pp. 274–277. Zurich, Switzerland, 2016. ISBN 9783954501670. 2.3.2, 2.4.1, 5.3
- [55] Thesnaar, E.J.: *Development of a Radiation Resistant Communication Node for Satellite Sub-Systems (MSc thesis)*. April. University of Stellenbosch, 2014.  
Available at: <http://hdl.handle.net/10019.1/86510> 2.3.2.1, 4.1.1.2.1, 4.1.1.3.1, 5.1
- [56] O'Neill, P.M., Badhwar, G.D. and Culpepper, W.X.: Risk assessment for heavy ions of parts tested with protons. *IEEE Transactions on Nuclear Science*, vol. 44, no. 6 PART 1, pp. 2311–2314, 1997. ISSN 00189499. 2.4.1, 2.6.8
- [57] Lum, G.K., Robinette, L. and Howard, A.: The use of proton testing for evaluating COTS: Example of a commercial camera for ISS. *IEEE Transactions on Nuclear Science*, vol. 48, no. 6 I, pp. 1885–1892, dec 2001. ISSN 00189499. 2.4.1, 2.6.8
- [58] Foster, C.C., O'Neill, P.M. and Kouba, C.K.: Risk assessment based on upset rates from high energy proton tests and monte carlo simulations. *IEEE Transactions on Nuclear Science*, vol. 55, no. 6, pp. 2962–2969, dec 2008. ISSN 00189499. 2.4.1, 2.6.8
- [59] Hiemstra, D.M. and Blackmore, E.W.: LET Spectra of Proton Energy Levels from 50 to 500 MeV and Their Effectiveness for Single Event Effects Characterization of Microelectronics. *IEEE Transactions on Nuclear Science*, vol. 50, no. 6 I, pp. 2245–2250, dec 2003. ISSN 00189499. 2.4.1, 2.6.8
- [60] Ladbury, R., Lauenstein, J.M. and Hayes, K.P.: Use of Proton SEE Data as a Proxy for Bounding Heavy-Ion SEE Susceptibility. *IEEE Transactions on Nuclear Science*, vol. 62, no. 6, pp. 2505–2510, dec 2015. ISSN 00189499. 2.4.1, 2.6.8
- [61] Alia, R.G., Brugger, M., Daly, E., Danzeca, S., Ferlet-Cavrois, V., Gaillard, R., Mekki, J., Poivey, C. and Zadeh, A.: Simplified SEE Sensitivity Screening for COTS Components in Space. *IEEE Transactions on Nuclear Science*, vol. 64, no. 2, pp. 882–890, feb 2017. ISSN 00189499. 2.4.1, 2.6.8
- [62] Subatomic Physics – Quasi mono-energetic Neutron beams. .  
Available at: <https://tlabs.ac.za/subatomic-physics/subatomic-physics-quasi-mono-energetic-neutron-beams/> 2.5.4
- [63] Han, J. and Guo, G.: Characteristics of energy deposition from 1-1000 MeV proton and neutron induced nuclear reactions in silicon. *AIP Advances*, vol. 7, no. 11, p. 115220, nov 2017. ISSN 2158-3226.  
Available at: <http://aip.scitation.org/doi/10.1063/1.4995529> 2.5.4
- [64] Subatomic Physics – K=600 Magnetic Spectrometer. .  
Available at: <https://tlabs.ac.za/subatomic-physics/k600-magnetic-spectrometer/> 2.5.5
- [65] Subatomic Physics – AFRODITE. .  
Available at: <https://tlabs.ac.za/subatomic-physics/afrodite/> 2.5.5



- [66] Lauenstein, J.: Standards for Radiation Effects Testing: Ensuring Scientific Rigor in the Face of Budget Realities and Modern Device Challenges. 2015.  
Available at: <http://ntrs.nasa.gov/search.jsp?R=20150011462> 2.6, 2.3, 2.4
- [67] JEDEC Solid State Technology Association: JEDEC Standard 234: Test Standard for the Measurement of Proton Radiation Single Event Effects in Electronics Devices. oct 2013. 2.6, 2.6.2, 2.9.1, A.3.1
- [68] USA DoD: *MIL-STD-750 - Test Method Standard - Test Methods for Semiconductor Devices*. Department of Defence, USA, 2013.  
Available at: <http://www.assistdocs.com/> 2.6, 2.6.3, 2.6.4
- [69] USA DoD: *MIL-STD-883J(5), Test Method Standard, Microcircuits*. Department of Defence, USA, 2015.  
Available at: <http://www.assistdocs.com/> 2.6, 2.6.4
- [70] ECSS: *Total Dose Steady-State Irradiation Test Method - ESCC Basic Specification No . 22900*. ESA Requirements and Standards Division, 2007. 2.6
- [71] ASTM F01 Committee: ASTM F1192-11, Standard Guide for the Measurement of Single Event Phenomena (SEP) Induced by Heavy Ion Irradiation of Semiconductor Devices. 2011.  
Available at: <http://dx.doi.org/10.1520/f1192-11> 2.6, 2.6.6
- [72] ASTM F01 Committee: Guide for Ionizing Radiation (Total Dose) Effects Testing of Semiconductor Devices. 2012.  
Available at: <http://dx.doi.org/10.1520/f1892-12> 2.6
- [73] ASTM F01 Committee: Guide for Neutron Irradiation of Unbiased Electronic Components. 2011.  
Available at: <http://dx.doi.org/10.1520/f1190-11> 2.6
- [74] USA DoD: *MIL-HDBK-814 - Ionizing dose and neutron hardness assurance guidelines for microcircuits and semiconductor devices*. Department of Defence, USA, 1994.  
Available at: <http://www.assistdocs.com/> 2.6
- [75] Berg, M. and LaBel, K.: NASA Electronic Parts and Packaging Field Programmable Gate Array Single Event Effects Test Guideline Update. Tech. Rep., NASA, 2018.  
Available at: <https://ntrs.nasa.gov/search.jsp?R=20180001945> 2.6, 2.9.1
- [76] USA DoD: *MIL-STD-750-1A - Environmental Test Methods for Semiconductor Devices Part 1: Test Methods 1000 Through 1999*. July. Department of Defence, USA, 2015. 2.6.3
- [77] USA DoD: *MIL-STD-750-5 - Test Method Standard, High Reliability Space Application Test Methods for Semiconductor Devices, Part 5: Test Methods 5000-5999*. Department of Defence, USA, 2012.  
Available at: <http://www.assistdocs.com/> 2.6.3
- [78] JEDEC Solid State Technology Association: JEDEC Standard 89A: Measurement and Reporting of Alpha Particles and Terrestrial Cosmic Ray-Induced Soft Errors in Semiconductor Devices. oct 2006.  
Available at: <http://www.jedec.org/download/search/JESD89A.pdf> 2.6.7
- [79] JYFL: RADEF - Radiation Effects Facility — Fysiikan laitos. 2019.  
Available at: <https://www.jyu.fi/fysiikka/en/research/accelerator/radef> 2.7, 2.7.1, 3.2.1

- [80] Virtanen, A., Harboe-Sorensen, R., Koivisto, H., Pirojenko, S. and Ranttila, K.: High penetration heavy ions at the RADEF test site. In: *2003 7th European Conference on Radiation and Its Effects on Components and Systems, RADECS 2003.*, pp. 499–502. 2003. ISSN 0379-6566. 2.7.1
- [81] Virtanen, A., Harboe-Sorensen, R., Javanainen, A., Kettunen, H., Koivisto, H. and Riihimaki, I.: Upgrades for the RADEF Facility. In: *2007 IEEE Radiation Effects Data Workshop*, vol. 0, pp. 38–41. IEEE, jul 2007. ISBN 1-4244-1464-4.  
Available at: <http://ieeexplore.ieee.org/lpdocs/epic03/wrapper.htm?arnumber=4342538> 2.7.1, 3.2.1
- [82] Javanainen, A., Sillanpaa, M., Trzaska, W.H., Virtanen, A., Berger, G., Hajdas, W., Harboe-Sorensen, R., Kettunen, H., Malkiewicz, T., Mutterer, M., Perkowski, J., Pirojenko, A., Riihimaki, I., Sajavaara, T., Tyurin, G. and Whitlow, H.J.: Experimental Linear Energy Transfer of Heavy Ions in Silicon for RADEF Cocktail Species. *IEEE Transactions on Nuclear Science*, vol. 56, no. 4, pp. 2242–2246, aug 2009. ISSN 0018-9499.  
Available at: <http://ieeexplore.ieee.org/lpdocs/epic03/wrapper.htm?arnumber=5204536> 2.7.1
- [83] Javanainen, A., Trzaska, W.H., Harboe-Sorensen, R., Virtanen, A., Berger, G. and Hajdas, W.: Semi-Empirical LET Descriptions of Heavy Ions Used in the European Component Irradiation Facilities. *IEEE Transactions on Nuclear Science*, vol. 57, no. 4, pp. 1946–1949, aug 2010. ISSN 0018-9499.  
Available at: <http://ieeexplore.ieee.org/lpdocs/epic03/wrapper.htm?arnumber=5550451> 2.7.1
- [84] Hajdas, W., Adams, L., Nickson, B. and Zehnder, A.: The Proton Irradiation Facility at the Paul Scherrer Institute. *Nuclear Instruments and Methods in Physics Research, Section B: Beam Interactions with Materials and Atoms*, vol. 113, no. 1-4, pp. 54–58, 1996. ISSN 0168583X. 2.7.2
- [85] Proton Irradiation Facility Home Page (PIF). 2019.  
Available at: <http://pif.web.psi.ch/pif.htm> 2.7.2
- [86] Hancock, J.: As Proton Centers Struggle, A Sign Of A Health Care Bubble? | Kaiser Health News. 2018.  
Available at: <https://khn.org/news/as-proton-centers-struggle-a-sign-of-a-health-care-bubble/> 2.7.3
- [87] PIF & NIF | TRIUMF : Canada’s particle accelerator centre. 2020.  
Available at: <https://www.triumf.ca/pif-nif> 2.7.3.1
- [88] BIRA-IASB: SPENVIS - Space Environment, Effects, and Education System. 2016.  
Available at: <http://www.spennis.oma.be/> 2.8
- [89] Knoll, G.F.: *Radiation Detection and Measurement, Third Edition*. John Wiley and Sons, Inc., 2000. ISBN 0471073385.  
Available at: <https://books.google.com/books/about/Radiation{ }Detection{ }and{ }Measurement.html?id=HKBVAAAAAMAAJ{ }&pgis=1> 2.9.3.1
- [90] McMahan, M.A., Blackmore, E., Cascio, E.W., Castaneda, C., von Przewoski, B. and Eisen, H.: Standard Practice for Dosimetry of Proton Beams for use in Radiation Effects Testing of Electronics. In: *2008 IEEE Radiation Effects Data Workshop*, pp. 135–141. IEEE, jul 2008. ISBN 978-1-4244-2545-7.  
Available at: <http://ieeexplore.ieee.org/document/4638629/> 2.9.3.1, 3.4.1

- [91] Ziegler, James, F.: SRIM - The Stopping and Range of Ions in Matter. 2017.  
Available at: <http://www.srim.org/> 3.2.1
- [92] Gottschalk, B.: Passive Beam Spreading in Proton Radiation Therapy. Tech. Rep., Harvard High Energy Physics Laboratory, 2004.  
Available at: <http://gray.mgh.harvard.edu/attachments/article/212/pbs.pdf> 3.2.2, 3.4.1, 3.5.3, A.3.1.4
- [93] BLM – Beam Loss Monitor Datasheet. 2018.  
Available at: <https://www.bergoz.com/sites/www.bergoz.com/files/blmdatashetv2.8> 3.3.1, 4.2.3.3.1
- [94] Ash, C.: *The probability tutoring book : an intuitive course for engineers and scientists (and everyone else!)*. IEEE Press, 1993. ISBN 9780780310513. 3.3.2
- [95] Potgieter, J.-P.: *Single event upset testing of flash based field programmable gate arrays (MSc thesis)*. Nelson Mandela Metropolitan University; Faculty of Engineering, the Built Environment and Information Technology, 2015.  
Available at: <http://hdl.handle.net/10948/12520> 3.4.1, 5.1
- [96] Van Aardt, S.: *Total ionizing dose and single event upset testing of flash based field programmable gate arrays (MSc thesis)*. Nelson Mandela Metropolitan University; Faculty of Engineering, the Built Environment and Information Technology, 2015.  
Available at: <http://hdl.handle.net/10948/12548> 3.4.1, 5.1
- [97] Dodds, N.A., Schwank, J.R., Shaneyfelt, M.R., Dodd, P.E., Doyle, B.L., Trinczek, M., Blackmore, E.W., Rodbell, K.P., Gordon, M.S., Reed, R.A., Pellish, J.A., LaBel, K.A., Marshall, P.W., Swanson, S.E., Vizkelethy, G., Van Deusen, S., Sexton, F.W. and Martinez, M.J.: Hardness Assurance for Proton Direct Ionization-Induced SEEs Using a High-Energy Proton Beam. *IEEE Transactions on Nuclear Science*, vol. 61, no. 6, pp. 2904–2914, dec 2014. ISSN 0018-9499.  
Available at: <http://ieeexplore.ieee.org/lpdocs/epic03/wrapper.htm?arnumber=6949165> 3.4.1
- [98] Blackmore, E., Dodd, P. and Shaneyfelt, M.: Improved capabilities for proton and neutron irradiations at TRIUMF. In: *2003 IEEE Radiation Effects Data Workshop*, pp. 149–155. IEEE, 2003. ISBN 0-7803-8127-0.  
Available at: <http://ieeexplore.ieee.org/lpdocs/epic03/wrapper.htm?arnumber=1281368> 3.5.3
- [99] Smith, F.: Single event upset mitigation by means of a sequential circuit state freeze. *Microelectronics Reliability*, vol. 52, no. 6, pp. 1233–1240, jun 2012. ISSN 00262714. 4.1.1.2.3, 5.1
- [100] Smith, F.: A new methodology for single event transient suppression in flash FPGAs. *Microprocessors and Microsystems*, vol. 37, no. 3, pp. 313–318, 2013. ISSN 01419331. 4.1.1.2.3, 5.1
- [101] Omolo, J.: *Mitigation of Single Event Upsets in a Xilinx Artix-7 Field Programmable Gate Array (MSc thesis)*. Nelson Mandela Metropolitan University; Faculty of Engineering, the Built Environment and Information Technology, 2018. 4.2.1.3.4, 4.2.1.4, 5.1
- [102] Malinda, M.: *Characterisation of single event effects and total ionising dose effects of an intel atom microprocessor (MEng thesis)*. Nelson Mandela University; Faculty of Engineering Built Environment and Information Technology, 2019. 4.2.3.3.8, 5.1

- 
- [103] Mosconi, M., Musonza, E., Buffler, A., Nolte, R., Röttger, S. and Smit, F.D.: Characterisation of the high-energy neutron beam at iThemba LABS. *Radiation Measurements*, vol. 45, no. 10, pp. 1342–1345, dec 2010. ISSN 13504487. 5.3
- [104] Belanger-Champagne, C., Blackmore, E., Lindsay, C., Hoehr, C. and Trinczek, M.: Simulation and measurements of collimator effects in proton and neutron radiation testing for single-event effects. *IEEE Transactions on Nuclear Science*, vol. 67, no. 1, pp. 161–168, jan 2020. ISSN 15581578. 5.3